Structural Engineering Report No. ST-96-5

A Distributed Plasticity Formulation for Three-Dimensional Rectangular Concrete-Filled Steel Tube Beam-Columns and Composite Frames

Paul H. Schiller and Jerome F. Hajjar

November 1996

Department of Civil Engineering
Institute of Technology
University of Minnesota
Minneapolis, Minnesota 55455

Abstract

This research presents a fiber-based distributed plasticity finite element formulation for conducting nonlinear analysis of composite frame structures composed of steel wide-flange girders framing into square or rectangular concrete-filled steel tube (CFT) beam-columns. The research focuses on the development of the CFT finite element formulation. A comparable formulation for steel wide-flange members is included, and the model is suitable for conducting geometrically and materially nonlinear analysis of complete three-dimensional frame structures or subassemblies. The current implementation includes structures subjected to monotonic proportional and nonproportional loading; a companion research project has extended this analysis capability to cyclic loading. This formulation is geared for conducting behavioral studies of CFT columns, beams, or beam-columns having a wide range of geometric and material properties for the purpose of developing interaction curves or design recommendations, or for predicting the behavior of experiments of CFT members or composite subassemblies. The model is also suitable for conducting second-order inelastic advanced analysis of composite frame structures for use directly in design, or for conducting second-order inelastic "push-over" analysis to determine the capacity of frame structures subjected to seismic loading.

In this stiffness-based fiber element formulation, element displacement and rotation degrees-of-freedom (DOFs) are located at the centroidal axis of each end cross section of the beam finite element. In addition, the end cross sections are discretized into

a grid of fibers, and the constitutive behavior of each fiber is tracked explicitly during the analysis. The steel material model is adapted from Shen et al. (1995) for both the cold-formed square and rectangular steel tubes, with or without concrete in the tube cavity, and for the steel-wide flange members. The steel computational model exhibits the gradual change in modulus which is seen in heavily cold-worked steel, and the variation in material properties and constitutive behavior between the corners and flanges of rectangular cold-formed steel tubes is accounted for directly in the analysis. The degree to which the steel stress-strain response is rounded may be controlled through input parameters. This allows calibration to a variety of steel types. The current application is intended for use primarily with ASTM A500 Grade B steel (for CFT sections) and ASTM A36 or A572/50 steel (for wide-flange sections). Residual stresses in steel wide-flange sections are also modeled.

The concrete material model is adapted from Chen and Buyukozturk (1985) for inelastic analysis of CFT members with compressive concrete strengths ranging from approximately 20 to 50 MPa, although a small number of CFT experiments with high strength concrete ranging up to 100 MPa are available in the literature and have been verified in this work. The model in compression includes a loading branch which has a gradually decreasing modulus, followed by a descending branch beginning at the peak compressive stress which extends to high strains while retaining some compressive load carrying capacity. Calibration of the descending branch includes consideration of the compressive strength of the concrete as well as the slenderness of the steel tube section to account implicitly for confining action. Tension modeling includes an elastic loading branch which extends to the cracking stress of the material, followed by an immediate loss of load carrying capacity. Crack opening and closing is also permitted.

Slip between the steel and concrete portions of the CFT elements is accounted for in the three-dimensional CFT beam-column element. To accomplish this, the CFT element has separate steel and concrete translational DOFs at each end node, yielding a total of 18 DOFs per element, to permit the connection of CFTs arbitrarily oriented in three-dimensions. Shear deformation compatibility is insured at the element ends

through the use of penalty functions in the global stiffness matrix; this permits slip in the longitudinal direction of the CFT, due either to axial or flexural loading. The virtual work equation of equilibrium is expanded to derive the low and high order geometrically nonlinear stiffness matrices based on the 18 DOFs. A technique is also developed for allow 12 DOF steel wide-flange beam elements to frame into 18 DOF CFT elements to form composite frame systems. The parameters of the constitutive relation governing the behavior of the steel/concrete slip interface are calibrated and verified versus experiments of steel I-girders framing into CFT beam-columns using simple shear connections, and of CFT beams in flexure (for which slip was measured). This CFT slip formulation is capable of modeling behavior ranging from perfect bond to perfect slip, and is particularly effective at detecting slip in the connection regions of steel I-beam-to-CFT connections.

A general purpose structural frame analysis computer program, CFTFiber, has been developed for implementation of this computational formulation. Using this software, computational results are compared to experimental test results for over thirty CFT columns, beams, and beam-columns. The computational results show excellent agreement with published experiments for a large range of geometric and material configurations. The experimental and computational curves match well for the entire loading history for the verification problems. Additional verification is provided by a comparison to a test on a composite subassembly composed of steel wide-flange beams which frame into a CFT beam-column. In addition, the effect of slip on the load carrying capacity and stiffness of CFT beams, columns, and beam-columns is investigated briefly. An analysis example is presented for a full-scale planar composite frame to demonstrate the capability of the formulation.

Acknowledgments

The authors would like to thank the contributions of Dr. H. Shakir-Khalil, University of Manchester, U. K., Dr. S. Morino, Mie University, Japan, Dr. T. Usami, Nagoya University, Japan, Dr. O. Buyukozturk, Massachusetts Institute of Technology, Dr. J. M. Ricles, Lehigh University, Dr. D. W. White, Georgia Institute of Technology, Mr. A. Molodan, University of Minnesota, and Mr. B. C. Gourley, Hammel, Green, and Abrahamson, Minneapolis, Minnesota, for providing details of their work and suggestions for the current research.

This research was supported by the National Science Foundation (Grant No. CMS-9410473) under Dr. Shih-Chi Liu and Dr. M. P. Singh, and the Department of Civil Engineering at the University of Minnesota. This support is gratefully acknowledged. Any opinions, findings, and conclusions or recommendations expressed in this material are those of the authors and do not necessarily reflect the views of the National Science Foundation.

Table of Contents

List of Figures

List of Tables

Chapter 1

Introduction

This research presents the computational formulation for an eighteen degree-of-freedom (DOF) distributed plasticity fiber-based beam finite element to model the behavior of square and rectangular concrete-filled steel tubes (CFT) used as the primary beam-columns in three-dimensional composite frame structures. The distributed plasticity model, based on a beam finite element formulation, discretizes the CFT cross sections at the beam ends into a grid of fibers, and the stress-strain behavior of each steel and concrete fiber is tracked explicitly during the load history. In addition to providing a thorough assessment of cross-section strength, geometrically nonlinear effects are incorporated in this stiffness-based formulation using a corotational approach so as to permit modeling CFT members of any length. In addition, the finite element includes six extra DOFs to account for slip between the steel tube and concrete core which may occur at connection regions or when CFT beams are subjected to flexure. Calibration of the slip model is presented, and a large suite of verification problems are compared to published experimental results of CFTs subjected to proportional and nonproportional monotonic loading.

A fully nonlinear software program has been developed which utilizes the 18 DOF CFT beam element. The program also implements a conventional 12 DOF beam fiber element to model steel wide-flange members. Together, these elements may be used to model composite frames consisting of steel I-girders framing rigidly into concrete-filled steel tube beam-columns. The software provides the capability to simulate the behavior of

CFTs used as beams, columns, beam-columns, or in composite frame structures. It may also be used to conduct parametric studies of CFT members, for example to develop parametric data suitable for use in improving current specification design provisions for the interaction of axial force and bending moment in CFTs (AISC, 1993). The software is also geared for conducting second order elastic or inelastic analysis of complete composite CFT frames for behavioral analysis (such as for use in seismic push-over analysis (Lawson et al., 1994)) or directly for design (SSRC, 1993; Hajjar et al., 1996d).

This chapter provides an overview of the published literature to date on analysis of square or rectangular CFTs. Also presented are the objectives and scope of the current formulation. Finally, the layout of the remaining chapters is discussed.

1.1 Background for Concrete-Filled Tube Computational Modeling

1.1.1 Overview of Experimental Research on Concrete-Filled Steel Tubes

Experimental tests on circular, square, and rectangular concrete-filled steel tubes (CFTs) have been conducted in earnest since the 1950s. Early tests focused on determination of the axial capacity of steel tubes which were filled with concrete or mortar (Klöppel and Goder, 1957). These early tests generally used low to medium strength concrete (Salani and Sims, 1964), and the experimental load histories were relatively simple. More recently, experimental programs have been carried out to determine the complete range of member strength for CFTs subjected to combined axial and flexural loading (Gardner and Jacobson, 1967; Neogi et al., 1969; Bridge, 1976; Tomii and Sakino, 1979a, b; Matsui and Tsuda, 1987; Prion and Boehme, 1989; Shakir-Khalil and Zeghiche, 1989; Shakir-Khalil and Mouli, 1990; Shakir-Khalil, 1991; Matsui et al., 1993, to name a few). These experiments have included proportional and non-proportional loading of short, moderate, and long columns and beam-columns, giving some insight into both the geometrically and materially nonlinear behavior of these members. In addition,

more tests are being conducted on specimens of high strength steel and concrete composition to determine the effect of these materials on member strength and overall behavior (Cederwall et al., 1990; Grauers, 1993; Webb, 1993). A review of much of the experimental literature on CFT beam-columns (in contrast to their connections) published up to 1995 may be found in Gourley et al. (1995).

Experimental research on the behavior of CFT members under cyclic loading has been conducted by Sakino and Tomii (1981), Matsui and Kawano (1988), Kawaguchi et al. (1991a, b), Sugano et al. (1992), Morino et al. (1993), and Hayashi et al. (1995), to name a few. In the past few years, research has also been initiated by Dunberry et al. (1987), Kanatani et al. (1988), Prion and McLellan (1992), Azizinamini and Prakesh (1993a, b), Kato et al. (1993), Shakir-Khalil (1993a, b, c; 1994b), Shakir-Khalil and Hassan (1994a), Shakir-Khalil and Al-Rawdan (1995), Packer (1995), Ricles et al. (1995), Alostaz and Schneider (1996), and others to determine the behavior of connections of steel wide-flange beams to rectangular CFT columns. This research has included investigation of the bond and slip characteristics of the steel-concrete interface at these connections. Much of the research on CFTs under cyclic loading and CFT connections is ongoing (Goel and Yamanouchi, 1992).

The information which has been gained through experimental research has allowed development of building codes and design guidelines for CFTs around the world (Roik and Bergmann, 1992). Much more information is required, however, in order to develop comprehensive building codes which include provisions for geometrically nonlinear behavior, high strength materials, connections, bond and slip, and accurate assessment of strength for CFT members.

1.1.2 Overview of Computational Research on Concrete-Filled Steel Tubes

A complement to experimental testing programs is the development of analysis software which accounts for significant geometrically and materially nonlinear behavior, and is capable of accurate prediction of CFT behavior. The software provides the capability to determine strength and deformation characteristics of a wide range of member sizes and lengths. Fiber analysis has been used, for example, in the development of the interaction equation for steel members which is included in the AISC LRFD Specification (Kanchanalai, 1977; AISC, 1993, 1994), and for comprehensive behavioral studies of steel frame structures (SSRC, 1993; Chen and Toma, 1994).

Several computational models for CFTs can be found in the literature. These models generally accompany experimental research, and they provide valuable insight into the available nonlinear material formulations for CFTs. Following is description of much of the published research on square and rectangular CFTs which include computational modeling.

CFT Cross Section Models

Computational models have been proposed for studying the behavior of circular, square, and rectangular CFTs under various loading conditions. Early models were geared for cross section analysis in order to determine interaction surfaces for zero length members. Grauers (1993) discussed how cross-sectional capacity may be determined using an approach similar to that used for reinforced concrete (ACI, 1995). In this approach, the steel tube is assumed to be plastified, and the concrete is assumed to achieve an ultimate state in which an equivalent rectangular compressive stress block can be defined. This assumes strain compatibility between the steel and concrete, ignores confinement and local buckling, and is not suitable to geometrically nonlinear analysis.

Tomii and Sakino (1979b) presented a computational model for studying the monotonic cross-section strength (moment-curvature-thrust) of rectangular CFTs. The model is essentially a two-dimensional cross-sectional fiber element approach with

material models calibrated to a corresponding set of experimental tests. The material models presented included a bilinear steel model with a parabolic strain hardening region in tension only, and a multilinear concrete model which had a post-failure branch calibrated to match the experimental test results. This model provided satisfactory agreement with the experimental results, but did not provide the capability of analyzing complete members or frames.

Sanz-Picon (1992) and El-Tawil et al. (1993) developed an interactive cross-section strength software program (COSBIAN) for steel beams, reinforced-concrete sections, and concrete-encased steel sections which was modified by Gourley and Hajjar (1994) to analyze rectangular and circular CFTs. This software utilized similar stress-strain curves to Tomii and Sakino (1979b), and it was used to generate a comprehensive set of cross-section interaction diagrams in three-dimensional force space (P-M_y-M_z).

CFT Beam Element Models

A number of researchers have presented computational models for simulating the behavior of CFT beam-columns, generally in two-dimensions for monotonic loading (Bode, 1976; Bridge, 1976; Shakir-Khalil and Zeghiche 1989; Kawaguchi et al., 1991a, b; Tsuji et al., 1991; Roik and Bergmann, 1992; Uy, 1996). Several of these approaches are summarized below.

Chen and Chen (1973) presented a computational model for two-dimensional planar analysis of CFT members using the Column Deflection Curve method. This method is based upon use of an empirical cross-sectional moment-curvature relationship which is evaluated incrementally to obtain curvatures, which in turn are integrated along the length of the member to compute rotation for a given level of moment. The computational results were used to develop moment-thrust interaction diagrams which accounted for member slenderness.

Bridge (1976) briefly presented the results of a computational model for comparison to experimental tests on square CFT beam-columns. The author presented the nonlinear material laws used in the software, including a multilinear steel model to match

the rounded stress-strain curve of the steel observed in his steel coupon tests, and a multilinear concrete model which compared well with a rounded uniaxial concrete stress-strain relationship. The software did not include the capability to model post-collapse behavior. The computational model compared well with experimentally observed lateral deflections for individual eccentrically loaded rectangular CFT beam-columns which were bent about one or both principal axes.

Shakir-Khalil and Zeghiche (1989) presented a planar fiber element formulation for conducting two-dimensional analysis of rectangular CFTs, including provisions for geometrically nonlinear behavior. In their analysis, only two degrees of freedom were modeled at any structural node, including the rotation and the transverse deformation. In one set of analyses, the deflected shape was assumed to be a sine wave. A second set of analyses was also presented using a standard beam element formulation based upon the use of cubic shape functions for modeling flexural deformations, although axial shortening of the member was neglected. The computational models were used to predict the effect of slenderness on the ultimate strength of individual rectangular CFT beam-columns.

Kawaguchi, et al. (1991a) presented a beam-column model for studying the cyclic load-deformation behavior of rectangular CFT members. The model was similar to that of Chen and Chen (1973), in that the moment-curvature relationship was generated for a cross-section, and these results were integrated along the column to obtain rotations. The model accounted for local buckling of the steel tube through an empirical stress-strain relationship for the steel tube. This relationship included definition of the local buckling strain for various points in the steel tube wall, depending upon the distance of the point from the tube corner. The concrete model assumed that the stress in the post-failure portion of the compressive concrete stress-strain curve was equal to the peak compressive stress, to account for confinement. The model was able to match the peak stress under cyclic loading for a set of experimental tests, but was not as accurate in predicting the shape of the load-deformation curve.

Gourley and Hajjar (1994) developed and calibrated a concentrated plasticity (macro) model for three-dimensional square and rectangular CFTs (Hajjar and Gourley,

1996a; Hajjar et al., 1996b, c, d). In this formulation, the materially nonlinear behavior was based on a bounding surface model, which included the use of two nested surfaces, an inner loading surface and an outer bounding surface, in three-dimensional force space. The material nonlinearity was concentrated in plastic hinges of zero length at the member ends. The shape and hardening properties of the loading surfaces in the plasticity model require direct calibration, and the calibration accounts implicitly for such effects as stiffness and strength degradation, a vanishing zone of linear elastic behavior, confinement of the concrete core by the steel tube, and local buckling of the steel tube. This formulation is compact and efficient, especially for analysis of complete composite frames, but it is less suitable for comprehensive analysis of individual CFTs and composite subassemblies since it lacks the capability to simulate the spread of plasticity through CFT elements. A comparable steel wide-flange element was implemented, and a computer program, CFTMacro was presented which performs static and transient dynamic analysis of three-dimensional composite frames using the concentrated plasticity approach. A set of experiments was chosen for calibration and verification that represent a wide range of material and geometric parameters. The computational results match experimental tests for both static and cyclic tests of individual CFTs and of composite subassemblies. The work by Gourley and Hajjar (1994) on analysis of rectangular CFTs directly precedes the current work as part of an ongoing research program at the University of Minnesota. The software developed by Gourley formed the framework for the spread of plasticity analysis software in the current computational model.

Several researchers have conducted analyses of CFTs using three-dimensional continuum analysis, usually in conjunction with presenting experimental results of CFT connections (e.g., Ge and Usami (1992), and Azizinamini and Prakash (1993a, b), Alostaz and Schneider (1996), to name a few). For example, Shakir-Khalil and Al-Rawdan (1996) presented the results of finite element analysis of a rectangular CFT column in the region around a simple steel beam-to-column connection using the finite element software package ABAQUS. The analysis used plate elements for the steel tube walls and brick elements for the concrete core. Contact elements were used between the steel and

concrete to study the effect of connection eccentricity on rotation and distortion of the gusset plate and connection zone. This analysis was not intended to study the load-deformation characteristics of CFTs, but rather to investigate the localized effects around connections which did not penetrate the concrete core. The finite element analysis showed extreme distortion of the steel tube walls in the localized region around the connection plate. This behavior has been observed by Shakir-Khalil (1993c, 1994b) and also by Dunberry et al. (1987) in experimental CFT connection tests. Finite element analysis of this sort is computationally expensive and prohibits investigation of complete structural frames or subassemblies.

1.1.3 Comparison of Existing Models to the Current Computational Formulation

The fiber-based finite element formulation developed in the current research provides an alternative to both concentrated plasticity and continuum element formulations. The fiber element approach uses a discretization scheme to model the gradual plastification of the element ends. This plastification is based on appropriate constitutive models for the steel and concrete rather than on an empirical calibration of the load-deformation behavior of the member, as a concentrated plasticity model uses. By using numerical integration through the cross section and interpolation along the element length, the spread of plasticity in the elements can be tracked with a high degree of accuracy. The fiber element approach also provides computational efficiency when compared to continuum finite element analysis. The current formulation is suitable for studying individual CFT members, composite subassemblies, or entire three-dimensional composite frame structures.

The current computational formulation can be extended to new material types (high strength concrete, or polymer-based composite wraps in lieu of steel tubes, for example) through calibration of the constitutive models, or development of new constitutive models. An additional advantage of the current formulation is the inclusion of slip between the steel and concrete. The macro model formulation is not capable of

accounting for slip, as the ability to track separate material rigidities in the steel and concrete, and of modeling partially plastified element properties, are required for this purpose. The current formulation can also directly model residual stresses in the steel, and variation of nominal material properties through the steel cross section.

1.2 Research Objectives

This work presents a portion of an ongoing computational research program at the University of Minnesota which aims to develop comprehensive formulations for predicting the monotonic and cyclic behavior of square and rectangular CFTs as members of braced or unbraced structural frames comprised of steel wide-flange beams framing into CFT beam-columns. Included in this research is analysis of individual CFT beam-columns, subassemblies of composite frame systems, and complete building structures in order to further the understanding of the behavior of CFTs. In addition, these formulations are suitable for providing a comprehensive assessment of the strength and stability of these types of systems, and are geared for providing the data necessary for enhancing specifications for the design of frames and connections which include CFT members.

The primary objective of the current research thus focuses on the development, calibration, and verification of a fiber-based beam-column finite element for nonlinear analysis of square and rectangular CFTs subjected to monotonic loading. A second objective of the current research is to study the effect of slip between the steel tube and the concrete core in square or rectangular CFTs. Many researchers have commented on the need to better understand how slip affects the overall behavior of CFTs, especially in connection regions (Bridge, 1976; Shakir-Khalil, 1993a, b). Thus, to account for slip, the fiber-based beam finite element presented in this work is based on an 18 degree-of-freedom element which allows slip at the interface between the steel and concrete of a CFT member. This element provides the capability to study the effect of slip at connections and along the length of elements, and to determine whether slip is detrimental

to the strength, stiffness, or ductility of these members. Experimental literature is utilized to determine the stiffness and strength of the nonlinear slip interface.

The computational model formulated in the current research accounts comprehensively for much of the significant geometrically and materially nonlinear behavior of CFTs. Details of the material constitutive model are presented in Molodan and Hajjar (1997) and Hajjar et al. (1996e, f), and are outlined only briefly in this work. In addition to CFT fiber elements, steel wide-flange sections are included in the current analytical model. The steel wide-flange beam fiber element is based on the work of White (1986), although the current research implements a different steel constitutive model. Inclusion of the steel wide-flange beam finite element allows modeling of complete composite frames with distributed plasticity in both the CFTs and the steel members. While the present work is limited to monotonic proportional or non-proportional loading (with elastic unloading permitted), related work by Molodan and Hajjar (1997) extends this research to cyclic analysis.

1.3 Scope of Research

The scope of the current research is outlined in this section. It includes a summary of several of the key assumptions made in the nonlinear formulation, as well as a description of the range of CFT parameters for which the CFT calibration is appropriate.

The low and high order geometrically nonlinear stiffness matrices are derived for the 18 DOF CFT finite element through expansion of the nonlinear terms of the virtual work equation of equilibrium. The stiffness-based, corotational formulation is similar to those presented by White (1986), Clarke (1992), Morales (1994), and Yang and Kuo (1994). The elastic stiffness matrix for a related composite beam element with slip at the steel-concrete interface was presented by Amadio and Fragiacomo (1993), however, inclusion of the geometrically nonlinear stiffness terms and material nonlinearity were not included in this publication. Although advances in composite beam computational

modeling have included semi-rigid connections and materially nonlinear behavior for beams with slip at the steel-concrete interface (Aribert, 1995), a geometrically nonlinear formulation for these types of members has not been published.

A geometrically nonlinear force recovery procedure is adapted from Morales (1994) which accounts for high order terms contributing to the geometrically nonlinear behavior. In addition, a quadratic shape function is adopted for axial deformation in order to more accurately describe the axial behavior of a partially plastified element.

Material nonlinear models which are applicable to proportional and nonproportional monotonic loading are presented for both steel and concrete; the loading may also include strain reversals. A bounding surface plasticity model based on Shen (1993) and Shen et al. (1995) is adopted to model the behavior of the steel fibers in the CFT (Hajjar et al., 1996e, f; Molodan and Hajjar, 1997). A main feature of this formulation is the ability to model the rounding of the stress-strain curve for steel which has been observed experimentally for cold-formed steel tubing (Sully and Hancock, 1994), which is the most common type of tubing used in the United States. The shape of the steel stress-strain curve can be controlled in the analysis through a number of input parameters. These parameters have been calibrated by Molodan and Hajjar (1997) for material similar to ASTM A500 grade B cold-formed rectangular steel tubing. In addition, separate steel properties may be assigned to the corners and the flange regions of the steel tube sections, with a continuous variation of properties around the perimeter of the tube. This modeling also accounts for the residual strains which result from the cold-forming process of the tube.

The compressive concrete stress-strain model is adapted from Chen and Buyukozturk (1985), Buyukozturk and Ameur-Moussa (1988), and Ameur-Moussa and Buyukozturk (1990). Like the steel formulation, this model is also a bounding surface plasticity formulation, with a failure surface that defines the initiation of compressive failure. The size of the failure surface is a function of an accumulated damage parameter which increases with compressive loading, especially in the post-peak region of the stress-strain curve. The parameters and calibrated equations which determine the accumulation

of damage have been extended significantly from the scope of the published results from the original papers. Molodan and Hajjar (1997) presents a full description of the adaptation of the compressive concrete model for use in the current application. A tensile concrete model is also implemented which accounts for elastic tensile loading and cracking (ASCE, 1982). Crack opening and closing on strain reversal are modeled in this formulation. The concrete model is currently calibrated and verified for concrete strengths ranging from 20-50 MPa, although a small number of experimental comparisons are included in this work for members having concrete strengths of 100 MPa.

As mentioned previously, the current work considers only proportional and non-proportional monotonic loading. Single strain reversals are expected under these loading conditions, however. The material models used in the current formulation include full capability to model strain reversals in tension and compression. These models are extended to include cyclic capability by Molodan and Hajjar (1997).

Several simplifying assumptions are required in the development of the CFT fiber element in order to limit the scope of the current research.

1. Plane sections that are initially plane and perpendicular to the centroidal axis are assumed to remain so (Euler-Bernoulli beam theory is assumed).
2. Torsional deformations are based on the initial elastic torsional rigidity of the element (i.e., material nonlinearity due to torsion is neglected). In addition, shear deformations associated with beam flexure are neglected.
3. The geometrically nonlinear terms associated with the bowing effect are neglected in the current formulation.
4. Flexural-torsional and lateral-torsional buckling are not detected by the current model, as these buckling modes are rare in CFTs.
5. Analysis is not continued beyond the limit point of the structure.

There are several local material phenomena which are not included in the current computational formulation. Many researchers have commented on the effect of

confinement in square and rectangular CFTs. It is generally agreed that these members provide little confining stress to the concrete core (Council on Tall Buildings and Urban Habitat, 1979). The ductility of the concrete is markedly improved, however (Chen and Chen, 1973). In the current formulation, concrete confinement is modeled approximately through modification of the compressive unloading slope of the concrete stress-strain curve (Hajjar et al., 1996e; Molodan and Hajjar, 1997). A similar approach was used by Tomii and Sakino (1979b) to account for confinement in cross-sectional analysis of square CFTs. The material models used in the current analysis are, however, multiaxial formulations which have been implemented here (with only uniaxial stress-strain behavior being activated) so as to permit extension of the CFT finite element model to future work which accounts directly for the effects of confinement.

A second effect which is not modeled directly is local buckling of the steel tube. Although the concrete core delays the onset of local buckling, many experimentalists have observed local buckling during testing of rectangular CFTs. This behavior often accompanies plastification of the steel tube at or near the limiting strength of the member. As the current formulation is intended only for pre-collapse analysis of composite frames, assuming no substantial change in behavior due to local buckling is adequate for the current application.

1.4 Organization of Report

Chapter 2 presents the finite element formulation for the 18 DOF beam finite element which is used to model CFTs in the current analysis. A virtual work formulation is employed which takes advantage of corotational kinematics to describe element deformations. The derivation of the low and high order geometrically nonlinear stiffness and force recovery terms is presented. Issues related to implementation of the 18 DOF element in a structural analysis computer code are also presented. Finally, the materially and geometrically nonlinear incremental solution procedure is presented.

Chapter 3 presents the calibration of the nonlinear slip model which is implemented in the current analysis. Experimental tests on rectangular CFT columns and connections are used to calibrate the strength and stiffness of the slip interface. Comparisons to experimental connection tests and beam tests demonstrate the capability of the slip model.

Chapter 4 outlines the nonlinear material models used for the CFT and steel wide-flange elements. Material behavior which is specifically important for square or rectangular CFTs (such as varying material properties caused by cold-forming) is discussed. A detailed description of the nonlinear material models is beyond the scope of this work, but may be found in Molodan and Hajjar (1997).

Chapter 5 presents comparisons of analyses which utilize the 18 DOF CFT beam element to experiments of square and rectangular CFT beams, columns, beam-columns, and subassemblies under proportional and non-proportional monotonic loading. A final example consisting of a multistory planar composite frame with steel wide-flange beams framing rigidly into CFT columns is analyzed to demonstrate the capabilities of the current finite element formulation. The geometrically and materially nonlinear behavior of the frame is described, as well as the slip which is observed for this example problem. The effect of slip on the strength and deformation of the frame is discussed.

Chapter 6 presents a summary discussion of the current computational model, particularly the accuracy of the analysis as compared to experiments of square and rectangular CFTs. General observations are made about the behavior of the 18 DOF beam finite element, the effect of slip in CFTs on overall frame behavior, and implications for structural design, building codes, and future research.

Chapter 2

Finite Element Formulation Including Interlayer Slip

Conventional beam finite elements for analysis of frame structures have typically been formulated with 3 translational and 3 rotational degrees-of-freedom (DOFs) at each end for a total of 12 DOFs per element. The occurrence of slip between the steel and concrete portions of a CFT beam-column requires additional DOFs in order to properly model the differential movement between these materials in space. To accommodate this movement, the current formulation adds three additional translational DOFs to each end of a 12 DOF beam finite element. These additional DOFs allow the steel and concrete independent axial deformations while retaining rotational and shear deformation compatibility. The shear deformation compatibility is ensured through the use of penalty functions in the global stiffness matrix (Zienkiewicz, 1977; Bathe, 1982).

In this chapter, a stiffness-based 18 DOF beam finite element is developed for geometrically and materially nonlinear analysis of CFT members. The low and high order geometric stiffness matrices for an 18 DOF element with interlayer slip are derived through expansion of the virtual work equation of equilibrium. An updated Lagrangian (UL) incremental formulation is employed for recovery of element strains (Bathe, 1982). The fiber element method is employed to model the spread of material nonlinearity through the element cross section. Shape functions are used to describe the change in stiffness along the element length for an element which is partially plastified (White, 1986).

Chapter 2 is structured as follows. Section 2.1 presents the derivation of the 18 DOF geometrically linear and nonlinear stiffness matrices. Section 2.2 presents issues related to the implementation of the 18 DOF element in a three-dimensional frame structure composed of both 18 DOF elements and conventional 12 DOF elements, and issues related to the use of penalty functions in the global stiffness matrix. Section 2.3 discusses the recovery of incremental element strains from incremental global displacements, and the procedure for materially nonlinear analysis. Finally, Section 2.4 presents the global iterative solution strategy which is developed for the analysis of space frames composed of both 12 and 18 DOF elements with geometrically and materially nonlinear behavior.

2.1 Derivation of Element Stiffness Matrices

This section presents the derivation of the linear elastic stiffness matrix as well as the low and high order geometric stiffness matrices for the 18 DOF beam finite element. The model for slip between the steel and concrete is adapted from the composite beam finite element presented by Amadio and Fragiacomo (1993). The element stiffness matrices are derived by expanding the virtual work equation of equilibrium following Bathe (1982), White (1986), and Yang and Kuo (1994).

2.1.1 The Virtual Work Equation of Equilibrium

The virtual work equation of equilibrium for a structural element has been presented by Bathe (1982):

$$\int_{^2V} {}^2\tau_{ij}\delta_2 e_{ij}\,{}^2dV = \int_{^2S} {}^2t_i\delta_2 u_i\,{}^2dS + \int_{^2V} {}^2f_i\delta_2 u_i\,{}^2dV \tag{2.1}$$

where: ${}^2V$ is the volume of the element in configuration C2

${}^2S$ is the surface of the element in configuration C2

${}^2\tau_{ij}$ is the Cauchy stress tensor measured in configuration C2

${}_2e_{ij}$ is the engineering strain tensor measured with respect to configuration C2

${}_2u_i$ are the element deformations measured with respect to configuration C2

${}^2t_i$ are the surface tractions in configuration C2

${}^2f_i$ are the body forces in configuration C2

Following the notation of Bathe (1982), left superscripts denote the configuration in which a quantity is measured, and left subscripts denote a reference state. In this work, the unknown state (or current configuration) will be referred to as configuration C2, the most recent converged state (or reference configuration) will be referred to as configuration C1, and the initial undeformed state will be referred to as configuration C0.

Equation 2.1 is valid for any combination of applied tractions and resultant stresses. This equation expresses the equilibrium for an arbitrary element volume, where the left side of the equation represents the virtual strain energy of the element and the right side of the equation represents the external work done by surface tractions and body forces acting through a virtual displacement (Bathe, 1982; Yang and Kuo, 1994). In the current work, body forces are neglected; therefore the second integral on the right hand side will be omitted hereafter.

The principle of virtual work has the advantage of being applicable to path-dependent material and loading. In addition, geometrically nonlinear effects can be easily considered through inclusion of the nonlinear strain components of the virtual work equation of equilibrium, as will be shown in the following sections (Yang and Kuo, 1994).

2.1.2 Addition of Strain Energy Due to Slip

Amadio and Fragiacomo (1993) presented a two-dimensional layered composite beam element to model the slip between an elastic steel beam and concrete modeled as a viscoelastic material to capture creep and shrinkage. This model proved accurate for determining the monotonic load-deflection behavior of composite beams. This model is adapted to simulate the slip which occurs between the steel tube and concrete core of a CFT beam-column due to beam shear and axial load transfer at connections (see also Chapter 3). In addition, geometric and material nonlinear capability is added to the Amadio and Fragiacomo model by expanding the nonlinear terms of the virtual work equation of equilibrium. This model has been further extended to cyclic analysis of CFTs by Molodan and Hajjar (1997).

For the purposes of deriving a beam-column stiffness matrix, the steel and concrete volumes are separated in the virtual work equation of equilibrium. The steel and concrete are assumed to be separated by a layer of nonlinear springs which determine the load transfer between the two materials based on a spring stiffness. The virtual work equation of equilibrium (Eq. 2.1) must therefore be modified to include the strain energy associated with the deformation of the layer of springs. Equation 2.2 presents the virtual work equation of equilibrium with the steel and concrete portions as separate integrals and the strain energy of the slip layer included as a new term on the left hand side of the equation. In this equation, a right superscript *c* denotes concrete and a right superscript *s* denotes steel.

$$\int_{^2V^c} {}^2\tau_{ij}^c \delta_2 e_{ij}^{c\,2} dV^c + \int_{^2V^s} {}^2\tau_{ij}^s \delta_2 e_{ij}^{s\,2} dV^s + \int_{^2I} {}^2\pi\, \delta_2 \psi^2 dI = \int_{^2S^c} {}^2t_i^c \delta_2 u_i^{c\,2} dS^c + \int_{^2S^s} {}^2t_i^s \delta_2 u_i^{s\,2} dS^s \tag{2.2}$$

where: ${}^2I$ is the steel-concrete interface in C2 (units of length^2)

${}^{2}\pi$ is the force transferred between the steel and concrete portions of the element through the slip layer per unit area of the interface (units of force/length^2)

${}_{2}\psi$ is the slip between the steel and the concrete at a point along the element length (units of length)

2.1.3 Updated Lagrangian Incremental Formulation

The updated Lagrangian (UL) incremental formulation is adopted for the current work in order to account for significant geometric nonlinear behavior and path-dependent material behavior. This formulation follows the work of White (1986) and Yang and Kuo (1994). The UL formulation employs the second Piola- Kirchhoff (PK2) stress and Green-Lagrange (GL) strain (Bathe, 1982). Unlike Cauchy stress and infinitesimal strain which are measured with respect to an axis fixed in space, PK2 stress and GL strain are measured with respect to a local coordinate system which moves with the rigid body motion of the element (White, 1986).

Using PK2 stress and GL strain, a virtual displacement relationship can be developed which references the known configuration, and which is accurate for problems involving moderate rigid body rotations and small incremental strains. Expressing Eq. 2.2 in terms of PK2 stress and GL strain, and assuming small incremental strains (and therefore a small volume change between the reference configuration, C1, and the current configuration, C2), Eq. 2.3 can be derived (Yang and Kuo, 1994).

$$\int_{{}^{1}V^{c}} {}_{1}^{2}S_{ij}^{c}\delta_1\varepsilon_{ij}^{c\,1}dV^{c} + \int_{{}^{1}V^{s}} {}_{1}^{2}S_{ij}^{s}\delta_1\varepsilon_{ij}^{s\,1}dV^{s} + \int_{{}^{1}I} {}^{2}\pi\,\delta_2\psi^{1}dI = \int_{{}^{1}S^{c}} {}^{2}t_i^{c}\delta_1 u_i^{c\,1}dS^{c} + \int_{{}^{1}S^{s}} {}^{2}t_i^{s}\delta_1 u_i^{s\,1}dS^{s} \tag{2.3}$$

where: ${}_{1}^{2}S_{ij}$ is the PK2 stress measured at C2 with respect to C1

${}_1\varepsilon_{ij}$ is the GL strain measured with respect to C1

Using an incremental approach, White (1986) and Yang and Kuo (1994) show that the PK2 stress can be assumed to be equivalent to the Cauchy stress at C1 plus the increment in PK2 stress from C1 to C2. In addition, the incremental PK2 stress terms can be replaced in the virtual work equation of equilibrium by considering the constitutive relationship between PK2 stress and GL strain. Bathe notes that the constitutive tensor developed for Cauchy stress and engineering strain can be used to represent the constitutive relationship between PK2 stress and GL strain. Also, because of the invariance of PK2 stress and GL strain under rigid body motions, "the use of the relation ... is completely equivalent to using Hooke's Law in infinitesimal displacement conditions" (Bathe, 1982). Equation 2.4 shows these relationships:

$${}_1^2S_{ij} = {}^1\tau_{ij} + \Delta S_{ij} = {}^1\tau_{ij} + {}_1C_{ijkl}\Delta\varepsilon_{ij} \tag{2.4}$$

where: Δ represents the change over the increment C1 to C2

${}_1C_{ijkl}$ is the material constitutive tensor in configuration C1

Equation 2.5 shows how the GL strain is conventionally separated into linear and nonlinear terms. This separation aids in the expansion of the virtual work equation of equilibrium because the higher order terms are more readily identifiable:

$${}_1\varepsilon_{ij} = {}_1e_{ij} + {}_1\eta_{ij} \tag{2.5}$$

where: ${}_1e_{ij}$ are the linear GL strain terms (equivalent to the infinitesimal strain)

${}_1\eta_{ij}$ are the nonlinear GL strain terms

By employing the simplifying relations described above, the incremental form of the virtual work equation of equilibrium with separate steel and concrete volumes can be written as follows (White, 1986):

$$\int_{{}^1V} C^c_{ijkl}\Delta e^c_{kl}\delta_1 e^{c\,1}_{ij}dV^c + \int_{{}^1V} \tau^c_{ij}\delta_1 \eta^{c\,1}_{ij}dV^c +$$
$$\int_{{}^1V} C^c_{ijkl}\Delta e^c_{kl}\delta_1 \eta^{c\,1}_{ij}dV^c + \int_{{}^1V} C^c_{ijkl}\Delta \eta^c_{kl}\delta_1 \eta^{c\,1}_{ij}dV^c + \int_{{}^1V} C^c_{ijkl}\Delta \eta^c_{kl}\delta_1 e^{c\,1}_{ij}dV^c +$$
$$\int_{{}^1V} C^s_{ijkl}\Delta e^s_{kl}\delta_1 e^{s\,1}_{ij}dV^s + \int_{{}^1V} \tau^s_{ij}\delta_1 \eta^{s\,1}_{ij}dV^s + \qquad (2.6)$$
$$\int_{{}^1V} C^s_{ijkl}\Delta e^s_{kl}\delta_1 \eta^{s\,1}_{ij}dV^s + \int_{{}^1V} C^s_{ijkl}\Delta \eta^s_{kl}\delta_1 \eta^{s\,1}_{ij}dV^s + \int_{{}^1V} C^s_{ijkl}\Delta \eta^s_{kl}\delta_1 e^{s\,1}_{ij}dV^s +$$
$$\int_{{}^1I} \Delta\pi\ \delta_1\psi^1 dI = \Delta\Re$$

where: $\Delta\Re$ is the incremental applied load such that:

$$\Delta\Re = \int_{{}^1S^c} {}^2t^c_i\delta_2 u^{c\,1}_i dS^c + \int_{{}^1S^s} {}^2t^s_i\delta_2 u^{s\,1}_i dS^s -$$
$$\int_{{}^1V} {}^1\tau^c_{ij}\delta_1 e^{c\,1}_{ij}dV^c - \int_{{}^1V} {}^1\tau^s_{ij}\delta_1 e^{s\,1}_{ij}dV^s - \int_{{}^1I} {}^1\pi\ \delta_1\psi^1 dI$$

${}^2\pi = {}^1\pi + \Delta\pi$ (see Section 2.1.5)

Yang and Kuo (1994) suggest, for a 12 DOF element, that an approximate geometrically nonlinear solution can be obtained by considering only the first, second, sixth and seventh integrals on the left hand side of Eq. 2.6, since the remaining terms represent products of strain increments, which are assumed to be small. The resulting equation is linear in the displacements and can be expanded to obtain linear elastic and geometrically nonlinear tangent stiffness matrices.

Morales (1994) suggests a method for considering all of the nonlinear terms in the force recovery except those associated with the bowing effect (elongation of the centroidal axis due to flexural bowing). This method recognizes that the third and fourth integrals on the left hand side of Eq. 2.6 can be approximated as the increment in concrete stress over the load increment. The same simplification is made for the incremental steel stresses associated with the eighth and ninth integrals. A strategy for updating the element geometric stiffness during incremental force recovery to include these terms is

also presented by Morales (1994). This scheme will be adopted in order to include in the force recovery the higher order geometric stiffness terms of the virtual work equation of equilibrium associated with the incremental stresses (see Section 2.3.1). Equation 2.7 gives the form of the virtual work equation of equilibrium used in this work to derive the CFT element linear elastic and geometrically nonlinear tangent stiffness matrices, as well as the nonlinear terms used only during force recovery. The third and sixth terms are derived from terms which are nonlinear in the displacements, and they are a function of the stress increment during the current increment; consequently they are not used to form the tangent stiffness matrix at the beginning of an increment. However, they will be included in element force recovery (see Section 2.3.1) using the technique presented by Morales (1994).

$$\begin{aligned}
&\int_{{}^1V} {}_1C^c_{ijkl}\Delta e^c_{kl}\delta_1 e^{c\,1}_{ij}\,dV^c + \int_{{}^1V} {}^1\tau^c_{ij}\delta_1\eta^{c\,1}_{ij}\,dV^c + \int_{{}^1V}\Delta\tau^c_{ij}\delta_1\eta^{c\,1}_{ij}\,dV^c + \\
&\int_{{}^1V} {}_1C^s_{ijkl}\Delta e^s_{kl}\delta_1 e^{s\,1}_{ij}\,dV^s + \int_{{}^1V} {}^1\tau^s_{ij}\delta_1\eta^{s\,1}_{ij}\,dV^s + \int_{{}^1V}\Delta\tau^s_{ij}\delta_1\eta^{s\,1}_{ij}\,dV^s + \\
&\int_{{}^1I}\Delta\pi\,\delta_1\psi\,{}^1dI = \Delta\Re
\end{aligned} \tag{2.7}$$

where: $\Delta\tau^c_{ij}$ is the increment in the concrete stress tensor from C1 to C2

$\Delta\tau^s_{ij}$ is the increment in the steel stress tensor from C1 to C2

Equation 2.7 neglects elongation of the element centroid due to bowing (i.e., integrals five and ten in Eq. 2.6 are thus neglected in both the element stiffness and the force recovery formulations of this work).

2.1.4 Corotational Reference Axes

Thus far, the virtual work equation of equilibrium has been written in terms of stresses and strains. The stiffness of structural elements, however is generally formulated in terms of force and deformation with respect to a reference axis. A corotational formulation is adopted in the present work which is consistent with the updated Lagrangian incremental formulation. A description of this approach is provided by Stolarski et al. (1995):

> In this approach the deforming body (or a part of it, like a finite element or particle's neighborhood) is observed from the point of view of a frame which 'closely' follows the body (its part), or, in other words, 'corotates' with it. Displacements relative to that corotating frame, termed *deformational*, are clearly the only ones affecting strains.

Numerous references are given by Stolarski which support the use of this approach for a variety of structural finite elements.

The specific corotational, or natural, axes for the CFT beam-column are shown in Fig. 2.1. The local x-axis connects the geometric center of the i and j ends of the member, and the local y and z-axes define the major and minor principal axes of the cross section at the i end of the member.

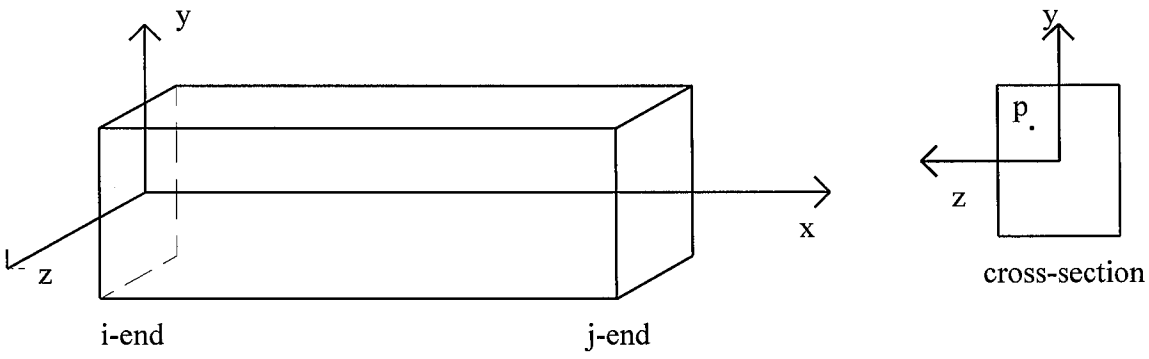

Figure 2.1: Element Corotational Axes at Configuration C1

For the current 18 DOF beam-column element, the steel and concrete nodes both lie upon the centroidal axis of the member, but need not coincide with each other at either end of the member. The corotational axes are assumed to coincide with the steel nodes of the 18 DOF finite element at the beginning of each load increment.

Assuming that cross sections which are plane and normal to the centroidal axis at the beginning of analysis remain plane and normal during deformation, the deformation of the point p in Fig. 2.1 can be completely described by the deformation of the centroidal axis of the member. In addition, the shear strains are assumed to be equal to zero, thus the tensor notation of the equations used in the previous sections can be reduced to the uniaxial component. Equation 2.8 gives the simplified relationship for the three dimensional element of Fig. 2.1, where the incremental deformation of the centroidal axis is given by $(\Delta u_c, \Delta v_c, \Delta w_c)$ and the incremental deformation of any point p is given by $(\Delta u, \Delta v, \Delta w)$ (Yang and Kuo, 1994). Positive $(\Delta u, \Delta v, \Delta w)$ is in the direction of the corotational axes, with positive rotations shown in Fig. 2.4 of Section 2.1.8.

$$\begin{aligned} \Delta u^c &= \Delta u_c^c - y\Delta v_c' - z\Delta w_c' \\ \Delta u^s &= \Delta u_c^s - y\Delta v_c' - z\Delta w_c' \\ \Delta v &= \Delta v_c - z\Delta\theta_x \\ \Delta w &= \Delta w_c + y\Delta\theta_x \end{aligned} \tag{2.8}$$

where: ' denotes differentiation with respect to x

$\Delta\theta_x$ is the incremental torsional rotation of the element

(x, y, z) define a point in the cross section

Using derivatives of Eq. 2.8, the incremental axial strain (Δe_{xx}) and the incremental shear strains (Δe_{xy} and Δe_{xz}) at any point in the element volume can be formulated in terms of the incremental deformations of the centroidal axis and the position in the element. Equation 2.9 presents the incremental element axial strains

(Yang and Kuo, 1994). In this work, the incremental shear strains are assumed to be zero throughout the analysis (White, 1986).

$$\Delta e_{xx}^{c} = \Delta u'^{c} = \Delta u'^{c}_{c} - y\Delta v_{c}'' - z\Delta w_{c}''$$
$$\Delta e_{xx}^{s} = \Delta u'^{s} = \Delta u'^{s}_{c} - y\Delta v_{c}'' - z\Delta w_{c}'' \qquad (2.9)$$

2.1.5 Slip Layer Kinematics

The current analytical formulation is intended to model the behavior of CFT beam-columns in which the two materials are allowed to slip along the centroidal axis with respect to each other. This type of formulation has been applied to composite beams composed of a steel girder and a concrete deck which are connected by a line of shear connectors. Kinematic models have been proposed which account for both the deformation of the connectors and the time dependent characteristics of the concrete (Bradford and Gilbert, 1992; Amadio and Fragiacomo, 1993; Aribert, 1995). These models have been shown to be accurate for modeling the time-dependent behavior of composite beams, and are also accurate for modeling the stiffness of a composite member if the material characteristics are time-independent (Al-Amery and Roberts, 1990). The current model assumes that the behavior of the materials is time-independent.

CFTs present a special case of the above mentioned models in two ways: First, the centroidal axes of the steel tube and the concrete core coincide in the initial state (C0) of the beam. Slip is therefore not induced due to flexure until the section becomes non-symmetric. The non-symmetry is caused by plastification of the steel and concrete, and also by cracking of the concrete in tension. Lu and Kennedy (1994) noted slip during pure flexure tests of rectangular CFTs, indicating that such behavior is probable in these members. Second, the slip interface of a CFT is a continuous surface which, for this work, relies on friction and bond for the transfer of forces (Shakir-Khalil, 1993a), rather than a line of shear connectors (as a composite beam might have). The stress-strain

characteristics of the slip interface for a rectangular CFT must therefore be examined to determine this relationship (see Chapter 3).

The kinematic relationships for a CFT beam-column with interlayer slip are based on a number of assumptions. The steel and concrete layers are assumed to be separated by a layer of nonlinear slip springs which allow the steel and concrete to exchange load based upon the stress-strain characteristics of the springs. However, since the concrete is encased within the steel, the two materials must take on the same shape for transverse displacement and rotation. Section 2.2 shows how penalty functions are used in the global stiffness matrix to impose the necessary shear constraints. The rotational constraints are imposed during expansion from corotational stiffness to element stiffness (see Appendix A).

The proposed slip model is shown in Fig. 2.2. As previously mentioned, the two materials are assumed to take on the same transverse displacement, and therefore slip stress is only caused by differential axial strain between the steel and concrete layers. This differential axial strain can be computed directly by considering the interpolation functions for axial displacement of the two materials (see Eq. 2.17). Since the geometric centers of the two materials coincide, the same corotational axes can be used for both materials.

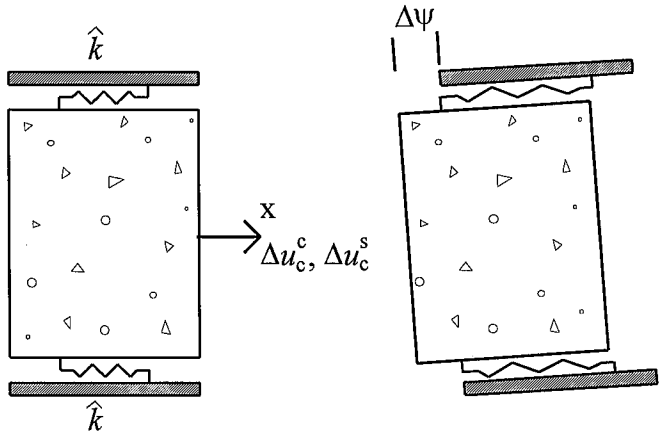

Figure 2.2: Finite Element Slip Model

The incremental deformation in the spring layer, $\Delta\psi$, is thus given by:

$$\Delta\psi = \Delta u_c^s - \Delta u_c^c \tag{2.10}$$

Equation 2.11 gives the equilibrium equation used to relate the incremental load transfer between the two materials per area of interface, $\Delta\pi$, and the incremental deformation of the spring layer, $\Delta\psi$ (Amadio and Fragiacomo, 1993). The stress in the slip layer is written in an incremental form which is similar to the incremental form of the material stress-strain relationship of Eq. 2.4.

$$^2\pi = {}^1\pi + \Delta\pi = {}^1\pi + \hat{k}\Delta\psi \tag{2.11}$$

where: $\hat{k}$ is the tangent stiffness of the interface (units of force/length^3)

The incremental linearization of the relationship allows the slip interface stiffness, $\hat{k}$, to be updated at the beginning of each global load increment. The nonlinear slip interface stiffness is thus assumed to be incrementally linear in the current formulation.

2.1.6 The Virtual Work Equation of Equilibrium in Expanded Form

The virtual work equation of equilibrium (Eq. 2.7) can be expanded by substitution of the expressions for strain developed in previous sections. The expanded form of the equation takes advantage of the simplifications which have been presented, in particular the assumption that the shear stresses and strains are zero. Equation 2.12 gives the notation that is used to represent the uniaxial components of stress and strain, as well as the simplified stress-strain constitutive tensor, which can now be represented by a scalar. The nonlinear term of the GL strain is also presented in expanded form (Bathe, 1982; White, 1986).

$$
\begin{aligned}
{}^1\tau_{ij}^c &= {}^1\tau_{11}^c = {}^1\tau^c & \delta_1 e_{ij}^c &= \delta_1 e_{xx}^c \\
{}^1\tau_{ij}^s &= {}^1\tau_{11}^s = {}^1\tau^s & \delta_1 e_{ij}^s &= \delta_1 e_{xx}^s \\
{}_1C_{ijkl}^c &= {}_1C_{1111}^c = {}_1E^c & \Delta e_{ij}^c &= \Delta e_{xx}^c \\
{}_1C_{ijkl}^s &= {}_1C_{1111}^s = {}_1E^s & \Delta e_{ij}^s &= \Delta e_{xx}^s \\
\Delta\eta_{ij}^c &= \Delta\eta_{xx}^c = \frac{1}{2}\left[\left(\Delta u'^c\right)^2 + \left(\Delta v'^c\right)^2 + \left(\Delta w'^c\right)^2\right] \\
\Delta\eta_{ij}^s &= \Delta\eta_{xx}^s = \frac{1}{2}\left[\left(\Delta u'^s\right)^2 + \left(\Delta v'^s\right)^2 + \left(\Delta w'^s\right)^2\right] \\
\delta_1\eta_{ij}^c &= \delta_1\eta_{xx}^c = \Delta u'^c\delta_1 u'^c + \Delta v'^c\delta_1 v'^c + \Delta w'^c\delta_1 w'^c \\
\delta_1\eta_{ij}^s &= \delta_1\eta_{xx}^s = \Delta u'^s\delta_1 u'^s + \Delta v'^s\delta_1 v'^s + \Delta w'^s\delta_1 w'^s
\end{aligned}
\tag{2.12}
$$

These relationships are substituted into the virtual work equation of equilibrium (Eq. 2.7) resulting in the following form of the equation:

$$
\begin{aligned}
&\int_{{}^1V} {}_1E^c(\Delta u'^c_c - y\Delta v_c'' - z\Delta w_c'')(\delta_1 u'^c_c - y\delta_1 v_c'' - z\delta_1 w_c'')\,{}^1dV^c + \\
&\int_{{}^1V} {}^1\tau^c(\Delta u'^c\delta_1 u'^c + \Delta v'\delta_1 v' + \Delta w'\delta_1 w')\,{}^1dV^c + \\
&\int_{{}^1V} \Delta\tau^c(\Delta u'^c\delta_1 u'^c + \Delta v'\delta_1 v' + \Delta w'\delta_1 w')\,{}^1dV^c + \\
&\int_{{}^1V} {}_1E^s(\Delta u'^s_c - y\Delta v_c'' - z\Delta w_c'')(\delta_1 u'^s_c - y\delta_1 v_c'' - z\delta_1 w_c'')\,{}^1dV^s + \\
&\int_{{}^1V} {}^1\tau^s(\Delta u'^s\delta_1 u'^s + \Delta v'\delta_1 v' + \Delta w'\delta_1 w')\,{}^1dV^s + \\
&\int_{{}^1V} \Delta\tau^s(\Delta u'^s\delta_1 u'^s + \Delta v'\delta_1 v' + \Delta w'\delta_1 w')\,{}^1dV^s + \\
&\int_{{}^1I} \hat{k}(\Delta u_c^s - \Delta u_c^c)(\delta_1 u_c^s - \delta_1 u_c^c)\,{}^1dI = \Delta\Re
\end{aligned}
\tag{2.13}
$$

The first and fourth integrals of Eq. 2.13 are conventionally referred to as the *small displacements* terms, whereas the second and fifth integrals are the *geometric* terms. A further distinction is made between low and high-order geometric stiffness terms, with the product of the rotations $(\Delta v'\delta_1 v' + \Delta w'\delta_1 w')$ comprising the low-order

terms, and the product of the axial strains ($\Delta u'\delta_1 u'$) comprising the high-order terms. This distinction is the result of the assumption of small incremental strains asserted in Section 2.1.3. The third and sixth integrals represent the increment in the geometric terms, and are used in force recovery as shown in Section 2.3. The seventh term is associated with slip between the steel and concrete portions of the element and is considered to be part of the *small displacements* terms. Further algebraic manipulation of the integrals includes expansion of the geometric terms using the first derivatives of the transverse displacements (which can be computed from Eq. 2.8), and expansion of the expressions in parentheses. Equation 2.14 shows the expanded form of Eq. 2.13. An excellent example of the expansion of the virtual work equation of equilibrium to element stiffness matrices is given in White (1986).

$$
\begin{aligned}
&\int_{{}^1V^c} {}_1E^c \begin{pmatrix} \Delta u_c^{c\prime}\delta_1 u_c^{c\prime} - y\Delta u_c^{c\prime}\delta_1 v_c^{c\prime\prime} - y\Delta v_c^{c\prime\prime}\delta_1 u_c^{c\prime} - z\Delta u_c^{c\prime}\delta_1 w_c^{c\prime\prime} - z\Delta w_c^{c\prime\prime}\delta_1 u_c^{c\prime} + \\ yz\Delta v_c^{c\prime\prime}\delta_1 w_c^{c\prime\prime} + yz\Delta w_c^{c\prime\prime}\delta_1 v_c^{c\prime\prime} + y^2\Delta v_c^{c\prime\prime}\delta_1 v_c^{c\prime\prime} + z^2\Delta w_c^{c\prime\prime}\delta_1 w_c^{c\prime\prime} \end{pmatrix} {}^1dV^c + \\
&\int_{{}^1V^c} {}^1\tau^c \begin{pmatrix} \Delta u_c^{c\prime}\delta_1 u_c^{c\prime} - y\Delta u_c^{c\prime}\delta_1 v_c^{c\prime\prime} - y\Delta v_c^{c\prime\prime}\delta_1 u_c^{c\prime} - z\Delta u_c^{c\prime}\delta_1 w_c^{c\prime\prime} - z\Delta w_c^{c\prime\prime}\delta_1 u_c^{c\prime} + \\ yz\Delta v_c^{c\prime\prime}\delta_1 w_c^{c\prime\prime} + yz\Delta w_c^{c\prime\prime}\delta_1 v_c^{c\prime\prime} + y^2\Delta v_c^{c\prime\prime}\delta_1 v_c^{c\prime\prime} + z^2\Delta w_c^{c\prime\prime}\delta_1 w_c^{c\prime\prime} + \\ \Delta v_c^{c\prime}\delta_1 v_c^{c\prime} - z\Delta v_c^{c\prime}\delta_1\theta_x' - z\Delta\theta_x'\delta_1 v_c^{c\prime} + z^2\Delta\theta_x'\delta_1\theta_x' + \\ \Delta w_c^{c\prime}\delta_1 w_c^{c\prime} + y\Delta w_c^{c\prime}\delta_1\theta_x' + y\Delta\theta_x'\delta_1 w_c^{c\prime} + y^2\Delta\theta_x'\delta_1\theta_x' \end{pmatrix} {}^1dV^c + \\
&\int_{{}^1V^c} \Delta\tau^c \begin{pmatrix} \Delta u_c^{c\prime}\delta_1 u_c^{c\prime} - y\Delta u_c^{c\prime}\delta_1 v_c^{c\prime\prime} - y\Delta v_c^{c\prime\prime}\delta_1 u_c^{c\prime} - z\Delta u_c^{c\prime}\delta_1 w_c^{c\prime\prime} - z\Delta w_c^{c\prime\prime}\delta_1 u_c^{c\prime} + \\ yz\Delta v_c^{c\prime\prime}\delta_1 w_c^{c\prime\prime} + yz\Delta w_c^{c\prime\prime}\delta_1 v_c^{c\prime\prime} + y^2\Delta v_c^{c\prime\prime}\delta_1 v_c^{c\prime\prime} + z^2\Delta w_c^{c\prime\prime}\delta_1 w_c^{c\prime\prime} + \\ \Delta v_c^{c\prime}\delta_1 v_c^{c\prime} - z\Delta v_c^{c\prime}\delta_1\theta_x' - z\Delta\theta_x'\delta_1 v_c^{c\prime} + z^2\Delta\theta_x'\delta_1\theta_x' + \\ \Delta w_c^{c\prime}\delta_1 w_c^{c\prime} + y\Delta w_c^{c\prime}\delta_1\theta_x' + y\Delta\theta_x'\delta_1 w_c^{c\prime} + y^2\Delta\theta_x'\delta_1\theta_x' \end{pmatrix} {}^1dV^c + \\
&\int_{{}^1V^s} {}_1E^s \begin{pmatrix} \Delta u_c^{s\prime}\delta_1 u_c^{s\prime} - y\Delta u_c^{s\prime}\delta_1 v_c^{s\prime\prime} - y\Delta v_c^{s\prime\prime}\delta_1 u_c^{s\prime} - z\Delta u_c^{s\prime}\delta_1 w_c^{s\prime\prime} - z\Delta w_c^{s\prime\prime}\delta_1 u_c^{s\prime} + \\ yz\Delta v_c^{s\prime\prime}\delta_1 w_c^{s\prime\prime} + yz\Delta w_c^{s\prime\prime}\delta_1 v_c^{s\prime\prime} + y^2\Delta v_c^{s\prime\prime}\delta_1 v_c^{s\prime\prime} + z^2\Delta w_c^{s\prime\prime}\delta_1 w_c^{s\prime\prime} \end{pmatrix} {}^1dV^s + \\
&\int_{{}^1V^s} {}^1\tau^s \begin{pmatrix} \Delta u_c^{s\prime}\delta_1 u_c^{s\prime} - y\Delta u_c^{s\prime}\delta_1 v_c^{s\prime\prime} - y\Delta v_c^{s\prime\prime}\delta_1 u_c^{s\prime} - z\Delta u_c^{s\prime}\delta_1 w_c^{s\prime\prime} - z\Delta w_c^{s\prime\prime}\delta_1 u_c^{s\prime} + \\ yz\Delta v_c^{s\prime\prime}\delta_1 w_c^{s\prime\prime} + yz\Delta w_c^{s\prime\prime}\delta_1 v_c^{s\prime\prime} + y^2\Delta v_c^{s\prime\prime}\delta_1 v_c^{s\prime\prime} + z^2\Delta w_c^{s\prime\prime}\delta_1 w_c^{s\prime\prime} + \\ \Delta v_c^{s\prime}\delta_1 v_c^{s\prime} - z\Delta v_c^{s\prime}\delta_1\theta_x' - z\Delta\theta_x'\delta_1 v_c^{s\prime} + z^2\Delta\theta_x'\delta_1\theta_x' + \\ \Delta w_c^{s\prime}\delta_1 w_c^{s\prime} + y\Delta w_c^{s\prime}\delta_1\theta_x' + y\Delta\theta_x'\delta_1 w_c^{s\prime} + y^2\Delta\theta_x'\delta_1\theta_x' \end{pmatrix} {}^1dV^s + \\
&\int_{{}^1V^s} \Delta\tau^s \begin{pmatrix} \Delta u_c^{s\prime}\delta_1 u_c^{s\prime} - y\Delta u_c^{s\prime}\delta_1 v_c^{s\prime\prime} - y\Delta v_c^{s\prime\prime}\delta_1 u_c^{s\prime} - z\Delta u_c^{s\prime}\delta_1 w_c^{s\prime\prime} - z\Delta w_c^{s\prime\prime}\delta_1 u_c^{s\prime} + \\ yz\Delta v_c^{s\prime\prime}\delta_1 w_c^{s\prime\prime} + yz\Delta w_c^{s\prime\prime}\delta_1 v_c^{s\prime\prime} + y^2\Delta v_c^{s\prime\prime}\delta_1 v_c^{s\prime\prime} + z^2\Delta w_c^{s\prime\prime}\delta_1 w_c^{s\prime\prime} + \\ \Delta v_c^{s\prime}\delta_1 v_c^{s\prime} - z\Delta v_c^{s\prime}\delta_1\theta_x' - z\Delta\theta_x'\delta_1 v_c^{s\prime} + z^2\Delta\theta_x'\delta_1\theta_x' + \\ \Delta w_c^{s\prime}\delta_1 w_c^{s\prime} + y\Delta w_c^{s\prime}\delta_1\theta_x' + y\Delta\theta_x'\delta_1 w_c^{s\prime} + y^2\Delta\theta_x'\delta_1\theta_x' \end{pmatrix} {}^1dV^s + \\
&\int_{{}^1I} \hat{k}(\Delta u_c^s\delta_1 u_c^s - \Delta u_c^c\delta_1 u_c^s - \Delta u_c^s\delta_1 u_c^c + \Delta u_c^c\delta_1 u_c^c)\,{}^1dI = \Delta\Re
\end{aligned}
\tag{2.14}
$$

2.1.7 The Fiber Element Approach for Modeling Spread of Plasticity

In order to evaluate the volume integrals of Eq. 2.14, the fiber element approach is used in this work. This scheme discretizes the element end cross sections into a grid of fibers, and the stress-strain behavior of each steel or concrete fiber is monitored explicitly during the loading history. Frame elements are modeled as line beam-column elements with their DOFs located at the centroidal axis at each element end. The cross-sectional rigidity and stress-resultants of each element end are obtained using numerical integration over all the fibers. Fiber elements have been used to model steel wide-flange sections in planar frames (White, 1986; Morales, 1994; Challa and Hall, 1994), reinforced concrete sections (Taucer, et al., 1991; Izzuddin, et al., 1993), and steel reinforced concrete sections (Elnashai and Elghazouli, 1993; El-Tawil et al., 1993; El-Tawil and Deierlein, 1996), to name a few. Fiber element models have also been used to investigate the behavior of CFTs by several researchers (see Chapter 1). The main advantage in using fiber elements is that computing time is greatly reduced when compared to using three-dimensional continuum finite elements. Since each fiber is only allowed to deform along the centroidal axis of the member, the number of computations can be reduced by one or more orders of magnitude over a similar array of continuum elements.

The fiber element formulation is a cross section integration technique, and does not involve *fibers* as such. The cross-sectional area at each of the two ends of a beam-column is discretized into a mesh of fibers, with each fiber of the mesh having a specified area and position with respect to the local element axis (Figure 2.3). The mesh need not be the same at the two ends of the element, as the fibers are never considered to have a real length. The state of stress and strain is updated for each increment in load at every fiber. Using numerical integration (summation of individual fiber properties over the cross-sectional area), stress-resultant forces and rigidity terms are calculated at the end cross sections of each element. Finite element interpolation functions are then used to describe the variation of the forces and rigidities over the length of the element. Using

approach, the spread of plasticity through a beam-column element can be accounted for with a high degree of accuracy.

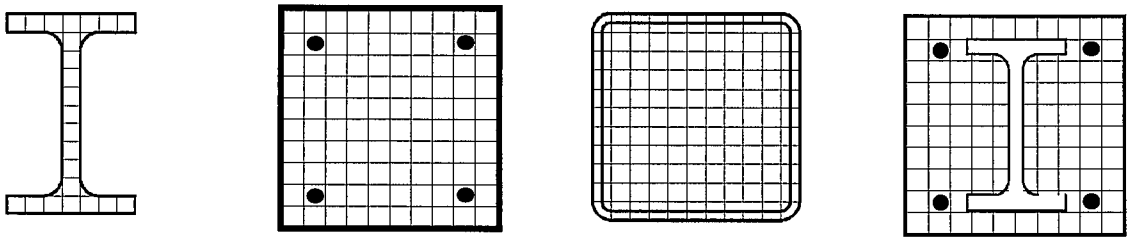

Figure 2.3: Fiber Element Discretization

To approximate the volume integrals which appear in the virtual work equation of equilibrium using the fiber element method, each volume integral of Eq. 2.14 is first decomposed into area and length integrals. The area integrals are then approximated by numerical integration over the fibers of each cross section. Equation 2.15 shows how numerical integration over all fibers, f, is used to approximate various area integrals.

As will be seen in Chapter 3, since there are only a limited number of appropriate experiments documented thoroughly in the literature to which to calibrate slip stiffness, the calibration of the value of $\hat{k}$ in the final term of the left hand column is kept simple. In this work, its value varies as an inverse function of the perimeter of the tube, such that $\hat{k} = k/\rho$, where k is a calibrated value of slip stiffness per unit length of interface, having units of force/length^2. Thus, in Chapter 3, the value of k is calibrated directly.

By evaluating the area integrals during incremental analysis after updating the tangent modulus of each fiber in the cross section, the spread of plasticity through the cross section is accounted for. The tangent modulus of individual fibers is computed based on the appropriate material constitutive models (see Chapter 4) and the fiber strain, which is computed from the local element deformations (see Section 2.3.2).

Note that the rigidity term associated with torque and the stress-resultant torque are not calculated through numerical integration. This is because the element formulation does not account directly for shear strains. The torsional rigidity is simplified in this work by assuming that the initial rigidity of the member does not change over the entire

load history. This approximation is believed to be sufficient for modeling the behavior of rectangular CFTs as members of structural frames, as these members exhibit high torsional rigidity (Kitada and Nakai, 1991).

$$
\begin{aligned}
&\int_{{}^1A} {}^1E^c\,{}^1dA = \sum_f \left({}^1E^c\,{}^1A\right)_f = EA^c && \int_{{}^1A} {}^1E^s\,{}^1dA = \sum_f \left({}^1E^s\,{}^1A\right)_f = EA^s \\
&\int_{{}^1A} {}^1E^c y\,{}^1dA = \sum_f \left({}^1E^c y\,{}^1A\right)_f = -EQ^c{}_z && \int_{{}^1A} {}^1E^s y\,{}^1dA = \sum_f \left({}^1E^s y\,{}^1A\right)_f = -EQ^s{}_z \\
&\int_{{}^1A} {}^1E^c z\,{}^1dA = \sum_f \left({}^1E^c z\,{}^1A\right)_f = -EQ^c{}_y && \int_{{}^1A} {}^1E^s z\,{}^1dA = \sum_f \left({}^1E^s z\,{}^1A\right)_f = -EQ^s{}_y \\
&\int_{{}^1A} {}^1E^c y^2\,{}^1dA = \sum_f \left({}^1E^c y^2\,{}^1A\right)_f = EI^c{}_{zz} && \int_{{}^1A} {}^1E^s y^2\,{}^1dA = \sum_f \left({}^1E^s y^2\,{}^1A\right)_f = EI^s{}_{zz} \\
&\int_{{}^1A} {}^1E^c z^2\,{}^1dA = \sum_f \left({}^1E^c z^2\,{}^1A\right)_f = EI^c{}_{yy} && \int_{{}^1A} {}^1E^s z^2\,{}^1dA = \sum_f \left({}^1E^s z^2\,{}^1A\right)_f = EI^s{}_{yy} \\
&\int_{{}^1A} {}^1E^c yz\,{}^1dA = \sum_f \left({}^1E^c yz\,{}^1A\right)_f = EI^c{}_{yz} && \int_{{}^1A} {}^1E^s yz\,{}^1dA = \sum_f \left({}^1E^s yz\,{}^1A\right)_f = EI^s{}_{yz} \\
&\int_{{}^1A} {}^1\tau^c\,{}^1dA = \sum_f \left({}^1\tau^c\,{}^1A\right)_f = P^c && \int_{{}^1A} {}^1\tau^s\,{}^1dA = \sum_f \left({}^1\tau^s\,{}^1A\right)_f = P^s \\
&\int_{{}^1A} {}^1\tau^c y\,{}^1dA = \sum_f \left({}^1\tau^c y\,{}^1A\right)_f = -M^c{}_z && \int_{{}^1A} {}^1\tau^s y\,{}^1dA = \sum_f \left({}^1\tau^s y\,{}^1A\right)_f = -M^s{}_z \\
&\int_{{}^1A} {}^1\tau^c z\,{}^1dA = \sum_f \left({}^1\tau^c z\,{}^1A\right)_f = -M^c{}_y && \int_{{}^1A} {}^1\tau^s z\,{}^1dA = \sum_f \left({}^1\tau^s z\,{}^1A\right)_f = -M^s{}_y \\
&\int_{{}^1A} {}^1\tau^c y^2\,{}^1dA = \sum_f \left({}^1\tau^c y^2\,{}^1A\right)_f = \zeta^c{}_{zz} && \int_{{}^1A} {}^1\tau^s y^2\,{}^1dA = \sum_f \left({}^1\tau^s y^2\,{}^1A\right)_f = \zeta^s{}_{zz} \\
&\int_{{}^1A} {}^1\tau^c z^2\,{}^1dA = \sum_f \left({}^1\tau^c z^2\,{}^1A\right)_f = \zeta^c{}_{yy} && \int_{{}^1A} {}^1\tau^s z^2\,{}^1dA = \sum_f \left({}^1\tau^s z^2\,{}^1A\right)_f = \zeta^s{}_{yy} \\
&\int_{{}^1A} {}^1\tau^c yz\,{}^1dA = \sum_f \left({}^1\tau^c yz\,{}^1A\right)_f = \zeta^c{}_{yz} && \int_{{}^1A} {}^1\tau^s yz\,{}^1dA = \sum_f \left({}^1\tau^s yz\,{}^1A\right)_f = \zeta^s{}_{yz}
\end{aligned}
\tag{2.15}
$$

$$
\int_{{}^1I} \hat{k}(\Delta u_c^s - \Delta u_c^c)(\delta_1 u_c^s - \delta_1 u_c^c)\,{}^1dI =
$$

$$
\int_{{}^1L} \rho \cdot \hat{k}(\Delta u_c^s - \Delta u_c^c)(\delta_1 u_c^s - \delta_1 u_c^c)\,{}^1dx = \int_{{}^1L} k(\Delta u_c^s - \Delta u_c^c)(\delta_1 u_c^s - \delta_1 u_c^c)\,{}^1dx
$$

Once numerical integration is used to compute the element forces and rigidity at the end nodes, shape functions are used to approximate the change in rigidity and force along the element length. The shape functions chosen for the element forces must satisfy

equilibrium and compatibility conditions. Traditionally, a constant shape function is chosen to describe the axial force in an element in order to satisfy static equilibrium of the element. However, because the element is divided into separate steel and concrete volumes which may exchange axial load along the element length, a linear shape function is used for axial force in this work. This shape function is exact for the case of elastic material behavior, including a linear slip relation, but becomes an approximation once the end cross sections become partially plastified. By choosing a linearly varying shape function, the virtual work equation of equilibrium remains linear in the displacements. A constant shape function is chosen for the torque, and a linear shape function is chosen for moments and higher order force resultant terms (i.e., ζ_{yy}.) Equation 2.16 shows how the linear shape function is applied.

$$F(x) = < N_l > \{F\} = \langle (1-i) \quad i \rangle \begin{Bmatrix} F_i \\ F_j \end{Bmatrix} \tag{2.16}$$

where: F_i is a generic resultant force or rigidity term at end i

$< N_l >$ is the standard linear shape function as shown

Linear shape functions are also chosen to represent the change in rigidity along the element length, except that the torsional rigidity is assumed to be constant along the length.

2.1.8 Corotational Element Displacement Interpolation Functions

Because of the corotational approach employed in the current formulation, the rigid body motions of the element are not used to define the kinematic relationships which cause element deformation. This approach is equivalent to considering deformations which are measured with respect to the corotational axes, which follow the rigid body motion of the element in space. For the traditional 12 DOF element, the deformations of the element which cause element straining are: 1) the elongation of the element centroid, 2) the rotation of each

end of the element about the local y and z axes, and 3) the element torsional rotation. These corotational deformations result in 6 unknown deformations for the element. The expansion from the 6 DOF corotational system to the conventional 12 DOF element system is performed by considering equilibrium of forces on the deformed element. This technique is employed by Cook (1981) to expand the corotational element stiffness matrix for planar steel elements.

The corotational kinematics for the 18 DOF beam finite element are similar to those for the traditional 12 DOF element. Several modifications are utilized, however, which are consistent with the slip formulation and the application of the element for use in nonlinear analysis. As the steel and concrete are formulated as separate volumes in the virtual work equation of equilibrium, the element deformations are defined so that the steel and concrete appear as essentially two separate elements with respect to their translational DOFs. This allows the steel and concrete shear DOFs to be defined separately when the corotational stiffness is expanded to the element stiffness. As will be seen in Section 2.2, the definition of separate shear DOFs for the steel and concrete is required for automated assembly of the global stiffness matrix during nonlinear analysis.

A second modification to the conventional 12 DOF kinematic formulation is the addition of midpoint axial degrees of freedom for the steel and concrete. This modification allows a quadratic axial displacement shape function to be employed. This approach is used by White (1986) for analysis of planar steel frames and has been used by others to describe the axial deformation of an element which is partially plastified. The quadratic axial displacement shape function yields a more accurate representation of the axial deformation for an element whose axial rigidity varies linearly between the element ends than the traditional linear axial displacement shape function used for prismatic beams. The extra midpoint DOFs are condensed out of the corotational stiffness before expansion to the local element stiffness (see Appendix A).

Figure 2.4 shows the deformations of the steel and concrete portions of the element. These deformational degrees-of-freedom will be used to derive the corotational element stiffness matrix for the 18 DOF beam finite element.

The corotational deformations of Fig. 2.4 are used to completely describe the deformation of the centroidal axis of the element through the use of finite element shape functions (Bathe, 1982). Conventional cubic Hermitian shape functions are used to describe the y and z deformations which are caused by flexural rotation of the element ends (Weaver and Gere, 1990). Also, a standard linear shape function is used to describe the torsional rotation of the element. A quadratic shape function is used to describe the axial deformation. Note that this shape function reverts to the linear form for the case when $\Delta e_m^c = \frac{\Delta e^c}{2}$ (and similarly for the steel axial shape function).

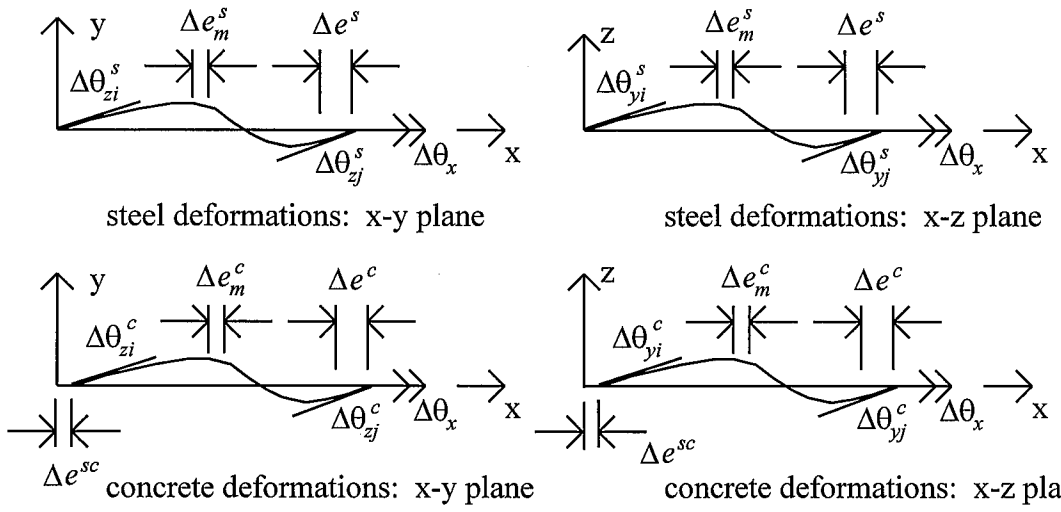

Figure 2.4: Corotational Deformations

The notation used in Fig. 2.4 is defined as:

- Δe_m^c is the incremental concrete elongation between the i-end node and the midpoint node
- Δe^c is the incremental concrete elongation between the i-end node and the j-end node
- $\Delta\theta_{yi}^c$ is the incremental rotation of the concrete i-end node about the y-axis
- $\Delta\theta_{yj}^c$ is the incremental rotation of the concrete j-end node about the y-axis

$\Delta\theta^c_{zi}$ is the incremental rotation of the concrete i-end node about the z-axis

$\Delta\theta^c_{zj}$ is the incremental rotation of the concrete j-end node about the z-axis

Similar definitions are given for the steel deformations.

Δe^{sc} is the incremental displacement of the concrete i-end node with respect to the corotational axes (which occurs due to slip)

$\Delta\theta_x$ is the incremental torsional rotation from the i-end node to the j-end node

Equation 2.17 gives the shape functions in matrix form. Expansion of the matrices yield the expressions which describe the deformation of an arbitrary point in the element volume based on the nodal deformations.

$$\{\Delta d^{nat}\} = < \Delta e^{sc} \quad \Delta e^{c} \quad \Delta\theta^c_{zi} \quad \Delta\theta^c_{yi} \quad \Delta\theta^c_{zj} \quad \Delta\theta^c_{yj} \quad \Delta e^{s} \quad \Delta\theta^s_{zi} \quad \Delta\theta^s_{yi} \quad \Delta\theta^s_{zj} \quad \Delta\theta^s_{yj} \quad \Delta\theta_x \quad \Delta e^c_m \quad \Delta e^s_m >^T$$

$$\begin{aligned}
\Delta u_c^{\ c} &= < N_u^c > \{\Delta d^{nat}\} \\
\Delta u_c^{\ s} &= < N_u^s > \{\Delta d^{nat}\} \\
\Delta v_c^{\ c} &= < N_v^c > \{\Delta d^{nat}\} \\
\Delta v_c^{\ s} &= < N_v^s > \{\Delta d^{nat}\} \\
\Delta w_c^{\ c} &= < N_w^c > \{\Delta d^{nat}\} \\
\Delta w_c^{\ s} &= < N_w^s > \{\Delta d^{nat}\} \\
\Delta\theta_x &= < N_\theta > \{\Delta d^{nat}\}
\end{aligned} \tag{2.17}$$

$$\begin{aligned}
< N_u^c > = < & 1 \quad -i+2i^2 \quad 0 \quad 0 \quad 0 \quad 0 \quad 0 \quad 0 \quad 0 \quad 0 \quad 0 \quad -4i^2+4i \quad 0 > \\
< N_u^s > = < & 0 \quad 0 \quad 0 \quad 0 \quad 0 \quad 0 \quad -i+2i^2 \quad 0 \quad 0 \quad 0 \quad 0 \quad 0 \quad 0 \quad -4i^2+4i > \\
< N_v^c > = < & 0 \quad 0 \quad L(i-2i^2+i^3) \quad 0 \quad L(-i^2+i^3) \quad 0 \quad 0 \quad 0 \quad 0 \quad 0 \quad 0 \quad 0 \quad 0 > \\
< N_v^s > = < & 0 \quad 0 \quad 0 \quad 0 \quad 0 \quad 0 \quad 0 \quad L(i-2i^2+i^3) \quad 0 \quad L(-i^2+i^3) \quad 0 \quad 0 \quad 0 > \\
< N_w^c > = < & 0 \quad 0 \quad 0 \quad L(i-2i^2+i^3) \quad 0 \quad L(-i^2+i^3) \quad 0 \quad 0 \quad 0 \quad 0 \quad 0 \quad 0 \quad 0 > \\
< N_w^s > = < & 0 \quad 0 \quad 0 \quad 0 \quad 0 \quad 0 \quad 0 \quad 0 \quad L(i-2i^2+i^3) \quad 0 \quad L(-i^2+i^3) \quad 0 \quad 0 > \\
< N_\theta > = < & 0 \quad 0 \quad 0 \quad 0 \quad 0 \quad 0 \quad 0 \quad 0 \quad 0 \quad 0 \quad 0 \quad i \quad 0 \quad 0 >
\end{aligned}$$

where: $i = \dfrac{x}{L}$

$\{\Delta d^{nat}\}$ are the incremental natural element deformations

The derivatives of the shape functions are used to describe the element strains when substituted into Eq. 2.8. A positive sign convention for internal stress and strain is

inherent in the above shape functions and Fig. 2.4. A positive axial strain increment ($\Delta u'^{c}$ and $\Delta u'^{s}$) indicates elongation of the element centroidal axis, and positive curvature increments ($\Delta v'', \Delta w''$) indicate compressive strain in the positive quadrant of the corotational axes at any cross section in the element. In addition, the positive sign convention for internal axial force and moment are defined so that they produce positive strain and curvature, and a positive torque produces positive torsional rotation.

2.1.9 Natural Element Stiffness Matrices

The finite element stiffness formulation presented in the previous sections is now used to derive the stiffness matrices which relate the natural element deformations with the element end forces. The expansion to stiffness matrices takes place in several steps. First, the integrals of Eq. 2.14 are decomposed into area and length integrals, as discussed in Section 2.1.7. Second, the area integrals are replaced by the numerical integration terms. Next, the shape functions from Eq. 2.17 are substituted for the strain and curvature terms. Equation 2.18 shows the resulting expression for the first integral term of the virtual work equation, and equation 2.19 shows the terms which contain the slip stiffness. All other terms are expanded similarly and are not shown here.

$$\int_0^L \begin{pmatrix} < N_l >\{{}_1EA^c\} < \delta d^{nat} > \{N_u^c\}' < N_u^c >' \{\Delta d^{nat}\} + \\ < N_l >\{{}_1EQ_z{}^c\} < \delta d^{nat} > \{N_v^c\}'' < N_u^c >' \{\Delta d^{nat}\} + \\ < N_l >\{{}_1EQ_z{}^c\} < \delta d^{nat} > \{N_u^c\}' < N_v^c >'' \{\Delta d^{nat}\} + \\ < N_l >\{{}_1EQ_y{}^c\} < \delta d^{nat} > \{N_w^c\}'' < N_u^c >' \{\Delta d^{nat}\} + \\ < N_l >\{{}_1EQ_y{}^c\} < \delta d^{nat} > \{N_u^c\}' < N_w^c >'' \{\Delta d^{nat}\} + \\ < N_l >\{{}_1EI_{yz}{}^c\} < \delta d^{nat} > \{N_w^c\}'' < N_v^c >'' \{\Delta d^{nat}\} + \\ < N_l >\{{}_1EI_{yz}{}^c\} < \delta d^{nat} > \{N_v^c\}'' < N_w^c >'' \{\Delta d^{nat}\} + \\ < N_l >\{{}_1EI_{zz}{}^c\} < \delta d^{nat} > \{N_v^c\}'' < N_v^c >'' \{\Delta d^{nat}\} + \\ < N_l >\{{}_1EI_{yy}{}^c\} < \delta d^{nat} > \{N_w^c\}'' < N_w^c >'' \{\Delta d^{nat}\} \end{pmatrix} {}^1dx \qquad (2.18)$$

where: $< x >$ is a row vector

$\{x\}$ is a column vector

$\{{}_1EA^c\} = \begin{Bmatrix} {}_1EA_i^c \\ {}_1EA_j^c \end{Bmatrix}$ and so on for the other rigidity terms

$$\int_0^L \begin{pmatrix} < N_l > \{k\} < \delta d^{nat} > \{N_u^c\} < N_u^s > \{\Delta d^{nat}\} - \\ < N_l > \{k\} < \delta d^{nat} > \{N_u^c\} < N_u^s > \{\Delta d^{nat}\} - \\ < N_l > \{k\} < \delta d^{nat} > \{N_u^s\} < N_u^c > \{\Delta d^{nat}\} + \\ < N_l > \{k\} < \delta d^{nat} > \{N_u^c\} < N_u^c > \{\Delta d^{nat}\} \end{pmatrix} {}^1dx \tag{2.19}$$

where: $\{k\} = \begin{Bmatrix} k_i \\ k_j \end{Bmatrix}$

Once the substitution and integration is completed for all the integrals of the virtual work equation of equilibrium, a stiffness relationship can be written in terms of the natural element deformations and the natural element forces. Equation 2.20 shows this relationship for the current formulation. The natural element elastic and geometric stiffness matrices are included in Appendix A.

$$\left[K^{nat}\right]\{\Delta d^{nat}\} = \left[K_e^{nat} + K_{g1}^{nat} + K_{g2}^{nat}\right]\{\Delta d^{nat}\} = \{\Delta f^{nat}\} \tag{2.20}$$

where: $[K^{nat}]$ is the natural element stiffness matrix

$[K_e^{nat}]$ is the natural element elastic stiffness matrix

$[K_{g1}^{nat}]$ is the natural element low-order geometric stiffness matrix

$[K_{g2}^{nat}]$ is the natural element high-order geometric stiffness matrix

$\{\Delta f^{nat}\}$ are the incremental natural element forces

2.1.10 Expansion to Local Element Stiffness Matrices

The current formulation assumes that external loads are applied only at the element ends. For this reason, the calculation of midpoint axial deformation is not required, and the midpoint DOFs are removed from the natural element stiffness matrix through the technique of static condensation. The use of static condensation to reduce the natural stiffness matrix from 14x14 to 12x12 is presented in Appendix A.

The reduced natural element stiffness matrix has 12 DOFs. In order to assemble finite elements into a global stiffness matrix, the rigid modes of deformation must be considered. These rigid modes include 3 rigid body translations and 3 rigid body rotations. Cook (1981) and Morales (1994) show how the rigid body deflections and rotations are included for planar steel elements. The conventional method of expansion to a local element stiffness matrix must be modified to accommodate three-dimensions and the separate steel and concrete DOFs in the current formulation.

In the current formulation, the local DOFs are numbered so that the assembly of the global stiffness matrix can be easily automated. In this numbering scheme, the first three DOFs at each end of the element correspond to the steel translations, the next three DOFs correspond to the rotations, and the final three DOFs correspond to the concrete translations. Figure 2.5 shows the natural element forces, including the shear forces which can be computed through static equilibrium. The separate steel and concrete bending moments in this figure are used to compute the separate steel and concrete shear forces, respectively, through static equilibrium. This separation between the steel and concrete moments in the corotational coordinate system is required in order to transform the corotational element stiffness matrix to the local element coordinate system. The sepatae steel and concrete moments at each end of the element are combined in the local element stiffness relationship because the steel and concrete rotations are the same at each end of the element.

Figure 2.6 shows the numbering scheme and positive sign convention adopted for the local element DOFs. This figure indicates the positive sign convention for both local element forces and local element deformations.

As mentioned previously, the incremental element shears (which are not modeled in the natural element stiffness formulation) are computed by considering static equilibrium of the element in the C2 configuration. By considering the incremental rigid body rotation of the element and the element forces at C1, it is apparent that the axial force at C1 affects the element stiffness. This is often referred to as the *P*-Δ effect, or the "external stiffness" of the element (Cook, 1981; Morales, 1994). In the current formulation, the axial force at C1 is assumed to act in the original direction of the element chord, even after the element has achieved the C2 configuration. It will be seen in Section 2.3 that the effect of the incremental axial force during the rigid body rotation from C1 to C2 is also included in the external stiffness of the element during force recovery (Morales, 1994).

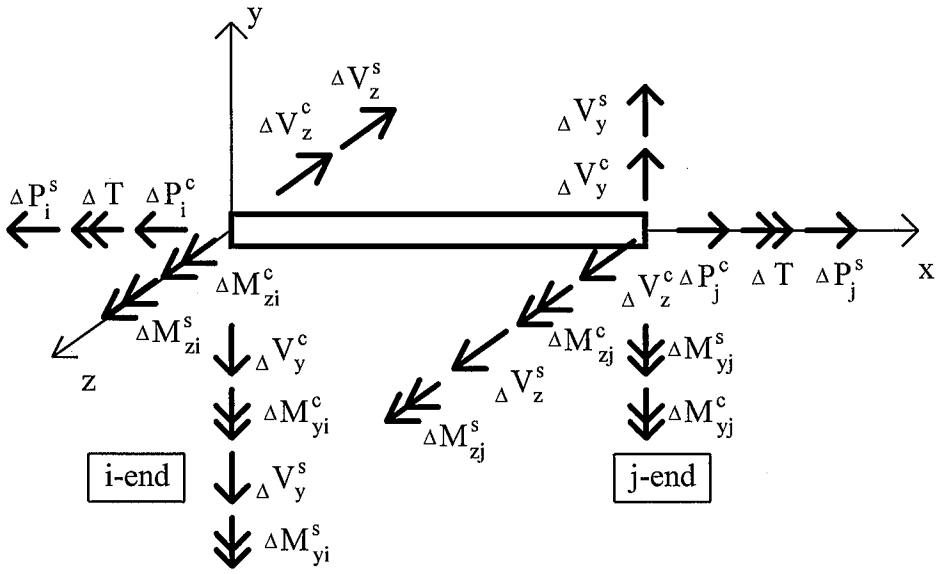

Figure 2.5: Natural Element Forces

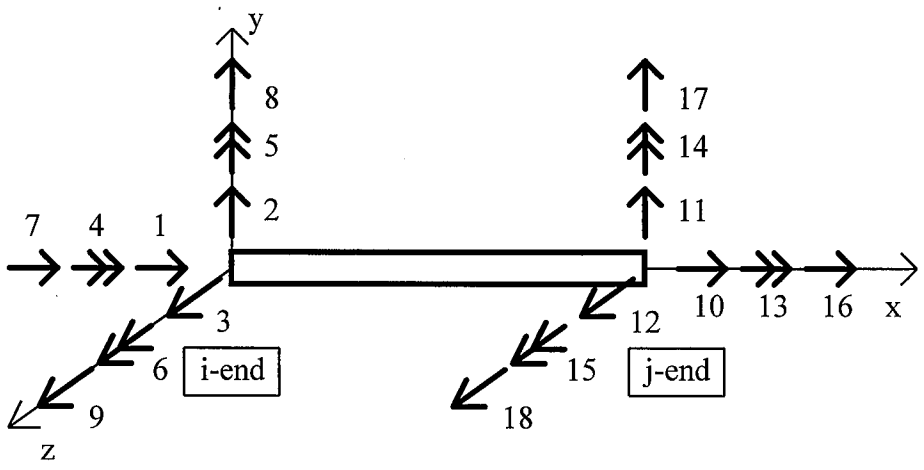

Figure 2.6: Local Element Degrees of Freedom

The issue of external stiffness is complicated by the separate steel and concrete axial forces, and the gradual transfer of axial force between the two materials along the length of the element. In conventional beam finite element formulations, the axial force is assumed to be constant in the element. This assumption remains true in the current formulation for the total force at any point along the element length, but the steel and concrete axial forces, taken separately, may vary from the i-end of the member to the j-end. As mentioned in Section 2.1.7, the axial forces in the steel and concrete respectively are allowed to vary linearly from one end of the member to the other. Using this assumption, the geometric nonlinear stiffness matrix remains linear in the displacements.

Cook (1981) shows how the corotational stiffness is expanded to local element stiffness for planar elements using a representation similar to that of Figs. 2.5 and 2.6. First, the incremental local element forces are expressed in terms of the incremental natural element forces. Next, the incremental natural deformations of the element are expressed in terms of the incremental element deflections. These relationships are expressed in matrix form, and the expanded local element stiffness is formed. The matrices used in expansion are presented in Appendix A. Equation 2.21 shows the general form of the equations used in expansion of the corotational stiffness.

$$[K^e]^{18x18} = [\Omega]^{18x12}[K^{nat}]^{12x12}[\Omega]^{T\,12x18} + [RB]^{18x18} \tag{2.21}$$

where: $[K^e]^{18x18}$ is the local element stiffness matrix, including geometric nonlinear terms

$[K^{nat}]^{12x12}$ is the natural element stiffness matrix, including geometric nonlinear terms

$[\Omega]^{18x12}$ is the natural-to-local transformation matrix

$[RB]^{18x18}$ is the matrix containing the rigid body geometric nonlinear stiffness terms (external stiffness)

2.2 Structural Analysis of Three-Dimensional Frames Using the 18 DOF Finite Element

The 18 DOF beam finite element described in the previous sections has the advantage of being able to model the slip between the steel and concrete portions of a CFT member. The element provides the capability to study the effect of slip on the overall behavior of CFT members which are part of structural frames. However, several modifications are required to the conventional global assembly and solution procedure for three-dimensional frames. First, the 18 DOF element must be compatible with conventional 12 DOF steel wide-flange beam elements. Second, the assembly of these elements into a global stiffness matrix must be easily automated using standard procedures. Finally, the shear compatibility conditions assumed during the finite element formulation must be imposed for the global structural system.

This section describes the procedure adopted for assembly of the global stiffness matrix which includes either 12 DOF steel beam-columns, 18 DOF CFT beam-columns, or a combination of these elements. Next, the use of penalty functions to impose shear deformation compatibility is discussed, along with issues related to the solution of the global system of equations.

2.2.1 Assembly of the Global Stiffness Matrix

Figure 2.6 shows the DOF numbering scheme for the 18 DOF CFT finite element. This numbering scheme was chosen so that the global stiffness matrix could be easily assembled through conventional techniques. In the current formulation, the first two sets of three DOFs at each joint represent the steel translations and the rotations respectively. This numbering scheme corresponds to the conventional formulation which has 6 DOFs per joint. The final three DOFs correspond to the concrete translations.

This numbering scheme has several advantages. First, the standard local-to-global transformation matrices can be used with the addition of six more rows and columns to account for the concrete translations. Second, when steel elements are used in combination with 18 DOF CFT elements, the steel beam elements are assembled directly into the first 6 DOFs at a joint. When there are no CFT elements at a joint, a flag may be set so that only 6 DOFs are considered at that joint. The assembly of steel beams with the steel translational DOFs of the CFT element is consistent with typical shear-tab connections and other connections which do not penetrate the steel tube wall. In this case, all girder shear must be transferred to the concrete core of the CFT through the steel-concrete slip interface. It will be seen in Chapter 3 that the slip interface is very stiff, such that the steel tube load often transfers to the concrete in a relatively short region above and below the connection. The modeling of this behavior is one of the main advantages of the current formulation. Typical through-type connections are common when full restraint is desired. These connection regions, as well as other situations where the concrete is fully engaged by the steel, can be modeled as slip-restrained in the current formulation by assigning restraints in the global system of equations (see Section 2.2.2). Comparison to experiments on shear transfer at a beam-to-column connection are given in Chapter 3.

2.2.2 Inclusion of Shear Constraints in the Global System of Equations

If 18 DOF CFT beam-column elements are used as members in a structural frame model, shear deformation compatibility constraints are required between the steel and concrete translational DOFs at each joint. For most practical structures, the CFT beam-columns will be aligned in vertical column stacks, requiring two global compatibility conditions (perpendicular to the axis of the column stack) at each joint. This may not always be the case, however, as other structural systems which may have arbitrary orientations of members entering each joint are possible. Moreover, initially aligned elements will become inclined due to geometric nonlinearity. For this reason, a general formulation for shear compatibility constraints is required which can be implemented in a structural frame matrix analysis program.

The technique adopted for imposing compatibility conditions on the CFT steel and concrete translational DOFs is the use of penalty functions imposed in the global coordinate system. This technique involves assigning a large (but finite) stiffness between two DOFs thus constraining their values to be nearly identical. Penalty functions are slightly less precise than the use of a technique such as Lagrange multipliers, but they do not complicate the solution of the global stiffness matrix.

Penalty functions are described by Bathe (1982) for use in structural analysis. The governing linearized global equilibrium equations are modified to include the new constraint equations, which are functions of the unknown displacements as shown in Eq. 2.22.

$$\left[[K_t^G] + \alpha\{e_i\} < e_i >^T\right] \cdot \{\Delta U\} = \{\Delta R\} + \alpha U_i^* \cdot \{e_i\} \qquad (2.22)$$

where: $[K_t^G]$ is the global tangent stiffness matrix

$\{e_i\}$ is the vector containing the global constraint equation

$\{\Delta U\}$ is the vector of global incremental displacements

α is a constant of relatively large magnitude

$\{\Delta R\}$ is the vector of global incremental applied loads

U_i^* is the right-hand side of the global constraint equation

The advantage of using penalty functions in the current formulation rather than other constraint techniques such as Lagrange multipliers is that the total number of global equations to be solved remains unchanged. In addition, the equations which are required to impose shear constraints are straight forward to formulate, and involve a minimal number of computations in the modification of the global stiffness matrix. Finally, U_i^* is always zero, so the right-hand side of the global system of equations remains unchanged.

The implementation of this procedure for a structure containing 18 DOF beam-column finite elements requires only the knowledge of the global nodes and directions in which the shear constraints are to be imposed. Consider the structural joint pictured in Fig. 2.7. The directions of shear compatibility can be easily determined by considering the cross section vectors of either element which enters the joint. The vector aligned with the element web and the vector aligned with the element flange are previously required in order to form the local-to-global transformation matrix for the element. Equation 2.23 shows how these vectors can be applied directly to the joint DOFs in order to form the compatibility constraint equations for the joint.

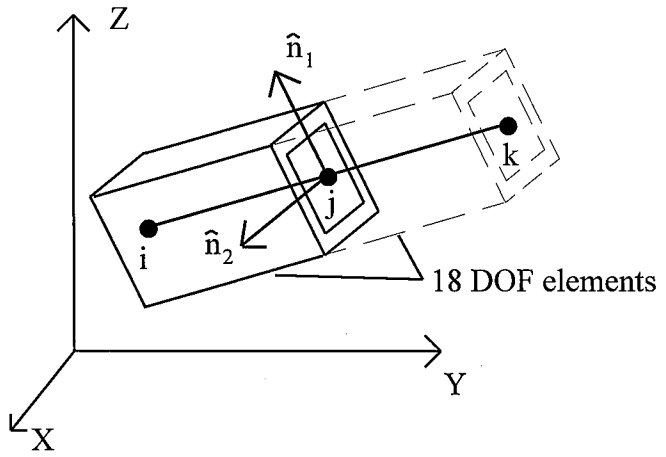

Figure 2.7: Global Directions of Element Translational DOFs at a Joint

$$< < 0 >^{1xi} \quad < e_j^* >^{1x9} \quad < 0 >^{1xk} > \begin{Bmatrix} \{\Delta U_i\} \\ \{\Delta U_j\} \\ \{\Delta U_k\} \end{Bmatrix} = 0 \tag{2.23}$$

where: $< e_j^* >= \left\langle \langle \hat{n} \rangle^{1x3} \quad \langle 0 \rangle^{1x3} \quad -\langle \hat{n} \rangle^{1x3} \right\rangle$

$\{\Delta U_i\}^{ix1}$ and $\{\Delta U_k\}^{kx1}$ are the global incremental displacements which do not correspond to the joint for which translational DOF constraints are being imposed

$\{\Delta U_j\}^{9x1}$ is the global incremental displacement vector which corresponds to the joint for which translational DOF constraints are being imposed

$< \hat{n} >^{1x3}$ is the unit vector in the global constraint direction

This equation shows an example of one constraint equation, but similar equations can be written for any other steel-concrete deformation constraints at a joint. The unit vectors contain at most 3 non-zero terms, for a total of 6 non-zero terms in the constraint equation $\{e_i\}$. The general form of Eq. 2.22 can be reduced to that of Eq. 2.24 and Eq. 2.25 for the 9x9 section of the global tangent stiffness matrix which corresponds to the joint for which the translational constraints are being imposed, with the remaining portions of the global stiffness matrix remaining unchanged. In Eq. 2.25, the dashed lines separate the 9x9 matrix into 3x3 sections.

$$\left[[K_j] + \alpha \{e_i^*\} < e_i^* > \right] \{\Delta U_j\} = \{\Delta R_j\} \tag{2.24}$$

$$\left[[K_j] + \alpha \{e_i^*\} < e_i^* > \right] = [K_j] + \left[\begin{array}{c:c:c} \alpha \{\hat{n}\} < \hat{n} > & 0 & -\alpha \{\hat{n}\} < \hat{n} > \\ \hdashline 0 & 0 & 0 \\ \hdashline -\alpha \{\hat{n}\} < \hat{n} > & 0 & \alpha \{\hat{n}\} < \hat{n} > \end{array}\right] \tag{2.25}$$

The accuracy of the penalty function method is dependent upon the magnitude of the multiplier α. A larger value for the multiplier produces a more accurate solution. Bathe (1982) suggests that α should be 100 to 1000 times as great as the largest diagonal term in the global stiffness matrix. Figure 2.8 shows an example of an axially loaded CFT beam-column which has slip restrained at both ends. The "exact" solution is calculated using Lagrange multipliers. The solutions using various magnitudes of the penalty functions are shown in Table 2.1. The analysis is extremely accurate for the case when the value for α is 1000 times the highest diagonal term.

Table 2.1: Axially Loaded Column Example Results

	Lagrange Multipliers	Penalty Function $\alpha = 10X$	Penalty Function $\alpha = 100X$	Penalty Function $\alpha = 1000X$
Δ steel (mm)	0.725226	0.729813	0.725848	0.725404
Δ concrete (mm)	0.725226	0.725353	0.725354	0.725354
% error steel	---	0.632	0.0858	0.0245
% error conc.	---	0.0175	0.0177	0.0177

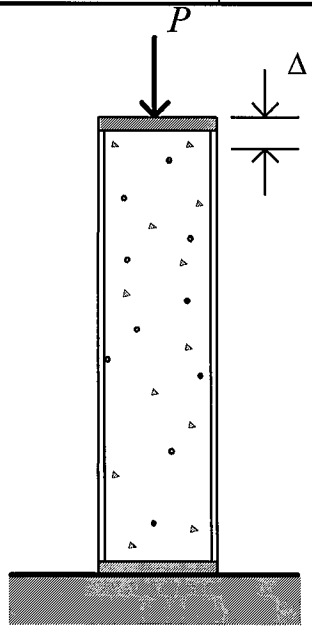

$EA^{stl} = 6.89\text{x}10^4$ kN

$EA^{conc} = 6.89\text{x}10^4$ kN

$L = 10^3$ mm

$P = 100$ kN

$K_{slip} = 10^4$ MPa

Figure 2.8: Axially Loaded Column Example

2.2.3 Additional Issues Related to the Use of Constraint Equations

In addition to the required shear constraints, there are practical analysis situations when the steel and concrete should not be allowed to slip in the axial direction at a structural node. These situations arise when mechanical shear connectors are provided at the node, when there is a change in CFT cross section sizes at a node, when CFT elements frame into a node from different directions, or when a beam-to-column connection includes diaphragms or through-bolts such that they enforce axial strain compatibility of the steel and concrete at a joint. In order to prevent slip at a node, an additional constraint equation of the same form as Eq. 2.23 is required in the direction of the element centroidal axis. This equation can be defined as an input parameter, or can be automated by considering the unit vector along the axis of an element which frames into such a joint.

An issue arises when conducting geometrically nonlinear analysis using constraint equations, in that the directions of shear constraint are required to be updated to reflect the changing geometry of the structure. In the current formulation, the required constraint equations are determined at the beginning of the analysis, and are assigned to nodal DOFs in the global stiffness matrix rather than to local DOFs at the element level. This scheme is adopted to avoid problems which may arise due to redundant equations resulting from multiple CFT elements entering at a single node, and to simplify the algorithm used in the computer implementation. The constraint directions are initialized based on the orientation of the structural members at the beginning of analysis. For geometrically linear analysis, the constraint equations are not updated. For geometrically nonlinear analysis, the constraint equations are assumed to rotate with the structural node at which they act. This approach assumes that all structural members are rigidly connected, an assumption which is consistent with the scope of the current formulation. The rotation of the constraint equation is a linear transformation of a vector in three-dimensional space (Weaver and Gere, 1990), and is computed directly from the nodal rotations. Equation 2.26 shows the general form of this transformation.

$$\{{}_2\hat{n}\} = [T]\{{}_1\hat{n}\} \tag{2.26}$$

where $\{{}_2\hat{n}\}$ is the unit vector in the constraint direction in configuration C2

$\{{}_1\hat{n}\}$ is the unit vector in the constraint direction in configuration C1

$[T]$ is the C1 to C2 transformation matrix given by:

$$[T] = \begin{bmatrix} \cos\Delta\beta\cdot\cos\Delta\gamma & \cos\Delta\beta\cdot\sin\Delta\gamma & \sin\Delta\beta \\ -\sin\Delta\alpha\cdot\sin\Delta\beta\cdot\cos\Delta\gamma & -\sin\Delta\alpha\cdot\sin\Delta\beta\cdot\sin\Delta\gamma & \sin\Delta\alpha\cdot\cos\Delta\beta \\ -\cos\Delta\alpha\cdot\sin\Delta\gamma & +\cos\Delta\alpha\cdot\cos\Delta\gamma & \\ -\cos\Delta\alpha\cdot\sin\Delta\beta\cdot\cos\Delta\gamma & -\cos\Delta\alpha\cdot\sin\Delta\beta\cdot\sin\Delta\gamma & \cos\Delta\alpha\cdot\cos\Delta\beta \\ +\sin\Delta\alpha\cdot\sin\Delta\gamma & -\sin\Delta\alpha\cdot\cos\Delta\gamma & \end{bmatrix}$$

where: $(\Delta\alpha, \Delta\beta, \Delta\gamma)$ is the incremental rotation of the joint in the global coordinate system

2.3 Force Recovery

The accuracy of the fiber element approach relies on the proper modeling of the constitutive behavior of the materials. In addition, the incremental strains for each fiber element must be recovered from the incremental global deformations in a manner consistent with the finite element formulation presented in Section 2.1. Based on the incremental strains and the constitutive models, forces may be recovered at the element ends. This section presents several key features of the force recovery procedure adopted for the current formulation. These include the technique for including the high-order geometrically nonlinear terms of the virtual work equation of equilibrium which are nonlinear in the displacements (integrals three and six of Eq. 2.14), recovery of element centroidal axis strain and curvature from the element corotational forces, and the technique used for materially nonlinear force recovery.

2.3.1 Inclusion of Incremental-Iterative Geometrically Nonlinear Terms

The high-order geometrically nonlinear stiffness terms of the virtual work equation of equilibrium that include the increment in stress cannot be accounted for when the tangent stiffness of the element is formed at the beginning of a load step or iteration since these terms are nonlinear in the displacements. However, Morales (1994) suggests a technique for including these terms (integrals 3 and 6 of Eq. 2.14) during force recovery. This technique takes advantage of the fact that the incremental elongation of an element can be computed directly from the element nodal deformations, accounting for the geometrically nonlinear elongation which takes place during the current iteration (Cook, 1981). The other incremental corotational deformations (element end rotations) are computed by subtracting the incremental rigid-body rotation from the incremental element end rotations. Once all the incremental corotational deformations have been computed in this fashion, the beginning-of-iteration corotational tangent stiffness matrix is used to compute the incremental axial forces in the steel and concrete at each end of the element by multiplying the first, second, and seventh rows of the natural stiffness matrix by the incremental element deformation vector $\{\Delta d^{nat}\}$. The steel and concrete incremental axial forces are used to update the axial force terms of the low-order geometric stiffness matrix $[K_{g1}^{nat}]$ to form the matrix $[K_{g1}^{nat}]^*$ in which the axial force terms are replaced by $(P^c = {}^1P^c + \Delta P^c)$, and $(P^s = {}^1P^s + \Delta P^s)$. The remaining corotational element end forces (bending moments) are computed using the updated natural stiffness matrix $[K^{nat}] = [K_e^{nat}] + [K_{g1}^{nat}]^* + [K_{g2}^{nat}]$. This technique accounts for the effect of the incremental axial force on the element stiffness during the current load step, i.e., it incorporates the third and sixth terms of Eq. 2.14 (see (Morales, 1994) for details of a similar force recovery technique).

2.3.2 Computation of Element Strains from Element Forces

The steel and concrete stress-strain relationships are discussed in Chapter 4. The element strains can be computed using the strain-displacement relationships developed in Section 2.1.4 (Eq. 2.9 and 2.10), but this method requires the calculation of midpoint axial deformation, thus eliminating the computational benefit of static condensation of the midpoint DOFs. The strain-displacement relationships may also produce strain discontinuities at element ends due to the lack of continuity of the derivatives of the finite element interpolation functions. For example, the interpolation function for curvature is linear (i.e., second derivative of the transverse deflection, which is cubic). Thus the curvature computed from the element end rotations and interpolation functions is based on the assumption that the element is prismatic.

A more consistent approach is to recover the element strains from the member end forces, as these forces are in equilibrium at the element ends (White, 1986). The strain-force relationship is developed by utilizing the material tangent stiffness relationship at a cross section, thus taking into account that the element may be partially plastified. Equation 2.27 shows the expansion of the integrals of Eq. 2.15 which include element forces.

$$
\begin{aligned}
\Delta P^c &= \int_{A_1^c} \Delta\tau^c dA^c = \int_{A_1^c} E^c \Delta u'^c dA^c = \int_{A_1^c} E^c \left(\Delta u'^c_c - y\Delta v''_c - z\Delta w''_c\right) dA^c \\
&= EA^c \Delta u'^c_c + EQ_z^c \Delta v''_c + EQ_y^c \Delta w''_c \\
\Delta P^s &= \int_{A_1^s} \Delta\tau^s dA^s = \int_{A_1^s} E^s \Delta u'^s dA^s = \int_{A_1^s} E^s \left(\Delta u'^s_c - y\Delta v''_c - z\Delta w''_c\right) dA^s \\
&= EA^s \Delta u'^s_c + EQ_z^s \Delta v''_c + EQ_y^s \Delta w''_c \\
\Delta M_z &= -\int_{A^{tot}} y\Delta\tau^c dA^c + y\Delta\tau^s dA^s = -\int_{A_1^s} y_1 E^s \Delta u'^s dA^s - \int_{A_1^c} y_1 E^c \Delta u'^c dA^c \\
&= \int_{A_1^s} E^s \left(-y\Delta u'^s_c + y^2 \Delta v''_c + yz\Delta w''_c\right) dA^s + \int_{A_1^c} E^c \left(-y\Delta u'^c_c + y^2 \Delta v''_c + yz\Delta w''_c\right) dA^c \\
&= EQ_z^c \Delta u'^c_c + EQ_z^s \Delta u'^s_c + EI_{zz}^{s+c} \Delta v''_c + EI_{yz}^{s+c} \Delta w''_c \\
\Delta M_y &= -\int_{A^{tot}} z\Delta\tau^c dA^c + z\Delta\tau^s dA^s = -\int_{A_1^s} z_1 E^s \Delta u'^s dA^s - \int_{A_1^c} z_1 E^c \Delta u'^c dA^c \\
&= \int_{A_1^s} E^s \left(-z\Delta u'^s_c + yz\Delta v''_c + z^2 \Delta w''_c\right) dA^s + \int_{A_1^c} E^c \left(-z\Delta u'^c_c + yz\Delta v''_c + z^2 \Delta w''_c\right) dA^c \\
&= EQ_y^c \Delta u'^c_c + EQ_y^s \Delta u'^s_c + EI_{yz}^{s+c} \Delta v''_c + EI_{yy}^{s+c} \Delta w''_c
\end{aligned}
\tag{2.27}
$$

Therefore:

$$\begin{Bmatrix} \Delta P^c \\ \Delta P^s \\ \Delta M_z \\ \Delta M_y \end{Bmatrix} = \begin{bmatrix} EA^c & 0 & EQ_z^c & EQ_y^c \\ 0 & EA^s & EQ_z^s & EQ_y^s \\ EQ_z^c & EQ_z^s & EI_{zz}^{s+c} & EI_{yz}^{s+c} \\ EQ_y^c & EQ_y^s & EI_{yz}^{s+c} & EI_{yy}^{s+c} \end{bmatrix} \begin{Bmatrix} \Delta u'^c_c \\ \Delta u'^s_c \\ \Delta v''_c \\ \Delta w''_c \end{Bmatrix} \tag{2.28}$$

The combined bending moment in the steel and concrete is used when considering the moment-strain relationship, as the steel and concrete have the same bending curvature at the member ends. Equation 2.28 shows the matrix representation of the strain-force relationship for the CFT beam-column with interlayer slip. This expression allows for calculation of separate steel and concrete axial strains, while retaining the same bending curvature for both materials. As mentioned previously, the strains are not influenced by the rigid-body motion of the element, and therefore, the axial strain and bending curvature are the corotational deformations of the element.

Once the incremental element end strains and curvatures have been determined for each end of the element using Eq. 2.28, the longitudinal strain at any point in the element can be determined using Eq. 2.9. Using this approach, an incremental strain is computed for each steel and concrete fiber of the end cross sections.

2.3.3 End-of-Iteration Element Force and Rigidity

Once the strain increment has been determined for a given fiber, the appropriate constitutive material model is used to update the stress (${}^2\tau$) and tangent modulus of the fiber (${}^2_1E_t$). For incremental-iterative analysis, care must be taken to use the appropriate reference state for the materials. Crisfield (1991) presents a discussion of the need for a consistent material nonlinear recovery scheme during iterations on the global structural system. If the stress and strain are updated at the end of each global iteration and used as a reference for subsequent iterations, spurious unloading may be detected during the

global load increment. Instead, the state of stress and strain for the material at the beginning of the global load increment is used as the reference state for material stress-strain calculations. The end-of-iteration tangent modulus determined for each fiber is used to form the tangent stiffness for the next load iteration or increment.

White (1986) and others have suggested techniques for insuring force equilibrium at the end of global load increments or iterations which include material nonlinear behavior. Typically, the incremental axial force is assumed to be constant along the member length, and therefore the incremental axial force computed using numerical integration is averaged at the two ends of the element. In addition, the incremental element end moments are computed through numerical integration, and the shears are computed directly from static equilibrium. These end-of-iteration forces are then compared to the applied load and an unbalanced force vector is formed. Using this procedure along with the Newton-Raphson iterative scheme (Bathe, 1982), the applied loads and resultant forces are in equilibrium at the end of each global load increment.

However, the current analytical formulation for slip combined with the sudden and extreme nonlinear behavior of concrete in tension gives rise to substantial changes in the unbalanced forces. The technique of numerical integration can be used effectively to determine the tangent stiffness of the 18 DOF CFT element, and can also be used to determine the end-of-iteration forces in the element, but the method for ensuring force equilibrium described in the previous paragraph causes unwanted material nonlinear behavior to occur. In particular, the technique of averaging axial force between the two ends of an element may result in the cracking of concrete at a cross section which should remain completely elastic. An example of this type of behavior is a cantilever beam with a transverse tip load. When the concrete cracks at the fixed support, the applied axial load is zero. Due to concrete material nonlinearity (cracking) which happens within the iteration, the recovered axial force is compressive. Using the conventional technique, the average axial force is assumed to act at each end of the element. In order to bring the element into equilibrium with the applied axial loading, a tensile force is applied to the element at each end during the subsequent iteration. This force causes substantial

cracking of the concrete at the free end of the element, which is obviously not the correct solution. The subsequent path dependent behavior often leads to incorrect results.

In order to avoid this problem, material nonlinear behavior is not included in the calculation of unbalanced force during the Newton-Raphson iterations. This method can be thought of as a simple-step incremental approach with respect to materially nonlinear behavior. Unbalanced forces caused by geometric nonlinearity are considered in the conventional fashion.

The issue of concrete cracking, and the separation of the steel and concrete axial DOFs, also affects the assembly of the end-of-step forces into the global end-of-step force vector, due to the unbalanced forces caused by geometrically nonlinear behavior. This may result in compressive unbalanced forces in some instances. The resulting geometrically nonlinear behavior is similar to that described above for materially nonlinear behavior. To mitigate the results of this type of behavior, the current formulation assumes that all external point loads are applied to the steel DOFs only. This assumption is consistent with the loading of CFTs as columns in structural frames if shear tab connections are used, where applied vertical loads are transferred from the girders to the steel tube, and must be transferred to the concrete core through interface stress. Alternately, loading the steel tube only, but then restraining slip at the joint, also models the direct transfer of load into the concrete that is often exhibited in fully restrained connections.

Additionally, the end-of-step forces from the force recovery procedure are assembled only into the steel DOFs of the elements (i.e., the steel and concrete axial forces from force recovery are assumed to act on the steel axial DOF for the purpose of assembling the global end-of-step force vector in preparation for computing the unbalanced force vector). The assumption that loads are applied only to steel DOFs and the subsequent assembly of recovered forces into the steel DOFs of the global structure does not affect the accuracy of the geometrically nonlinear formulation (see Appendix B), or the accuracy of the resulting analysis of individual CFT members under axial, flexural, or combined loading (see Chapter 5). Rather, this approach is taken here to ensure a

stable convergence to a null unbalanced force vector, without invoking inappropriate path-dependent behavior of the concrete constitutive formulation.

2.4 Global Solution Strategy for Material and Geometric Nonlinear Analysis

The global solution strategy for material and geometric nonlinear analysis of structures which include the 18 DOF CFT beam-column element follows closely the strategy presented by Bathe (1982) and White (1986) (for steel frame structures), with a few notable exceptions. A step-by-step procedure is outlined below, with specific reference to the points which differ from conventional solution strategies. This flowchart is presented within the context of executing an incremental/iterative Newton-Raphson solution strategy (Bathe, 1982).

1. At the beginning of a global solution increment, the structure is assumed to be at a converged equilibrium state, and each element is assumed to be represented by a straight line joining the two end nodes. The element stiffness matrices are formed based on the converged values of force and rigidity. The stiffness matrices are formed in the corotational coordinate system and are then transformed to the local element coordinate system. It is important to note that the concrete material nonlinear phenomena of tensile cracking and compressive unloading require each element geometric nonlinear stiffness matrix to be based on the globally recovered element forces from the previous load step rather than the forces recovered from fiber element numerical integration of the previous iteration (Crisfield, 1991). This is done because the technique for enforcing element axial force equilibrium including updated assessment of the material state may cause grossly erroneous material behavior, as discussed in Section 2.3.3.

2. During subsequent Newton-Raphson iterations, the element stiffness matrices are formed using the tangent modulus at each fiber at the end of the previous iteration.
3. The midpoint DOFs of the CFT elements are condensed out of the local element stiffness matrices as shown in Appendix A. The same procedure is used to condense out the midpoint DOFs of the 12 DOF steel wide-flange beam elements, as shown by White (1986).
4. The element stiffness matrices are rotated from the local element coordinate system to the global coordinate system based on the geometry of the global nodes at the end of the previous iteration.
5. The equations used in the global stiffness matrix to enforce equilibrium between the steel and concrete deflections for the CFT elements are also rotated in the global coordinate system as discussed in Section 2.2.3. By rotating the constraint equations as such, they always act in the appropriate global direction for the deformed structure during geometrically nonlinear analysis.
6. The element stiffness matrices are assembled to form the global stiffness matrix in the conventional fashion. The global constraints are then assembled into the global stiffness matrix in the form of penalty functions, as described in Section 2.2.2. The magnitude of α for the penalty functions is determined at each step by scanning the diagonal of the global stiffness matrix for the highest term. The value of α is chosen to be 1000 times the highest diagonal term, and is used for all constraint equations.
7. The global incremental load vector is formed as the remainder of the applied loads and the unbalanced forces at the end of the previous iteration. If the previous iteration ended in convergence, the global incremental load vector is still formed as the applied load vector for the current load step minus the unbalanced forces at the end of the previous load step (for simple-step incremental analysis, subtracting the unbalanced forces from the previous step helps ensure that the internal forces of the structure remain in equilibrium with the applied loads). The unbalanced forces from the previous step are due to the convergence tolerance, which may leave some unbalanced force when convergence is achieved.

8. Gauss elimination (LDU decomposition) is used to solve the global system of equations. The computer code is given by Bathe (1982) for LDU decomposition of a matrix stored in skyline form. A global limit point is detected by a negative on the diagonal of the decomposed global stiffness matrix. When a global limit point is detected, the structure becomes unstable and the analysis is stopped.
9. The deformations of the elements are recovered using the geometrically nonlinear force recovery procedure of Morales (1994) as described in Section 2.3.1. First, the incremental axial force is computed directly from the elongation of the element centroid. The incremental axial force is then used to update the axial force terms of the element geometric nonlinear stiffness matrix before the other local element forces are recovered. This technique accounts for some of the high order terms of the virtual work equation of equilibrium (Morales, 1994).
10. The element end cross section strain and curvatures are computed from the element end force-strain relationship as shown in Section 2.3.2. This technique is employed by White (1986). It is more accurate than strain recovery using the shape functions to compute strains, as the derivatives of the shape functions may be discontinuous between elements at a node (White, 1986).
11. For each cross section in the structure, the element end strains are used to compute the incremental strain for every fiber. Material constitutive states are updated and used to compute the uniaxial stress and the tangent modulus of each fiber.
12. Numerical integration is used at each cross section to determine the end-of-iteration rigidity. Numerical integration can also be used to determine the end-of-iteration element end forces, but these forces are not used to enforce element equilibrium. Rather, it is assumed that material nonlinearity does not affect the equilibrium of the elements. This approach is, again, adopted to avoid numerical problems that result from concrete nonlinear phenomena. Given sufficiently small solution steps, however, the analysis yields accurate results.
13. The total local element forces are computed as the previously computed total force plus the incremental forces from the current iteration. The local element forces are

transformed to the global configuration based on the position of global nodes at the end-of-iteration. The element forces are assembled into a global end-of-iteration total force vector. The total forces are compared to the total applied loads, and an unbalanced force vector is computed. The Newton-Raphson iterative solution strategy is used to converged on an equilibrium configuration for the global structure. For this type of analysis, the global incremental work is compared to a tolerance to detect convergence to an equilibrium configuration. If a non-iterative approach is taken (i.e., simple-step incremental analysis), the end-of-step configuration is assumed to be an equilibrium state, and the negated unbalanced force vector is applied to the global load vector for the next load step as described in step 1 above. Steps 2-13 are repeated until global convergence is achieved or a global limit point is detected. If convergence is detected, a new global solution increment begins with step 1.

Chapter 3

Bond and Slip in Rectangular CFTs

CFT researchers disagree about the effect of bond and slip on the deformation and load capacity of CFT columns and beam-columns. Slip and loss of bond have been observed in experimental tests which were designed to induce this behavior (Virdi and Dowling, 1980; Tomii, 1985; Lu and Kennedy, 1994; Shakir-Khalil, 1993a, b, c, 1994b; Shakir-Khalil and Hassan, 1994a; Shakir-Khalil and Al-Rawdan, 1995, 1996). Correspondingly, many building codes for composite construction require mechanical shear connectors if the calculated interface stress in a CFT column exceeds a limiting value (BS5400, 1979; AIJ, 1980). However, the effect of slip on the overall performance of CFTs remains a subject of research, and it is possible that for frame structures the effect of loss of bond is relatively small, especially with respect to the global frame behavior.

To provide comprehensive modeling of slip, the computational formulation presented in Chapter 2 allows the steel and concrete in a CFT element to have independent axial deformation. The two materials exchange axial force based on the properties of a slip layer which separates them. The model is intended to capture the major slip attributes observed in experiments on rectangular CFTs. The primary causes of slip are loss of bond at connections of steel beams to CFT columns, and loss of bond in

flexure due to concrete cracking and composite beam action. Behavior ranging from perfect bond to perfect slip may be modeled.

It will be seen in the following sections that mechanical shear connectors effectively prevent slip, provided that enough connectors are present to transfer applied loads to the concrete core. CFTs with mechanical shear connectors are therefore a trivial case and do not require special consideration. The computational model presented in Chapter 2 is intended to model CFT elements which do not have shear connectors and which have no special surface preparation to promote or inhibit bond.

This chapter is structured as follows. Section 3.1 presents a review of the experimental research which has been conducted to determine the slip and bond characteristics of rectangular CFTs. Section 3.2 presents the general characteristics of bond and slip which are observed experimentally, and which are modeled by the current computational formulation. Section 3.3 presents a general description of the capabilities of the computational slip model. Section 3.4 presents the calibration of slip and bond parameters which are required input for the computational model. The parameters are determined by examination and comparison to published experimental research. A set of calibrated parameters are determined which can be applied to all structural configurations which may include slip, including analysis of isolated CFT beams and columns, and connection regions consisting of steel beams which frame into rectangular CFT columns at connections that do not penetrate the steel tube. Alternately, perfect bond may be modeled in connection regions where the concrete is engaged directly (see Section 2.2.3) Finally, in Section 3.5 the calibrated parameters are applied to additional verification examples in which the computational model is compared to published experimental test results.

3.1 Review of Experimental Literature

Research on CFTs has historically focused on determining the strength and deformation characteristics of individual members (Gourley et al., 1995). Early tests did not consider the effects of bond or slip, as the specimens were usually axially loaded columns with capped ends, ensuring that the applied load was evenly distributed to both materials (Bridge, 1987; Cederwall, 1990; Shakir-Khalil, 1991, to name a few). Some experimentalists commented on slip and bond however, and suggested that the effect on overall behavior should be determined (Bridge, 1976; Orito et al., 1987; Matsumura and Konno, 1989; Grauers, 1993).

Recently, researchers have begun to examine the parameters of CFTs which have more complex, subtle effects on overall behavior than nominal dimensions and material strength. These research programs have included for example, testing of a variety of new connection details for steel wide flange beams framing into circular or rectangular CFTs (Dunberry et al., 1987; Ji et al., 1990, 1991; Kamba, 1991; Azizinamini et al., 1992a, b; Azizinamini and Prakash, 1993a, b; Kato, 1993; Shakir-Khalil, 1993c, 1994b; Azizinamini and Shekar, 1994; Shakir-Khalil and Al-Rawdan, 1995, 1996, Ricles et al., 1995; Alostaz and Schnieder, 1996). Supplementary push-out tests have been performed to determine the bond capacity at these connections (Morishita et al., 1979a, b; Tomii et al., 1980a, b; Virdi and Dowling, 1980; Shakir-Khalil, 1993a, b; Shakir-Khalil and Hassan, 1994a; Shakir-Khalil and Al-Rawdan, 1995, 1996). Other researchers have instrumented beam specimens to investigate slip which may occur during flexural tests (Lu and Kennedy, 1994). These three categories, push-out studies, connection studies, and flexural tests, form the available literature to date which provides information on bond and slip in rectangular CFTs. The following sections present summaries of the major publications which represent landmark research on slip and bond in CFTs. Several of the publications will be used in the slip model calibration and verification.

3.1.1 Push-Out Studies of Concrete-Filled Steel Tubes

Push-out studies have been used to develop building codes and design recommendations for the bond strength of the steel-concrete interface in rectangular CFTs. In push-out tests, the concrete is cast in the steel tube so that a gap is left between the concrete and the loading platen during testing (Fig. 3.1a). By loading only the concrete at one end of the specimen and supporting only the steel tube at the other end, all applied load is required to be transferred through the steel-concrete interface. Early testing programs focused exclusively on the determination of bond strength.

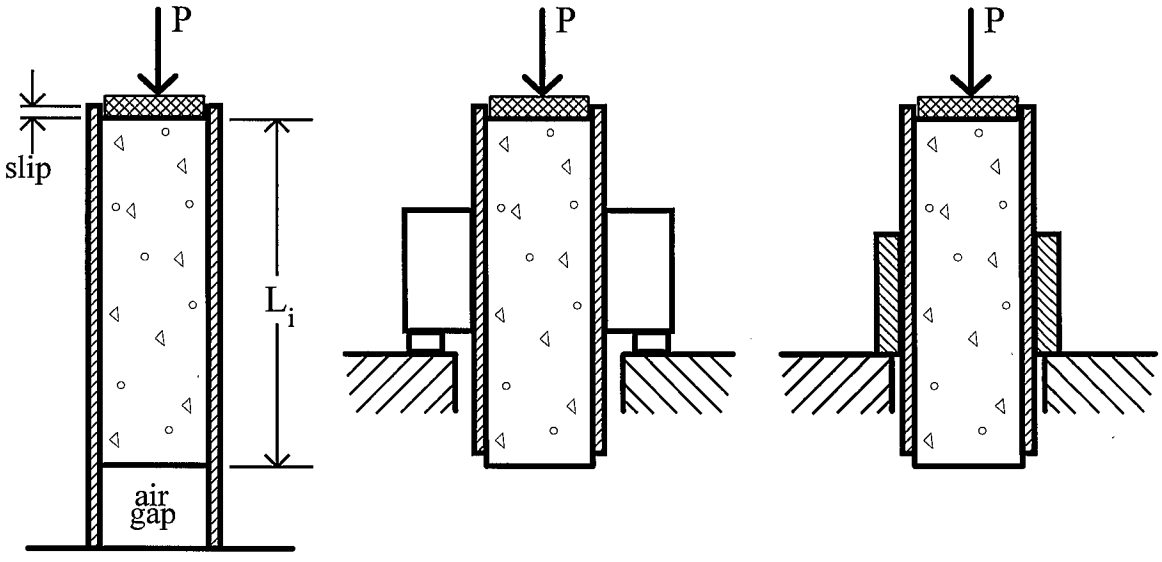

(a) (b) connection on flat side (c) connection on corner (d)

Figure 3.1: Experimental Push-Out Test Setup

The push-out studies which have been conducted recently by Shakir-Khalil were instrumented to measure slip and load transfer from the steel to the concrete during testing. These publications provide the first insight into the load-slip relationship at the interface between the steel and concrete in rectangular CFTs. This series of tests also

included various other support conditions such as gusset plates welded to the sides or corners of the tube, and thick plates welded flat to the side of the tube (Fig. 3.1b, c, d).

Following is a description of several of the key publications on the push-out resistance of CFTs (focusing on square or rectangular CFTs). As will be seen, these publications are not used directly in the calibration of the computational model, but provide information about the effect of various support conditions as well as the load-slip relationship and bond mechanisms.

Virdi and Dowling (1980):

One of the earliest published works on bond in CFTs was by Virdi and Dowling (1980). They presented the results of over 100 push-out tests conducted on circular CFT stub columns. The results of this experimental program gave the first indication of the bond strength in circular tubes, but the experimental scatter was significant. The authors suggested a bond strength of 0.41 MPa. However, values as high as 2.1 MPa were recorded.

Tomii (1985):

A research program was conducted in Japan to develop recommendations for bond strength to be used in the AIJ standards for composite construction. The program included tests published by Morishita et al. (1979a, b) and Tomii et al. (1980a, b), to name a few. These publications were discussed by Tomii (1985) in the context of design recommendations. In this paper, Tomii discusses the sources of interface stress and methods for calculating stresses at service conditions. The mechanisms include shear transfer from the steel tube to the concrete core at beam-to-column connections, as well as composite beam shear which is induced by cracking of the concrete in tension. He suggests a technique for calculating interface stress and gives recommendations for providing shear connectors or other mechanical shear transfer mechanisms.

Shakir-Khalil (1993a):

Shakir-Khalil (1993a) presented the results of 40 push-out tests on rectangular, square, and circular specimens with and without structural bolts as shear connectors. In addition to mechanical connection, the length of the steel-concrete interface and the conditioning of the interface were studied. Several of the specimens were oiled to prevent adhesion of the concrete to the steel tube walls. For the unoiled rectangular specimens without mechanical connectors, the calculated bond strength varied from 0.33 MPa to 0.59 MPa with an average value of 0.44 MPa, suggesting that the BS5400 value of 0.4 MPa was a reasonable estimate of bond strength. The circular sections which had no mechanical shear connectors and were unoiled had bond strength values ranging from 0.65 to 0.93 MPa with an average bond strength of 0.80 MPa. The length of the steel-concrete interface did not affect the bond strength of the specimens.

The tube walls were cut away from several specimens to observe the condition of the concrete after testing. Abrasions near the corners of the rectangular specimens indicated that most of the slip resistance occurred due to surface irregularities, especially in the corners where the tube walls provided higher resistance to bulging. The circular specimens showed an even distribution of abrasion marks, indicating that the circular specimens were more effective in resisting slip around the entire perimeter of the section.

The published results included graphs of applied loading verses measured slip in the specimens. Although the load-slip behavior was not the focus of the research, it provides valuable insight into the shape of the curve. The shape of the load-slip curve for specimens with no mechanical connectors was nearly rigid-perfectly-plastic. The specimens with mechanical connectors showed much more ductile behavior.

Shakir-Khalil (1993b):

Shakir-Khalil (1993b) presented the results of 56 push-out tests on square and circular CFT specimens with and without Hilti nails or structural bolts as mechanical connectors. In this series of tests, the length of the steel-concrete interface was held constant. Different methods of supporting the steel tube were investigated to determine if

the support conditions affected the test results. Figure 3.1 shows the various support configurations employed. Some specimens were supported at the base as in the previous investigation (Fig 3.1a), while others were supported at midheight by gusset plates welded to the flat side walls or corners of the tube (Fig 3.1b, c). Still others were supported on thick steel plates welded flat to the sides of the tube (Fig 3.1d).

Published results include tabulated values of bond strength as well as graphs of load verses slip, and of strain measurements at various points along the steel tube. The test results again show a nearly rigid-perfectly-plastic load-slip relationship for the specimens with no mechanical shear connectors. The most significant result, however, is the dramatic change in bond strength observed for various support conditions. The rectangular specimens supported at their base gave an average bond strength of 0.2 MPa, while the specimens supported through gusset plates had bond strength values ranging from 0.76 to 1.06 MPa. The specimens supported through thick steel plates had an average bond strength of 0.44 MPa. The specimens were cut open to observe the concrete core, revealing abrasion marks near the top of the gussets for the specimens supported on gusset connections. This suggests that a localized mechanism develops at these connections characterized by a high normal force which develops near the base of the gusset due to rotation of the tube walls. This phenomenon is discussed further in Section 3.1.2. These results also suggest that standard push-out tests (Fig. 3.1a) may not produce values that are representative of the slip stiffness or bond strength which exists in the region around gusset plate connections.

Shakir-Khalil and Hassan (1994a):

Shakir-Khalil and Hassan (1994a) presented the results of 52 push-out tests on rectangular CFT specimens. Bolts or threaded bars of various lengths and configurations were used in some of the specimens as mechanical shear connectors. Many of the specimens had no shear connectors but were included to study the effect of concrete curing time, compressive strength, and mix proportions. These specimens were tested for slip at 28, 56, and 84 days to study the effect of concrete shrinkage on bond strength. The

various concrete mixes contained low, medium, and high cement content which was expected to affect both the compressive strength and shrinkage of the specimens. Published test results included graphs of load verses slip for the specimens with shear connectors as well as some of the tests with no shear connectors. The load-slip curves for the plain specimens again suggested a nearly rigid-perfectly-plastic relationship. The measured bond strength was reported for all of the plain specimens. These results indicated that cement content had a dramatic effect on the bond strength of specimens, with low cement content specimens having a higher bond strength due to reduced shrinkage. The bond strength showed significant scatter with values ranging from 0.146 MPa to 0.533 MPa. Age of testing had a smaller but measurable effect on the bond strength of specimens, suggesting that continued shrinkage reduces bond strength over time.

3.1.2 Connection Studies of Concrete-Filled Steel Tubes

Column connection tests which are instrumented to measure load transfer from the steel tube to the concrete core or which are instrumented to measure slip provide an alternative to push-out studies for determining bond strength and slip stiffness. Connection tests represent a more realistic loading condition because they more closely model the loading conditions and geometry which may induce slip in composite CFT frames. In these tests, axial load is applied to both steel and concrete at the top of the specimen and additional load is introduced through beam-to-column connections (figure 3.2). The axial load applied to the column represents loads from floors higher in the structure, whereas the shear loads applied to the connections represent loads from the floor framing into the connection.

Traditional connections to steel tubes are made by welding or bolting various configurations of connection plates, angles, or tee-stubs to the sides of the tube. Providing connections to the flanges of the beam (such as with plates or tee-stubs) is thought to provide a fully-restrained connection. Often slip in the connection region of

bolted connections is minimal since load is directly transferred to the concrete by the connecting elements. If the connection is made only to the beam web, the connection is considered to be a simple connection, providing little resistance to rotation. The connection studies which provide insight into bond and slip have all been conducted on simple connections made of either single gusset plates or tee-cleats welded to the outside of the steel tube. Figure 3.3 shows these connection types.

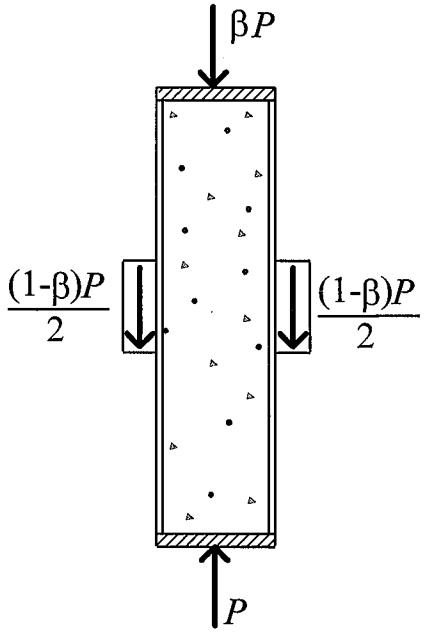

Figure 3.2: Connection Test Experimental Setup

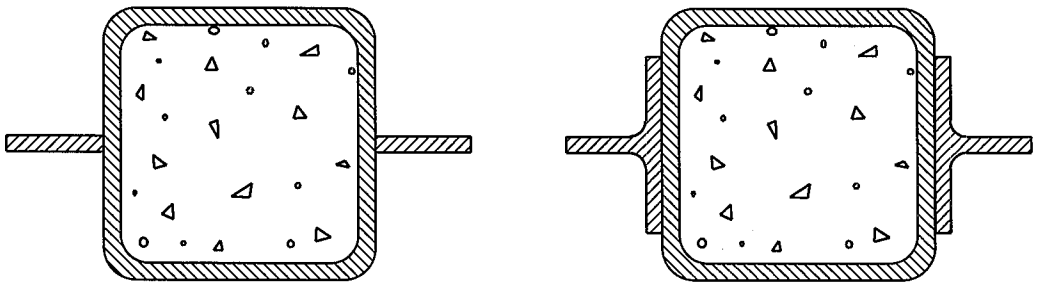

Figure 3.3: Simple Connection Types (Dunberry et al., 1987)

As mentioned earlier, the connection studies represent a more realistic loading condition for CFT columns. For this reason, they will be used in lieu of push-out studies to calibrate the current computational finite element model for interface slip. Following is a description of several of the key experimental publications, some of which will be used in the calibration.

Dunberry, et al. (1987):

Dunberry, et al. (1987) presented the results of 24 column tests on short, square CFTs under pure axial load. In these experiments, some or all of the axial load was applied through connections to the steel tube which do not penetrate the tube walls. In addition, some of the axial load was applied to both materials at the top of the specimen to simulate loads from the upper floors of a building. The connections to the steel tube walls varied from single plate shear tabs to structural tee sections (see Fig. 3.3). This series of tests is exceptionally useful because the specimens were instrumented with demic points to measure slip in the region around the connection.

Detailed information was provided for one of the specimens about the measured slip in the region around the connection. The authors noted a region above and below the connection which lost bond prior to achieving the ultimate strength of the specimen. The measured strain in the steel was plotted for the specimen at or near the failure load, and the corresponding load in the steel and concrete were also presented. Graphic comparisons were shown of the various connection types. Little difference can be seen between the behavior of connections made with structural tees and those made with gusset plates. The length of the connection region also has limited effect on the load carrying capacity of the section.

An interesting comparison is made between two specimens with all parameters held constant except that one specimen is capped to prevent slip at the top while the other is not. The specimens achieve a similar ultimate capacity, but the measured load transfer is significantly different. As expected, the concrete core of the uncapped specimen gradually receives the load from the connection, with no load at the top and a maximum

near the bottom of the connection, while some of the connection load is transferred through bearing of the end plate at the top of the capped specimen. The data from this publication is used for calibration and verification of the current computational model.

Shakir-Khalil (1993c):

Results of experiments on 8 simple beam connections to rectangular CFT columns are presented. The connections are made by welding single plate gussets to the walls of the steel tube (see Fig. 3.3a). The experimental failure loads for the columns are compared to the capacity predicted by the design recommendations of BS5400. In all cases, the capacity of the column exceeds the code recommended capacity, suggesting that the design recommendations may be overly conservative.

Failure of the specimens was found to be controlled by the eccentricity of the beam loads. The four specimens which had a lower eccentricity of the applied load at the shear tabs failed due to column instability after extensive material inelasticity and local buckling had occurred. The four specimens with a larger eccentricity failed at the connections, by tearing of the welds where the gusset plate connected to the steel tube wall. It was found that a membrane mechanism developed when the tension end of the connection pulled away from the concrete core due to rotation of the gusset plate. The concrete core prevented the corners of the tube from moving toward each other. The membrane forces combined with residual stresses from the welding process at the gusset-to-steel tube interface caused material failure on the tension side of the connection. Residual stresses from the seam weld in the cold-formed steel tube may have also contributed to the local material failure.

Strain measurements were reported along the height of the specimen for the loading history. These measurements showed that the beam shear force was transferred to the concrete core over a short distance above and below the connection plate. The author suggests that the transfer distance above and below the plate is no more than the depth of the column. Examination of the strain plots show a nonlinear load-strain relationship during the test. The nonlinear straining becomes more pronounced as the test

progresses, indicating either loss of bond or materially nonlinear behavior. Because of the localized materially nonlinear behavior and the experimentally observed local buckling at the connection, the results from this publication are not used in the calibration of the current computational model.

Shakir-Khalil (1994b):

Results of experiments on 8 simple beam connections to rectangular CFT columns are presented. The columns have similar dimensions and geometry to the series of test presented in Shakir-Khalil (1993c). This series of tests, however studies connections that are made by welding tee-cleats to the tube walls (see Fig. 3.1b). The experimental failure loads for the columns are compared to the capacity predicted by the design recommendations of BS5400. In all cases, the capacity of the column exceeds the code recommended capacity, suggesting that the design recommendations may be overly conservative.

The observed mode of failure is column instability, which occurs only after significant material yielding reduces the rigidity of the section. Large forces were observed in the lateral bracing after yielding had occurred, indicating that materially nonlinear behavior resulted in a non-symmetric section. In no case did the connection limit the capacity of the column. The yield-line mechanism hypothesized for the tee cleat was accompanied by membrane action, as the concrete core prevented the corners of the tube from moving inward. The resulting behavior was a combination of membrane action leading to a yield-line mechanism, in which a gap formed between the tee cleat and the tube wall at the tension side of the connection. The author also suggests that the pinching effect caused by membrane action provides a key mechanism in the transfer of beam shear to the concrete core. Shakir-Khalil and Al-Rawdan (1996) confirm this mechanism through three-dimensional finite element computational modeling of the connection region. This mechanism provides both a higher resistance to slip and a higher bond strength in the connection regions than the traditional push-out studies indicate.

The results reported in the publication includes graphs of steel strain measured throughout the height of the column at various load levels. The strain measurements near the connection show erratic values due to rotation of the connection plates, local buckling of the tube walls below the connection, and other localized effects. Other strain measurements above and below the connection region provide useful information, however, especially for the load levels below which a linear load-strain relationship is seen. The strain measurements presented will be used to calibrate the slip and bond parameters of the current computational model. In particular, the steel strains will be used to calibrate the slip stiffness prior to loss of bond.

3.1.3 Flexural Studies of Concrete-Filled Steel Tubes

A study of bond and slip due to flexure is presented by Lu and Kennedy (1994). This is the only test program found in the literature which presents extensive slip measurements taken during flexural loading of square or rectangular CFTs. As such, the effect of slip and bond loss due to flexure remains a matter of debate.

Lu and Kennedy (1994)

Lu and Kennedy (1994) presented the results of 12 flexural tests on rectangular and square CFTs. The test program included four different tubular cross-sections which were oriented so that bending was induced in either the strong or weak axis. The specimens were simply supported at the ends and were loaded symmetrically at two points, resulting in a constant moment region in the middle of the span. Various shear span-to-depth ratios were used to investigate the effect of shear transfer length on strength, ductility and slip.

The specimens were instrumented to detect slip at a number of points along the length and through the depth of the specimen. The instrumentation consisted of demic points in the concrete which were visible through round holes drilled in the steel tube. At the ends of the specimen, LVDTs were used to measure relative movement between the

steel and concrete. Strain gages were also used to track the strain in the steel tube and to determine the strain distribution and position of the neutral axis at various cross-sections.

Four supplementary tests were conducted on hollow steel sections for comparison to the CFT tests. The comparison showed an increase in both flexural strength and stiffness when concrete was added to the core of the tube section. The local buckling which terminated the tests on bare steel tubes was delayed significantly in the CFT sections. A marked increase in ductility was also noted.

The slip measured for various moments is presented for one of the flexural specimens. The graph shows that a slip of less than 0.2 mm was detected at 90% of the ultimate moment of the section. After this point, the slip at the ends increases, but is also accompanied by local buckling in the compression flange of the tube in the constant moment region. The interaction between slip and local buckling is not investigated. The measured slip at ultimate moment is presented for all the specimens. The maximum slip detected in any specimen is 3.9 mm, but the authors comment that this reading may be erroneous. Most specimens have a maximum slip at the ends of 1.0 mm or less. The results from this publication are used to verify the calibrated parameters for the current computational model.

3.1.4 Discussion of Experimental Literature

Several conclusions may be drawn from the published experimental research on bond and slip. First, even though push-out studies are the most numerous tests available, they do not accurately represent the bond strength of actual CFTs, especially at simple beam-to-column connections. For this reason, they are eliminated from consideration for the purpose of calibrating the bond strength parameter of the current computational model. Similarly, they may under-represent the initial slip stiffness of the steel concrete interface. They do, however, provide insight into the shape of the load-slip relationship at the steel-concrete interface. Second, the bond strength at simple beam-to-column connections of rectangular CFTs to wide-flange beams which have no shear connectors

and no surface treatment to prohibit or promote bond is seen to be higher than the design recommendations of AIJ or BS5400. Finally, local distortions should be expected to occur in and around the connection plates and steel tube walls at such connections. The rotation of the connection and the resulting pinching effect often improves the bond strength and slip stiffness at these connections. The connection studies of Dunberry et al. (1987) and Shakir-Khalil (1994b) will be used to calibrate the current computational formulation for slip.

3.2 Experimentally Observed Load-Slip Behavior

The push-out tests of Shakir-Khalil (1993a, b) and Shakir-Khalil and Hassan (1994a) provide the best insight into the shape of the load-slip behavior of rectangular CFT sections. Shakir-Khalil was the only researcher who provided graphs of the load-slip data for push-out tests he conducted. These graphs indicate a bilinear relationship (Fig. 3.4).

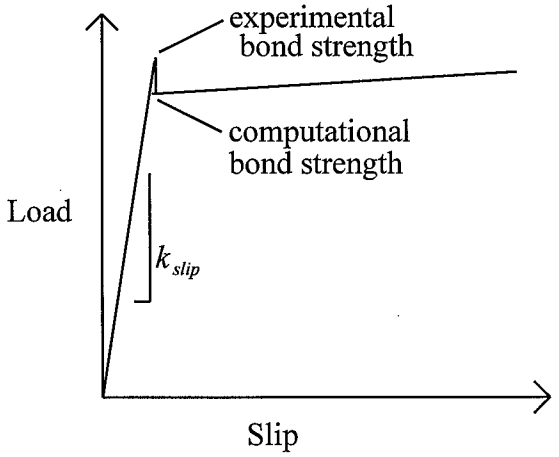

Figure 3.4: Bilinear Load-Slip Relationship

The initial load-slip stiffness (k_{slip}) of the interface is very high, and may vary due to the experimental measuring schemes used in the push-out studies. For example, measurement of slip as the relative position of the loading platen to the top of the specimen in a push-out test may give a different load-slip relationship than a measuring scheme where demic points in the concrete are observed through holes drilled in the steel tube walls. Localized crushing of the concrete under the loading platen or gradual contact of the concrete core with the irregularities in the steel section may be the major sources of experimentally observed slip before loss of bond occurs. In many of the publications, the scale of the plotted graphs prohibits accurate determination of the exact load-slip relationship, and a straight-line approximation of the initial slip stiffness may result in significant error from the actual data points.

In all the published load-slip graphs from push-out studies, the initial slip stiffness is very high. In fact, there may be essentially no slip before loss of bond occurs, suggesting that k_{slip} is infinite. The current computational model is capable of capturing the full range of behavior including perfect bond, and the calibration of the computational model in the following section will provide further insight into the most appropriate value for k_{slip}.

The specimens tend to lose the initial stiffness suddenly, at a point which corresponds to the bond strength of the interface (f_{bond}). Some of the load-slip graphs show a sudden loss of load capacity after the bond strength is achieved. The upper limit point is traditionally reported as the bond strength, but the lower limit point more closely represents the bilinear load-slip behavior which is used in the computational model. These limit points are shown in Fig. 3.4.

A very low stiffness is observed after the interface bond breaks down. Depending on the scale of the graph, this stiffness is nearly zero. Some of the graphs also indicate a slight negative slope in this region.

An elastic-plastic load-slip relationship is adopted for the current computational slip model (the flat portion of the load-slip relationship is assigned a slope near zero).

This model requires only two parameters, the initial stiffness of the steel-concrete interface and the bond strength. The experimental data provided by Dunberry et al. (1987), Shakir-Khalil (1994b), and Lu and Kennedy (1994) will be used to calibrate and verify the slip stiffness parameters for the current analytical model. The calibration and verification are presented in the Sections 3.4 and 3.5 respectively.

3.3 Capability and Limitations of the Computational Slip Model

3.3.1 Axial Load Transfer at Connections

The current computational model presented in Chapter 2 was developed to study the effect of slip on the overall behavior of CFTs, including individual members and CFT composite frames. The most promising capability of the formulation is simulation of gradual axial load transfer from the steel tube to the concrete core at beam-to-column connections. When no mechanical shear connectors are provided, this load transfer relies on bond and the keying action caused by geometric imperfections in the tube walls (Grauers, 1993).

An example of the gradual transfer of load from the steel to the concrete based on the current computational model is shown in Figure 3.5. This example is intended to be similar to the connection studies published by Dunberry et al. (1987) and Shakir-Khalil (1993c, 1994b), and Shakir-Khalil and Al-Rawdan (1995), except that slip is allowed at the top of the column, and all the axial load is applied through the beam-to-column connection (i.e., the steel tube and concrete core are free to move at the top and $\beta = 0.0$ in Fig. 3.2). The bond strength of the interface is assumed to be infinite, and all materials are assumed to be linear elastic. The axial rigidity of the concrete core and the steel tube are assumed to be equal. Geometric nonlinearity is not accounted for. 10 elements are used along the length of the column, with the load applied at the node corresponding to the middle of the connection. The figure demonstrates the effect of varying the slip

stiffness. As k_{slip} is increased, the concrete participates more fully in the load carrying capacity of the member. Note that for the highest value of k_{slip} the steel and concrete carry an equal portion of the applied load at the bottom of the column. For this case, the gradual transfer of load to the concrete core (P^c) over the height of the column can be clearly seen.

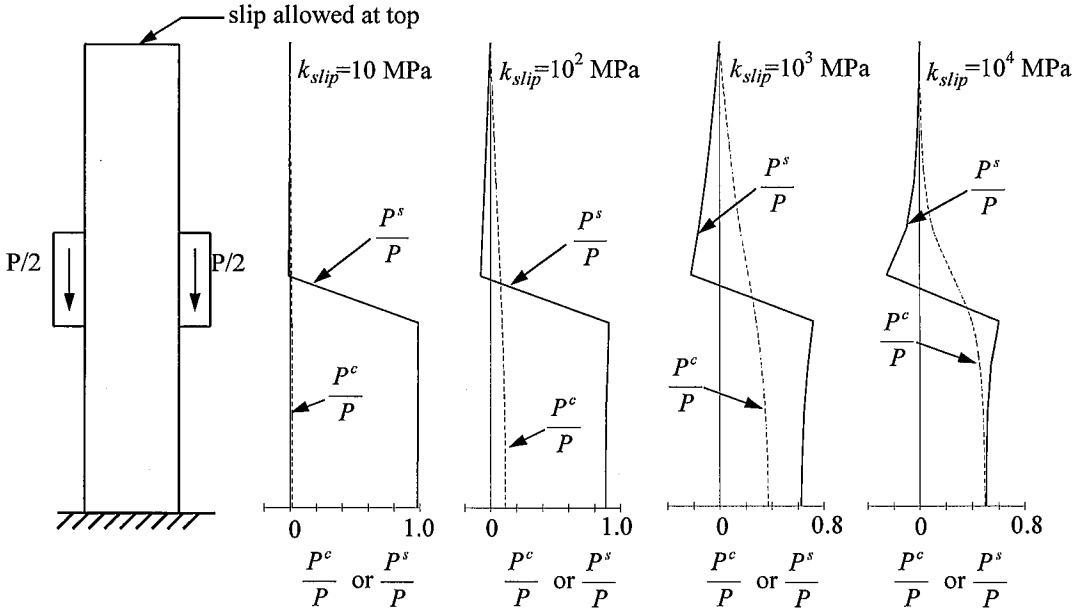

Figure 3.5: Gradual Load Transfer at Beam-to-Column Connections

The example above demonstrates the potential importance of the relative value of the slip stiffness on both the strength and stiffness of CFT members in the computational model. The formulation must therefore be able to capture any slip stiffness ranging from perfect bond to perfect slip. This capability is tested through a second example of an axially loaded column. The rigidity of the member is examined by considering the load-deformation behavior. The deflection of a homogeneous elastic column under pure axial load is given by:

$$\Delta = \frac{PL}{EA} \tag{3.1}$$

For a CFT with slip between the steel and concrete, the applied load must be distributed to both materials according to the proportion of rigidity for each component. Complete transfer at a loading point (perfect bond) may be achieved in experiments through loading plates or capping of the ends of the test specimen. For these cases, the rigidity of the column is given by:

$$EA = EA^s + EA^c \tag{3.2}$$

Alternately, if only the steel tube is loaded and perfect slip is allowed, the rigidity of the column is simply the rigidity of the steel tube alone. For this case, the rigidity of the column is given by:

$$EA = EA^s \tag{3.3}$$

In a real structure where load is introduced at connections to the steel tube only (such as the previous example), the load transfer occurs over a finite region. The "apparent" rigidity of the CFT column (based on the measured deflection of the loading point) will always lie somewhere between perfect bond (Eq. 3.2) and perfect slip (Eq. 3.3).

Figure 3.6 shows the computational model used to test the variation in rigidity of the axially loaded CFT element with slip for various values of k_{slip}. In this example, the springs which make up the slip layer are assumed to have infinite bond strength, and thus a constant slip stiffness. The load is applied to the steel only at the top of the element. Geometrically and materially nonlinear behavior are neglected.

The apparent axial rigidity of the column is calculated by solving Eq. 3.1 for the term EA. Figure 3.7 shows the variation of apparent axial rigidity for values of slip stiffness which range from perfect bond to perfect slip. This figure demonstrates the ability of the current analysis to model a range of slip behavior. Note that in this example

as well as the previous one, a 10,000 MPa slip stiffness effectively prevents slip in the element, while a 0.1 MPa slip stiffness provides practically no interaction between the two materials.

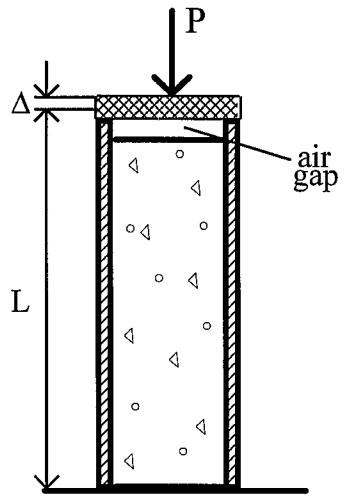

$$EA^s = 4.65 \cdot 10^5 \text{ kN}$$

$$EA^c = 1.92 \cdot 10^5 \text{ kN}$$

Figure 3.6: Axially Loaded Column Example

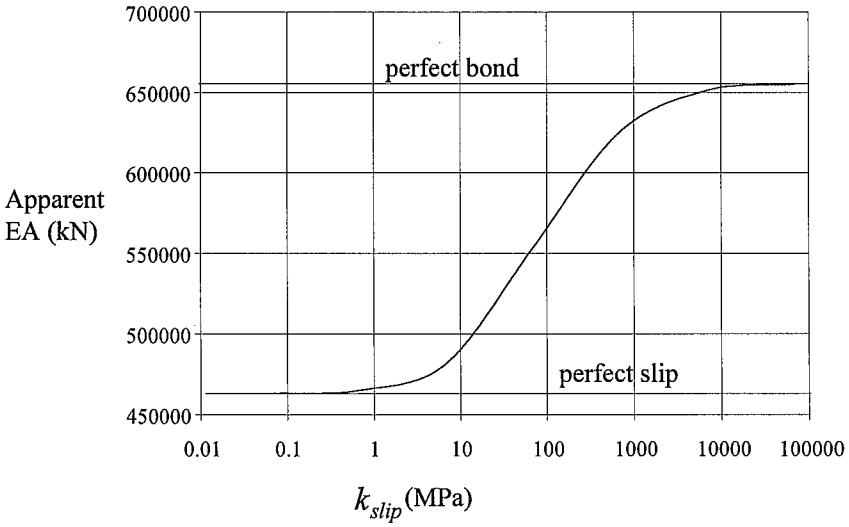

Figure 3.7: Apparent Rigidity of Axially Loaded Column

3.3.2 Slip Due to Flexure

A second application is slip caused by composite beam action during flexure. This mechanism is triggered by cracking of the concrete core in tension which results in an unsymmetric section (similar to a composite beam). The eccentricity of the uncracked concrete section with respect to the steel section causes longitudinal stress to develop in the materials under pure flexural loading. The CFT flexural tests performed by Lu and Kennedy (1994) validate this mechanism. Figure 3.8 shows a CFT member subjected to pure flexure, and the resulting unsymmetric section.

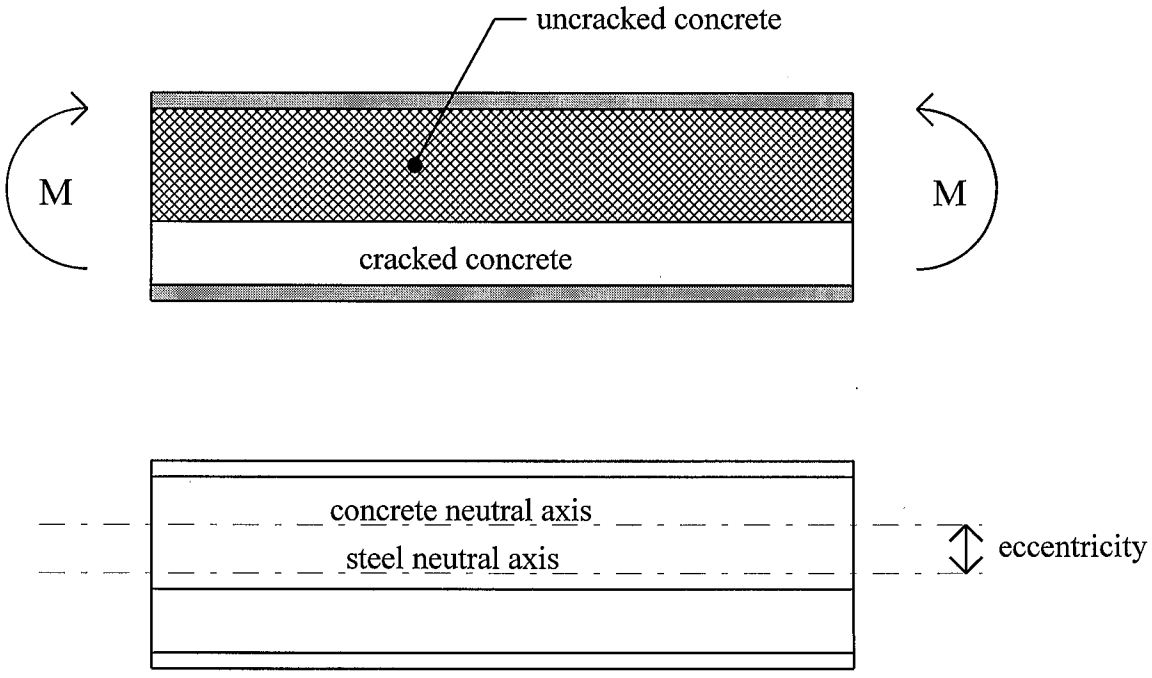

Figure 3.8: Unsymmetric Section Caused by Concrete Cracking

Slip tends to reduce the flexural rigidity of a CFT subjected to pure bending after cracking occurs in the concrete in tension because part of the longitudinal stress which the concrete is required to carry under perfect bond conditions is lost due to slip. For

perfect bond conditions, plane sections are assumed to remain plane and therefore the concrete is more effective in the compression zone of the beam element.

An example showing the effect of slip stiffness on the flexural rigidity of a CFT beam member is not presented at this point because material inelasticity (concrete cracking) is required in order to induce slip. The effect of slip during pure flexural testing is discussed in Section 3.5 when the calibrated parameters are used in the computational model for comparison to the experimental results of Lu and Kennedy (1994).

3.3.3 Computational Limitations of the Slip Model

The current computational formulation includes several simplifications and limitations. First, the bilinear load-slip relationship may not be representative of all load transfer situations which occur in CFTs. However, this relationship is believed to be the most accurate representation for the current formulation based on the available experimental results. Also, the slip which is caused by flexure has not been extensively documented and it is unclear whether the load-slip curve for this type of loading is represented by the bilinear model.

A second limitation of the computational formulation is that shear stress caused by shear deformation is not modeled. The only slip which is allowed is a uniform axial slip between the steel and concrete portions of the element. It is unclear whether shear deformations would induce significant slip at the steel-concrete interface. Lu and Kennedy (1994) attempted to investigate this phenomenon by varying the shear span-to-depth in their flexural tests. The test results indicated that the ratio had a negligible effect on the slip behavior of the beams, but more investigation is warranted.

Third, the effects on slip and bond due to tension or compression normal to the tube wall, as may occur in a connection region, are not accounted for directly. However, they are accounted for to some extent implicitly in the calibration.

3.4 Calibration of Computational Slip Parameters

The load-slip behavior of rectangular CFTs depends on a large number of parameters, including concrete mix proportions, internal tube surface treatment, geometric imperfections, presence of mechanical shear connectors, and loading conditions at connections. The computational formulation developed in Chapter 2 is general, and is accurate for any set of parameters provided that calibration and verification can be accomplished. In order to limit the scope of the current work, the slip model is developed for the computational parameters which are believed to be the most common in modern construction practice for structures using CFTs as beam-columns.

For the current computational calibration, it is assumed that no mechanical connectors are used to improve the bond strength or load-slip behavior. In addition, it is assumed that the concrete is cast in the steel tube without any bond inhibiting or promoting schemes, and with no special surface treatment of the inner walls of the steel tube. The concrete mix proportions are assumed to be standard, that is to say, there is no attempt to alter the mix proportions to limit or promote shrinkage.

These conditions are similar to the available set of experimental tests by Dunberry et al. (1987), Shakir-Khalil (1993c, 1994b), and Shakir-Khalil and Al-Rawdan (1995), which are used for parametric calibration in the following sections. It is important to note that the publications used for calibration are all connection studies rather than push-out studies since the connection studies provide a more realistic representation of the slip behavior. Therefore, the pinching effect and other effects localized to connection regions may affect the calibration. This is acceptable for a number of reasons. First, connection regions are the only locations in CFT composite frame structures where slip is expected. Even though the flexural tests of Lu and Kennedy (1994) showed loss of bond, this behavior was not observed until the limit point of the beams was reached and was accompanied by extensive local buckling of the tube walls. In addition, CFTs are not commonly used as simple beams or under pure flexure with open ends and short shear span-to-depth ratios. Second, there is strong experimental evidence, including push-out

test results (Shakir-Khalil, 1993a, b; Shakir-Khalil and Hassan, 1994a) and connection test results (Dunberry et al., 1987), that slip which occurs before loss of bond is only coincidental and may be the result of experimental apparatus or slip measuring schemes. There is very little slip in any region under any loading condition prior to loss of bond. It will be seen in the following section that the experimentally observed initial slip stiffness is high enough to essentially be considered perfect bond in the computational slip model (see the example of perfect bond in section 3.3.1), and that the values of initial slip stiffness from push-out tests are far below the values which produce acceptable results for the calibration examples.

3.4.1 Calibration of Initial Slip Stiffness

The load-slip graphs presented by Shakir-Khalil (1993a, b) and Shakir-Khalil and Hassan (1994a) for push-out studies give the first indication of the initial slip stiffness in rectangular CFTs. Table 3.1 below shows the approximate initial slip stiffness for the push-out studies on plain specimens. The nomenclature in column one is from the original publications. The table includes all types of support conditions (which are indicated in the right hand column according to Fig 3.1). The initial slip stiffness, k_{slip}, values are obtained by dividing the initial slope of the load-slip curve by the length of the slip interface.

Table 3.1: Initial Slip Stiffness Values from Experimental Tests (Shakir-Khalil, 1993a, b)

Specimen	Length (mm)	Perimeter (mm)	Approximate k_{slip} (MPa)	Test setup (Fig 3.1)
Data from Shakir-Khalil (1993a)				
A1b	400	560	250	a
C1b	400	560	1000	b
C2b	400	560	1000	c
E1b	400	750	1170	b
G1	400	560	420	d
Data from Shakir-Khalil (1993b)				
X1b	396	360	1010	a
Y3a, b	600	560	333	a

The initial slip stiffness ranges from 250 MPa to 1170 MPa. It is interesting to note that the specimens which were supported on connections using gusset plates generally have a higher initial stiffness than the standard push-out tests, with the exception of the specimens in series "X". Because of the scale of many of the published graphs, it is difficult to discern the slope of the initial load-slip graph, and the actual slip stiffness in all cases may well be higher than that reported in Table 3.1.

This data gives an indication of the stiffness of the interface prior to loss of bond in push-out studies. Thus, the strain measurements from the connection studies of Shakir-Khalil (1994b) will be used to test values of k_{slip} that range from 10^3 MPa and up, and the range will be adjusted until agreement is achieved between the computational and the experimental results.

The experiment which provides the most data for calibration of initial slip stiffness is presented by Shakir-Khalil (1994b). In this publication, strain measurements at a number of positions along the height of the specimen are presented as a function of applied load. This data provides information in the materially elastic range on the transfer of load from the steel to the concrete in the region above and below the connection. Because the material is elastic in this range, the slip behavior can be decoupled from the materially nonlinear behavior.

Figure 3.9 presents the experimental setup for specimen E6, including the instrumentation and location of strain gages, and the experimental parameters provided by the author (Shakir-Khalil, 1994b). The test specimens were constructed from 150x150x5 square structural tubing with tee-cleat connections. The tee-cleats were welded to the steel tube along the edges of the flanges, but not along the top or bottom of the connection. The connection load was applied upward, with the connection load and the load at the base of the column being increased in the same proportion. The strain measurements have been reproduced from the original set of figures and are shown in Fig. 3.10.

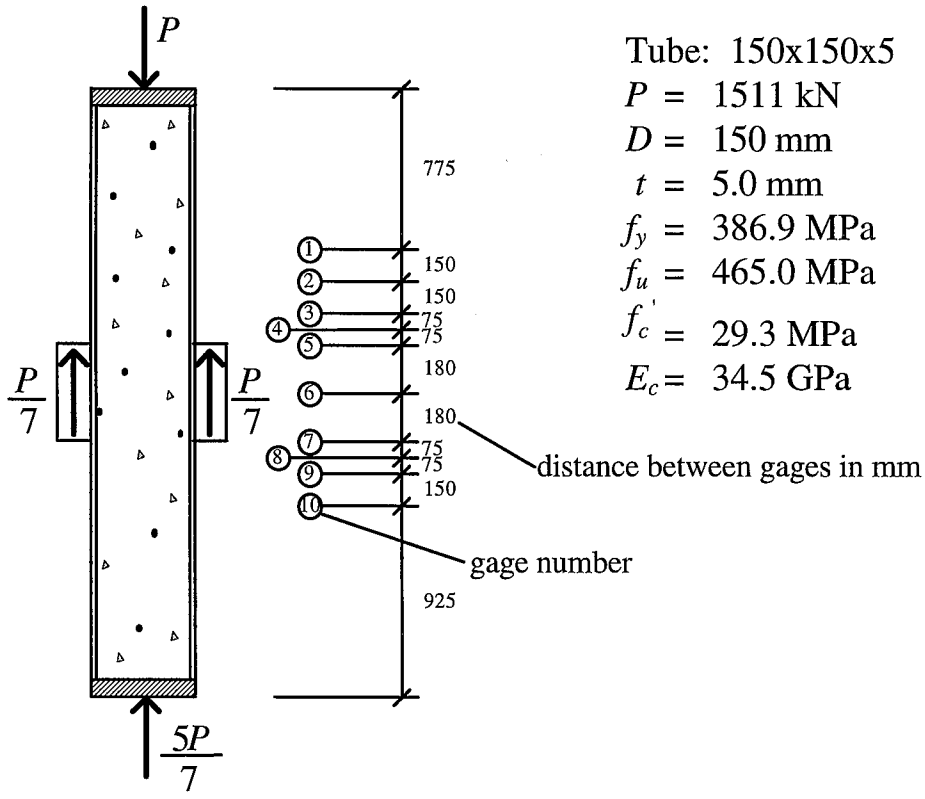

Figure 3.9: Experimental Connection Test Setup (Shakir-Khalil, 1994b, Specimen E6)

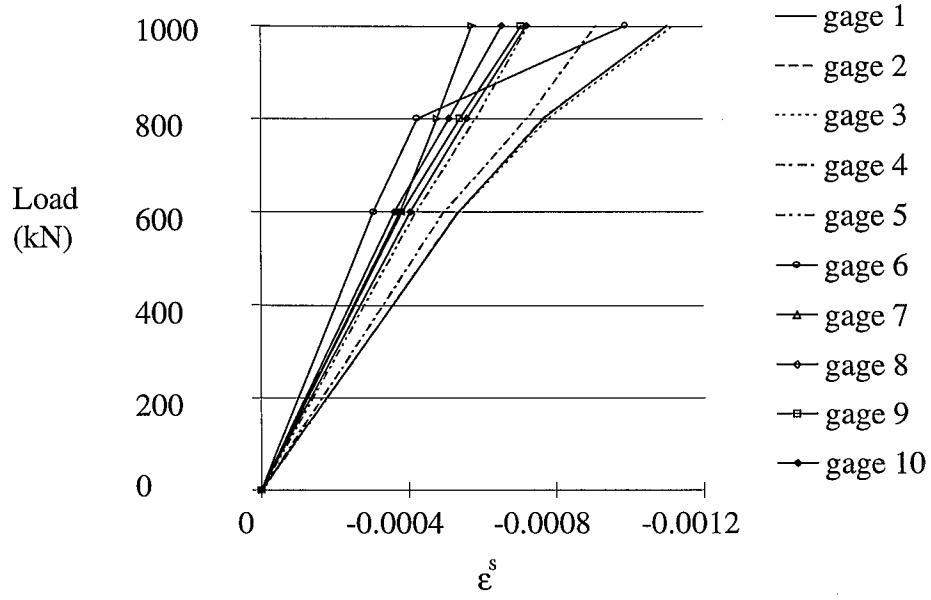

Figure 3.10: Experimental Strain Measurements (Shakir-Khalil, 1994b, Specimen E6)

The computational model was run with varying initial slip layer stiffness' in order to match the strain readings of Fig. 3.10. In the computational model, a node is assigned at each of the strain gage positions shown in Fig. 3.9, as well as at the top and bottom of the specimen. The load applied at the connection is split between the nodes corresponding to gages 5, 6, and 7 in the ratio of 25% - 50% - 25% to simulate the transfer of load along the connection plate. In addition, the experimentally observed concrete elastic modulus is used in the analysis rather than the empirical equation used in the concrete constitutive model so as to better match the elastic behavior of the test. The constitutive model utilizes the empirical equation: $E_c = 3300\sqrt{f'_c} + 6900$ (in MPa) (Carrasquillo et al., 1981).

The first comparison is made at a level of applied load, P, corresponding to 600 kN. Fig 3.11 shows the prediction of the strain in the steel verses the height along the specimen for the computational model and the experiment. The introduction of the connection load to the steel tube in the connection region is clearly seen, along with a localized strain concentration below the connection. This strain concentration is partially due to slip, but is also due to membrane action in the tube wall. The strain measurements of gages 1, 2, and 3 above the connection show that the majority of load is transferred to the concrete in the connection region (since the strain differs little between these three gages), a trend which is only matched well by the highest of the k_{slip} values. Note that the value for k_{slip} of 10^3 MPa (i.e., representative of the push-out studies) produces a strain diagram that over-predicts the length of the load-transfer region (as seen by the gradually sloping data from the computational model).

Table 3.2 shows an analysis of the results including a tabulation of the percent error between the computed and experimental strains. The analysis is presented for all the data points, and then for the data corresponding to gages 1, 2, 3, and 10, which are farthest from the connection region.

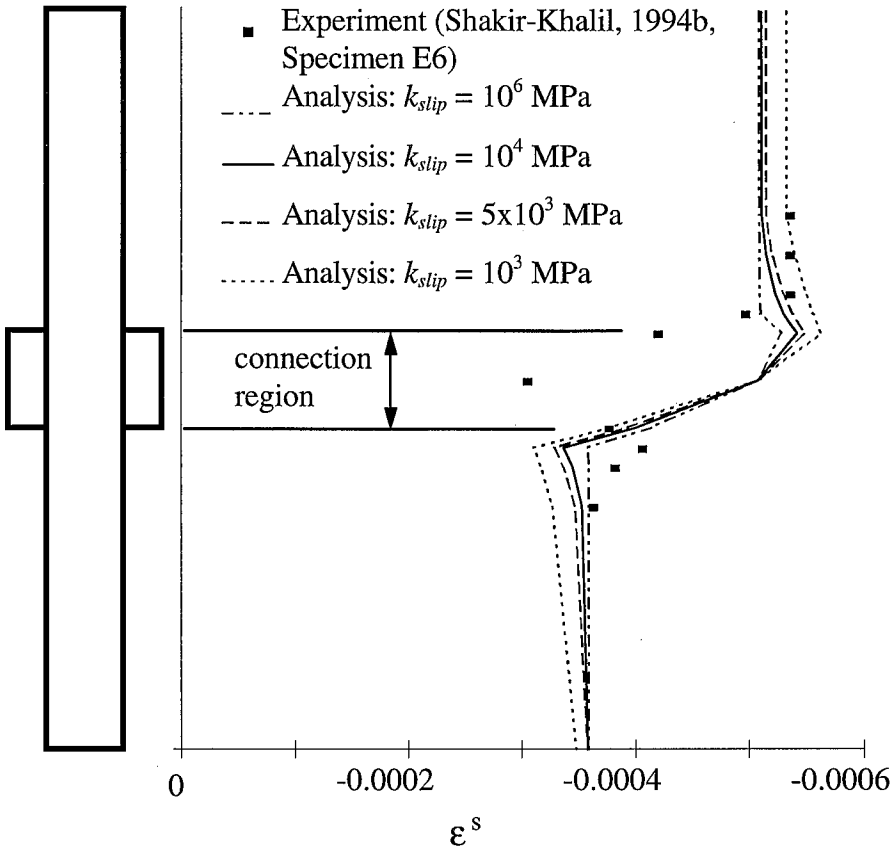

Figure 3.11: Strain Comparison at Total Load of 600 kN

The computational model matches the experimental strain measurements well at this load level. There is no clear pattern to the results, however, as the lowest value of slip stiffness provides the lowest average percent error, but has the highest standard deviation. All values of k_{slip} produce approximately the same average percent error, between 6% and 7%, and the highest value of slip stiffness produces the lowest standard deviation, again indicating a better match to the shape of the strain distribution. The highest values of k_{slip}, which match the load transfer region with more accuracy, are in the range that correspond to perfect bond (see the example problem in Section 3.3.1), suggesting that the portions of the specimen outside the load transfer region may experience little or no slip at this level of loading. It is important to note that the computational model did not encounter numerical instability even with k_{slip}=10^6 MPa.

Table 3.2: Comparison of Experimental and Computational Results for (Shakir-Khalil, 1994b, Specimen E6, P=600 kN)

		% error of ε^s			
	Gage Number	k_{slip} = 10^6 MPa	k_{slip} = 10^4 MPa	k_{slip} = $5x10^3$ MPa	k_{slip} = 10^3 MPa
	1	4.93	4.55	3.80	0.44
	2	4.93	3.80	2.87	-0.86
	3	4.93	2.31	1.00	-2.37
	4	-3.67	-7.73	-9.36	-13.0
	5	-23.0	-26.3	-27.9	-31.2
	6	-63.2	-63.2	-63.2	-63.2
	7	-12.5	-8.72	-6.82	-2.74
	8	11.8	16.9	18.9	23.3
	9	7.19	10.8	12.9	18.0
	10	2.43	4.06	5.69	11.1
All Gages	mean	-6.62	-6.34	-6.21	-6.07
	std dev.	21.3	22.1	22.6	24.0
Gages 1,2,3,10	mean	4.30	3.68	3.34	1.99
	std dev.	1.08	0.84	1.69	5.39

A second comparison is made to the same experimental specimen for a higher load level corresponding to a total load of 800 kN. Figure 3.12 shows the computational results for various values of k_{slip} compared to the experimentally observed data points.

Table 3.3 presents an analysis of this data. The data shows a similar pattern to the results of Table 3.2. The values of k_{slip} which provide the best average percent error again have the highest standard deviation. However, examination of the shape of the graphs again indicates that the highest values of initial slip stiffness give a better prediction of the length over which load transfer takes place. The lower values over-predict the length of the load transfer region.

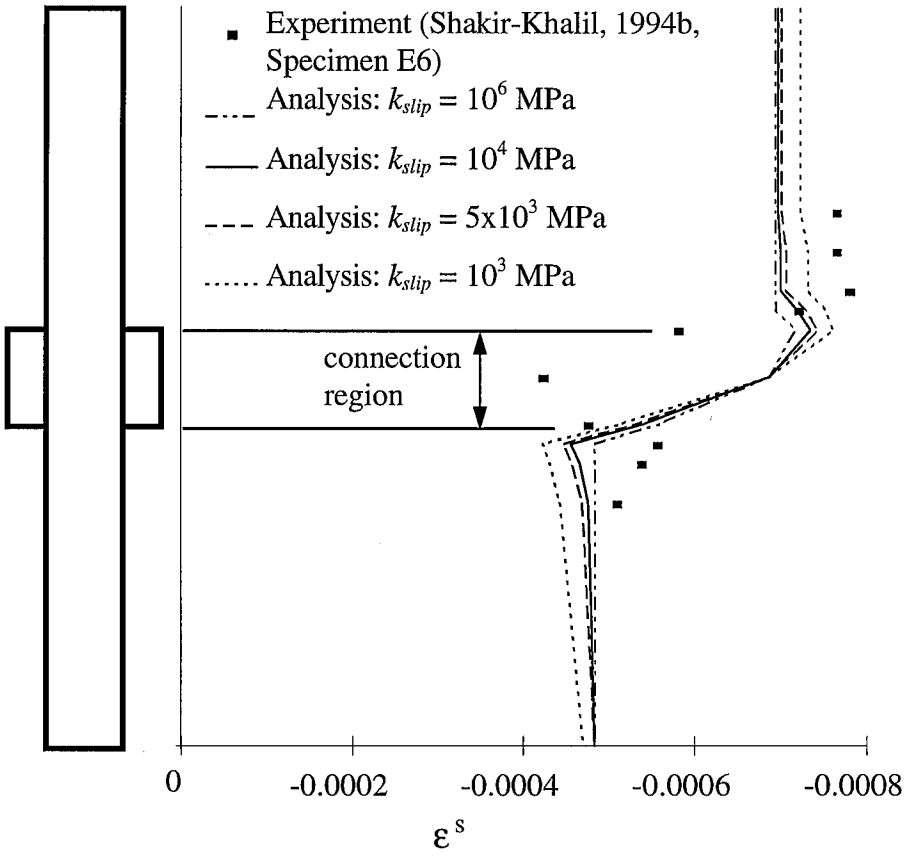

Figure 3.12: Strain Comparison at Total Load of 800 kN

Shakir-Khalil (1994b) also publishes strain readings from a second specimen, E8, which has the same dimensions and strain gage positions as specimen E6 (see Fig. 3.9), but a slightly higher concrete compressive strength ($f'_c = 32.5$ MPa, $E_c = 36.7$ GPa). Only four gages (7-10) are reported. The published strain gage readings are reproduced in Figure 3.13. Gage 7 is clearly reading a localized anomaly associated with connection behavior (seen from its nonlinear shape and low strain values during the early stages of loading) and will be discarded from the current calibration.

The computational slip model is used to predict the strain in the steel tube at the levels of the strain gages. Figure 3.14 shows the comparison of the computational model to the experimental data points. An analysis of the results is shown in Table 3.4.

Table 3.3: Comparison of Experimental and Computational Results for (Shakir-Khalil,1994b, Specimen E6, P=800 kN)

		% error of ε^s			
	Gage Number	k_{slip} = 10^6 MPa	k_{slip} = 10^4 MPa	k_{slip} = $5x10^3$ MPa	k_{slip} = 10^3 MPa
	1	10.07	9.68	9.16	6.31
	2	10.07	9.29	8.38	5.15
	3	12.26	11.5	10.6	7.46
	4	3.94	0.62	-0.76	-3.94
	5	-22.6	-25.5	-27.0	-30.1
	6	-61.6	-61.8	-61.8	-61.8
	7	-18.5	-14.5	-12.8	-8.76
	8	13.2	18.1	19.7	24.0
	9	9.99	13.3	15.0	19.9
	10	4.99	6.56	7.94	13.0
All Gages	mean	-3.81	-3.27	-3.16	-2.88
	std dev.	22.7	23.3	23.6	24.5
Gages 1,2,3,10	mean	9.35	9.26	9.03	7.99
	std dev.	2.67	1.77	1.02	3.03

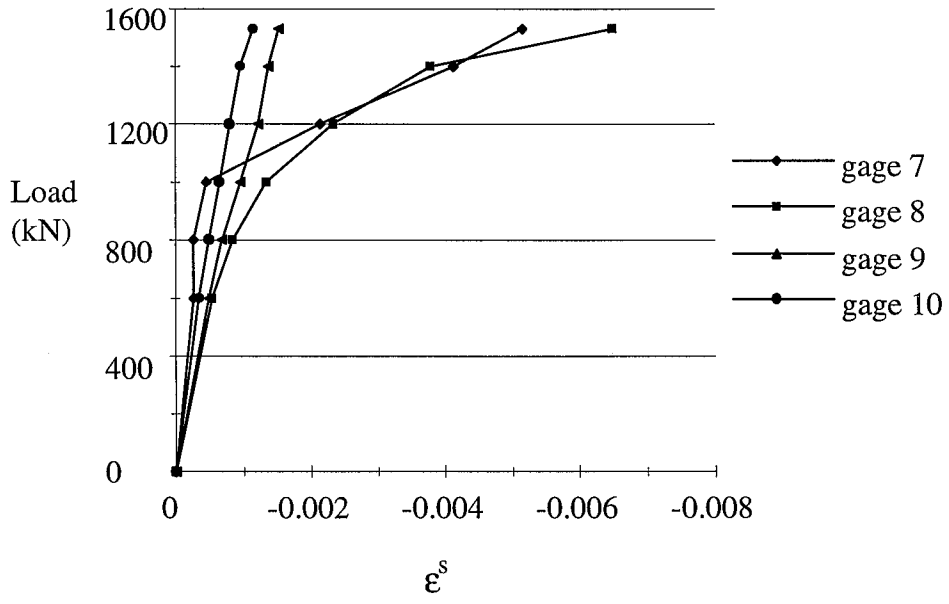

Figure 3.13: Experimental Strain Measurements (Shakir-Khalil, 1994b, Specimen E8)

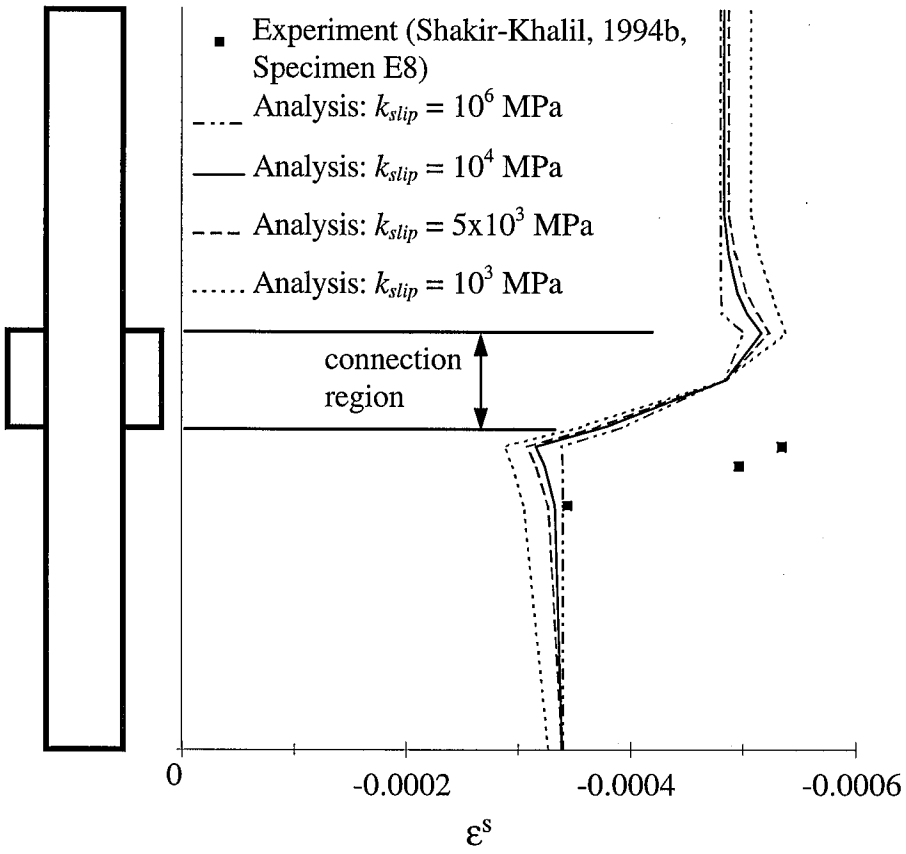

Figure 3.14: Strain Comparison at Total Load of 600 kN

Table 3.4: Comparison of Experimental and Computational Results for (Shakir-Khalil, 1994b, Specimen E8, P = 600 kN)

		% error of ε^s			
	Gage Number	k_{slip} = 10^6 MPa	k_{slip} = 10^4 MPa	k_{slip} = $5x10^3$ MPa	k_{slip} = 10^3 MPa
	8	36.6	40.9	42.4	46.2
	9	31.6	34.8	36.4	40.6
	10	1.15	3.18	4.93	11.3
All Gages	mean	23.1	26.3	27.9	32.7
	std dev.	15.7	16.5	16.4	15.3

The data analysis shows that the highest value for initial slip stiffness results in the lowest average percent error. The average error and standard deviation in this set

of results is significant due to the apparent shift between the computational and experimental results. The shift in results is due in part to the load application scheme (25-50-25% in the connection region), and could be reduced by varying this scheme. Note however that the shift in results for specimen E6 was in the opposite direction from the current example, suggesting that this is a random phenomenon and may be caused by localized straining such as connection rotation or local buckles forming in the tube walls.

The strain is not predicted well in the region close to the connection, but the rate of load transfer is seen to be consistent with the experimental results. The computational results farthest from the connection compare well with the experimental data point for gage 10. The highest value of initial slip stiffness gives an error of 1.15%. The overall straining of the column, including magnitude of the strain and shape of the strain distribution along the specimen length is predicted well by the computational model.

The comparisons presented in this section show evidence that the value of k_{slip} from the push-out studies (10^3 MPa) over-predicts the length of the load transfer region around connections. The experimental results from this set of tests, as well as the observations of other researchers (Dunberry et al., 1987), suggests that there is little or no slip outside the load transfer region, especially in the initial stages of loading. This condition is only predicted accurately by the highest values of k_{slip}. The value of $k_{slip} = 10^6$ MPa was seen to consistently provide an accurate prediction of the load transfer region as well as accurately predicting straining levels. However, both 10^4 and 10^6 MPa lie within the range that can be considered nearly perfect bond (before bond strength is reached) in the computational model (see Section 3.3.1). The value of slip stiffness of 10^4 MPa provides the best balance of mean error and standard deviation in the results. Consequently, the value of initial slip stiffness for the current computational model is chosen to be $k_{slip} = 10^4$ MPa. The experimental data and comparison to the computational model shows that very little slip occurs before the bond strength of the steel-concrete interface is reached. Some gradual transfer of load does occur, however, within a short distance above and below the connection region as indicated by the

localized strain concentrations in both the experimental data and computational results. The computational slip model is required in order to model this localized strain concentration. It will be seen in the following sections that loss of bond aggravates the localized straining in the connection region.

3.4.2 Calibration of Bond Strength

As mentioned previously, push-out studies are not representative of the bond strength at simple beam-to-column connections due to the pinching action caused by connection rotation. One series of push-out tests by Shakir-Khalil (1993a) which were supported on shear tab connections had an average bond strength of 0.97 MPa while another series of specimens having the same connections but larger tube dimensions failed to reach the predicted bond stress of 0.4 MPa. This data suggests that push-out studies are not a reliable method of determining the bond strength at a beam-to-column connection.

In order to study bond strength, connection specimens from Dunberry et al. (1987) are utilized. A much higher percentage of the total load is applied at the connections for this series of tests compared to Shakir-Khalil (1994b). This creates more slip and bond loss and provides a better indication of the bond strength at these connections. Dunberry et al. (1987) present graphs of the experimentally measured slip, strain, and total load in the steel and concrete at a load level near the limit point of the column. These graphs are utilized in calibrating the bond strength of the steel-concrete interface for the current computational model. Note that material nonlinearity in the steel and concrete contribute significantly to the straining of the specimens near their ultimate loads for the example problems in this section. As comparisons with the computational model are made near the ultimate strength of the member, by necessity the materially nonlinear portions of the computational model play a significant role in the results of the calibration of bond strength (see Chapter 4 for a description of the material constitutive models).

Specimen D1 from Dunberry et al. (1987) is presented in the most thorough fashion and will be used for the initial calibration of bond strength. Figure 3.15 shows the experimental setup and test parameters. The loads in this series of tests are applied downward rather than upward as in Shakir-Khalil (1994b). A detailed description of the strain gage locations is not provided by the authors, but the specimens were instrumented to measure steel strain with strain gages, and concrete strain as well as slip with demic points which were visible through holes in the steel tube walls.

The computational model is implemented for comparison to the published slip at various locations along the steel tube for a given load level. The computational model uses 11 elements, with the loading applied to the top, middle, and bottom of the connection region in a ratio of 20-20-60% to simulate the gradual transfer of load in this region. This loading scheme is different than the one used in the previous section since this loading pattern better reflects the load transfer seen in this specific experiment. The loading scheme used in the previous section is also presented later so as to demonstrate the effect that the loading pattern has on the accuracy of the computational results for this type of connection. The initial slip stiffness from the calibration of the previous section ($k_{slip} = 10^4$ MPa) is used far all computational results in the bond calibration.

This test used the same nominal tube size and had approximately the same material properties as the Shakir-Khalil (1994b) specimens E6 and E8, which were used for calibration of initial slip stiffness. The initial elastic modulus of the concrete was not reported and the value predicted by the empirical equation implemented in the concrete constitutive model (Molodan and Hajjar, 1997) had to be adjusted to match the experimental rigidity of the column. The elastic modulus predicted by the empirical equation resulted in the concrete carrying a disproportionate amount of the load compared to the experimental results. The concrete modulus was reduced until agreement was reached between the predicted and experimentally observed concrete rigidity. The resulting concrete modulus was 19.3 GPa (0.77 of the value predicted by the empirical equation).

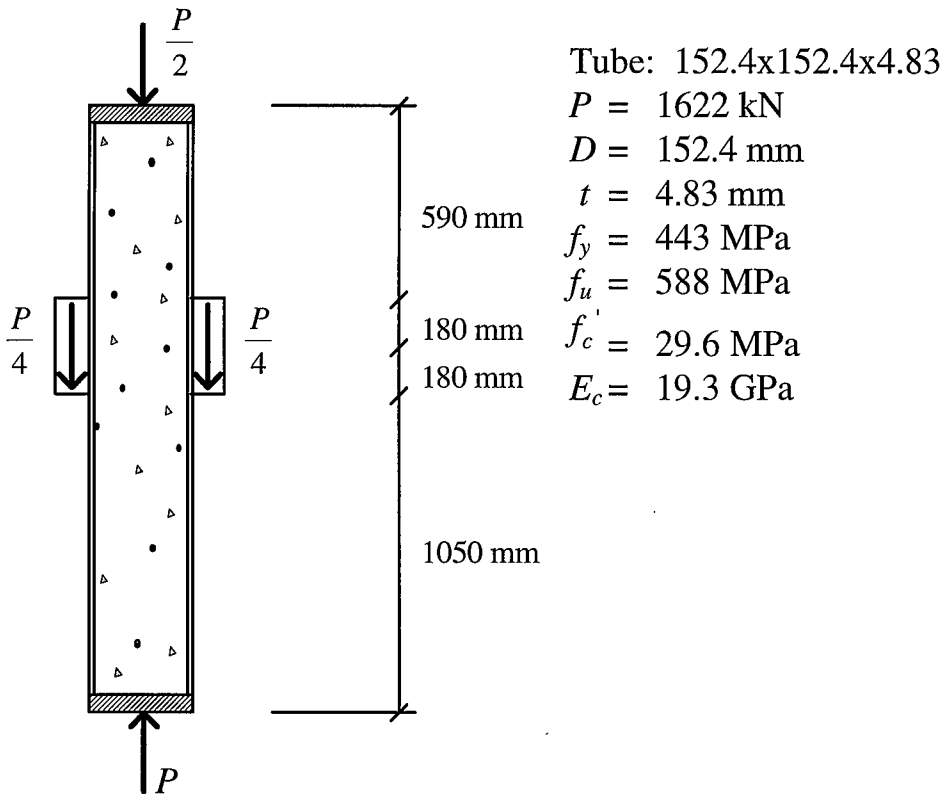

Figure 3.15: Experimental Setup of (Dunberry et al., 1987, Specimen D1)

Figure 3.16 shows the comparison of the computational model to the published experimental results at a load level of 1560 kN for various values of bond strength. Slip between the concrete core and the steel tube is shown at points along the length of the steel tube. Table 3.5 presents an analysis of the data.

The computational model predicts the shape and magnitude of the slip along the column with better accuracy below the connection than above it. This phenomenon can again be attributed to connection rotation and the resulting pinching mechanism which results. The high average percent error in Table 3.5 is the result of the very low values of experimental slip which are in the denominator of the percent error equation for the data points outside the load transfer region. Rather than use the average percent error for the entire length of the member, a better indication of the accuracy of the computational model can be seen in the last row of the table where the maximum computed slip is

compared to the experimentally observed value. The value of $f_{bond} = 0.6$ MPa provides the most accurate prediction of maximum slip with an error of 2.5%.

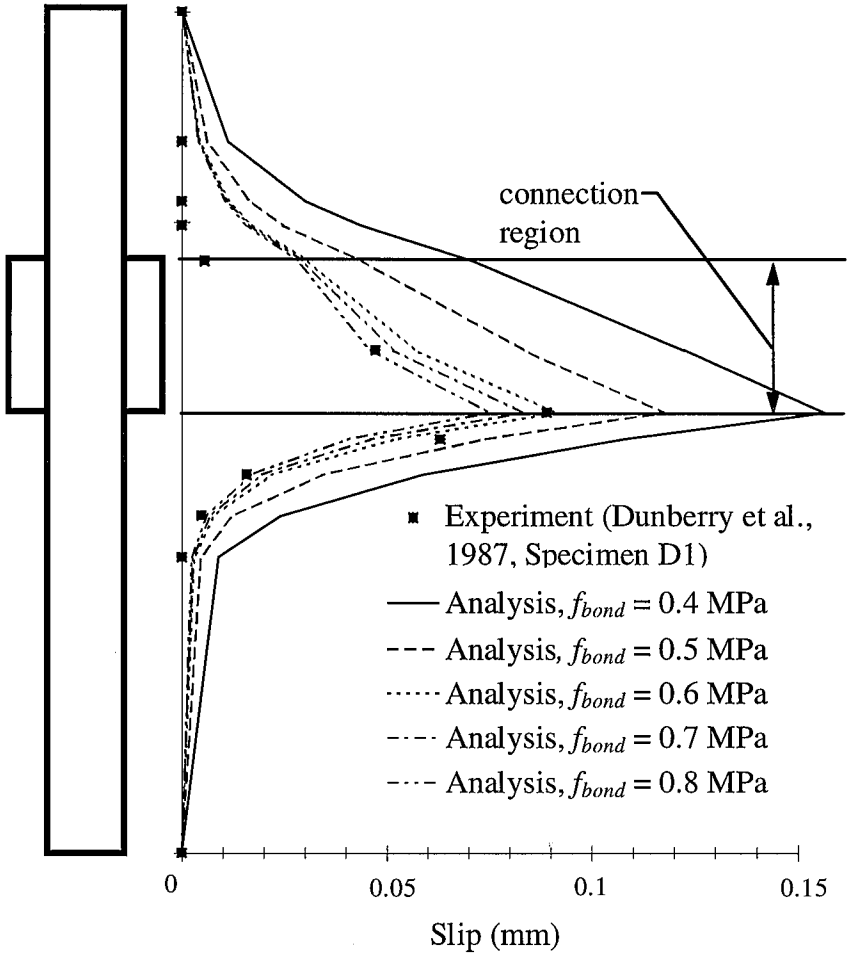

Figure 3.16: Measured Verses Computed Slip (Dunberry et al., 1987, Specimen D1)

Table 3.5: Comparison of Experimental and Computational Results for (Dunberry et al., 1987, Specimen D1)

f_{bond}	0.4 MPa	0.5 MPa	0.6 MPa	0.8 MPa	1.0 MPa
average % error	-362	-183	-93.9	-79.7	-65.3
std. dev.	388	235	164	160	156
max slip (mm)	0.157	0.118	0.0914	0.0834	0.0750
%error max slip	-75.6	-31.9	-2.50	6.55	15.9

The loading scheme used in the computational formulation also affects the accuracy of the results. For example, Fig. 3.17 shows the computed verses measured slip which results when a loading scheme of 25-50-25% is used in the connection region.

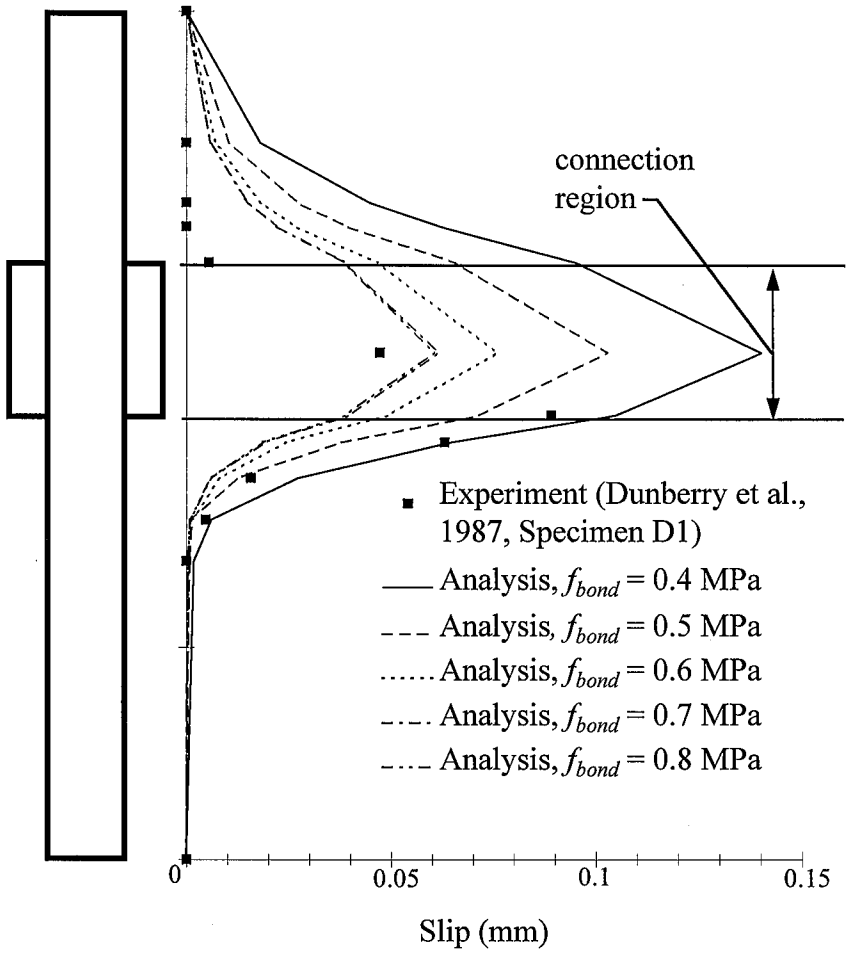

Figure 3.17: Measured Verses Computed Slip for Alternate Computational Loading (Dunberry et al., 1987, Specimen D1)

The magnitude of the analysis results along the length of the member become less accurate than the scheme used in the previous example, although the shapes of the analysis graphs show good correlation with the experiments.

The distribution of load between the steel and concrete portions of specimen D1 along the length of the column is presented by Dunberry et al. (1987) for a load level

slightly below the ultimate load of the column. The total load in the specimen, and the proportion applied at the connection, can be calculated by adding the steel and concrete loads at various points along the length. The published experimental graph indicates that the total applied loads are 680 kN at the top of the specimen and 880 kN at the connection. This data contradicts the tabulated values of Dunberry et al. (1987), which state that 50% of the total load is applied at the connection, and that the total load graphed is 1622 kN. In order to compare to the published results, however, the loads are assumed to be those which are computed by summing the steel and concrete loads in the published experimental graph.

Figure 3.18 shows the comparison between the published results and the prediction of the computational model for various values of bond strength. Table 3.6 gives an analysis of the results. A bond strength of 1.0 MPa produces the best results when compared to the experimental data. However, the other values presented show similar percent error. A bond strength of 0.6 MPa gives acceptable results and matches the maximum slip much better than the value of 1.0 MPa. Both of the higher values of bond strength in the computational model match the overall shape of the load diagram more accurately than the lowest value. This trend is especially apparent in the concrete load in the region around the connection. The experimental data points suggest that all the load transfer from the steel to the concrete occurs in the region indicated on the graph. Only the highest values of bond strength result in a load transfer within this region, with the lowest bond strength value showing transfer over a much larger region.

Based on the examples provided in this section, a bond strength of 0.6 MPa provides the best correlation between experimental and computational results. This value provides the best prediction of total slip, loss of bond around the connection region, and transfer of load from the steel tube to the concrete core after loss of bond occurs. The calibration has also shown that the computational model is more accurate for the region at the compression end of a connection than the tension end because of localized behavior in the experiments caused by connection rotation.

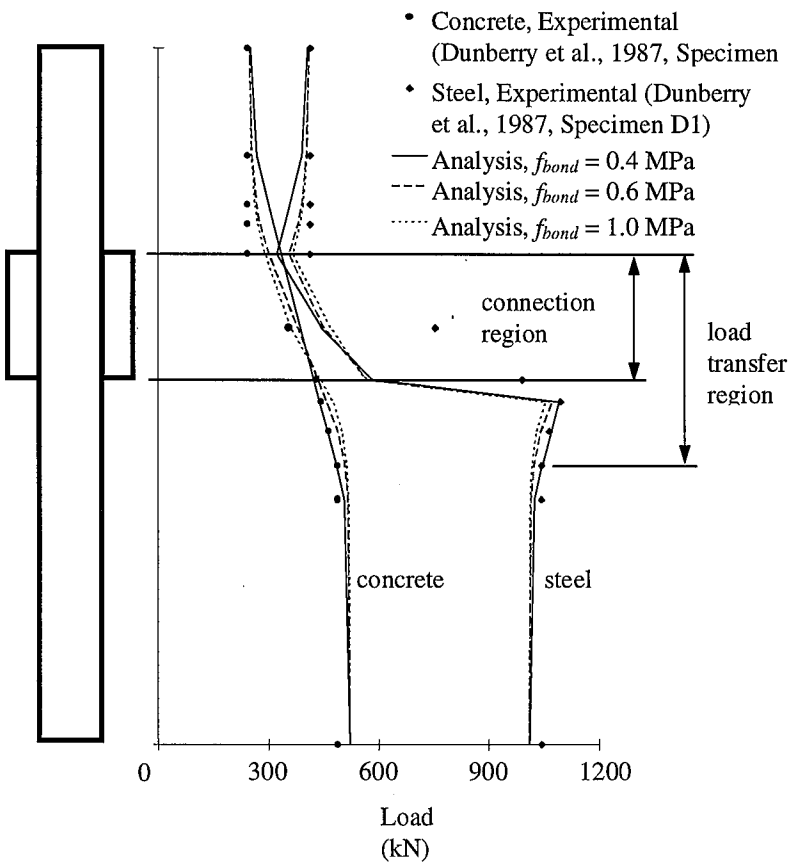

Figure 3.18: Measured Verses Computed Load in the Steel and Concrete Portions of the Column (Dunberry et al., 1987, Specimen D1)

Table 3.6: Comparison of Experimental and Computational Results for (Dunberry et al., 1987, Specimen D1)

f_{bond}	0.4 MPa	0.6 MPa	1.0 MPa
	concrete load results		
average % error	-9.85	-7.29	-6.86
std. dev.	12.4	5.98	4.67
	steel load results		
average % error	12.2	10.5	10.2
std. dev.	14.7	14.2	13.7

3.5 Verification Examples for Slip in Concrete-Filled Steel Tubes

The parameters of the computational slip model were calibrated in the previous section. The values which provide the most accurate comparison to published experimental test results are:

$$f_{bond} = 0.6 \text{ MPa}$$
$$k_{slip} = 10^4 \text{ MPa}$$

The experimental tests which documented slip most completely have been used in the calibration studies. Several other published test results will be used for verification of the calibrated slip parameters.

The series of tests conducted by Dunberry et al. (1987) included a specimen (C1) which was loaded only at the connections, and had no cap or other means of preventing slip at the top of the specimen. Figure 3.19 gives the experimental parameters for this tests.

A plot of the experimentally observed load in the concrete over the height of the column is presented for a given load of $P = 608$ kN. Figure 3.20 shows the comparison of the computational model using the calibrated parameters to the experimental data points. In this comparison, the concrete elastic modulus is reduced to 0.77 of the value predicted by the empirical equation used by the computational model (as it was for specimen D1) in order to match the experimentally observed load in the concrete. The shape and magnitude of the load distribution is well predicted by the computational model, with the load gradually entering the concrete core above the connection, and in a region below the connection as well. The slight shift in the computational results may be caused by the initial rigidity of the concrete being too stiff.

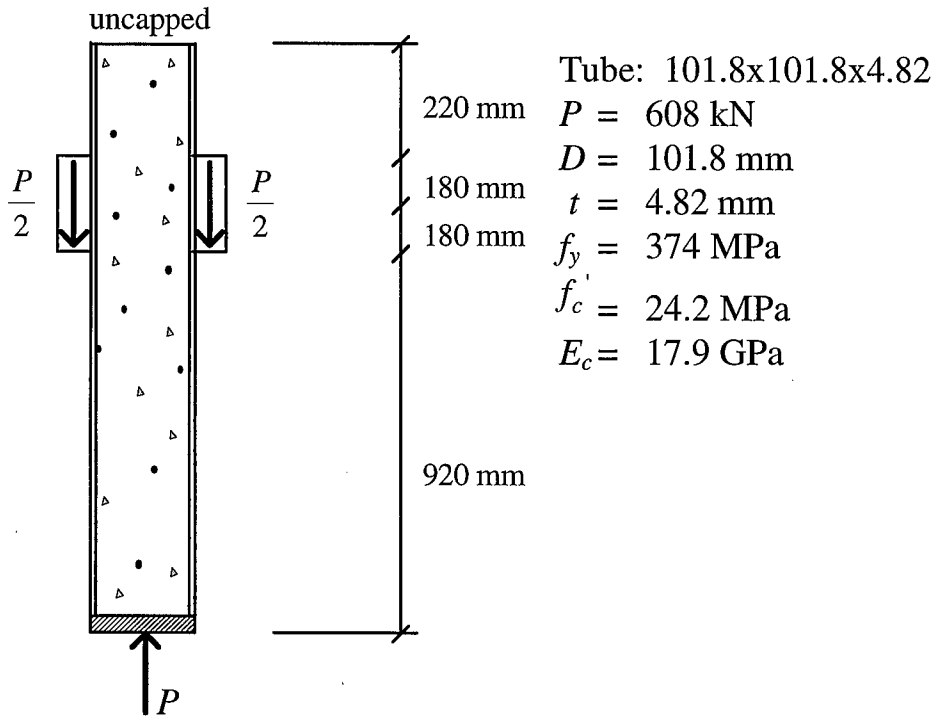

Figure 3.19: Experimental Parameters from (Dunberry et al., 1987, Specimen C1)

A second verification example is provided to demonstrate the capability of the computational formulation to predict the slip due to flexure in CFTs. This behavior is caused by cracking of the concrete in tension which results in an unsymmetric section similar to a composite beam. Lu and Kennedy (1994) present the results of flexural testing of rectangular CFTs which were instrumented to detect slip, through the use of LVDTs at the specimen ends. The experimentally observed slip was reported for specimen CB33. The specimen was rectangular in section and was tested in major axis bending. The beam had no end plates or other means of preventing slip along the specimen. Figure 3.21 shows the experimental setup and gives a number of the material parameters.

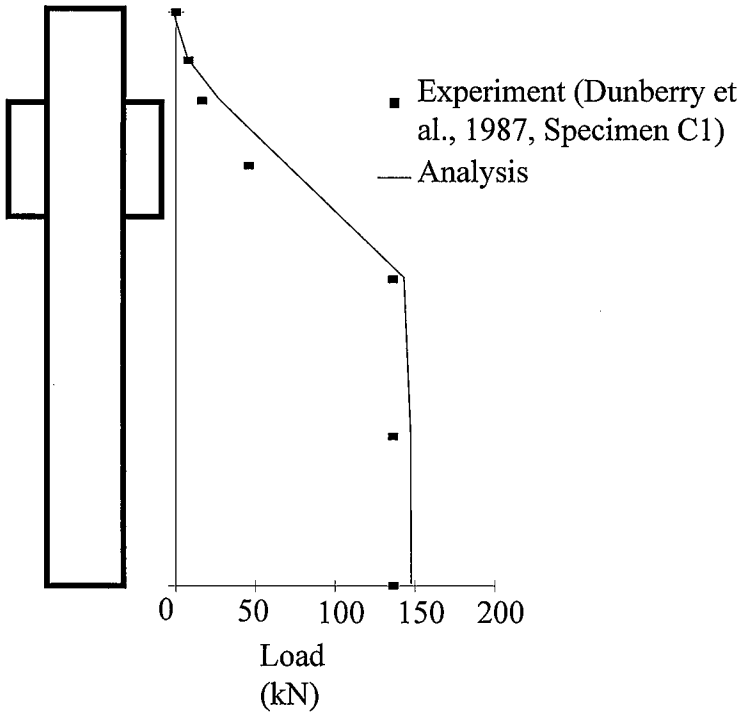

Figure 3.20: Concrete Load in Uncapped Specimen (Dunberry et al., 1987, Specimen C1)

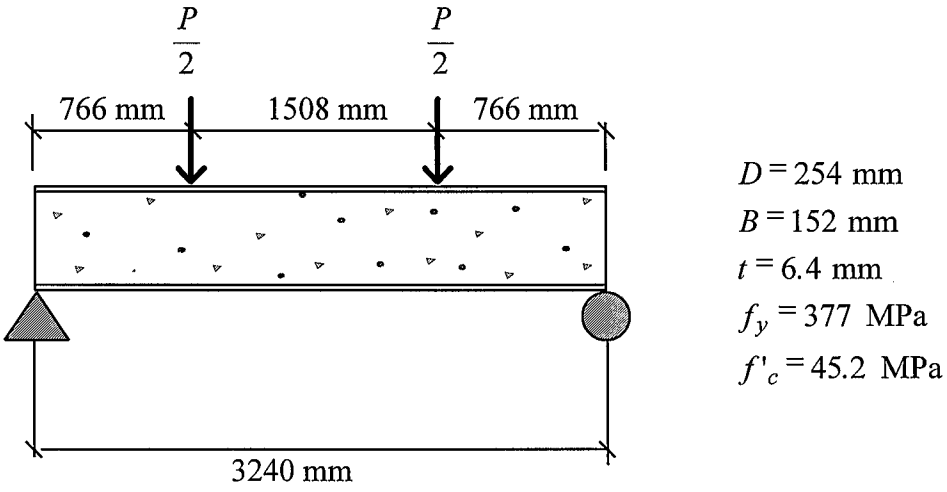

Figure 3.21: Experimental Parameters from (Lu and Kennedy, 1994, Specimen CB33)

Figure 3.22 shows the comparison between the experimentally observed slip and the slip predicted by the computational model using the calibrated parameters. This

graph provides evidence that the calibration based on connection tests is accurate for other types of loading situations as well. The maximum slip as well as the point where loss of bond occurs are predicted well by the computational model.

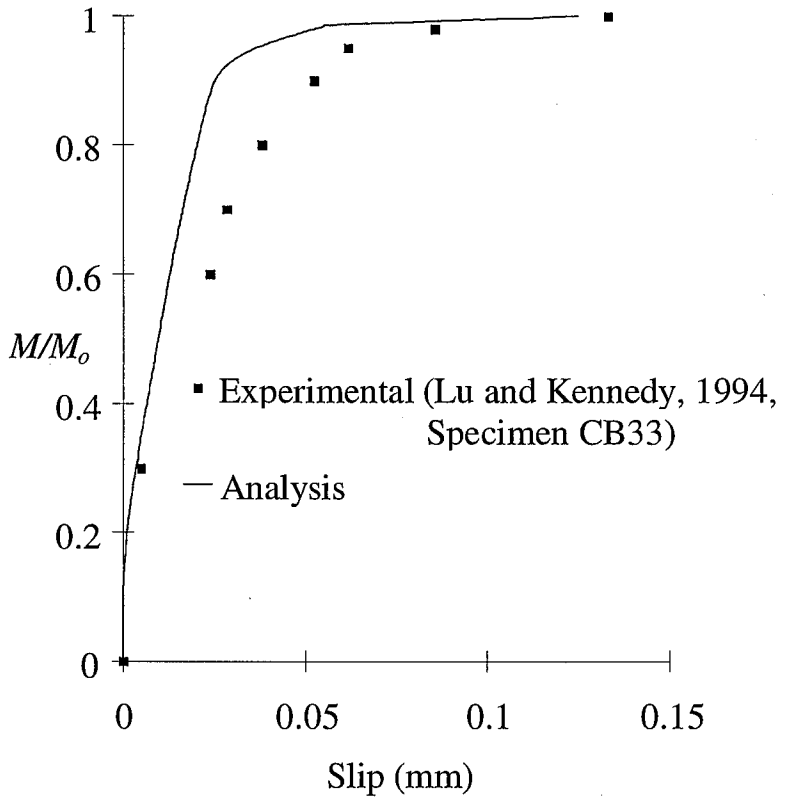

Figure 3.22: Measured Verses Predicted Slip in Flexural Specimen (Lu and Kennedy, 1994, Specimen CB33)

This graph also provides evidence that the experimentally observed slip does not occur purely as the result of local buckling. Rather, the local buckling may be partially the result of loss of bond. This example also demonstrates that loss of bond can occur in flexural specimens which do not have capped ends. This behavior would be mitigated by capping the tube ends, or by using CFTs as flexural members which are continuously connected through positive and negative moment regions. In such a structure, the regions which do not experience loss of bond may prevent slip from occurring in other areas.

Chapter 4

Nonlinear Material Models for Rectangular CFTs

The formulation for material nonlinear analysis using the fiber element approach requires accurate and robust material models for both steel and concrete in order to properly model the material nonlinear behavior of rectangular CFTs. White (1986) states:

> Accuracy of the computed fiber stresses is essential for realistic modeling of local frame behavior and for adequate force recovery in the iterative-incremental solution schemes.... Also, for correct prediction of bifurcation behavior, and for speed of convergence using the iterative-incremental schemes, it is desirable to obtain a realistic estimate of the global tangent stiffness. Thus, the modeled material tangent modulus at cross-section fibers should closely represent that in the actual structure.

The uniaxial constitutive relationships for the steel and concrete components of a rectangular CFT which are required in the fiber element approach are in fact the result of a number of multiaxial effects. These include residual stresses caused by cold-forming and welding (Sully and Hancock, 1994), local buckling of the steel tube walls, shrinkage or expansion of the concrete during curing (Shakir-Khalil, 1993b; Tomii and Sakino, 1979a), and confinement of the concrete core by the steel tube which causes tension in the steel tube walls and compression in the concrete core. Consequently, in this research, multiaxial stress-space plasticity formulations have been implemented to permit future extension of the fiber element to directly account for multiaxial effects. In the current work, only uniaxial stress-strain behavior is tracked, and multiaxial effects are accounted

for implicitly through the calibration of the stress-strain curves. Time-dependent effects such as aging of the steel or shrinkage and creep of the concrete are beyond the scope of the current computational formulation.

This chapter briefly outlines the steel and concrete constitutive models adapted for use with the fiber element formulation. The chapter is organized as follows. Section 4.1 describes the steel constitutive model. Emphasis is placed on describing the key features of the model which most effect CFT behavior. Section 4.2 describes the concrete stress-strain model. Characteristics of the model which are specific to modeling square and rectangular CFTs are discussed, including the modification of the descending compression branch of the stress-strain curve to account implicitly for confined. Section 4.3 outlines the calibration of these models.

4.1 Steel Constitutive Model

The constitutive model used to predict the behavior of the steel tube in the current CFT fiber element formulation dominates the computational results in many cases, since the steel tube is often the major source of flexural, torsional, and axial rigidity and strength in CFTs which are used as beam-columns in frame structures. For this reason, the steel material model should be as comprehensive as possible, within the scope of the current research. The current implementation includes a multi-surface cyclic plasticity formulation developed by (Shen, 1993; Mamaghani et al., 1995; Shen et al., 1995). A brief description of the model is provided here. Details of the modifications made to Shen's model for analysis of rectangular CFTs, and of the calibration to experimental results, can be found in Hajjar et al. (1996e, f) and Molodan and Hajjar (1997) and are not repeated here.

The steel constitutive model utilizes a bounding surface formulation in stress-space. This plasticity formulation uses two nested surfaces, an inner loading surface and an outer bounding surface. The inner loading surface represents the locus of stresses which cause the initiation of yielding at the stress point (i.e., at the fiber). The outer

surface represents the stress state at which a limiting stiffness of the steel fiber is achieved. When the stress point lies within the loading surface, the material undergoes elastic behavior. Once the stress point has contacted the loading surface, the response is governed by a number of hardening rules which determine subsequent inelastic behavior. As the steel fiber is loaded inelastically, both the loading and the bounding surfaces may translate (kinematic hardening), or contract or expand (isotropic hardening), to model key material phenomena. The plastic modulus of the fiber changes nonlinearly from infinity to a limiting bounding value as the stress point moves from initial contact with the loading surface to the bounding surface. The von Mises surface establishes the shape for both the loading and bounding surfaces (Shen et al., 1995). The value of the plastic modulus is a function of the distance between the two surfaces.

This steel model has several key features geared specifically to capturing appropriate stress-strain behavior necessary for obtaining the CFT stress-resultant behavior discussed in the previous section. Coupons taken from cold-formed steel tubes usually do not exhibit a yield plateau, especially for the material in the corners of the tube, due to the cold-working process (Sully and Hancock, 1994). Consequently, no yield plateau is modeled in this work. In addition, the steel formulation unloads elastically until the loading surface is recontacted. This behavior may occur in monotonically loaded members under non-proportionally applied loading. The Bauschinger effect is also captured well in this formulation, predominantly due to kinematic hardening of the loading surface. This steel bounding surface model also achieves a limiting bounding value of the plastic modulus once the stress point contacts the bounding surface, and this value of the plastic modulus is retained until a load reversal occurs.

In addition to the above features, several of which were inherent to the Shen model (Shen et al., 1995), the different stress-strain characteristics in the corners and flanges of the steel tube are accounted for in this research. This modeling also accounts for the residual strains which result from the cold-forming process of the tube. These effects will be described briefly in Section 4.3.

4.2 Concrete Constitutive Model

An accurate nonlinear material constitutive model for the concrete core of a CFT is essential if the overall load-deformation behavior of the member is to be predicted for any type of loading. The stress-strain characteristics of concrete introduce nonlinearity to a CFT member even under loads that are conventionally considered elastic. This behavior is due in part to cracking of the concrete in tension, which may occur at very low strains. Once a crack has formed in concrete, it is no longer able to sustain any tensile loading, resulting in a non-symmetric section when a CFT is subjected to flexural loads that cause cracking. In addition to tensile cracking, the compressive stress-strain relationship of concrete is nonlinear upon loading, and the material softens under continued compressive strain once the peak compressive stress of the material is reached.

In this work, several distinct regions of the stress-strain relationship are isolated so that the appropriate material constitutive model can be applied. These regions include compressive loading, compressive unloading, post-failure, tensile loading, and tensile unloading. These five regions of the concrete stress-strain curve are modeled using two concrete constitutive formulations.

The tensile behavior of the concrete is based on a formulation presented in (ASCE, 1982) and is modeled as being linear elastic (with a stiffness equal to the tangent stiffness at the point at which the stress changes from compressive to tensile) up to the rupture stress. After rupture, the fiber loses all capacity to retain stress in tension, thus modeling the opening of the crack. Upon reversed loading, compressive behavior is reinitiated at the point at which tensile behavior first initiated, thus simulating crack closure (ASCE, 1982).

The concrete model developed by Chen and Buyukozturk (1985) is adapted to this research for modeling the compressive behavior of each fiber in the concrete core. This model is also based on a bounding surface formulation, and it contains several features critical to capturing the complex behavior of concrete in CFT cores subjected to

monotonic loading, including strain reversals. For details of this formulation, see Chen and Buyukozturk (1985), Buyukozturk and Ameur-Moussa (1988), Ameur-Moussa and Buyukozturk (1990), and Pagnoni et al. (1992). A brief description of the model is provided here. Details of the modifications made to Chen's model for analysis of rectangular CFTs, and of the calibration to experimental results, can be found in Hajjar et al. (1996e, f) and Molodan and Hajjar (1997) and are not repeated here.

Since the stress-strain curve of concrete in compression is observed to be nonlinear even at low stress values, the concrete model does not assume the existence of an elastic zone. In the context of a more traditional bounding surface formulation, this model may be thought of as having a point loading surface (Dafalias and Popov, 1977). Consequently, prior to contacting the bounding surface, the plastic modulus varies continuously as a function of the normalized distance between the current stress point and an image point on the bounding surface measured in the deviatoric plane. The size of the bounding surface defines the peak concrete strength that may be achieved prior to initiating softening behavior. Thus, after the stress point at a concrete fiber contacts the bounding surface, the peak concrete strength is achieved (initially equal to $f_c^{'}$ for uniaxial loading), and the concrete softens, asymptotically approaching a zero stress level as it crushes fully in this post-failure region.

In this model, a scalar damage parameter, K, is used to account approximately for the microcrack formation in the concrete at every stage of compressive loading and unloading, including the post-failure region. In the post-failure range, Ameur-Moussa and Buyukozturk (1990) chose to calculate the increment in the damage parameter using an empirical expression for the plastic shear modulus, H^P. In this range, this expression must be independent of the distance between the stress point and the bounding surface, which becomes zero. The equation of the plastic shear modulus in the post-failure region was chosen to provide a fit to the post-failure branch of the uniaxial concrete stress-strain curve. This approach leads to a satisfactory prediction of the material response, provided that the strain range covered is relatively small. The equation is given by (Ameur-Moussa and Buyukozturk, 1990):

$$H^p = -0.15 \cdot \exp\left[-0.025 \cdot \left(K_{max} - 1\right)^2\right] \cdot F_2 \qquad (4.1)$$

where K_{max} is the maximum value of the damage parameter K achieved in the loading history, and F_2 is a multiaxial factor described in the next section. This equation causes the plastic shear modulus to decrease to zero very rapidly with the increase of the maximum damage value. It is this equation which is calibrated in this work to approximate the effects of confinement on the concrete behavior within the context of using only a uniaxial stress-strain behavior of the concrete (see Hajjar et al. (1996e, f) and Molodan and Hajjar (1997) for details of this calibration).

4.3 Calibration of the Steel and Concrete Constitutive Formulations

The calibration of the CFT fiber element involves explicit calibration of both the steel and the concrete constitutive models. For the steel, the uniaxial load-deformation curve obtained from stub column tests of rectangular steel tubes varies depending on the manufacturing process used in forming the tube. The current computational formulation and calibration are intended to be used with ASTM A500 Grade B square and rectangular tubing, which is the most commonly available tube steel in the United States (AISC, 1994). This grade of steel tubing is manufactured by cold-forming ASTM-A36 steel plate and welding a seam along the longitudinal axis of the member (AISC, 1994). This manufacturing process produces a number of residual effects which have been observed experimentally. First, the cold-forming procedure produces residual stresses in the hoop direction of the tube. These stresses are highest near the corners, and drop to near zero at the middle of the flat sidewalls. Second, the welding process produces residual stresses near the weld seam; these localized residual stresses due to welding are neglected in the current work. The general effect of the cold-forming process is that the uniaxial stress-

strain curve of a steel coupon extracted either from the flanges or corners of a steel tube is distinctly rounded, showing no yield plateau, and having a proportional limit substantially below the 0.2% offset yield stress of the material (Lu and Kennedy, 1994; Sully and Hancock, 1994).

Shen et al. (1995) calibrated their steel model to tests of structural steel box columns. This steel showed a definitive yield plateau when stressing a virgin specimen. Thus, it was necessary to accommodate the lower proportional limit and the rounded stress-strain curve exhibited in cold-formed steel tubes. In this research, the loading surface size is a function of the maximum amount of plastic strain that has been accumulated at the steel fiber in the loading history: as the amount of plastic strain increases, the size of the loading surface decreases to model a shrinking size of the elastic zone (see Molodan and Hajjar (1997) for details of this relation). By specifying an initial plastic strain, the initial size of the loading surface is reduced, thus resulting in a proportional limit that is approximately 60% of the 0.2% offset yield stress of the steel tube. This initial plastic strain, $\varepsilon_{p\,initial}$, was calibrated by Molodan and Hajjar (1997) and differs for the fibers in the corners and the flanges of the steel tube. By comparing directly to tensile test results of steel coupons extracted from the flanges and corners of a steel tube by Sully and Hancock (1994), a value of initial strain of 0.0006 was found to provide an accurate calibration for the steel in the corners of the tube, and a value of 0.0004 was found to be accurate for the steel in the flanges of the tube (for the modeling of annealed tubes, these values are taken as zero). The value adopted for the corners is greater to account for the higher degree of cold-working experienced by the corners, relative to the flat portions of the tube. This causes the ratio of the initial elastic zone to the yield stress to be smaller for the corners, producing a more rounded stress-strain curve, which corresponds to the experimental observations (Lu and Kennedy, 1994; Sully and Hancock, 1994). While these initial strains seem small, they substantially affect the size of the elastic zone and the ability to model cold-formed steel accurately (Molodan and Hajjar, 1997).

In addition to the ratio of the proportional limit to the yield stress being different in the corners and flanges, Bridge (1976) and Sully and Hancock (1996) showed that the

initial yield stress of the steel tube material differs in the corners and flanges, with the yield stress in the corners as much as 25% higher. Thus, at the next stage of the calibration process, the average stress-average strain curve was obtained from the results of the stub-column test for which the actual yield stresses of the flange and corner portions of the tube were reported in Sully and Hancock (1996). Using a calibration procedure outlined in Molodan and Hajjar (1997), the yield stress in this model is varied from a minimum value in the flanges (0.96 times the reported nominal yield stress) to a peak in the corners (1.2 times the reported nominal yield stress), with an eighth order polynomial used to vary the yield stress continuously along the depth of each flange of the tube. The eighth order polynomial was chosen to approximate the variation of the yield stresses along the tube side reported by Bridge (1976).

After the steel parameters were calibrated, an analysis of the steel stub column using the measured yield stresses was performed, and the calculated load-deformation curve matched well to the experimental results of Sully and Hancock (1996). Additionally, an axially loaded steel stub-column reported by Lu and Kennedy (1994) was analyzed, and the results also compared well to the experimental data (see (Hajjar et al. 1996e, f; Molodan and Hajjar 1997)).

Once the monotonic steel behavior was calibrated, the monotonic stress-strain curve of the concrete was calibrated to match the results from several CFT flexural experiments conducted by Tomii and Sakino (1979a, b) which yielded moment-curvature-thrust data. In particular, the post-failure plastic modulus of the uniaxial concrete stress-strain response was increased substantially from the modulus established for unconfined concrete by Ameur-Moussa and Buyukozturk (1990) in their original calibration (i.e., Eq. 4.1). This more gradual loss of strength represents the added ductility commonly exhibited in square and rectangular CFTs as a result of the moderate confinement exhibited in these members.

In Eq. 4.1, F_2 is a factor which accounts for the multiaxial stress state of the concrete. In the implementation of Buyukozturk and Ameur-Moussa (1988), the value of F_2 varies between 1.0 for unconfined concrete and 0.025 for highly confined concrete.

The value of the F_2 parameter of Eq. 4.1 was altered in the current research so as to provide a strong correlation with experimental results, and in particular a sufficient level of curvature ductility.

It was determined that the factor which most affected the post-peak ductility of the concrete is the *D/t* ratio of the steel tube (Hajjar and Gourley, 1996). The CFT monotonic moment-curvature-thrust results of Tomii and Sakino (1979a, b) were chosen in order to investigate the effect of the *D/t* ratio on the post-peak behavior of the concrete, and on the curvature ductility of individual CFT members. The experimental results used for this calibration included two groups of CFTs, each loaded first with a constant axial force, and then in flexure with a uniform bending moment. For the first group, *D/t* was equal to 24; for the second group, *D/t* was equal to 44. Each group consisted of five square CFT beam columns, with similar geometric and material properties. The ratio of applied axial force to the axial capacity of the column varied between the tests. The steel tubes where annealed and had yield stresses ranging from 280 to 340 MPa. The concrete strength was approximately 25 MPa (see (Tomii and Sakino, 1979a, b; Molodan and Hajjar, 1997) for details of these experiments).

While it is possible to vary F_2 as a function of D/t, a constant value of 0.05 was found to be sufficient to obtain strong correlation with the experimental results. This value was used in Eq. 4.1 for all subsequent analyses in this work. The verification results of Chapter 5 confirm the accuracy of these calibrations.

Chapter 5

Verification of CFT Plasticity Formulation

This chapter contains verification problems which demonstrate the accuracy of the current computational formulation for analysis of rectangular CFT columns, beams, beam-columns, and composite frames consisting of steel wide-flange beams which frame rigidly into CFT beam-columns. As mentioned previously, a fully nonlinear structural frame analysis program (CFTFiber) was developed to implement this finite element formulation. The computer program is used to conduct the computational analyses in this chapter. The calibrations of the slip model outlined in Chapter 3 and the steel and concrete constitutive models outlined in Chapter 4 are used for all analyses in this chapter. Verification of the steel wide-flange beam finite element is presented in Appendix B. Verification of the 18 DOF CFT geometrically nonlinear finite element formulation is also presented in Appendix B for a variety of materially elastic stability problems. Further details of the computer program, including a sample input file can be found in Appendix C of this thesis.

The chapter is separated into sections, each representing a specific loading condition or structural configuration. An analysis of the error in the computational results when compared to the experiments is presented. The final section presents an example of a 4-story 4-bay planar frame to demonstrate the application of the current formulation.

5.1 Comparison to Experimental CFT Column Test

Many CFT researchers have conducted experimental squash load tests of CFTs to determine the overall load-deformation characteristics of CFT columns subjected to pure axial load. Figure 5.1 below shows the result of one such calibration study for the experimental stub-column test conducted by Lu and Kennedy (1994). The experimental parameters for this test are given in Table 5.1.

Table 5.1: CFT Column Example

Test (Specimen)	Nominal Tube Dimensions (mm)	D/t	f_c (MPa)	f_y (MPa)	Other Information
Lu and Kennedy, 1994 (Section 2)	152.4x152.4x8.95	16	47.0	432	Capped ends

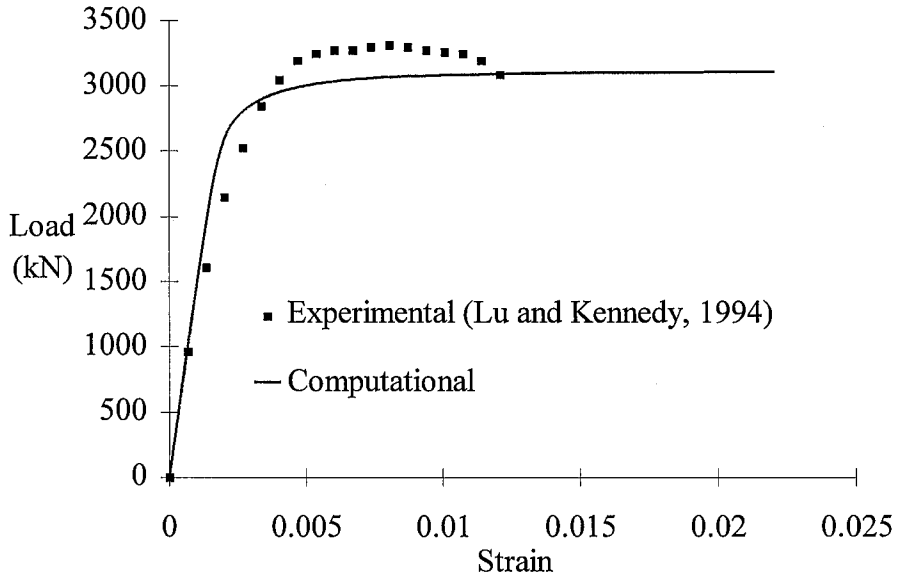

Figure 5.1: Comparison of Computational and Experimental Results for a CFT Column Test (Lu and Kennedy, 1994)

The discrepancy between the computational and experimental results can be attributed mainly to a slight increase in the concrete load carrying capacity due to

confinement by the steel tube. The increase in compressive strength is not modeled in the current formulation. However, the increase in ductility is part of the calibration of Molodan and Hajjar (1996), as discussed in Chapter 4. The load-deformation plot of the experimental specimen becomes considerably nonlinear at approximately one half of the ultimate load. This behavior is due to both the concrete nonlinear stress-strain behavior and the early proportional limit exhibited by cold-formed steel tubing. For this example, the computational model under-predicts the ultimate capacity of the specimen by approximately 7.5% at peak load, as well as under-predicting the roundness of the load-deformation curve.

5.2 Comparison to Experimental CFT Beam Tests

CFT flexural experiments have been conducted by Lu and Kennedy (1994) on rectangular CFTs, and were also included as part of a study of nonproportionally loaded, square CFT beam-columns by Tomii and Sakino (1979a). However, the experimental setups were significantly different for these two research programs. The computational model for each is given schematically in Fig. 5.2. The tests by Lu and Kennedy included measurement of slip in the flexural specimens, and specimen CB33 was used as a verification problem for the slip calibration of Ch. 3. Lu and Kennedy also included minor axis bending of rectangular CFTs and a variety of D/t and L/D ratios. The experimental parameters are given in Table 5.2.

The computational and experimental results are plotted for the verification examples in Figs. 5.3 through 5.10. Note that for all comparisons in this chapter, the mean and standard deviation of the error is presented in Section 5.5. The initial stiffness and the bounding stiffness predicted by the computational model compare well with the experimental data points. The computational model also tends to slightly the ductility of beams subjected to pure flexure for the problems presented in this section. The computational data has been truncated at approximately the same ductility as the

experimental results. In practice, experimental tests are generally truncated by excessive deflections which may reach the limits of the testing apparatus.

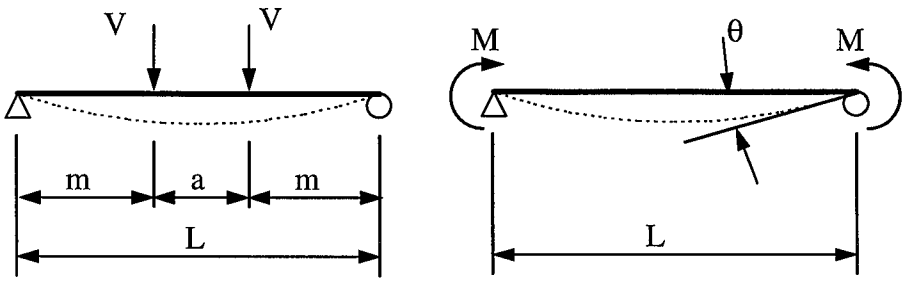

Figure 5.2: Computational Models for Flexural Verification Studies: (a) (Lu and Kennedy, 1994) (b) (Tomii and Sakino, 1979a)

Table 5.2: CFT Beam Verification Tests

Test (Specimen)	Nominal Dimensions (mm)	*D/t* major (minor)	f_c' (MPa)	f_y (MPa)	Other Data
Lu and Kennedy, 1994 (CB12)	152.4x152.4x 4.43	31.7	47.0	389	a = 235 mm m = 1305 mm
Lu and Kennedy, 1994 (CB22)	152.4x152.4x 8.95	16	46.9	432	a = 236 mm m = 1305 mm
Lu and Kennedy, 1994 (CB33)	253.4x152.0x 6.17	39.7 (23.8)	45.2	377	a = 766 mm m = 1508 mm
Lu and Kennedy, 1994 (CB45)	253.0x152.2x 9.04	26.7 (16)	43.8	394	a = 1276 mm m = 1508 mm
Lu and Kennedy, 1994 (CB53)	152.0x253.4x 6.17	39.7 (23.8)	42.1	377	a = 463 mm m = 1305 mm minor axis bending
Tomii and Sakino, 1979a (II-0)	100x100x2.27	44	21.6	305	annealed tube L = 300 mm
Tomii and Sakino, 1979a (III-0)	100x100x2.98	33	20.6	289	annealed tube L = 300 mm
Tomii and Sakino, 1979a (IV-0)	100x100x4.25	24	18.6	284	annealed tube L = 300 mm

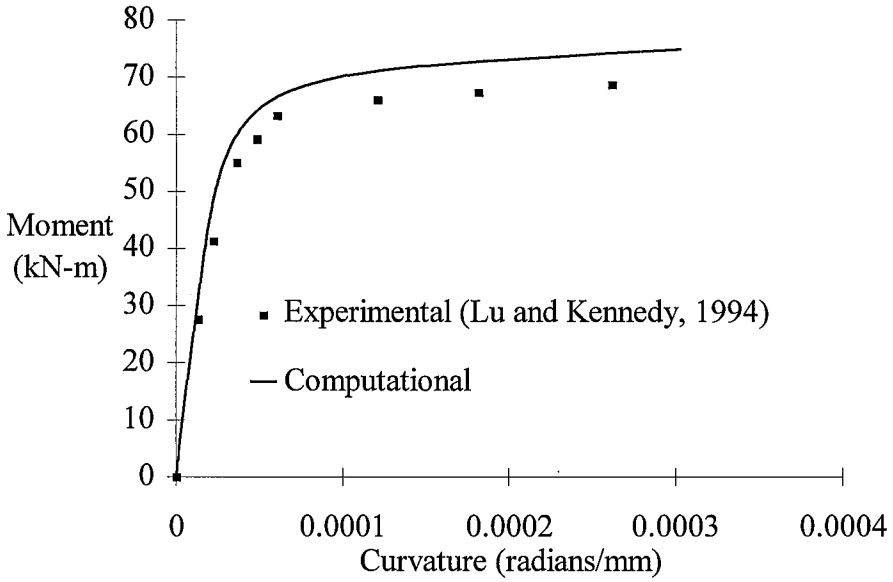

Figure 5.3: Comparison of Computational and Experimental Results for a CFT Flexural Test (Lu and Kennedy, 1994, Specimen CB12)

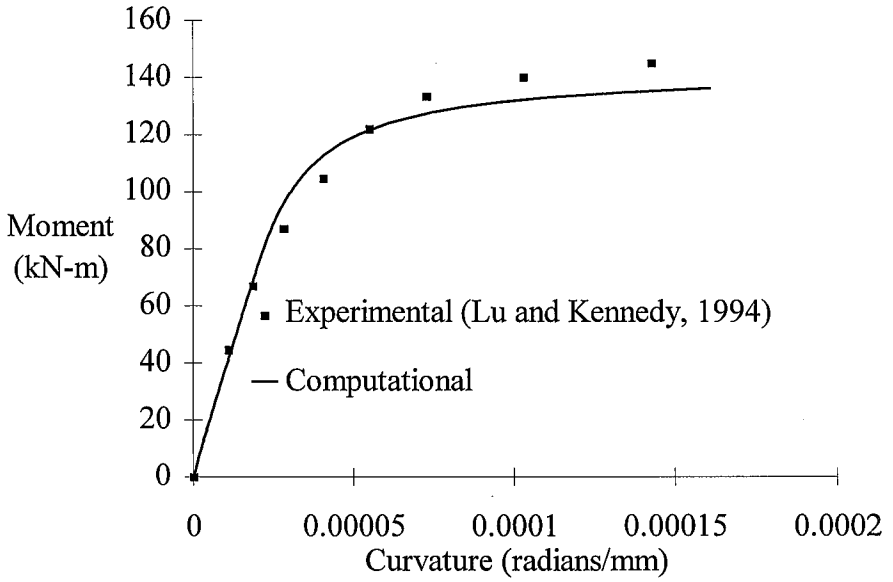

Figure 5.4: Comparison of Computational and Experimental Results for a CFT Flexural Test (Lu and Kennedy, 1994, Specimen CB22)

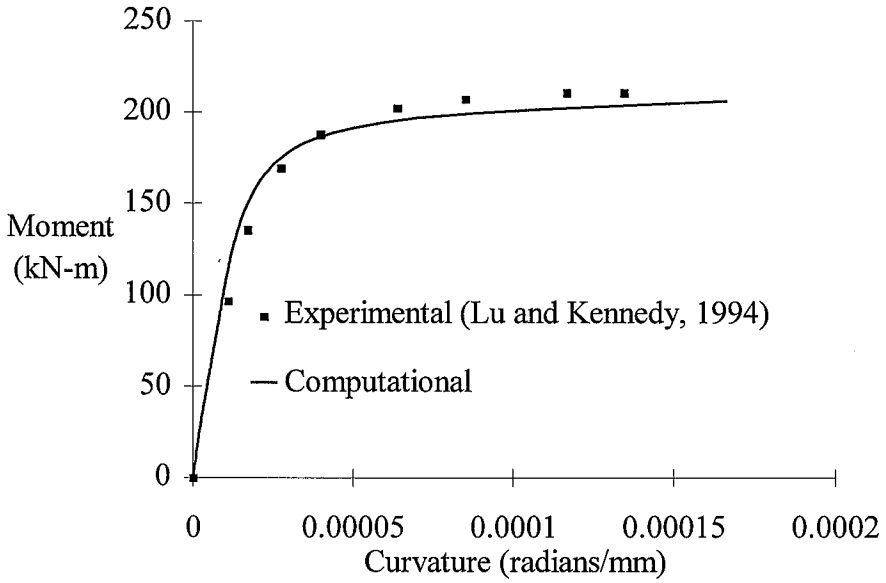

Figure 5.5: Comparison of Computational and Experimental Results for a CFT Flexural Test (Lu and Kennedy, 1994, Specimen CB33)

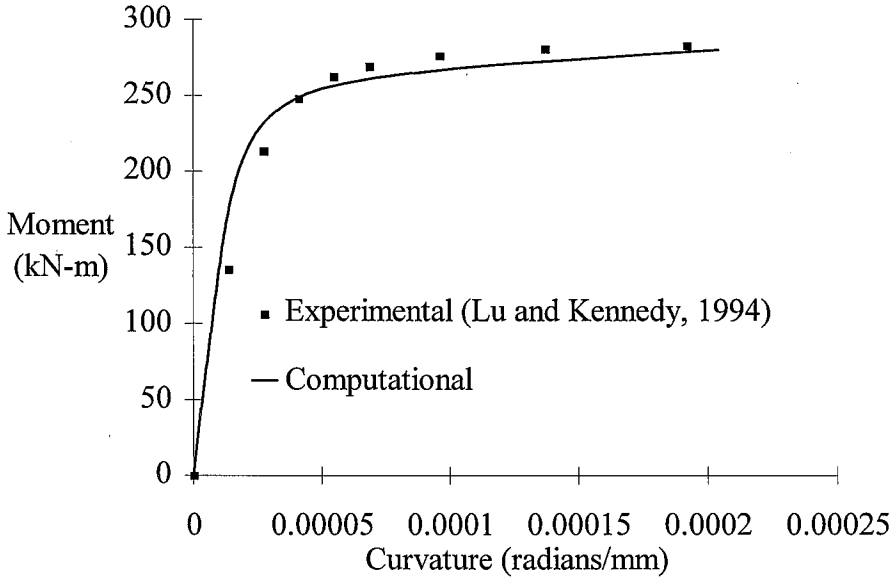

Figure 5.6: Comparison of Computational and Experimental Results for a CFT Flexural Test (Lu and Kennedy, 1994, Specimen CB45)

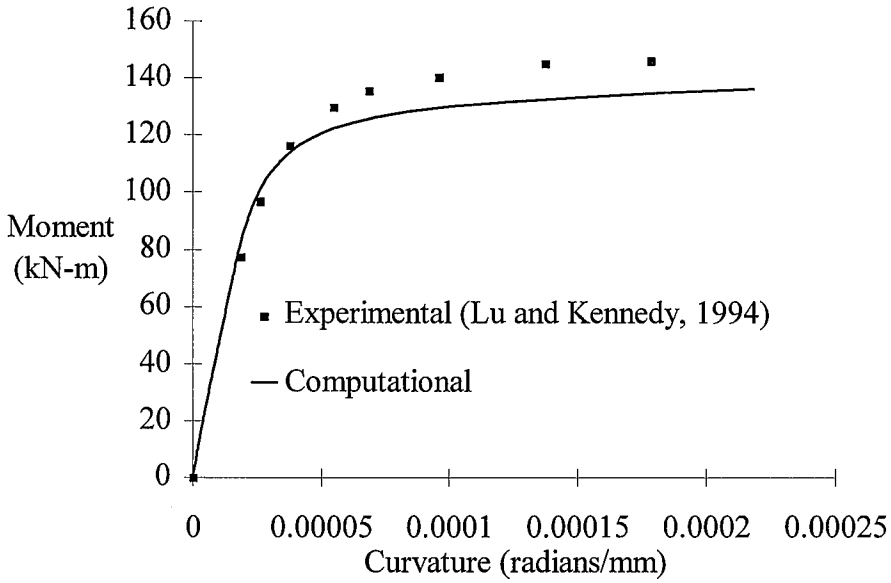

Figure 5.7: Comparison of Computational and Experimental Results for a CFT Flexural Test (Lu and Kennedy, 1994, Specimen CB53)

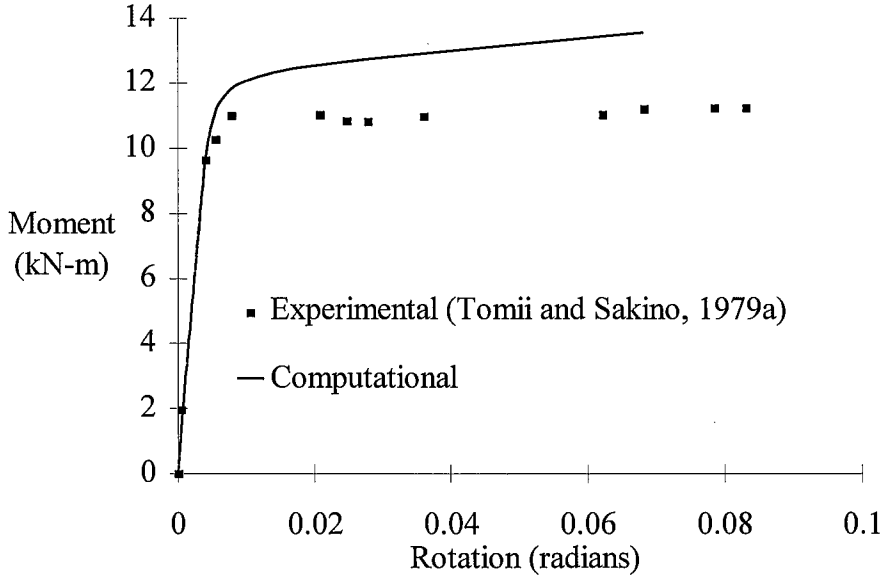

Figure 5.8: Comparison of Computational and Experimental Results for a CFT Flexural Test (Tomii and Sakino, 1979a, Specimen II-0)

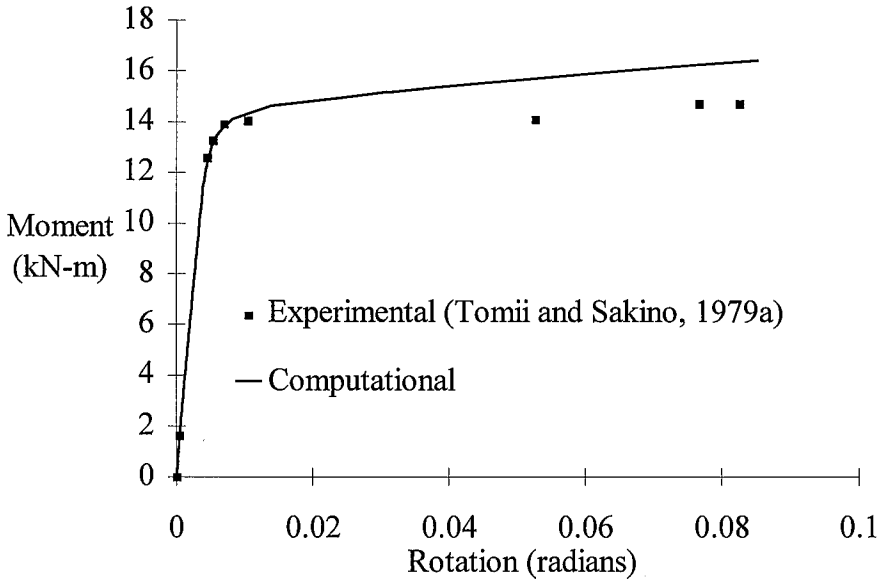

Figure 5.9: Comparison of Computational and Experimental Results for a CFT Flexural Test (Tomii and Sakino, 1979a, Specimen III-0)

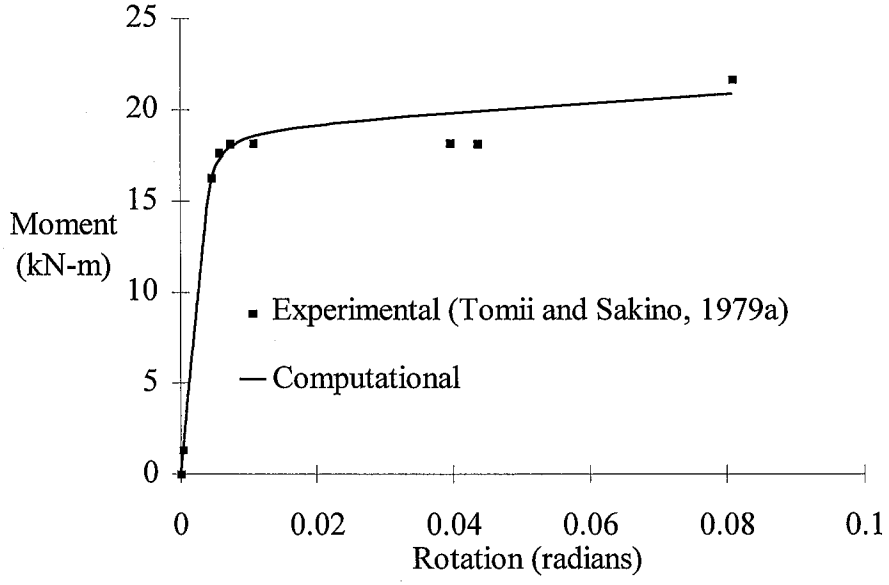

Figure 5.10: Comparison of Computational and Experimental Results for a CFT Flexural Test (Tomii and Sakino, 1979a, Specimen IV-0)

5.3 Comparison to Experimental CFT Beam-Column Tests

Comparison to beam-column experiments serves to verify both the geometrically and materially nonlinear formulation. Both proportionally and nonproportionally loaded beam-columns are verified in the following sections.

5.3.1 Proportionally Loaded CFT Beam-Columns

Several CFT researchers have conducted beam-column tests on rectangular CFTs under proportional, eccentric loading. In this loading scheme, the axial load is applied at a given eccentricity so that the end moment and axial force increase in the same proportion during the test. An example of the corresponding computational model is shown schematically in Fig. 5.11. The experimental tests which are used for verification are shown in Table 5.3.

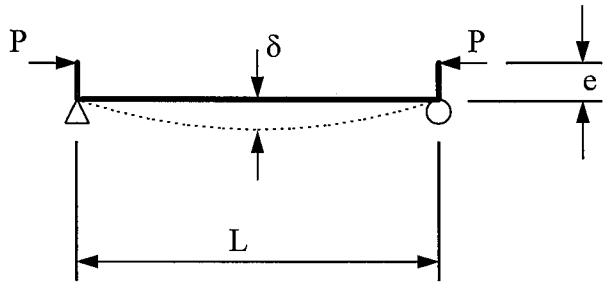

Figure 5.11: Eccentrically Loaded Beam-Column Computational Model

Table 5.3: Proportionally Loaded CFT Beam-Column Verification Tests

Test (Specimen)	Nominal Dimensions (mm)	*L/D* major (minor)	*D/t* major (minor)	f_c (MPa)	f_y (MPa)	Other Data
Bridge (1976) (SHC-1)	203.7x203.9 x9.96	10.5	20	29.9**	291	e = 38 mm
Bridge (1976) (SHC-3)	203.3x202.8 x10.03	10.5	20	37.2**	313	e = 38 mm $\alpha = 30°$
Bridge (1976) (SHC-4)	202.8x203.4 x9.88	10.5	20	39.2**	317	e = 38 mm $\alpha = 45°$
Bridge (1976) (SHC-5)	202.6x203.2 x10.01	15	20	44.3**	319	e = 38 mm $\alpha = 30°$
Bridge (1976) (SHC-6)	203.2x202.1 x9.78	15	20	36.1**	317	e = 64 mm $\alpha = 45°$
Bridge (1976) (SHC-7)	152.5x152.3 x6.48	20	23	31.1**	254	e = 38 mm
Bridge (1976) (SHC-8)	152.5x152.3 x6.48	20	23	31.1**	254	e = 64 mm
Cederwall et al., 1990 (1)	120x120x5	25	24	47	304	e_{major} = 20 mm
Cederwall et al., 1990 (2)	120x120x5	25	24	46	438	e_{major} = 20 mm
Cederwall et al., 1990 (6)	120x120x8	25	15	46	300	e_{major} = 20 mm
Cederwall et al., 1990 (7)	120x120x8	25	15	47	376	e_{major} = 20 mm
Cederwall et al., 1990 (9)	120x120x8	25	15	103	379	e_{major} = 20 mm
Cederwall et al., 1990 (10)	120x120x8	25	15	39	379	e_{major} = 20 mm
Cederwall et al., 1990 (13)	120x120x8	25	15	80	390	e_{major} = 10 mm
Shakir-Khalil and Zeghiche, 1989 (2)	120x80x4.5	23 (34.5)	24 (16)	40*	386.3	e_{major} = 24 mm
Shakir-Khalil and Zeghiche, 1989 (5)	120x80x4.47	23 (34.5)	24 (16)	43*	343.3	e_{minor} = 40 mm
Shakir-Khalil and Zeghiche, 1989 (6)	120x80x4.47	23 (34.5)	24 (16)	45*	343.3	e_{major} = 24 mm e_{minor} = 16 mm

Table 5.3 (cont'd)

Test (Specimen)	Nominal Dimensions (mm)	*L/D* major (minor)	*D/t* major (minor)	f_c' (MPa)	f_y (MPa)	Other Data
Shakir-Khalil and Zeghiche, 1989 (7)	120x80x4.44	23 (34.5)	24 (16)	44*	357.5	e_{major} = 60 mm e_{minor} = 40 mm
Shakir-Khalil, 1991 (4)	150x100x5	25.5 (38.3)	30 (20)	40.3	350.5	e_{major} = 45 mm
Shakir-Khalil, 1991 (9)	150x100x5	31.6 (47.4)	30 (20)	38.2	350.5	e_{major} = 75 mm
Shakir-Khalil, 1991 (10)	150x100x5	26.7 (40.0)	30 (20)	40.6	368	e_{minor} = 30 mm

* compressive strength reported from cube tests rather than cylinder tests

** concrete strength at age of testing

Figures 5.12 through 5.32 show the graphs of load verses midpoint deflection for both the experimental and computational results for these tests. The computational model provides an excellent prediction of the initial stiffness, gradual softening, and ultimate capacity of the members. The model is able to predict the behavior of the 6 biaxially loaded beam-columns as well (Bridge (1976) Specimens BR3-BR6 and Shakir-Khalil and Zeghiche (1989) specimens 6 and 7), with only slightly less accuracy than uniaxially loaded specimens. The ultimate strength of the CFT members containing high-strength concrete (f_c' greater than 70 MPa) are not predicted as well by the computational model, although the initial stiffness and roundness of the curve match the experimental results. As the concrete constitutive model of Molodan and Hajjar (1997) was not calibrated to high strength concrete, these results are not surprising. Nevertheless, the current formulation provides a reasonable approximation to beam-column behavior even with high strength concrete. Again, the mean and standard deviation of the error in these results are summarized in Section 5.5.

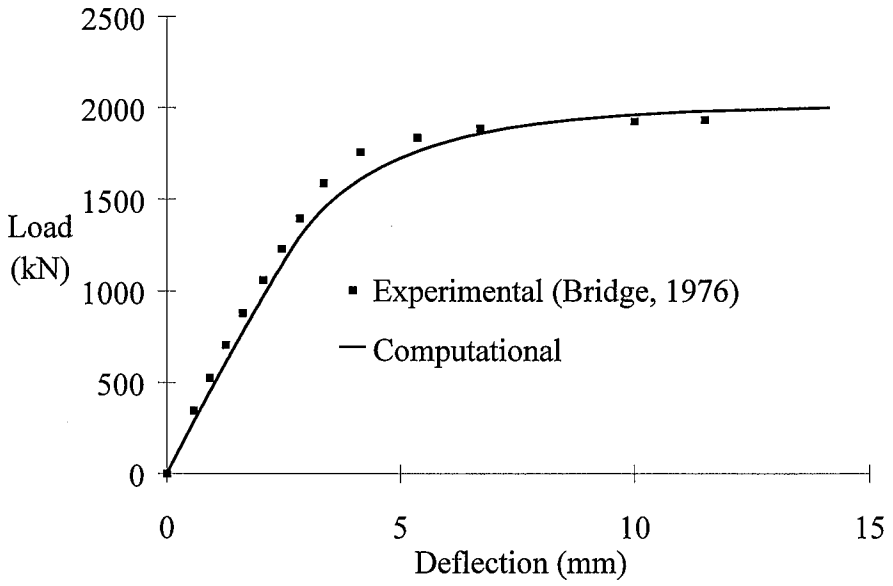

Figure 5.12: Comparison of Computational and Experimental Results for an Eccentrically Loaded CFT Beam-Column (Bridge, 1976, Specimen 1)

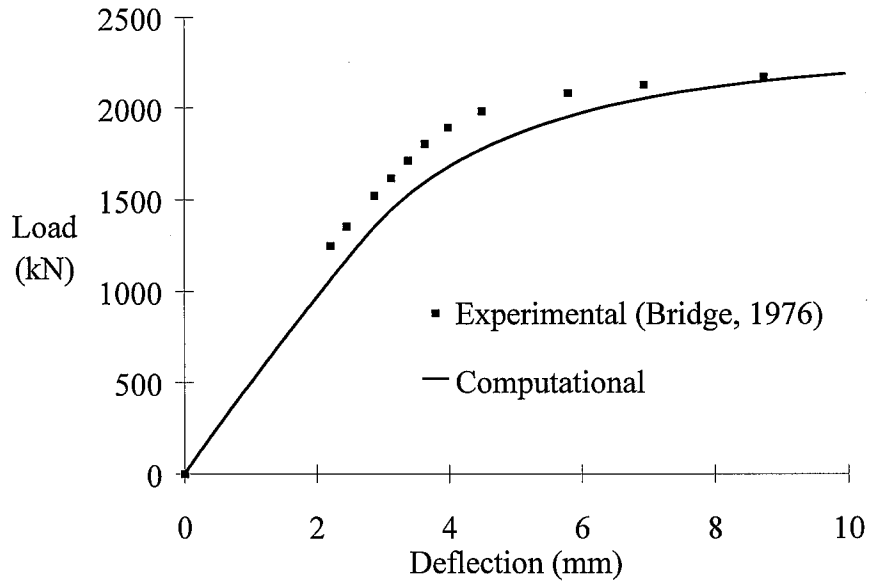

Figure 5.13: Comparison of Computational and Experimental Results for an Eccentrically Loaded CFT Beam-Column (Bridge, 1976, Specimen 3)

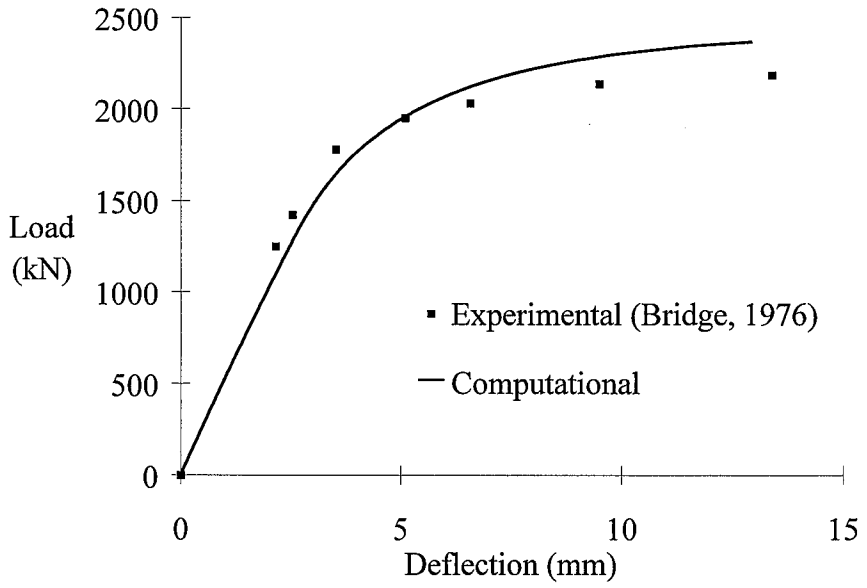

Figure 5.14: Comparison of Computational and Experimental Results for an Eccentrically Loaded CFT Beam-Column (Bridge, 1976, Specimen 4)

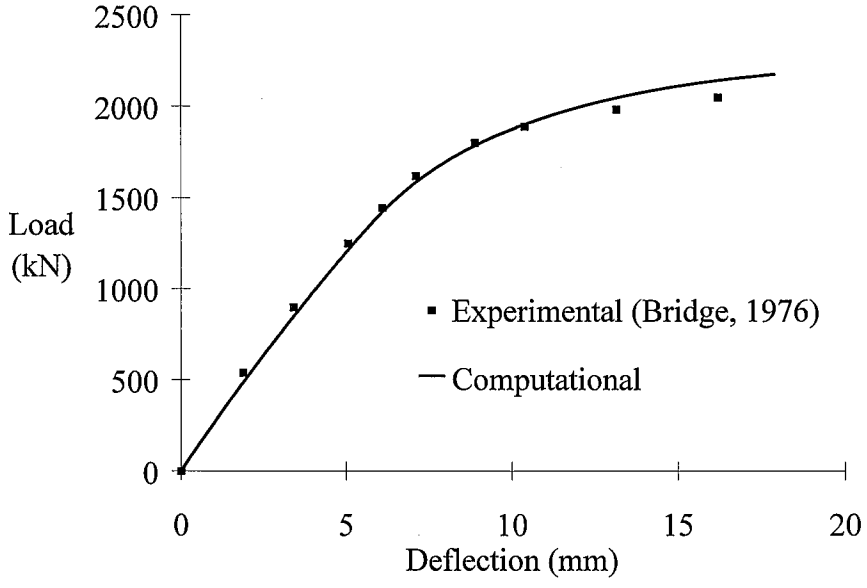

Figure 5.15: Comparison of Computational and Experimental Results for an Eccentrically Loaded CFT Beam-Column (Bridge, 1976, Specimen 5)

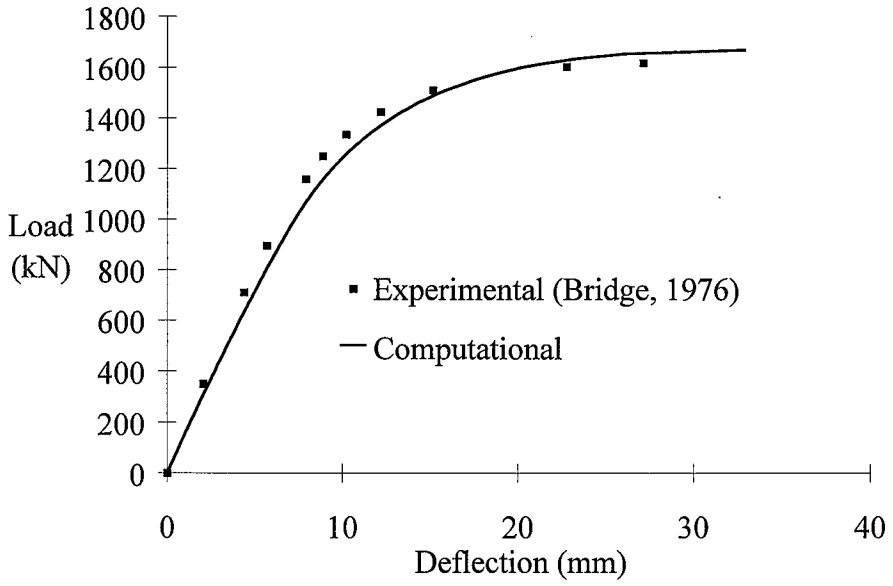

Figure 5.16: Comparison of Computational and Experimental Results for an Eccentrically Loaded CFT Beam-Column (Bridge, 1976, Specimen 6)

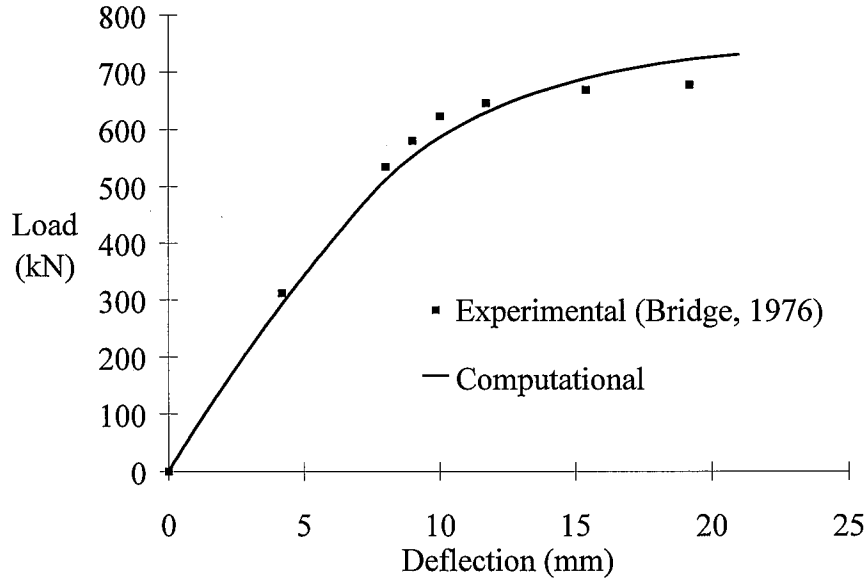

Figure 5.17: Comparison of Computational and Experimental Results for an Eccentrically Loaded CFT Beam-Column (Bridge, 1976, Specimen 7)

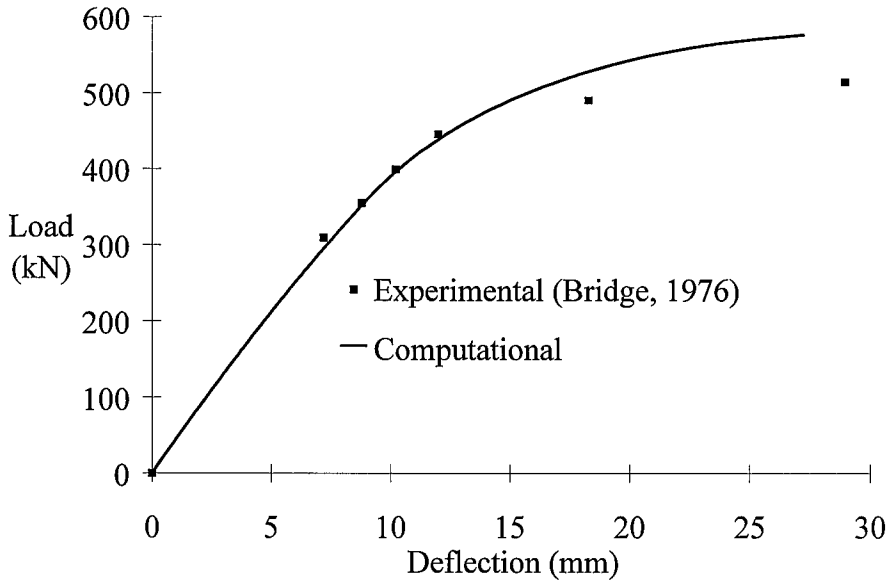

Figure 5.18: Comparison of Computational and Experimental Results for an Eccentrically Loaded CFT Beam-Column (Bridge, 1976, Specimen 8)

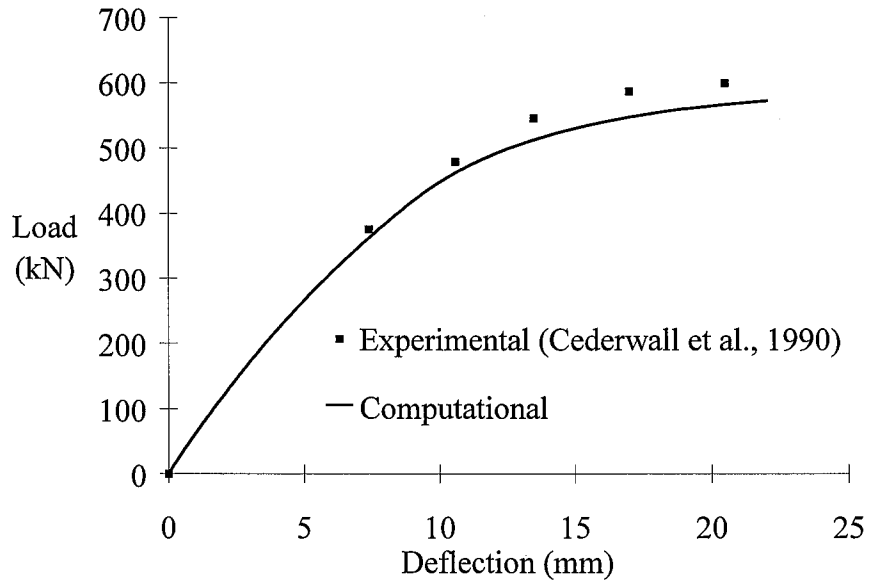

Figure 5.19: Comparison of Computational and Experimental Results for an Eccentrically Loaded CFT Beam-Column (Cederwall et al., 1990, Specimen 1)

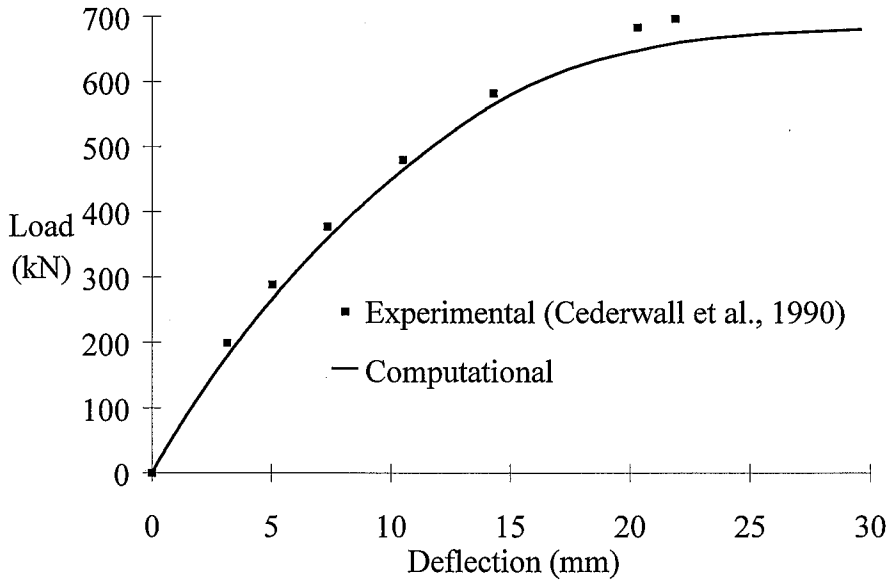

Figure 5.20: Comparison of Computational and Experimental Results for an Eccentrically Loaded CFT Beam-Column (Cederwall et al., 1990, Specimen 2)

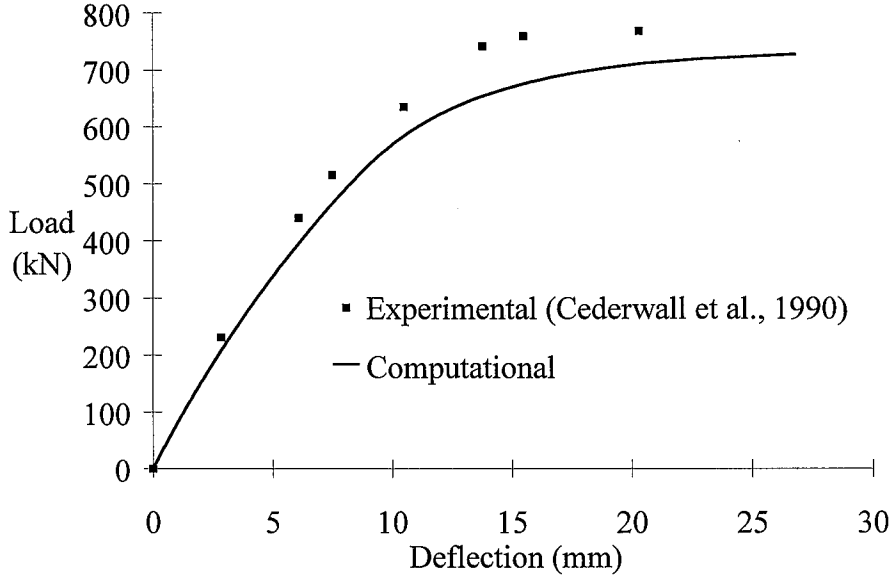

Figure 5.21: Comparison of Computational and Experimental Results for an Eccentrically Loaded CFT Beam-Column (Cederwall et al., 1990, Specimen 6)

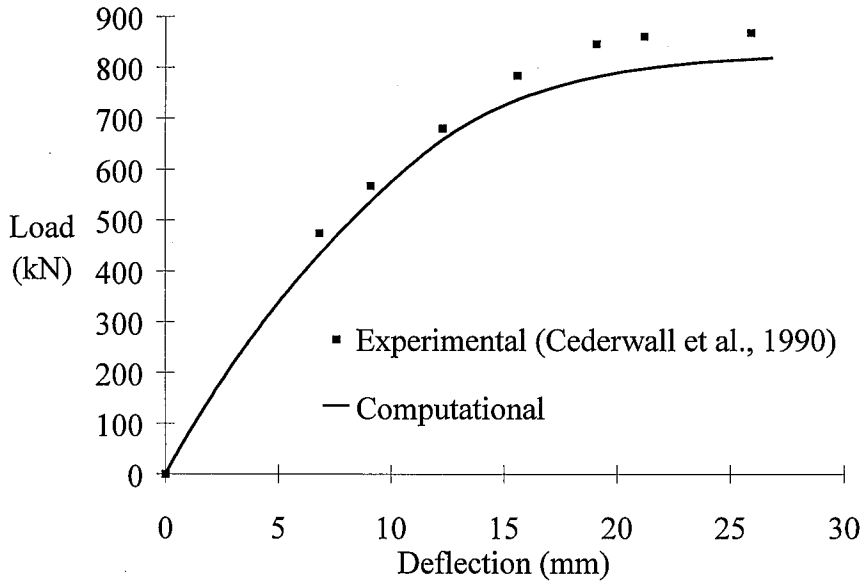

Figure 5.22: Comparison of Computational and Experimental Results for an Eccentrically Loaded CFT Beam-Column (Cederwall et al., 1990, Specimen 7)

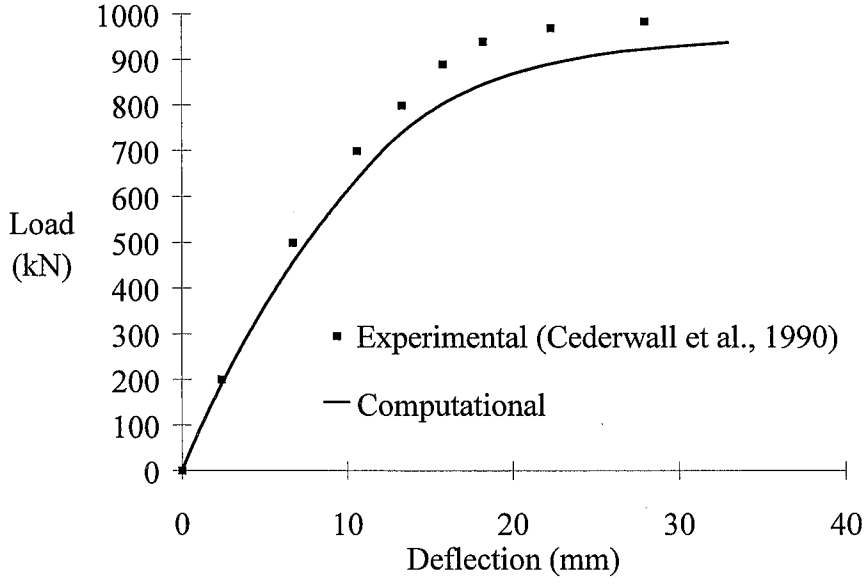

Figure 5.23: Comparison of Computational and Experimental Results for an Eccentrically Loaded CFT Beam-Column (Cederwall et al., 1990, Specimen 9)

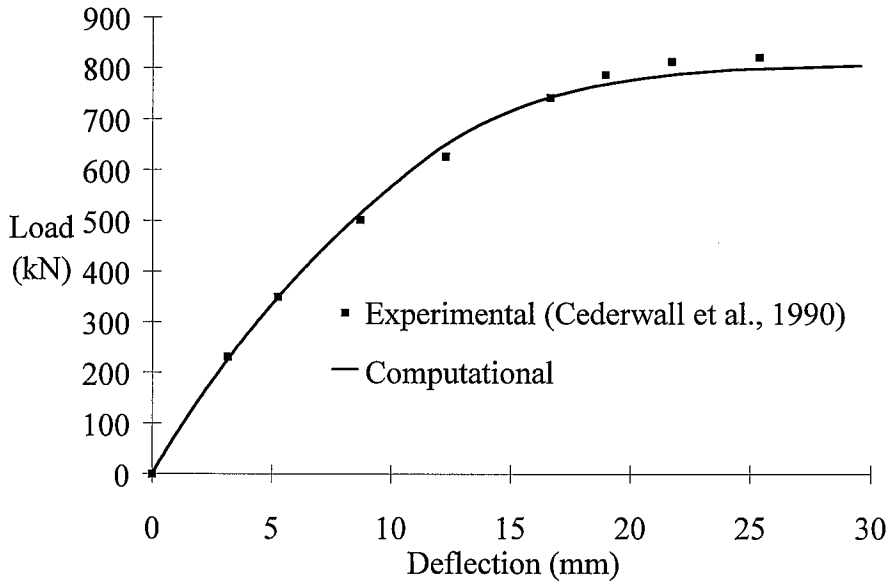

Figure 5.24: Comparison of Computational and Experimental Results for an Eccentrically Loaded CFT Beam-Column (Cederwall et al., 1990, Specimen 10)

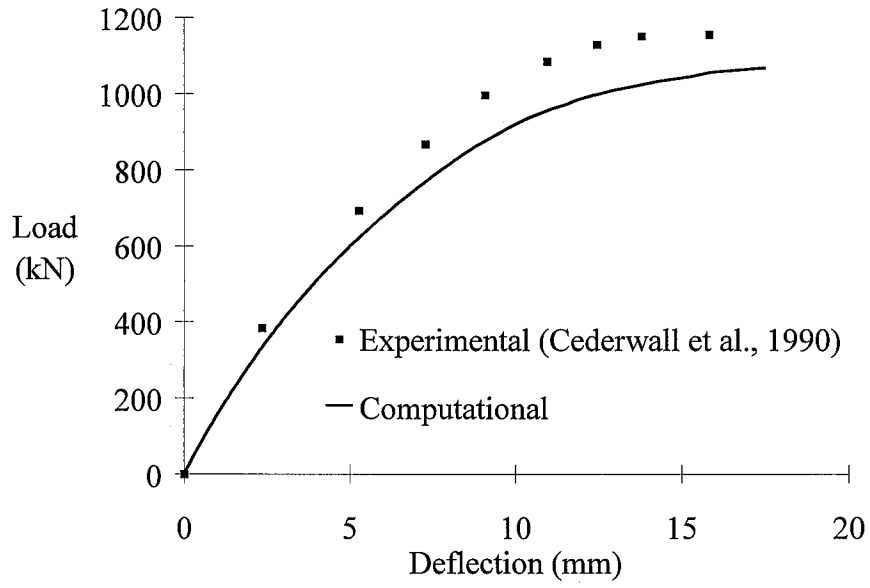

Figure 5.25: Comparison of Computational and Experimental Results for an Eccentrically Loaded CFT Beam-Column (Cederwall et al., 1990, Specimen 13)

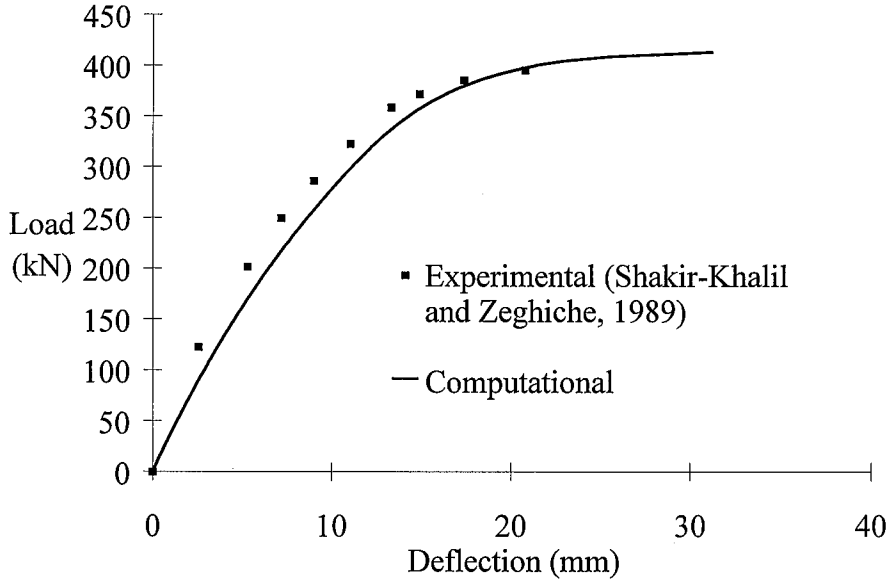

Figure 5.26: Comparison of Computational and Experimental Results for an Eccentrically Loaded CFT Beam-Column (Shakir-Khalil and Zeghiche, 1989, Specimen 2)

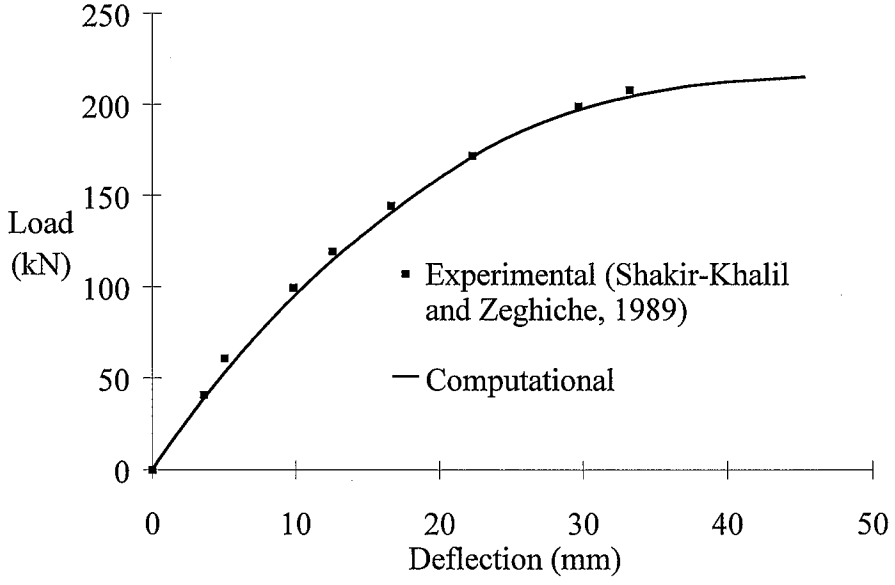

Figure 5.27: Comparison of Computational and Experimental Results for an Eccentrically Loaded CFT Beam-Column (Shakir-Khalil and Zeghiche, 1989, Specimen 5)

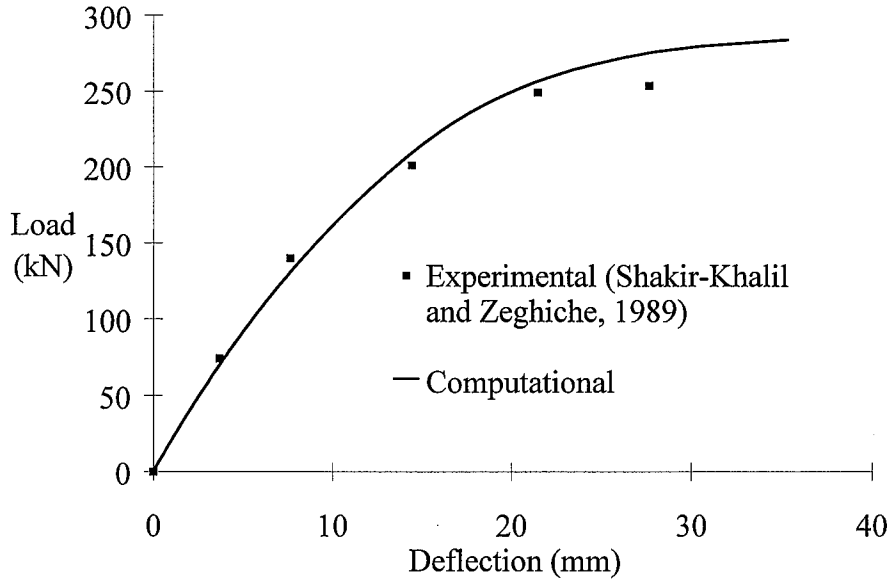

Figure 5.28: Comparison of Computational and Experimental Results for an Eccentrically Loaded CFT Beam-Column (Shakir-Khalil and Zeghiche, 1989, Specimen 6)

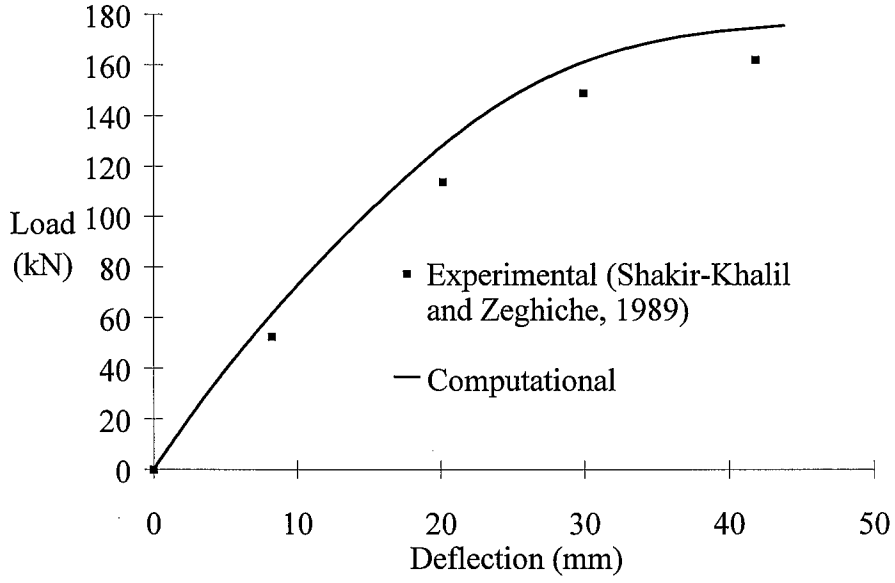

Figure 5.29: Comparison of Computational and Experimental Results for an Eccentrically Loaded CFT Beam-Column (Shakir-Khalil and Zeghiche, 1989, Specimen 7)

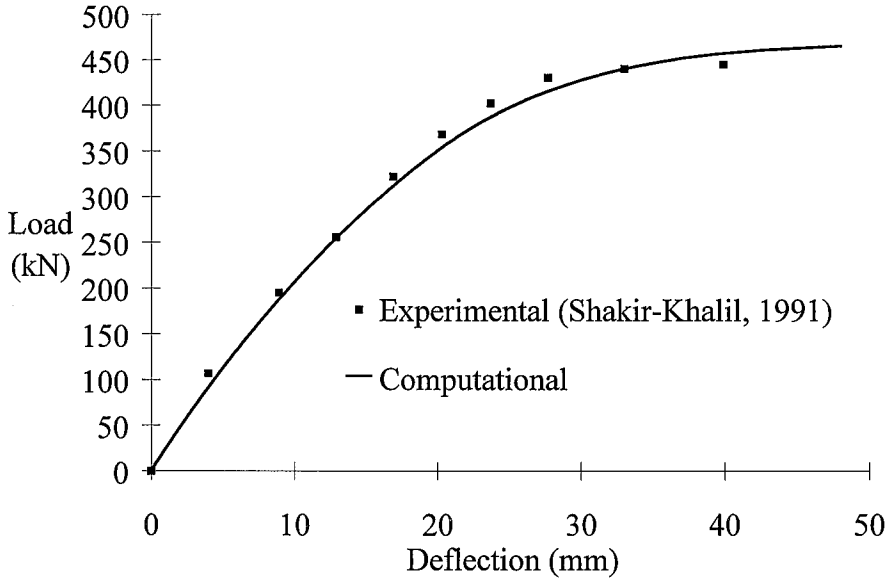

Figure 5.30: Comparison of Computational and Experimental Results for an Eccentrically Loaded CFT Beam-Column
(Shakir-Khalil, 1991, Specimen 4)

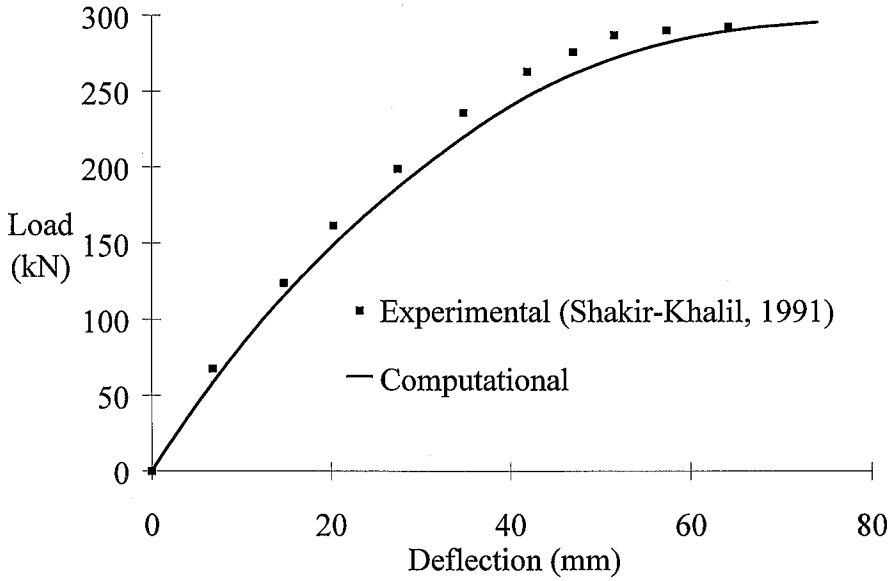

Figure 5.31: Comparison of Computational and Experimental Results for an Eccentrically Loaded CFT Beam-Column
(Shakir-Khalil, 1991, Specimen 9)

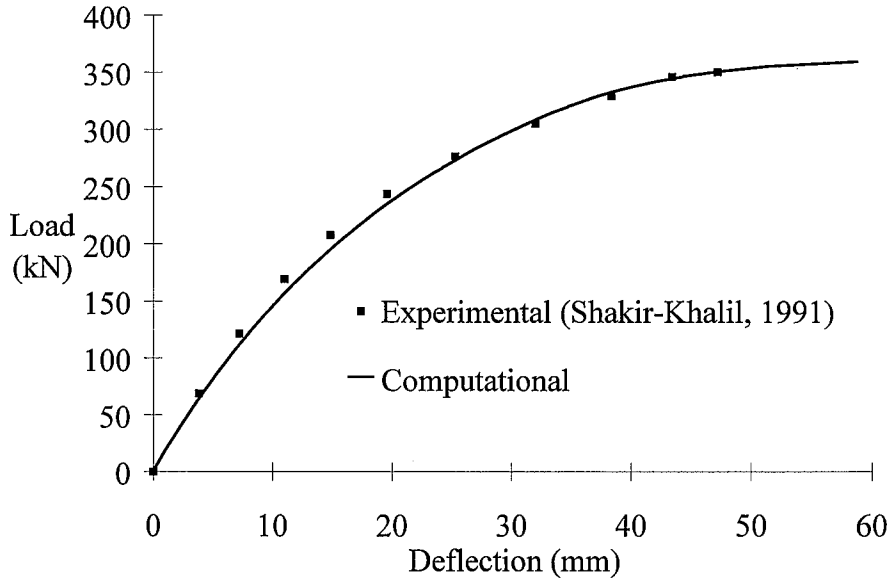

Figure 5.32: Comparison of Computational and Experimental Results for an Eccentrically Loaded CFT Beam-Column
(Shakir-Khalil, 1991, Specimen 10)

5.3.2 Nonproportionally Loaded CFT Beam-Columns

Nonproportionally loaded beam-columns are members which are loaded with both axial force and flexure, but the loads are increased in different proportions. These tests are generally thought to be more difficult to predict with computational models, because of the path-dependency of the materials. In nonproportional loading, the materials may to undergo strain reversals. The current computational formulation accounts for the path-dependency of the materials as well as strain reversals.

The most thorough experimental program on rectangular CFTs under nonproportional monotonic loading was conducted by Tomii and Sakino (1979a, b). The experimental research program included several important parameters, including the D/t ratio of the steel tubes and the magnitude of the applied axial load. In these experiments, the axial load is applied in its entirety before any flexural loading is applied.

It is important to note that Tomii and Sakino conducted their studies on annealed steel tubes. For this reason, the initial plastic strain for the steel computational model is

assumed to be zero, producing a nearly bilinear stress-strain curve. In addition, expansive mortar was used in the concrete mix to reduce the possibility for slip between the steel and concrete. This may have had the consequence of adding some initial confinement to the concrete core which is manifest in a higher concrete compressive strength. Tomii and Sakino used a factor of 1.2 for the concrete strength in their computational model for predicting the moment-curvature relationship of the CFT members. A factor of 1.0 is used in the current analysis.

Figure 5.33 shows the nonproportionally loaded beam-column model. Tomii and Sakino measured rotation of the member ends. However, they presented their results in terms of curvature, using the average of the member end rotations divided by the length of the constant moment region to compute the curvature. In order to be consistent with the experimental measuring scheme, the curvature presented for the experiments was converted to rotation for the graphs presented in this section. Table 5.4 gives the experimental parameters for the verification tests.

Figures 5.34 to 5.39 present the moment-rotation relationships for this set of verification examples. Two other series of tests were presented by Tomii and Sakino with *D/t* ratios of 24 and 44. These tests were used to calibrate the concrete constitutive model and are therefore omitted from the verification set. The moment-rotation graphs for the other series of tests show similar accuracy to the verification set (Molodan and Hajjar, 1997).

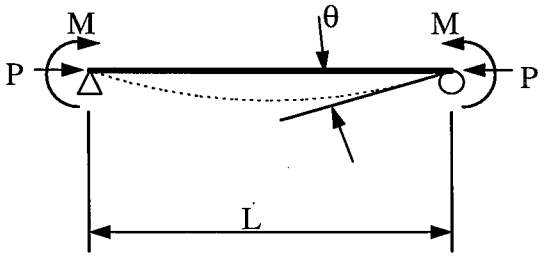

Figure 5.33: Nonproportionally Loaded Beam-Column Computational Model

Table 5.4: Nonproportionally Loaded CFT Beam-Column Verification Tests

Test (Specimen)	Nominal Dimensions (mm)	*L/D* major (minor)	*D/t* major (minor)	f_c' (MPa)	f_y (MPa)	Other Data
Tomii and Sakino, 1979a (III-1)	100x100x 2.98	3	33	20.6	289	$P/P_o = 0.10$
Tomii and Sakino, 1979a (III-2)	100x100x 2.98	3	33	20.6	289	$P/P_o = 0.20$
Tomii and Sakino, 1979a (III-3)	100x100x 2.99	3	33	20.6	289	$P/P_o = 0.30$
Tomii and Sakino, 1979a (III-4)	100x100x 2.99	3	33	20.6	289	$P/P_o = 0.40$
Tomii and Sakino, 1979a (III-5)	100x100x 2.99	3	33	20.6	289	$P/P_o = 0.50$
Tomii and Sakino, 1979a (III-6)	100x100x 2.99	3	33	20.6	289	$P/P_o = 0.60$

where $P_o = A_s f_y + A_c f'_c$

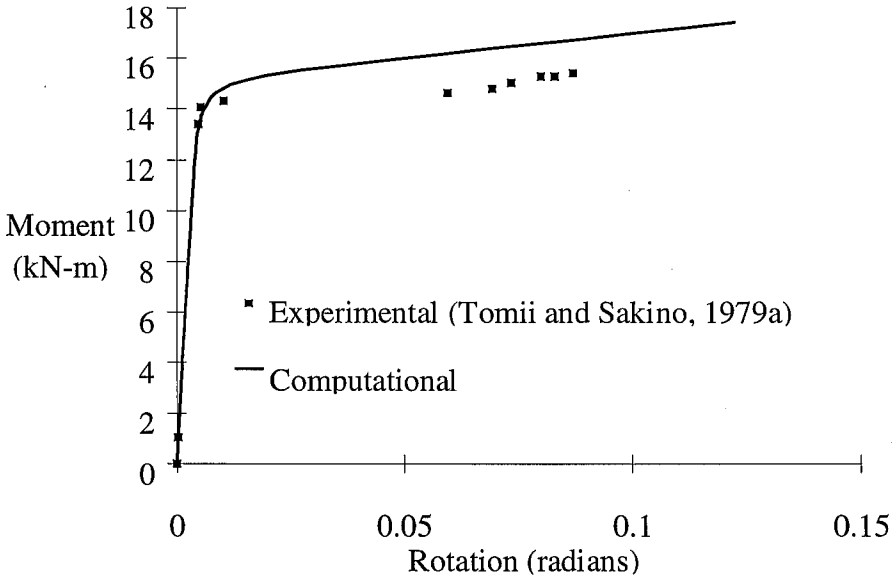

Figure 5.34: Comparison of Computational and Experimental Results for a Nonproportionally Loaded CFT Beam-Column (Tomii and Sakino, 1979a, Specimen III-1)

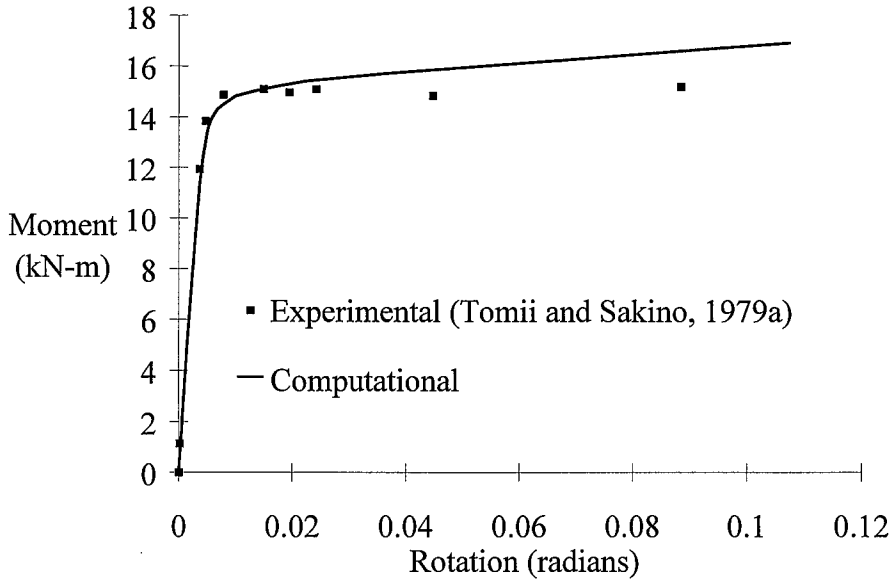

Figure 5.35: Comparison of Computational and Experimental Results for a Nonproportionally Loaded CFT Beam-Column (Tomii and Sakino, 1979a, Specimen III-2)

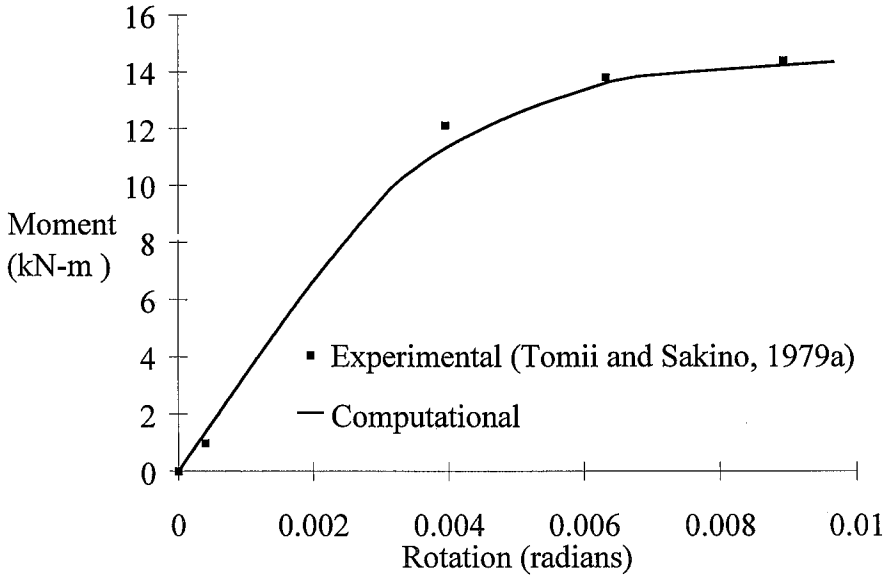

Figure 5.36: Comparison of Computational and Experimental Results for a Nonproportionally Loaded CFT Beam-Column (Tomii and Sakino, 1979a, Specimen III-3)

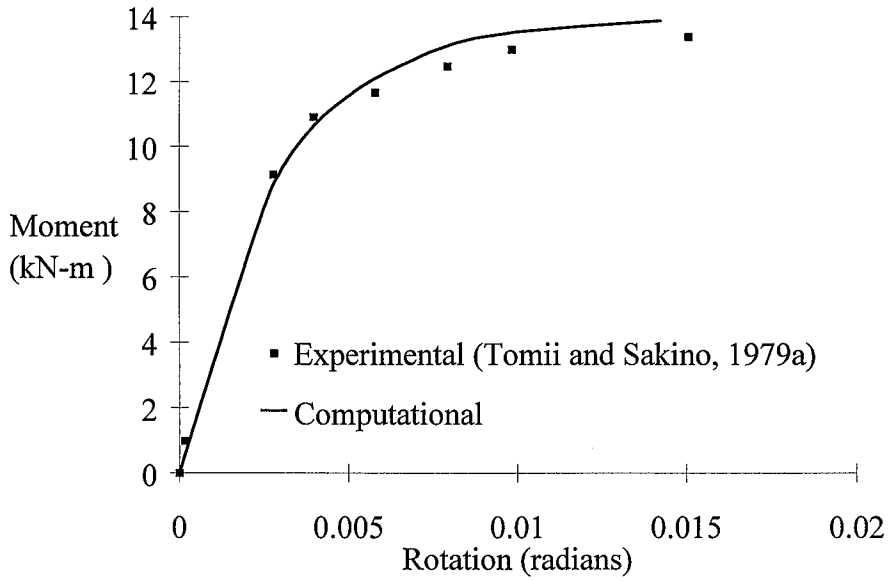

Figure 5.37: Comparison of Computational and Experimental Results for a Nonproportionally Loaded CFT Beam-Column (Tomii and Sakino, 1979a, Specimen III-4)

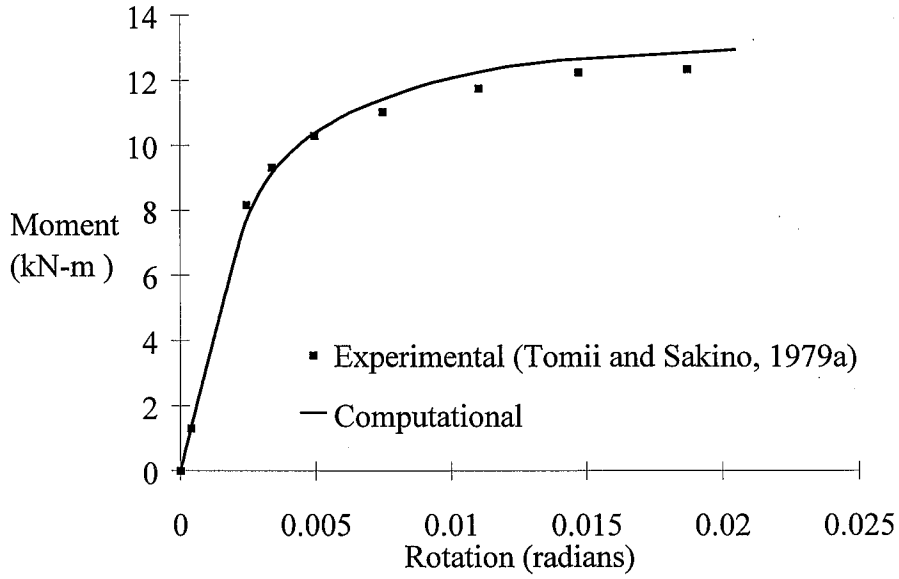

Figure 5.38: Comparison of Computational and Experimental Results for a Nonproportionally Loaded CFT Beam-Column (Tomii and Sakino, 1979a, Specimen III-5)

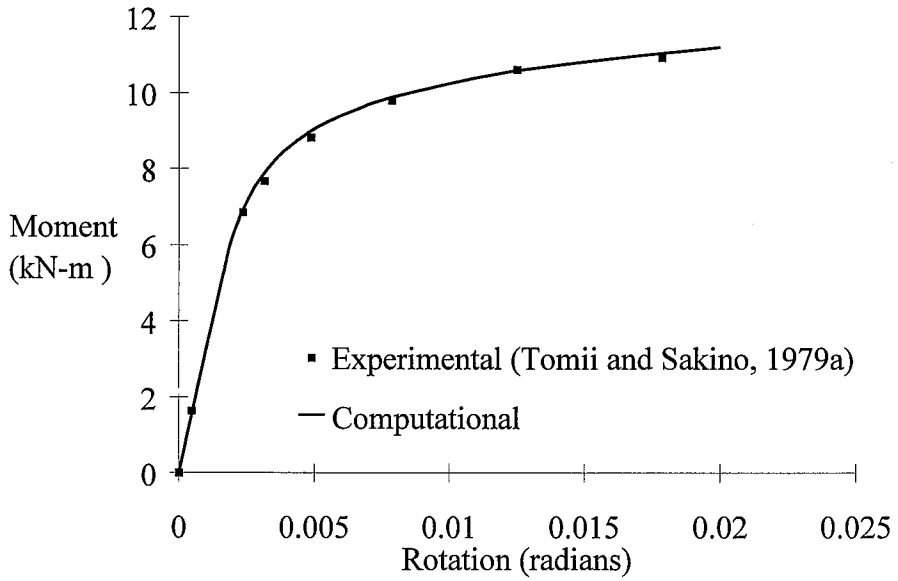

Figure 5.39: Comparison of Computational and Experimental Results for a Nonproportionally Loaded CFT Beam-Column (Tomii and Sakino, 1979a, Specimen III-6)

5.4 Comparison to Experimental Subassemblies of Steel Beams and CFT Columns

The current computational formulation has been developed for three-dimensional analysis of composite frame structures. Several experimental research programs are underway in Japan to investigate such frames (Kawaguchi et al, 1996), however this research is ongoing and little information is currently available. One set of tests is available from Kawaguchi et al. (1991b) and Morino et al. (1993), who conducted a set of tests on three-dimensional composite frames consisting of steel I-girders framing rigidly into CFT beam-columns, subjected to nonproportional cyclic loading. The tests were conducted under constant axial load, constant minor-direction beam loading, and alternating major-direction beam loading under displacement control. The experimental setup and computational model are shown in Fig. 5.40. The experimental specimens

were designed so that failure did not occur in the beam-to-column connection or in the steel wide-flange beams.

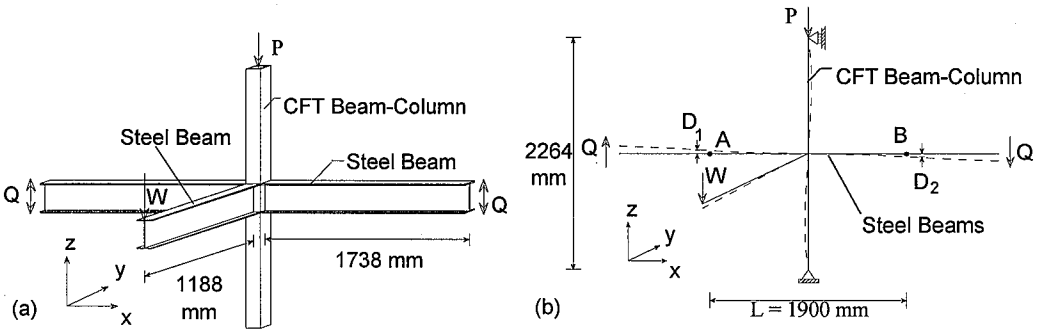

Figure 5.40: Three-Dimensional Subassembly: a) Experimental Setup (after (Morino et al., 1993)); b) Computational Model (after (Hajjar et al., 1996b))

One of the specimens is used as the final verification problem for the current computational model. This specimen used built-up steel wide-flange sections with dimensions of 250x125x6x9 mm for the beams, with a square CFT column with dimensions of 125x125x6 mm. The concrete compressive strength was 20.0 MPa; the steel yield stress of the CFT was 394.9 MPa. In the experiment, several elastic cycles were applied to the specimen before the amplitude of the loading was increased. The comparison to the computational model is made for the first experimental quarter-cycle which shows significant nonlinear behavior. Figure 5.41 shows the shear at the beam ends in the X-Z plane plotted versus the drift rotation of the specimen, as measured by the deformation of the beams at the points D1 and D2 shown in Fig. 5.40b. The computational model predicts the strength and stiffness of the specimen for the entire loading with excellent accuracy.

This verification example suggests that the current computational formulation produces acceptable results for three-dimensional analysis of composite frames composed of steel wide-flange beams framing rigidly into CFT columns. It also demonstrates the predictive capability of the current formulation for analysis or testing of composite frame structures.

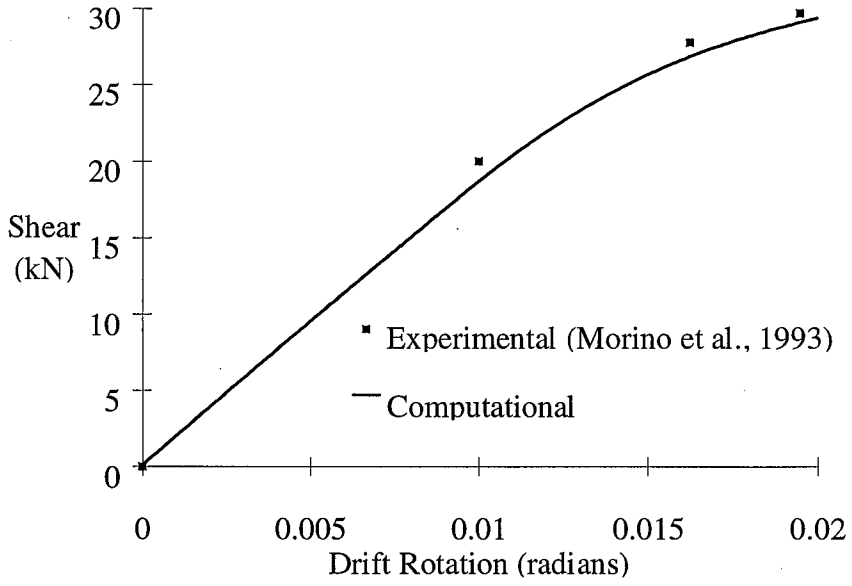

Figure 5.41: Comparison of Experimental and Computational Results for Three-Dimensional Composite Subassembly (Morino et al., 1993, Specimen SCC-20)

5.5 Analysis of Results

The verification problems presented in the previous sections were chosen to represent a variety of loading conditions, as well as a wide range of material strengths, *L/D* ratios, and *D/t* ratios. The problems were chosen from a variety of researchers to minimize the possibility of errors which may result from verifying with a limited set of experimental results.

Following is an analysis comparing the experimental results to the computational results. The entire set of results is used to show the accuracy of the computational model, and several subsets are also presented to determine if the computational model is more accurate for different types of loading, geometry, or material types.

5.5.1 Statistical Methods and Results for All Verification Examples

In this section, the experimental and computational results are compared at two different points within each analysis. Figure 5.42 shows the points in the analysis at which results are compared statistically. First, a comparison is made at the deformation level corresponding to the lesser of the experimental and computational maximum loads (point d1 in Fig 5.42). As an indication of the accuracy of the computational model to predict the spread of plasticity, a second comparison is made at half of this deformation level (point d2 in Fig 5.42). Finally, the initial slope of the two plots are compared.

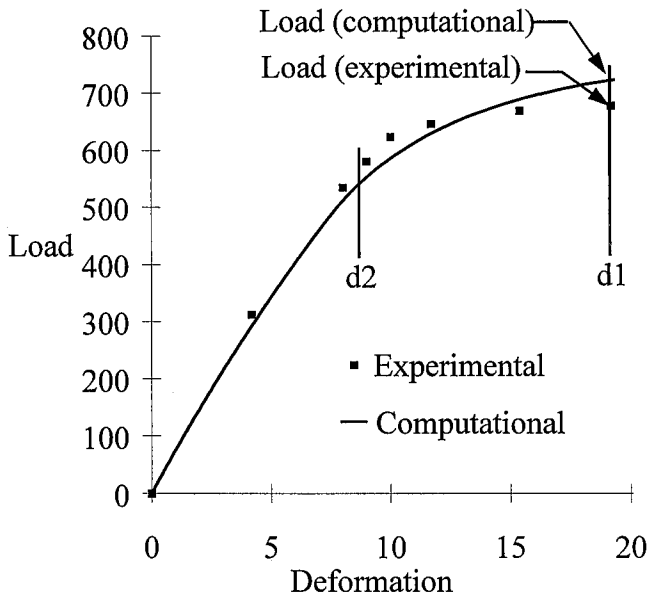

Figure 5.42: Example of Statistical Sampling Points

Table 5.5 shows the statistical comparison for all the verification problems presented in this chapter. The computational model over-predicts the strength of CFT beams, columns and composite frames an average of 1.79%, with a standard deviation of 6.89%, when compared to experimental results.

A second comparison can be made at a lower deformation level corresponding to the line d2 in Fig. 5.42. The loads at this deformation level have an average percent error of only 0.15% and a standard deviation of 6.72%, suggesting that the spread of plasticity through the CFT elements is predicted with excellent accuracy. Finally, comparison of the initial stiffness gives an average error of 2.30%, although the standard deviation is quite high for this comparison at 12.30%. The stiffness of CFTs beams and beam-columns at low load levels depends on a number of factors that are difficult to predict with high accuracy, including initial out-of-straightness, concrete stress-strain behavior, and concrete tensile strength. The data analysis suggests that the computational model predicts the initial stiffness of these members with acceptable accuracy, although significant scatter in the results may occur due to the aforementioned effects.

Table 5.5: Comparison of Computational Results with Experiments for All Verification Problems

	Percent Error of Analysis From Experiment		
Test (Notation)	Load at d1	Load at d2	Initial stiffness
Lu and Kennedy, 1994 (CB12)	-8.11	-8.01	-25.1
Lu and Kennedy, 1994 (CB22)	7.86	5.75	-16.1
Lu and Kennedy, 1994 (CB33)	3.32	3.23	-22.6
Lu and Kennedy, 1994 (CB45)	1.36	3.29	-36.4
Lu and Kennedy, 1994 (CB53)	7.74	7.35	-7.32
Tomii and Sakino, 1979a (II-0)	-21.1	-17.9	-1.63
Tomii and Sakino, 1979a (III-0)	-11.4	-9.68	3.86
Bridge, 1976 (SHC-1)	-2.46	2.98	9.18
Bridge, 1976 (SHC-3)	1.09	10.6	15.9
Bridge, 1976 (SHC-4)	-8.67	-4.76	12.9
Bridge, 1976 (SHC-5)	-4.46	0.87	3.57
Bridge, 1976 (SHC-6)	-2.31	2.21	11.4
Bridge, 1976 (SHC-7)	-6.53	5.50	6.43
Bridge, 1976 (SHC-8)	-12.9	-2.60	5.37
Cederwall et al., 1990 (1)	5.50	3.06	4.73
Cederwall et al., 1990 (2)	5.41	2.91	6.04
Cederwall et al., 1990 (6)	7.53	7.85	12.6

Table 5.5 (cont'd)

Test (Notation)	Percent Error of Analysis From Experiment		
	Load at d1	Load at d2	Initial stiffness
Cederwall et al., 1990 (7)	5.99	3.38	11.6
Cederwall et al., 1990 (9)	6.23	7.96	11.3
Cederwall et al., 1990 (10)	2.81	-3.74	-3.75
Cederwall et al., 1990 (13)	8.69	11.3	14.5
Shakir-Khalil and Zeghiche, 1989 (2)	-0.64	8.11	19.0
Shakir-Khalil and Zeghiche, 1989 (5)	1.74	2.68	4.93
Shakir-Khalil and Zeghiche, 1989 (6)	-8.51	-3.86	8.38
Shakir-Khalil and Zeghiche, 1989 (7)	-7.80	-13.0	-17.0
Shakir-Khalil, 1991 (4)	-2.76	3.85	0.42
Shakir-Khalil, 1991 (9)	1.05	6.50	9.85
Shakir-Khalil, 1991 (10)	-0.11	1.68	8.18
Tomii and Sakino ,1979a (III-1)	-8.63	-9.27	1.27
Tomii and Sakino ,1979a (III-2)	-9.29	-6.69	7.98
Tomii and Sakino ,1979a (III-3)	-9.31	-3.95	13.2
Tomii and Sakino ,1979a (III-4)	-3.93	-5.11	4.50
Tomii and Sakino ,1979a (III-5)	-4.11	-4.56	8.97
Tomii and Sakino ,1979a (III-6)	-1.04	-0.89	-2.31
Morino et al., 1993 (SCC-20)	5.03	-1.65	-3.24
Average Percent Error	-1.79	0.15	2.30
Standard Deviation	6.98	6.72	12.3

5.5.2 Results for Various Groups of Verification Examples

Computational formulations may be more accurate for some types of loading conditions or geometries than for others, due to the specifics of their stiffness formulation, force recovery, or meshing procedures. The experimental research program may also have an effect on the comparison between the experimental and computational results.

For example, the end bearing supports used by Cederwall et al. (1987) for eccentrically loaded CFT beam-columns differ from the supports used by other researchers such as Bridge (1976) and Shakir-Khalil (1991), and may thus offer differing levels of restraint. As another example, Tomii and Sakino (1979a) were the only researchers to use both annealed steel tubes and expansive cement mortar when casting their CFT specimens. All of these items may have an effect on the load-deformation behavior obtained from the experiments.

In order to investigate some of these phenomenon, the CFT verification tests are grouped as shown in Table 5.6. In this table, the only comparison which is made is for the load at the deformation level corresponding to point d1 in Fig. 5.42.

Table 5.6: Comparison of Various Groups of CFT Tests

Description of Group	Average % Error	Standard Deviation
Pure Flexure	-2.90	10.1
Eccentrically Loaded Beam-Columns	-0.53	5.90
Non-Proportionally Loaded Beam-Columns	-6.05	3.19
Composite Frame Subassembly	5.03	N.A.
Tests from Bridge, 1976	-5.18	4.30
Tests from Tomii and Sakino ,1979a	-8.59	5.74
Tests from Cederwall et al., 1990	6.03	1.71
Tests from Shakir-Khalil and Zeghiche, 1989 and Shakir-Khalil, 1991	-2.43	3.85
Tests from Lu and Kennedy, 1994	2.43	5.84
Tests with $D/t > 24$	-4.22	6.88
Tests with $D/t < 24$	-0.08	6.45
Tests with Non-Annealed Steel Tubing	0.04	6.0
Tests with $f_c' <$ 40.0 MPa	-6.31	6.37
Tests with $f_c' >$ 40.0 MPa	0.07	6.28
Tests with $f_c' >$ 70.0 MPa	7.46	1.23

This table shows that the computational model provides excellent accuracy for a number of loading conditions and CFT geometries. Of the loading categories, the computational model predicts the behavior of eccentrically loaded beam-columns with the most accuracy,

over-predicting the strength of these members with an average error of 0.53%. The model also produces excellent accuracy for members with a D/t ratio less than 24, suggesting that the steel computational model provides better prediction of the behavior of the members than the concrete computational model, as may be expected. In addition, the behavior of CFTs with medium to high concrete compressive strength are reproduced reasonably well by the computational model. The model under-predicts the strength of CFTs with high concrete compressive strength while over-predicting strength for CFTs with low concrete strength.

5.6 Slip and Bond Effects

5.6.1 Effect of Bond and Slip on Flexural Behavior

The purpose of including slip in the formulation of the CFT element is primarily to determine whether or not loss of bond occurs in CFT members used as part of structural frames. This section, as well as the final example of a four-story frame, provide the results of a preliminary study to determine the effect of slip on CFT behavior, and in particular whether an assumption of perfect bond may be appropriate for analysis and design computations.

Chapter 3 focused primarily on slip induced due to axial behavior in which only the steel tube is loaded directly. Clearly, if sufficient axial force is applied to a CFT, slip may be induced. The effect of slip on flexural behavior is more difficult to quantify than it is for axial behavior, because material nonlinearity is required before any interface stress develops in flexure. The final example problem of Chapter 3 demonstrated that a small amount of slip occurs during flexural loading, and that loss of bond may occur near the limit point of the member. While complexities such as contact between the concrete core and the steel tube are not modeled directly in this formulation, the calibrated slip model provided strong correlation with those experimental results. This phenomenon merits

further investigation, as it is important to understand whether the overall load-deformation behavior of flexural members is altered significantly if slip occurs.

Several example problems from Lu and Kennedy (1994) are presented in this section. The experimental parameters may be found in Section 5.2. For each test, the parameters of the computational slip model were varied to study the effect of bond strength on the load-deformation behavior of the members.

Figures 5.43 through 5.45 show how bond strength and initial slip layer stiffness affect the moment-curvature diagrams of these CFTs. In these figures, the computational results are truncated approximately at the experimentally observed maximum curvature. Reducing the initial slip layer stiffness by two orders of magnitude slightly reduces the nonlinear flexural stiffness of the members for a given level of curvature relative to using the calibrated parameters. However, it does not significantly affect the ultimate strength of the member at high curvature levels, as is seen in Table 5.7, which reports the moment at the maximum curvature value plotted in the figures. Similarly, using a lower bond strength does not affect the computational results until the behavior becomes nonlinear, and for these specimens the reduction in strength remains small. Reducing the bond strength to two-thirds of the calibrated value (i.e., to a value of 0.4 MPa) did not affect the load-deformation curves, and these results are not presented. Lowering the bond strength to one-third of the calibrated value (0.2 MPa) affected the load at which nonlinear behavior may first be seen, as well as reducing the strength slightly (Table 5.7). However, it may be seen that the general magnitude of strength, as well as the stiffness of the members, changes very little for the full duration of loading, and the computational curves all match the experimental results equally well.

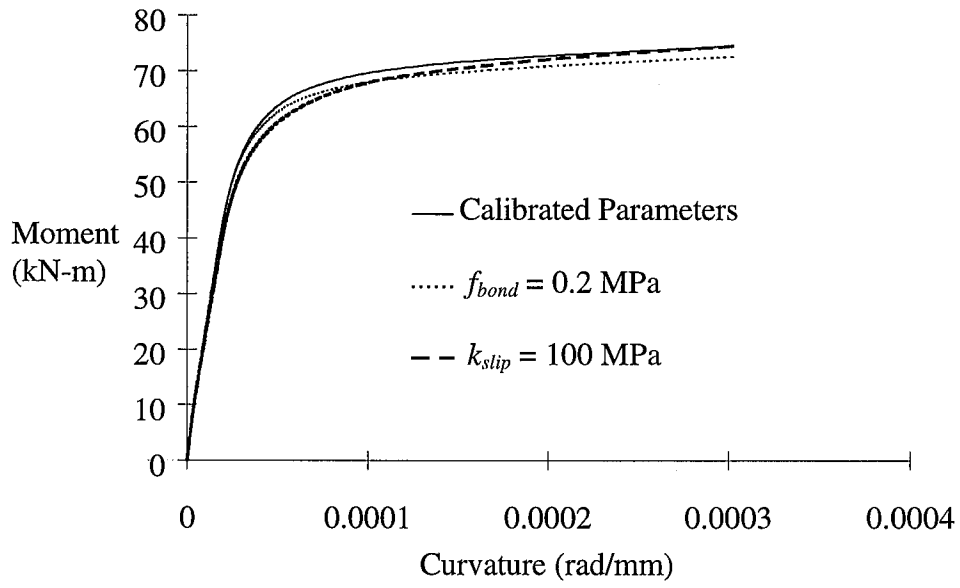

Figure 5.43: Effect of Varying Bond Strength on the Behavior of (Lu and Kennedy, 1994, Specimen CB12)

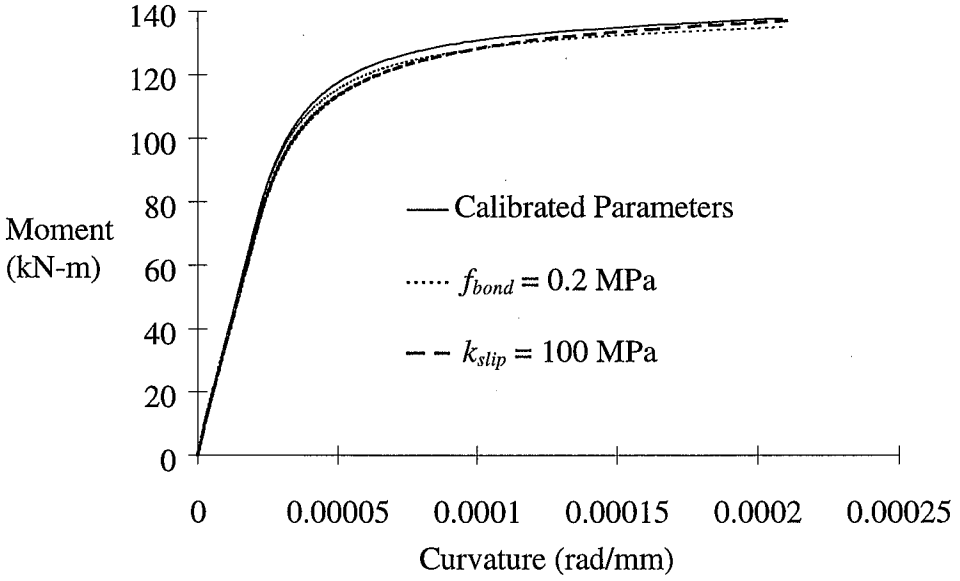

Figure 5.44: Effect of Varying Bond Strength on the Behavior of (Lu and Kennedy, 1994, Specimen CB22)

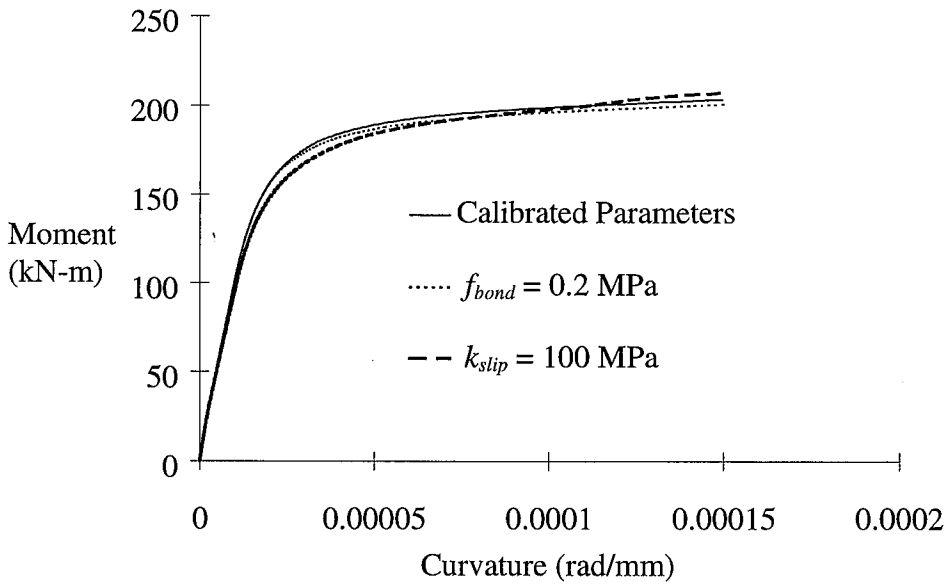

Figure 5.45: Effect of Varying Bond Strength on the Behavior of (Lu and Kennedy, 1994, Specimen CB33)

Table 5.7: Effect of Bond Strength on Flexural Load-Deformation Behavior

Test (Notation)	Experimental Maximum Curvature (rad/mm)	Percent Reduction in Moment Strength From Case Where f_b = 0.6 MPa, k_{slip} = 10^4 MPa	
		f_b = 0.2 MPa	k_{slip} = 10^2 MPa
Lu and Kennedy, 1994 (CB12)	0.0003	2.54	-0.032
Lu and Kennedy, 1994 (CB22)	0.0002	1.95	0.57
Lu and Kennedy, 1994 (CB33)	0.00015	1.33	-1.91
	Average	1.94	-0.46

5.6.2 Composite Frame Design Example

The CFT fiber element formulation was used to analyze a four-story composite CFT frame structure subjected to a combination of gravity and wind loading. This frame was taken from a feasibility study by Fetterer and Hajjar (1997) conducted to determine the economy and strength of such frames using second-order inelastic analysis (SSRC, 1993; Hajjar et al., 1996c). Figure 5.46 illustrates the members, geometry, structural parameters, and unfactored loading. The frame is proportioned so as to achieve all

factored load combinations [specifically, a load factor of 1.0/0.9 = 1.11 times the factored loads to account for the AISC LRFD (AISC, 1993) resistance factor in the analysis] without collapsing due to combined geometric and material nonlinear behavior. In the analysis for the AISC LRFD (1993) wind load combination, which controls the design, the gravity and lateral loads are increased proportionally, so that at a load factor of 1.0, the applied loads equal the factored loads for the load combination. The frame shown actually reaches its structural limit point at a load factor of approximately 1.4, thus yielding a safe and serviceable design. The computational model utilizes the 18 DOF CFT beam-column fiber element for the columns, and a comparable 12 DOF steel beam-column fiber element for the girders (White, 1986; Morales, 1994). Twelve elements are used to model each girder and column, and the fiber mesh densities at each cross section are similar to those used for the CFT verification studies.

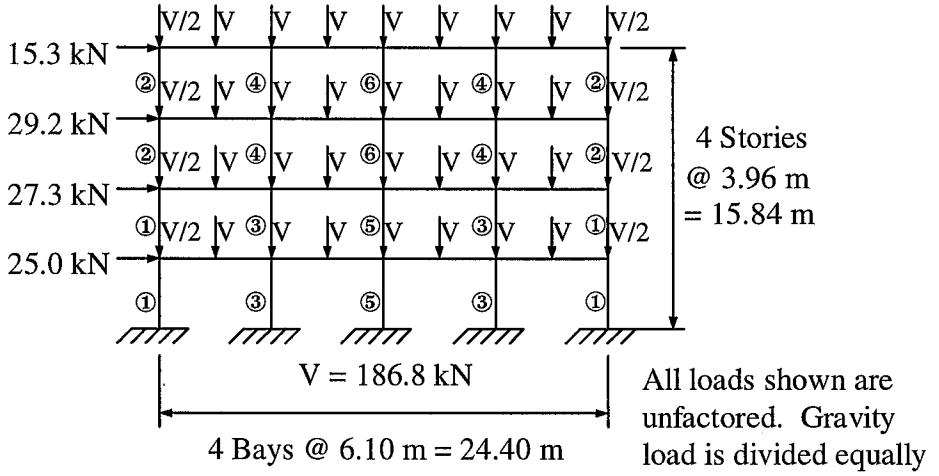

Girders:

W410x60; f_y= 248.2 MPa

CFT Sections:

①TS 177.8x177.8x6.35
②TS 152.4x152.4x4.76
③TS 254.0x203.2x6.35
④TS 203.2x152.4x6.35
⑤TS 203.2x203.2x6.35
⑥TS 152.4x152.4x6.35

f_y = 317.2 MPa, f_c' = 34.5 MPa

Analysis Cases:

Case I: No Slip Permitted
Case II: Slip Restrained at Bottom of Column Stacks; Calibrated Parameters
Case III: Case II, $k_{slip} = 10^2$ MPa
Case IV: Case II, f_{bond}= 0.1 MPa

Figure 5.46: Four-Story Frame Computational Model

The AISC LRFD interaction equation values for the individual members were also computed at a load factor of 1.0. Even at this load level, several of the columns exceeded the allowable LRFD interaction equation value. The distributed plasticity analysis not only indicates that the frame has a higher ultimate capacity, but also that the members are largely elastic at a load factor of 1.0. This result illustrates the generally conservative approach that design codes have adopted currently for CFT members.

Four cases were investigated to determine the effect of slip parameters on the behavior of the frame. As seen in Fig. 5.46, in Case I the steel girder was assumed to engage the concrete directly through the connection; no slip was permitted at the beam-to-column joints, but slip was permitted along the length of each column between the joints. In the other cases, the steel girder was assumed to engage only the tube, load was transferred to the concrete through the slip interface, and the concrete was free to protrude from the top of the column stack. Case II used the calibrated parameters for f_{bond} and k_{slip}. In Case III, the value of k_{slip} was decreased to 10^2 MPa. In Case IV, the value of f_{bond} was decreased to 0.1 MPa. Each analysis was carried out to the limit point of the structure.

Figure 5.47 shows the load-deformation response of this structure for Cases I and II. Neither the load capacity nor the stiffness of the frame were affected when slip was permitted at the beam-to column joints. In fact, there were no perceivable differences in the entire load-deformation responses for any of the four analysis cases, thus indicating that slip has a negligible effect on the overall load-deformation behavior of this frame.

However, the potential effects of slip on local behavior of CFTs are more evident. Figure 5.48 shows the slip and bond stress along the length of each CFT column stack for Cases II, III, and IV. The slip plotted as positive to the right of each column stack indicates that the concrete core is moving vertically relative to the steel tube (i.e., it tends to protrude through the top of the column stack). Figure 5.49 shows the axial force in the concrete core and in the steel tube along the length of each CFT column stack for the same cases. All results are shown at a load factor of 1.0 for the wind load combination. The bond stress is not breached in Case II at this load level, although bond stresses exceed

0.6 MPa at the top of each column stack at a load level just over 1.1. The concentration of slip and bond stress at each connection is evident (Fig. 5.48), as is the gradual transfer of load from the steel tube to the concrete core both above and below each connection. The effects of tension just above many of the connections are evident as well, with the compressive axial force in the steel tube decreasing rapidly over a short distance as a portion of the gravity load at the floor level is carried by the tube above the connection as well as below (Fig. 5.49b). However, the magnitude of the slip is relatively small in this case, as may be expected for unbraced framing action, and it does not change significantly even up to the failure load.

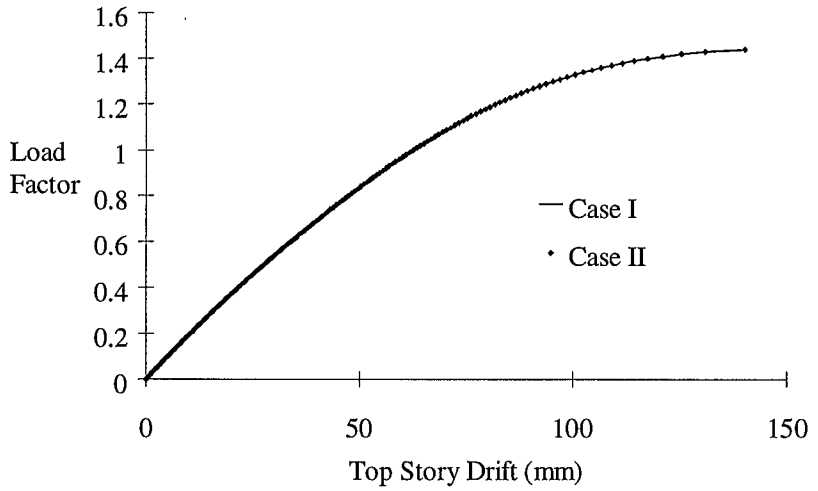

Figure 5.47: Global Load-Deformation Response of the 4-Story Frame

For Case III, the slip is an order of magnitude larger than for Case II because of the reduced slip stiffness (Fig. 5.48a). Correspondingly, the transfer of load from the connection regions occurs over nearly the entire length of each CFT column. As compared to that of Case II, the concrete load for Case III is seen in Fig. 5.49 to increase consistently along the member length, while the steel tube continuously sheds load to the concrete along the tube length. In addition, because of this more gradual transfer of load, the maximum interface stress values in the CFTs of Case III are seen to be well below those of Case II (Fig. 5.48b).

For Case IV, the bond stress of 0.1 MPa is breached at a load factor of 0.19. Since the slip stiffness is small at locations which have breached f_{bond}, the bond stress is effectively capped at this value, as is seen by the dotted line in Fig. 5.48b. The magnitude of slip is more than double that of Case II at a factored load level of 1.0, and the transfer of loads from the connections takes place over nearly the entire length of the CFT, as in Case III (Fig. 5.49). The bond stress and slip profile at the failure load of the structure (not shown) indicate substantially more slip and breaching of the bond strength occurring along nearly the entire length of the three central CFT column stacks, indicating that continued loading substantially increases the bond loss in these members.

The frame was also analyzed for the AISC LRFD (1993) gravity load combination using the calibrated parameters to determine if loss of bond is detected under the increased vertical loading. For this loading combination, the interface stress of 0.6 MPa was breached at 0.68 times the factored load, suggesting that the increased vertical load that must be transferred at connections due to factored gravity loading may cause bond loss in CFT members before the design load level of the frame is reached.

For this specific frame, the top of each column stack consistently has the highest magnitudes of slip and bond stress for all loading combinations. Capping the CFTs at the top of the column stacks alleviates the slippage at that location, but localized slip in the connection regions at each floor level is still seen when using the calibrated parameters. Global behavior, however, is unaffected by slip in these analyses for all load combinations. Of course, engaging the concrete directly in each connection, and thus restraining slip, facilitates immediate transfer of the load to the connection region.

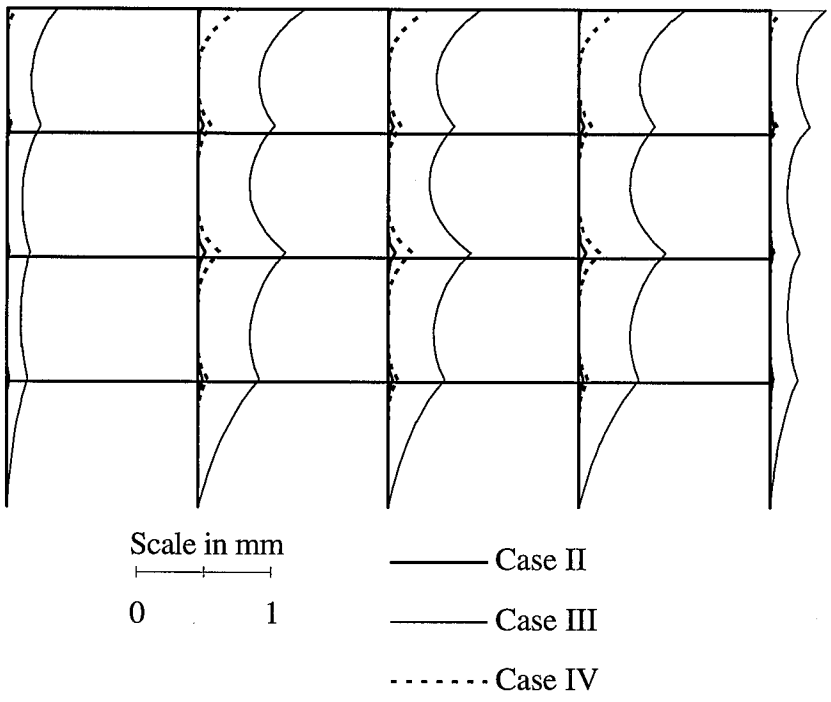

a) Slip in CFTs at a factored load level of 1.0

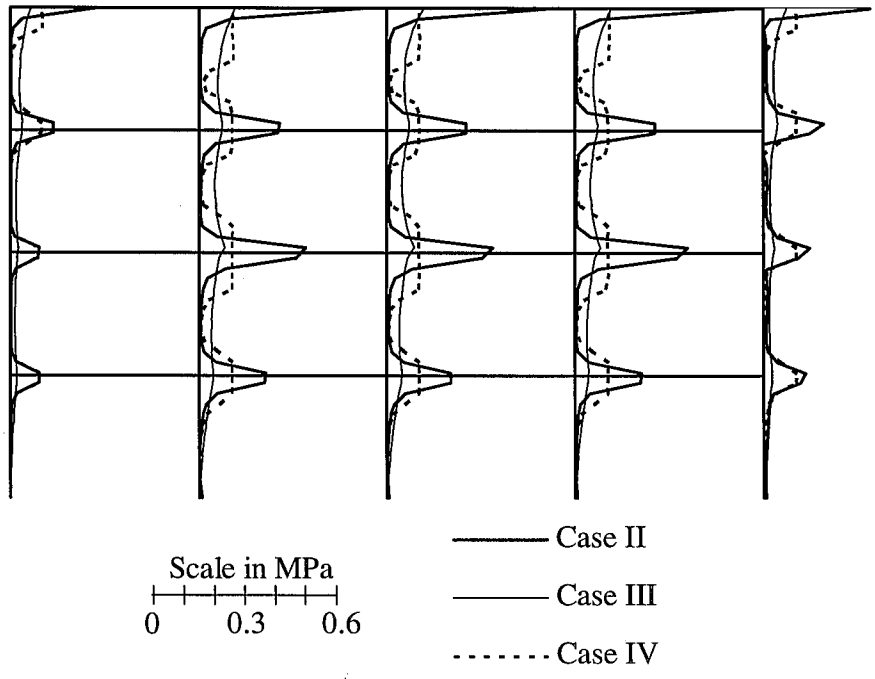

b) Bond stress in CFTs at a factored load level of 1.0

Figure 5.48: Slip and Bond Stress in the Composite Frame at the Factored Design Load

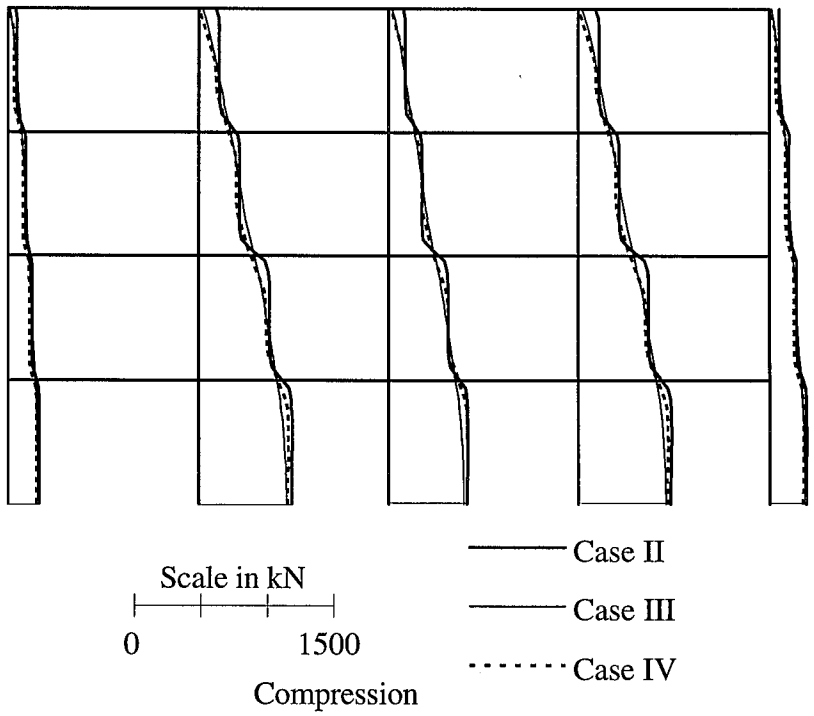

a) Axial force in CFT concrete cores at a factored load level of 1.0

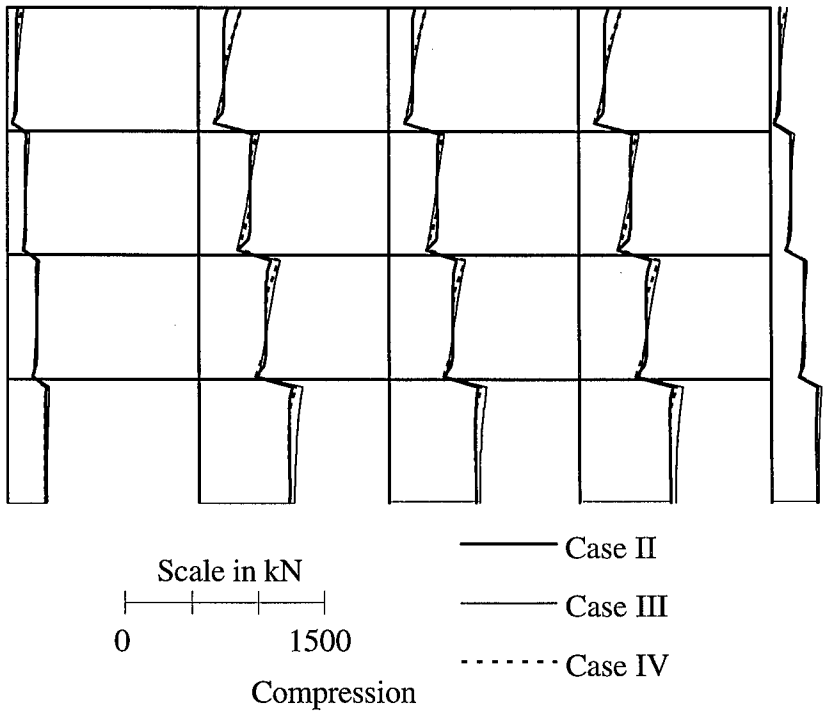

b) Axial force in CFT steel tubes at a factored load level of 1.0

Figure 5.49: Axial Force in the Concrete Core and Steel Tube in the Composite

Chapter 6

Conclusions

The current research includes the formulation of a three-dimensional 18 DOF beam finite element for geometrically and materially nonlinear analysis of square and rectangular concrete-filled steel tube beam-columns. A fiber-based distributed plasticity formulation is used, such that numerical integration is carried out through the cross section and along the member length for both stiffness formulation and force recovery. The fiber element approach is adopted because of its computational efficiency coupled with a high degree of accuracy. This approach is able to model the spread of plasticity throughout the elements using stress-strain relations at each material fiber, while retaining degrees-of-freedom only at the centroidal axis of the two member ends. The formulation incorporates slip between the steel tube and the concrete core, and it incorporates constitutive formulations which model the significant behavior specific to CFTs. Geometric nonlinearity is modeled comprehensively using a corotational formulation which captures all significant P-Δ and P-δ effects exhibited by beam-columns in braced or unbraced frame structures. A comparable three-dimensional 12 DOF steel wide-flange beam element is also included (following the formulation of White (1986)) which is used for modeling steel beams or beam-columns as components in steel or composite frames. The current research is geared for modeling either proportional or nonproportional monotonic loading, although the formulation is extended by Hajjar et al. (1996e) and Molodan and Hajjar (1997) to model cyclic loading. A global solution strategy is developed for analysis of three-

dimensional composite frames composed of both 18 DOF CFT elements and 12 DOF steel wide-flange elements.

A structural analysis computer program, CFTFiber, has been developed for implementation of these finite element formulations, and has been used for calibration and verification of the elements. The parameters which affect the nonlinear slip behavior of the 18 DOF CFT element, including the initial slip stiffness of the steel/concrete interface and the bond strength of that interface, are calibrated against experimental tests which measured slip in CFTs, and several additional examples are provided for verification. The calibration of the steel and concrete nonlinear material models is presented by Hajjar et al. (1996e) and Molodan and Hajjar (1997). The research concludes with verification of the CFT element formulation for proportionally and nonproportionally loaded beams, beam-columns, and composite subassemblages through comparison to over thirty experimental tests.

This chapter summarizes the results of the current research, focusing on the formulation for slip in CFTs. A discussion is presented on the accuracy of the current formulation as compared to experimental tests. Finally, specific suggestions are presented for future research on the nonlinear behavior of CFT beam-columns and composite CFT frames.

6.1 Summary of Research on the 18 DOF CFT Finite Element

The effect of slip on the behavior of CFTs as part of composite frames has not been thoroughly investigated. Consequently, inclusion of slip between the steel and concrete portions of the element was a prime focus of this research for the finite element formulation, as described in Chapter 2. The composite beam literature includes several finite element formulations for slip between the steel beam and concrete slab in such members (Amadio and Fragiacomo, 1993, Aribert, 1995). However, geometrically nonlinear behavior of these members is not addressed, as such behavior may often be neglected in composite beams. The current formulation includes a detailed derivation of

the geometrically nonlinear stiffness matrices for an 18 DOF three-dimensional composite beam-column element which includes slip between the steel and concrete.

Implementation of the element in a geometrically nonlinear global solution scheme provided several insights into the use of such an element. First, the steel and concrete translational stiffness must remain separated at the element ends in the local element stiffness matrix because of the coupling of axial and shear stiffness of adjacent elements during assembly of the global stiffness matrix. This requirement can be neglected if all the elements are colinear, which is an implicit assumption in much of the composite beam literature. For geometrically nonlinear analysis using the current finite element formulation, however, the members may become skewed during the analysis, and thus they must retain separate translational DOFs for the steel and concrete. This requirement necessitates the use of shear compatibility constraints which insure that the only slip which occurs in these elements is along the centroidal axis of the member. The penalty function approach was chosen to impose these shear constraints. The penalty functions are applied to the global stiffness matrix rather than the local element stiffness matrices to avoid redundant equations which may result when multiple elements meet at different orientations at a global node. For geometrically nonlinear incremental/iterative analysis, the global direction of the penalty function is updated based on the rotation of the global node.

As described in Chapter 3, calibration of the nonlinear slip interface of the 18 DOF element versus experiments on square and rectangular CFTs shows that the load-slip behavior of this interface is generally bilinear. Only two parameters are therefore required for the slip calibration, the initial slip stiffness of the steel/concrete interface, and the bond strength of this interface. Comparison to experiments of steel I-girders framing into CFT beam-columns with simple connections shows that the best prediction of the load transfer from the steel to the concrete at such connections uses an initial slip stiffness of 10^4 MPa and a bond strength of 0.6 MPa. The initial slip stiffness is in the range of values which produces deformations similar to the case of perfect bond (i.e., perfect strain compatibility between the steel and concrete). However, even at this high value of initial stiffness, some gradual transfer of load from the steel to the concrete at the connections can be observed

in both the computational model and the experimental results, suggesting that the current formulation provides an accurate prediction of the slip strains at or near a connection of a steel beam to a CFT column.

The calibrated value of bond strength is somewhat higher than the design recommendations of the British standard for composite construction (BS5400, 1979), which gives a value of 0.4 MPa, and the Japanese standard (AIJ, 1980), which gives a value of 0.1 MPa. These composite construction codes take into account other effects, however, such as long-term loading, and inherently provide a factor of safety against loss of bond. The calibrated parameters in the current research are not intended for application to the design of such members. Rather they are intended to be used for further research on the effect of slip and bond on the overall behavior of square or rectangular CFTs as part of composite frames.

Chapter 4 presents an overview of the material constitutive relationships adopted in the current research. The steel constitutive model is able to capture the important stress-strain characteristics observed experimentally for cold-formed square and rectangular steel tubing, such as the nonlinear stress-strain response caused by the cold-forming process, elastic unloading, and the different behavior of the steel and the corners and flanges of a steel tube. The concrete constitutive model is able to capture the gradually softening stress-strain curve observed in experiments for compressive loading. The compressive post-failure branch of the curve is calibrated against CFT experimental tests to provide an accurate prediction of the ductility of these members (Molodan and Hajjar, 1997). A tensile model is implemented which is able to predict cracking as well as crack closing upon reversal in the straining direction. The material constitutive models are implemented for analysis of both CFTs and steel wide-flange beams.

In Chapter 5, a preliminary parametric study is performed on the moment-curvature behavior of three flexural members tested by Lu and Kennedy (1994). Varying the slip parameters substantially did little to change the nonlinear response of the members. In addition, an example is provided of the analysis of a four-story, four-bay composite unbraced frame composed of steel wide-flange beams framing into CFT

columns with rigid connections. The effect of bond and slip restraint at the beam-to-column connections is investigated for several different cases of slip parameters and boundary conditions. The slip and bond stress at factored loads in each column stack is reported, as is the transfer of load from the steel to the concrete. Restraining the beam-to-column joints against slip has virtually no effect on the overall load-deformation behavior of the structure -- as may be expected, the global frame behavior is similar for the frames which have substantial slip and bond breakage along the column stack versus those where slip is restrained. However, noticeable slip and bond stress occurs in the connection regions, coupled with gradual transfer of axial force along each column stack, if slip is permitted along the full length of the column (regardless of whether slip is prevented at the top of the column stack). The analysis indicates that the bond strength may be well be breached for CFTs in unbraced frames in the local region of the connection, and that the transfer of force to the concrete may occur over a long length of the member once bond is breached. The effect of slip and bond loss may also result in local phenomenon such as local buckling and localized material failure at connections, ultimately affecting the strength and serviceability of the CFT. However, further parametric studies are required to bolster the findings of this preliminary study.

6.2 Accuracy of the Current Finite Element Formulation

Over thirty verification examples are presented in Chapter 5, including comparisons to experiments from six different researchers, for CFT beams, proportionally and nonproportionally loaded beam-columns, and subassemblies of composite frame structures. These examples include CFTs subjected to axial load plus either major or minor axis bending, as well as biaxial bending. The examples include tests dominated by materially nonlinear behavior (short members), geometrically nonlinear behavior (long members under axial compression), and a combination of both. CFTs with a wide variety of D/t ratios are investigated, which result in the steel and concrete contributing different proportions of the total strength of the members. The calibrated parameters for slip, as

well as the calibrated parameters for the steel and concrete constitutive models, are held constant for all of these comparisons (noting that the parameters for annealed tubes are different than those for tubes which are not annealed).

An analysis of the results is presented in Chapter 5. The computational model (using the calibrated parameters) provides excellent predictive capability, with an average error of 1.79% when compared to experimental results (this comparison is made at the experimentally observed deformation level which corresponds to peak strength).

When the results are broken down into categories, several important distinctions can be made. First, the model predicts the behavior of proportionally loaded beam-columns with the best accuracy compared to other loading schemes. This is typical of many computational models, in that proportional loading often exercises the least complexity in the constitutive models. The model provides the least accurate prediction for nonproportionally loaded beam-columns, due to the path-dependent nature of the materials, although the error for these members is also quite low (6.05%). However, an additional explanation is that the only nonproportionally loaded beam-column experiments published in enough detail for use in verification have annealed steel tubing (Tomii and Sakino, 1979a), which deviates from the calibrated parameters for the steel material model (as mentioned previously). In addition, expansive mortar was used in the concrete in these tests, perhaps having the unintended effect of adding confinement to the concrete near the beginning of the test, thus increasing the ultimate strength of the concrete and slightly lowering the yield strength of the steel tube. Such behavior is not accounted for in the computational model.

The model also provides a more accurate prediction of the member strength for cross-sections with a lower *D/t* ratio, indicating that the steel material model is more accurate than the concrete material model. This result is not unexpected, as concrete is not as homogeneous and consistent in properties as structural steel. In addition, the effect of confinement has only been accounted for in an approximate fashion, through calibration of the concrete constitutive model. Also, local buckling has been neglected, and may influence the behavior of members with a high *D/t* ratio.

6.3 Suggestions for Future Research

This research is part of an ongoing program at the University of Minnesota to develop advanced analysis software for CFTs and composite frames. This work is the second step in this program, being preceded by the development of a concentrated plasticity finite element formulation for rectangular CFTs and composite frames by Gourley and Hajjar (1994). Concurrent research includes calibration of the material models for cyclic analysis by Molodan and Hajjar (1997).

Gourley and Hajjar (1994) identified several areas of experimental research which are lacking, including experiments on CFTs with high strength steel and concrete, and with a broader range of cross-sections. The current research also indicates that new experimental tests could often include provisions for measuring slip and bond loss in CFTs, as there are still relatively few experimental studies on slip in CFT beams, beam-columns, composite frames, and connections.

Several refinements of the current computational formulation arise from the conclusions presented in this chapter. First, there exists a need for comprehensive computational models for composite connections of steel beams to CFTs, as well as composite beams to CFTs. These models should account for the limiting cases of pinned and rigid connections, as well as partially restrained connections. Such research has initiated at the University of Minnesota. Second, inclusion of confinement of the concrete core by the steel tube should be considered within the limitations of the fiber element approach. The current research includes multiaxial material models and is intended for future research which accounts for multiaxial effects. Third, the effect of local buckling of the steel tube should be included, perhaps through modification of the stress-strain relationships. Fourth, the current formulation could be extended to nonlinear analysis of composite beams as members of structural frames. Finally, the current computational model could be utilized to conduct a comprehensive set of parametric studies to determine the effect of slip on CFT strength, ductility, and rigidity.

Appendix A

Stiffness Matrices and Supplemental Information

This Appendix presents the natural (corotational) element stiffness matrices for the 18 DOF beam finite element presented in Chapter 2. Other information about static condensation of the midpoint DOFs and the expansion of the natural element stiffness matrices to the local element stiffness coordinates is also included.

This Appendix is organized as follows. Section A.1 outlines the natural element stiffness matrices. Section A.2 presents the static condensation procedure used to condense the midpoint DOFs from the natural element stiffness matrix. Section A.3 shows the expansion from the natural element stiffness matrix to the local element 18 DOF stiffness matrix.

A.1 Natural Element Stiffness Matrices

Tables A.1-A.3 at the end of this Appendix show the closed-form natural element stiffness matrices which result from the corotational finite element formulation presented in Chapter 2. These matrices include the small displacements stiffness matrix $[K_e^{nat}]$, the low-order geometrically nonlinear stiffness matrix $[K_{g1}^{nat}]$, and the high-order geometrically nonlinear stiffness matrix $[K_{g2}^{nat}]$. These matrices are added together to form the natural element stiffness matrix as shown in Equation A.1.

$$[K^{nat}] = [K_e^{nat}] + [K_{g1}^{nat}] + [K_{g2}^{nat}] \tag{A.1}$$

Material nonlinearity is incorporated through variance of the steel and concrete moduli at each fiber. If material nonlinearity is active in the analysis, these matrices are not constructed in closed form, but are generated through numerical integration of the cross-sectional rigidity as shown in Chapter 2. Additional information about the finite element formulation can be found in Chapter 2. All symbols are defined in Appendix D.

A.2 Static Condensation of the Midpoint Degrees-of-Freedom

The current 18 DOF beam finite element formulation assumes that loads are applied only at the ends of members. Therefore, the midpoint nodes associated with the steel and concrete axial deformations are assigned no applied load. In addition, the actual deformation of these midpoint nodes is of little use, as the cross sectional strains can be recovered directly from the applied forces at the ends of the elements (see Chapter 2). Using static condensation of the natural element stiffness matrix, the calculation of deformations for the midpoint nodes can be avoided, thus reducing the number of local element DOFs by 2.

The deformation vectors have been set up so that the following equivalent matrix representation can be written:

$$[K^{nat}]\{\Delta d^{nat}\} = \{\Delta f^{nat}\} \tag{A.2}$$

where: $\{\Delta d^{nat}\}$ is the vector of the natural element incremental deformations (in the natural element coordinate system)

$\{\Delta f^{nat}\}$ is the vector of the natural element incremental forces (in the natural element coordinate system)

This equation may be partitioned as shown in Equation A.3, with the midpoint nodes associated with the rows and columns *s*, and the remaining DOFs associated with the rows and columns *r*.

$$\begin{bmatrix} [K_{rr}^{nat}]^{12x12} & [K_{rs}^{nat}]^{12x2} \\ [K_{sr}^{nat}]^{2x12} & [K_{ss}^{nat}]^{2x2} \end{bmatrix} \begin{Bmatrix} \{\Delta d^{nat}\}^{12x1} \\ \{\Delta d_m^{nat}\}^{2x1} \end{Bmatrix} = \begin{Bmatrix} \{\Delta f^{nat}\}^{12x1} \\ \{\Delta f_m^{nat}\}^{2x1} \end{Bmatrix} \tag{A.3}$$

where: $\{\Delta d_m^{nat}\}$ is the vector of midpoint incremental deformations

$\{\Delta f_m^{nat}\}$ is the vector of midpoint incremental forces (equal to the null vector).

Thus, through static condensation:

$$\left[K_{condensed}^{nat} \right]^{12x12} \{\Delta d^{nat}\}^{12x1} = \{\Delta f^{nat}\}^{12x1} \tag{A.4}$$

where $\left[K_{condensed}^{nat} \right]$ is the condensed natural element stiffness matrix:

$$[K^{condensed}] = [K_{rr}^{nat}]^{12x12} - [K_{rs}^{nat}]^{12x2} [[K_{ss}^{nat}]^{2x2}]^{-1} [K_{sr}^{nat}]^{2x12} \tag{A.5}$$

A.3 Expansion to the Local Element Stiffness Matrix

The expansion from the natural coordinate system to the local coordinate system for the conventional 12 DOF beam finite element has been presented by Chen and Lui (1987), Yang and Kuo (1994), and others. This transformation for the 18 DOF beam finite element used in the current research differs slightly, in that the steel and concrete have separate translational and rotational DOFs in the natural element stiffness matrix

(see Section A.1). In addition, because the steel and concrete rotations are assumed to be equal along the length of the element, the separate rotational DOFs in the natural system are combined into a single set of rotational DOFs in the local system.

In the expansion from the natural system to the local system, three rigid-body translations and three rigid-body rotations are accounted for. Figure A.1 shows the positive sign convention for the local element forces and deformations.

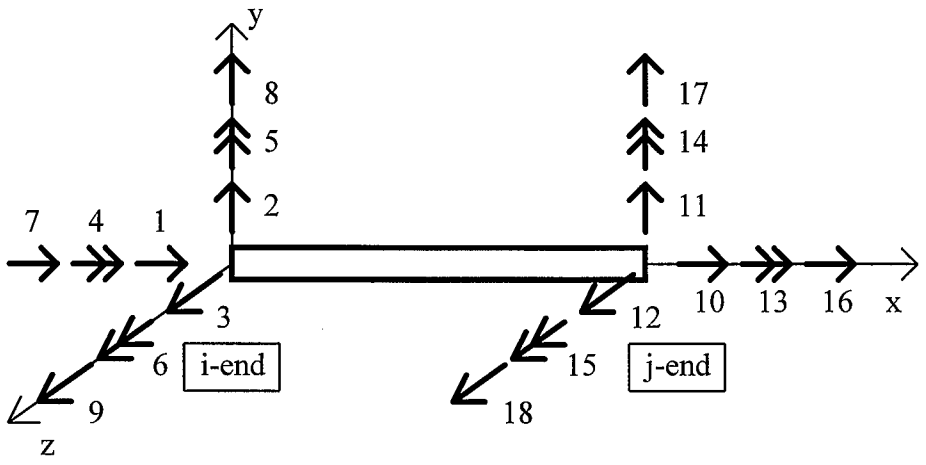

Figure A.1: Positive Sign Convention for Local Element DOFs

While the axial forces, bending forces, and deformations may be translated to the local coordinate system using a transformation matrix, the element end shear forces must be computed in the local coordinate system using static equilibrium of the natural element forces. For the geometrically nonlinear finite element formulation, the rigid body deformation of the element must also be accounted for when computing the element shear forces. This is accomplished by considering the natural element forces which act in the C1 direction at the beginning of the load step. Due to rigid body rotation of the element, the element end axial force causes additional shear forces. The additional force is computed by taking moments about the end of the element in the C2 configuration. The geometrically nonlinear shear forces which result from the element axial force have been referred to as the "external stiffness" by Yang and Kuo (1994) and others.

For the 18 DOF beam finite element, the separate steel and concrete axial forces and shears require special consideration. The steel axial force is assumed to affect only the steel shear forces, and the concrete axial force is assumed to affect only the concrete shear forces. The steel and concrete axial forces also change along the length of the element, according to the finite element formulation for slip. As mentioned in Chapter 2, the variation of the axial forces is assumed to be linear along the length of the element, and is equivalent to a uniformly distributed axial force traction along the element length. Figure A.2 shows a planar representation of how the steel and concrete axial forces affect the element shears.

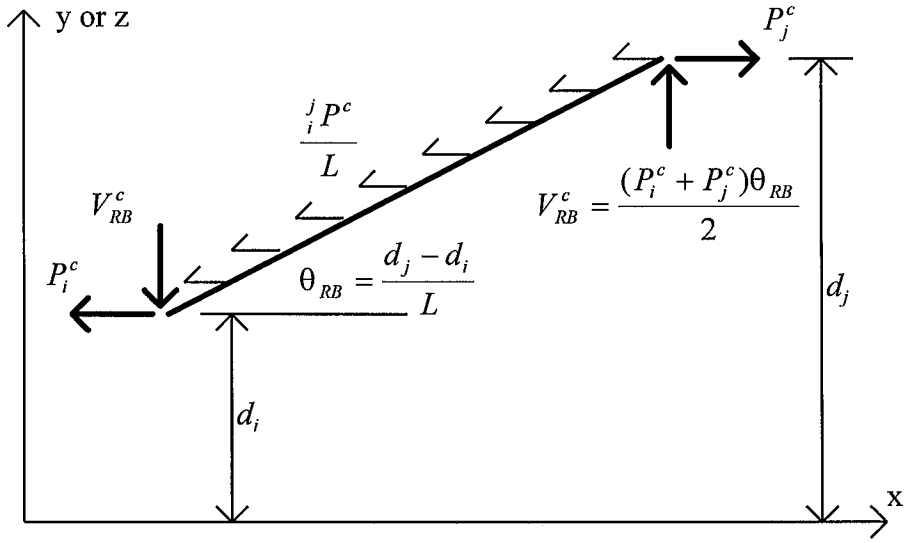

Figure A.2: External Stiffness for the 18 DOF Beam Finite Element

In this figure, the shear deformation at the i-end of the member (d_i) and the shear deformation at the j-end of the member (d_j) are measured with respect to the natural coordinate system at C1. The length of the element used in the equations is the distance between the i and j end nodes of the element at C1. The rigid-body rotation of the element is assumed to represented by the rigid-body deformation divided by the length. The distributed axial load is assumed to linear with a magnitude of ${}_i^j P^c = P_j^c - P_i^c$.

Using this relationship in three-dimensions, the complete relationship between the natural element forces and the local element forces (which include the rigid-body modes of deformation) can be formed. Equation A.6 shows the matrix representation of this transformation. Table A.4 shows the transformation matrix $[\Omega]^{18x12}$.

$$\{\Delta f^e\}^{18x1} = [\Omega]^{18x12}\{\Delta f^{nat}\}^{12x1} + \{rb\}^{18x1} \tag{A.6}$$

where: $\{\Delta f^e\}^{18x1}$ is the vector of local element incremental forces

$[\Omega]^{18x12}$ is the natural-to-local transformation matrix

$\{\Delta f^{nat}\}^{12x1}$ is the vector of natural element incremental forces

$\{rb\}^{18x1}$ is the vector containing the rigid-body geometrically nonlinear force terms (external stiffness)

A second relationship must be developed between the natural element deformations and the local element deformations. This relationship involves only kinematic relationships, and furthermore, must be the identical transformation used for the element forces (Cook, 1981). Equation A.7 shows how this relationship is applied to transform the local element deformations to the natural element deformations.

$$\{\Delta d^{nat}\}^{12x1} = \left[[\Omega]^T\right]^{2x18}\{\Delta d^e\}^{18x1} \tag{A.7}$$

where: $\{\Delta d^e\}^{18x1}$ is the vector of local element incremental deformations

$\{\Delta d^{nat}\}^{12x1}$ is the vector of natural element incremental deformations

Equations A.6 and A.7 are substituted into the natural element force-deformation relationship, and the expression for the local element stiffness matrix results. Equation

A.8 shows the matrix for the transformation from the natural element stiffness matrix to the local element stiffness matrix.

$$\left[K^{e}\right]^{18x18} = \left[\Omega\right]^{18x12}\left[K^{nat}\right]^{12x12}\left[\left[\Omega\right]^{T}\right]^{2x18} + \left[RB\right]^{18x18} \tag{A.8}$$

where: $\left[K^{e}\right]^{18x18}$ is the local element stiffness matrix, including geometric nonlinear terms

$\left[K^{nat}\right]^{12x12}$ is the natural element stiffness matrix, including geometric nonlinear terms

$\left[\Omega\right]^{18x12}$ is the natural-to-local expansion matrix

$\left[RB\right]^{18x18}$ is the matrix containing the rigid body geometric nonlinear stiffness terms (Table A.5)

Table A.1: Small Displacements Natural Stiffness Matrix $[K_e^{nat}]$

Δe^{sc}	Δe^{c}	$\Delta\theta^{c}_{zi}$	$\Delta\theta^{c}_{yi}$	$\Delta\theta^{c}_{zj}$	$\Delta\theta^{c}_{yj}$	Δe^{s}	$\Delta\theta^{s}_{zi}$	$\Delta\theta^{s}_{yi}$	$\Delta\theta^{s}_{zj}$	$\Delta\theta^{s}_{yj}$	$\Delta\theta_{x}$	Δe^{c}_{m}	Δe^{s}_{m}
$Lk_{slip}+\frac{L_i^j k_{slip}}{2}$	$\frac{Lk_{slip}}{6}+\frac{L_i^j k_{slip}}{6}$	0	0	0	0	$-\frac{Lk_{slip}}{6}-\frac{L_i^j k_{slip}}{6}$	0	0	0	0	0	$\frac{2Lk_{slip}}{3}+\frac{L_i^j k_{slip}}{3}$	$-\frac{2Lk_{slip}}{3}-\frac{L_i^j k_{slip}}{3}$
	$\frac{7EA^e}{3L}+\frac{11_i^j EA^e}{6L}+$ $\frac{2Lk_{slip}}{15}+\frac{7L_i^j k_{slip}}{60}$	$\frac{EQ_z^e}{L}+\frac{2_i^j EQ_z^e}{3L}$	$\frac{EQ_y^e}{L}+\frac{2_i^j EQ_y^e}{3L}$	$\frac{3EQ_z^e}{L}+\frac{7_i^j EQ_z^e}{3L}$	$\frac{3EQ_y^e}{L}+\frac{7_i^j EQ_y^e}{3L}$	$-\frac{2Lk_{slip}}{15}-\frac{7L_i^j k_{slip}}{60}$	0	0	0	0	0	$\frac{Lk_{slip}}{15}+\frac{L_i^j k_{slip}}{15}-$ $\frac{8EA^e}{3L}-\frac{2_i^j EA^e}{L}$	$\frac{Lk_{slip}}{15}+\frac{L_i^j k_{slip}}{15}$
		$\frac{4EI_{zz}^e}{L}+\frac{{}_i^j EI_{zz}^e}{L}$	$\frac{4EI_{yz}^e}{L}+\frac{{}_i^j EI_{yz}^e}{L}$	$\frac{2EI_{zz}^e}{L}+\frac{{}_i^j EI_{zz}^e}{L}$	$\frac{2EI_{yz}^e}{L}+\frac{{}_i^j EI_{yz}^e}{L}$	0	0	0	0	0	0	$-4\frac{EQ_z^e}{L}-\frac{4_i^j EQ_z^e}{3L}$	0
			$\frac{4EI_{yy}^e}{L}+\frac{{}_i^j EI_{yy}^e}{L}$	$\frac{2EI_{yz}^e}{L}+\frac{{}_i^j EI_{yz}^e}{L}$	$\frac{2EI_{yy}^e}{L}+\frac{{}_i^j EI_{yy}^e}{L}$	0	0	0	0	0	0	$-\frac{4EQ_y^e}{L}-\frac{4_i^j EQ_y^e}{3L}$	0
				$\frac{4EI_{zz}^e}{L}+\frac{3_i^j EI_{zz}^e}{L}$	$\frac{4EI_{yz}^e}{L}+\frac{3_i^j EI_{yz}^e}{L}$	0	0	0	0	0	0	$-4\frac{EQ_z^e}{L}-\frac{8_i^j EQ_z^e}{3L}$	0
					$\frac{4EI_{yy}^e}{L}+\frac{3_i^j EI_{yy}^e}{L}$	0	0	0	0	0	0	$-\frac{4EQ_y^e}{L}-\frac{8_i^j EQ_y^e}{3L}$	0
						$\frac{7EA^s}{3L}+\frac{11_i^j EA^s}{6L}+$ $\frac{2Lk_{slip}}{15}+\frac{7L_i^j k_{slip}}{60}$	$\frac{EQ_z^s}{L}+\frac{2_i^j EQ_z^s}{3L}$	$\frac{EQ_y^s}{L}+\frac{2_i^j EQ_y^s}{3L}$	$\frac{3EQ_z^s}{L}+\frac{7_i^j EQ_z^s}{3L}$	$\frac{3EQ_y^s}{L}+\frac{7_i^j EQ_y^s}{3L}$	0	$-\frac{Lk_{slip}}{15}-\frac{L_i^j k_{slip}}{15}$	$\frac{Lk_{slip}}{15}+\frac{L_i^j k_{slip}}{15}$ $-\frac{8EA^s}{3L}-\frac{2_i^j EA^s}{L}$
							$\frac{4EI_{zz}^s}{L}+\frac{{}_i^j EI_{zz}^s}{L}$	$\frac{4EI_{yz}^s}{L}+\frac{{}_i^j EI_{yz}^s}{L}$	$\frac{2EI_{zz}^s}{L}+\frac{{}_i^j EI_{zz}^s}{L}$	$\frac{2EI_{yz}^s}{L}+\frac{{}_i^j EI_{yz}^s}{L}$	0	0	$-4\frac{EQ_z^s}{L}-\frac{4_i^j EQ_z^s}{3L}$
								$\frac{4EI_{yy}^s}{L}+\frac{{}_i^j EI_{yy}^s}{L}$	$\frac{2EI_{yz}^s}{L}+\frac{{}_i^j EI_{yz}^s}{L}$	$\frac{2EI_{yy}^s}{L}+\frac{{}_i^j EI_{yy}^s}{L}$	0	0	$-\frac{4EQ_y^s}{L}-\frac{4_i^j EQ_y^s}{3L}$
									$\frac{4EI_{zz}^s}{L}+\frac{3_i^j EI_{zz}^s}{L}$	$\frac{4EI_{yz}^s}{L}+\frac{3_i^j EI_{yz}^s}{L}$	0	0	$-4\frac{EQ_z^s}{L}-\frac{8_i^j EQ_z^s}{3L}$
										$\frac{4EI_{yy}^s}{L}+\frac{3_i^j EI_{yy}^s}{L}$	0	0	$-\frac{4EQ_y^s}{L}-\frac{8_i^j EQ_y^s}{3L}$
											$\frac{GJ}{L}$	0	0
												$\frac{8Lk_{slip}}{15}+\frac{4L_i^j k_{slip}}{15}$ $+\frac{16EA^e}{3L}+\frac{8_i^j EA^e}{3L}$	$-\frac{8Lk_{slip}}{15}-\frac{4L_i^j k_{slip}}{15}$
													$\frac{8Lk_{slip}}{15}+\frac{4L_i^j k_{slip}}{15}$ $+\frac{16EA^s}{3L}+\frac{8_i^j EA^s}{3L}$

symmetric

Table A.2: Low Order Geometrically Nonlinear Stiffness Matrix $[K_{g1}^{nat}]$

Δe^{sc}	Δe^{c}	$\Delta\theta_{zi}^{c}$	$\Delta\theta_{yi}^{c}$	$\Delta\theta_{zj}^{c}$	$\Delta\theta_{yj}^{c}$	Δe^{s}	$\Delta\theta_{zi}^{s}$	$\Delta\theta_{yi}^{s}$	$\Delta\theta_{zj}^{s}$	$\Delta\theta_{yj}^{s}$	$\Delta\theta_{x}$	Δe_{m}^{c}	Δe_{m}^{s}
0	0	0	0	0	0	0	0	0	0	0	0	0	0
	0	0	0	0	0	0	0	0	0	0	0	0	0
		$\frac{L(3P_i^c + P_j^c)}{30}$	0	$-\frac{L(P_i^c + P_j^c)}{60}$	0	0	0	0	0	0	0	0	0
			$\frac{L(3P_i^c + P_j^c)}{30}$	0	$-\frac{L(P_i^c + P_j^c)}{60}$	0	0	0	0	0	0	0	0
				$\frac{L(3P_j^c + P_i^c)}{30}$	0	0	0	0	0	0	0	0	0
					$\frac{L(3P_j^c + P_i^c)}{30}$	0	0	0	0	0	0	0	0
						0	0	0	0	0	0	0	0
							$\frac{L(3P_i^s + P_j^s)}{30}$	0	$-\frac{L(P_i^s + P_j^s)}{60}$	0	0	0	0
								$\frac{L(3P_i^s + P_j^s)}{30}$	0	$-\frac{L(P_i^s + P_j^s)}{60}$	0	0	0
									$\frac{L(3P_j^s + P_i^s)}{30}$	0	0	0	0
										$\frac{L(3P_j^s + P_i^s)}{30}$	0	0	0
											0	0	0
												0	0
													0

symmetric

Table A.3: High Order Geometrically Nonlinear Stiffness Matrix $[K_{g2}^{nat}]$

Δe^{sc}	Δe^{c}	$\Delta\theta^{c}_{zi}$	$\Delta\theta^{c}_{yi}$	$\Delta\theta^{c}_{zj}$	$\Delta\theta^{c}_{yj}$	Δe^{s}	$\Delta\theta^{s}_{zi}$	$\Delta\theta^{s}_{yi}$	$\Delta\theta^{s}_{zj}$	$\Delta\theta^{s}_{yj}$	$\Delta\theta_{x}$	Δe^{c}_{m}	Δe^{s}_{m}
0	0	0	0	0	0	0	0	0	0	0	0	0	0
	$\frac{7P_i^c}{3L}+\frac{11_i^jP^c}{6L}$	$\frac{M_{zi}^c}{L}+\frac{2_i^jM_z^c}{3L}$	$\frac{M_{yi}^c}{L}+\frac{2_i^jM_y^c}{3L}$	$\frac{3M_{zi}^c}{L}+\frac{7_i^jM_z^e}{3L}$	$\frac{3M_{yi}^c}{L}+\frac{7_i^jM_y^e}{3L}$	0	0	0	0	0	0	$-8\frac{P_i^c}{3L}-\frac{2_i^jP^c}{L}$	0
		$\frac{4\zeta_{zzi}^c}{L}+\frac{{}_i^j\zeta_{zz}^c}{L}$	$\frac{4\zeta_{yzi}^c}{L}+\frac{{}_i^j\zeta_{yz}^c}{L}$	$\frac{2\zeta_{zzi}^c}{L}+\frac{{}_i^j\zeta_{zz}^c}{L}$	$\frac{2\zeta_{yzi}^c}{L}+\frac{{}_i^j\zeta_{yz}^c}{L}$	0	0	0	0	0	$\frac{M_{yi}^c-M_{yj}^c}{12}$	$-4\frac{M_{zi}^c}{L}-\frac{4_i^jM_z^c}{3L}$	0
			$\frac{4\zeta_{yyi}^c}{L}+\frac{{}_i^j\zeta_{yy}^c}{L}$	$\frac{2\zeta_{yzi}^c}{L}+\frac{{}_i^j\zeta_{yz}^c}{L}$	$\frac{2\zeta_{yyi}^c}{L}+\frac{{}_i^j\zeta_{yy}^c}{L}$	0	0	0	0	0	$\frac{M_{zj}^c-M_{zi}^c}{12}$	$-\frac{4M_{yi}^c}{L}-\frac{4_i^jM_y^c}{3L}$	0
				$\frac{4\zeta_{zzi}^c}{L}+\frac{3_i^j\zeta_{zz}^c}{L}$	$\frac{4\zeta_{yzi}^c}{L}+\frac{3_i^j\zeta_{yz}^c}{L}$	0	0	0	0	0	$\frac{M_{yj}^c-M_{yi}^c}{12}$	$-4\frac{M_{zi}^c}{L}-\frac{8_i^jM_z^c}{3L}$	0
					$\frac{4\zeta_{yyi}^c}{L}+\frac{3_i^j\zeta_{yy}^c}{L}$	0	0	0	0	0	$\frac{M_{zi}^c-M_{zj}^c}{12}$	$-\frac{4M_{yi}^c}{L}-\frac{8_i^jM_y^c}{3L}$	0
						$\frac{7P_i^s}{3L}+\frac{11_i^jP^s}{6L}$	$\frac{M_{zi}^s}{L}+\frac{2_i^jM_z^s}{3L}$	$\frac{M_{yi}^s}{L}+\frac{2_i^jM_y^s}{3L}$	$\frac{3M_{zi}^s}{L}+\frac{7_i^jM_z^s}{3L}$	$\frac{3M_{yi}^s}{L}+\frac{7_i^jM_y^s}{3L}$	0	0	$-8\frac{P_i^s}{3L}-\frac{2_i^jP^s}{L}$
							$\frac{4\zeta_{zzi}^s}{L}+\frac{{}_i^j\zeta_{zz}^s}{L}$	$\frac{4\zeta_{yzi}^s}{L}+\frac{{}_i^j\zeta_{yz}^s}{L}$	$\frac{2\zeta_{zzi}^s}{L}+\frac{{}_i^j\zeta_{zz}^s}{L}$	$\frac{2\zeta_{yzi}^s}{L}+\frac{{}_i^j\zeta_{yz}^s}{L}$	$\frac{M_{yi}^s-M_{yj}^s}{12}$	0	$-4\frac{M_{zi}^s}{L}-\frac{4_i^jM_z^s}{3L}$
								$\frac{4\zeta_{yyi}^s}{L}+\frac{{}_i^j\zeta_{yy}^s}{L}$	$\frac{2\zeta_{yzi}^s}{L}+\frac{{}_i^j\zeta_{yz}^s}{L}$	$\frac{2\zeta_{yyi}^s}{L}+\frac{{}_i^j\zeta_{yy}^s}{L}$	$\frac{M_{zj}^s-M_{zi}^s}{12}$	0	$-\frac{4M_{yi}^s}{L}-\frac{4_i^jM_y^s}{3L}$
									$\frac{4\zeta_{zzi}^s}{L}+\frac{3_i^j\zeta_{zz}^s}{L}$	$\frac{4\zeta_{yzi}^s}{L}+\frac{3_i^j\zeta_{yz}^s}{L}$	$\frac{M_{yj}^s-M_{yi}^s}{12}$	0	$-4\frac{M_{zi}^s}{L}-\frac{8_i^jM_z^s}{3L}$
										$\frac{4\zeta_{yyi}^s}{L}+\frac{3_i^j\zeta_{yy}^s}{L}$	$\frac{M_{zi}^s-M_{zj}^s}{12}$	0	$-\frac{4M_{yi}^s}{L}-\frac{8_i^jM_y^s}{3L}$
											$\frac{\zeta_{yyi}^s+\zeta_{yyi}^e+\zeta_{zzi}^s+\zeta_{zzi}^e}{L}+\frac{{}_i^j\zeta_{yy}^s+{}_i^j\zeta_{yy}^e+{}_i^j\zeta_{zz}^s+{}_i^j\zeta_{zz}^e}{2L}$	0	0
												$\frac{16P_i^e}{3L}+\frac{8_i^jP^e}{3L}$	0
													$\frac{16P_i^s}{3L}+\frac{8_i^jP^s}{3L}$

symmetric

Table A.4: Natural-to-Local Transformation Matrix [Ω]

-1	0	0	0	0	0	-1	0	0	0	0	0
0	0	0	0	0	0	0	1/L	0	1/L	0	0
0	0	0	0	0	0	0	0	1/L	0	1/L	0
0	0	0	0	0	0	0	0	0	0	0	-1
0	0	0	-1	0	0	0	0	-1	0	0	0
0	0	1	0	0	0	0	1	0	0	0	0
1	-1	0	0	0	0	0	0	0	0	0	0
0	0	1/L	0	1/L	0	0	0	0	0	0	0
0	0	0	1/L	0	1/L	0	0	0	0	0	0
0	0	0	0	0	0	1	0	0	0	0	0
0	0	0	0	0	0	0	-1/L	0	-1/L	0	0
0	0	0	0	0	0	0	0	-1/L	0	-1/L	0
0	0	0	0	0	0	0	0	0	0	0	1
0	0	0	0	0	-1	0	0	0	0	-1	0
0	0	0	0	1	0	0	0	0	1	0	0
0	1	0	0	0	0	0	0	0	0	0	0
0	0	-1/L	0	-1/L	0	0	0	0	0	0	0
0	0	0	-1/L	0	-1/L	0	0	0	0	0	0

Table A.5: Rigid-Body External Stiffness Matrix $[RB]$

0	0	0	0	0	0	0	0	0	0	0	0	0	0	0	0	0	0
	$\frac{P_i^s + P_j^s}{L}$	0	0	0	0	0	0	0	0	$-\frac{P_i^r + P_j^r}{L}$	0	0	0	0	0	0	0
		$\frac{P_i^s + P_j^s}{L}$	0	0	0	0	0	0	0	0	$-\frac{P_i^r + P_j^r}{L}$	0	0	0	0	0	0
			0	0	0	0	0	0	0	0	0	0	0	0	0	0	0
				0	0	0	0	0	0	0	0	0	0	0	0	0	0
					0	0	0	0	0	0	0	0	0	0	0	0	0
						0	0	0	0	0	0	0	0	0	0	0	0
							$\frac{P_i^e + P_j^e}{L}$	0	0	0	0	0	0	0	0	$-\frac{P_i^e + P_j^e}{L}$	0
								$\frac{P_i^e + P_j^e}{L}$	0	0	0	0	0	0	0	0	$-\frac{P_i^e + P_j^e}{L}$
									0	0	0	0	0	0	0	0	0
										$\frac{P_i^s + P_j^s}{L}$	0	0	0	0	0	0	0
											$\frac{P_i^s + P_j^s}{L}$	0	0	0	0	0	0
												0	0	0	0	0	0
													0	0	0	0	0
														0	0	0	0
															0	0	0
																$\frac{P_i^e + P_j^e}{L}$	0
																	$\frac{P_i^e + P_j^e}{L}$

symmetric

Appendix B

CFTFiber Program Verification

This appendix provides examples which verify the accuracy of the second-order finite element formulations employed in the computer program CFTFiber. The 12 degree-of-freedom (DOF) beam element used to model wide-flange members, and the 18 DOF beam element with slip used to model CFT members are evaluated using comparisons to benchmark problems. This Appendix presents verification of the geometrically nonlinear, materially elastic analysis capabilities of the program, but an additional verification problem is presented for verification of the 12 DOF steel beam element which includes material nonlinearity.

A variety of planar frame systems are examined under loading which induces geometrically nonlinear behavior. The results of the analyses are compared to benchmark test problems from Clark, et al. (1993) who presented the solutions to planar elastic buckling problems based on the solution to stability functions, and Mattiasson (1981) who solved large deflection elastica problems using elliptical integrals.

B.1 12 DOF Steel Element Verification

The 12 DOF beam finite element formulation, adapted from White (1986) and Yang and Kuo (1994) is used in this work to model the behavior of steel wide-flange sections. This element employs 3 translational and 3 rotational DOFs at each end node.

B.1.1 Geometric Nonlinear Analysis

Example problems are presented which test the accuracy of both the geometric nonlinear matrix formulation and the incremental/iterative Newton-Raphson solution scheme employed by CFTFiber. For the following analyses, all members are assumed to have linear elastic material, and to be doubly symmetric, and prismatic. Geometrically nonlinear effects which are modeled include the P-Δ effect (member chord rotation), the P-δ effect (member curvature), and changing length due to axial shortening. Axial shortening caused by member curvature (the *bowing effect*) is not modeled by CFTFiber. The effect of element discretization, incremental solution algorithms, and load step size are investigated.

B.1.1.1 Detection of Euler Buckling

An important characteristic of the geometrically nonlinear formulation is the ability to accurately determine the point at which a member becomes unstable and buckles. The two problems presented in this section test the ability of the 12 DOF beam element to detect the elastic Euler buckling load. Figure B.1a shows an axially loaded cantilever and Figure B.1b shows a simply-supported column. Both columns are loaded with a concentric axial load with no initial imperfections in the members.

The buckling loads for these cases are given by:

a) $$P_{cr} = \frac{\pi^2 EI}{(2L)^2} \tag{B.1}$$

b) $$P_{cr} = \frac{\pi^2 EI}{L^2} \tag{B.2}$$

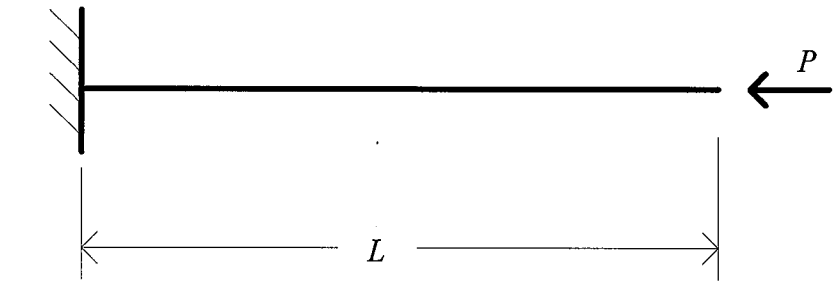

a) Fixed-Free Column

$E = 200$ Gpa

$I = 4.16 \times 10^7$ mm^4

$A = 6.45 \times 10^6$ mm^2

$L = 3.05 \times 10^3$ mm

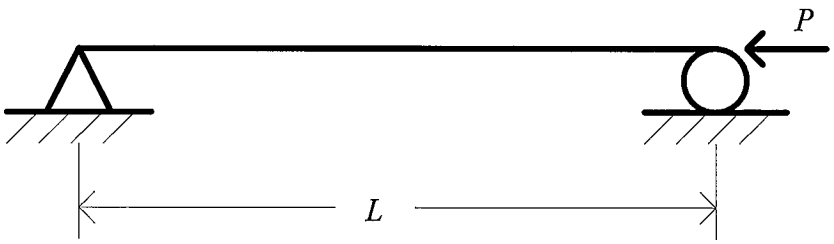

b) Simply-Supported Column

Figure B.1. Euler Columns

Table B.1 compares the computational and analytical buckling loads for each case shown above for 1, 3, and 5 elements per column. In the computational solution, the buckling load is defined as the load at which a limit point is detected. White and Hajjar (1991) state that three elements are sufficient to model the buckling load for both cases with a geometrically nonlinear formulation similar to that used in this work. The current computational formulation using 3 or more elements per column predicts the Euler buckling load with excellent accuracy.

Table B.1. Euler Buckling Loads (in kN)

	Fixed-Free Column	Simply-Supported Column	% error Fixed-Free	% error Simply-Supported
Theory	2210	8841	--	--
1 elem	2227	10755	0.76%	22.0%
3 elems	2211	8856	0.016%	0.17%
5 elems	2210	8844	0.0060%	0.030%

B.1.1.2 Two Span Beam-Column

A two span beam-column with axial load and symmetric transverse point loads at the midpoints of the beams is shown in Fig. B.2. This problem may assume two possible buckled shapes, as indicated in Fig. B.2. The buckling load for the mode with perfect symmetry about the center support is 16164 kN, whereas the asymmetric mode (lower energy mode) has a critical buckling load of 7904 kN. Due to numerical rounding which occurs during analysis and the asymmetric support conditions, the asymmetric mode is always detected if the structure is not fixed against rotation at the center support.

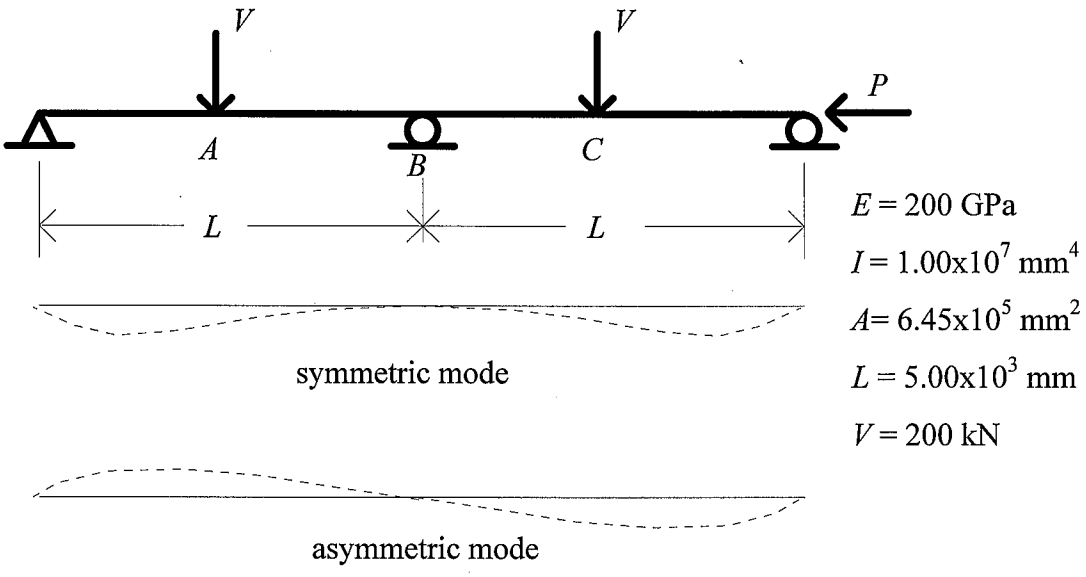

Figure B.2. Two Span Beam-Column with Buckling Modes

The analysis is performed using a total of eight elements (four in each span) and a constant axial load increment (ΔP = 2.0 kN). The transverse load is applied first, and then the axial load is increased linearly. The incremental/iterative Newton-Raphson solution strategy is used. The program detects a limit point at P = 7886 kN (0.2% error), and the deformed shape conforms to the asymmetric buckling mode. Table B.2 shows

the results of the analysis compared with the results of a stability function analysis of the problem for different levels of axial force (Clarke, et al., 1993).

Table B.2. Two Span Beam-Column

	Stability Function Analysis Results CFTFiber Results Percent Error				
P (kN)	v_a (mm)	v_c (mm)	M_b (kN-m)	M_a (kN-m)	M_c (kN-m)
2000	12.88	12.88	207.4	172.1	172.1
	12.73	12.73	207.4	172.2	172.2
	1.18%	1.18%	0.0%	0.07%	0.07%
4000	14.88	14.88	233.4	192.8	192.8
	14.50	14.50	232.4	192.2	192.2
	2.56%	2.56%	0.38%	0.29%	0.29%
6000	17.63	17.63	269.1	221.1	221.1
	16.89	16.89	265.9	219.0	219.0
	4.18%	4.18%	1.18%	0.97%	0.97%

B.1.1.3 Cantilever With Lateral and Axial Load

This example tests the behavior of a cantilever beam under axial compression and lateral loading. This loading induces P-Δ and P-δ effects in the beam. This problem tests the accuracy of the internal force computation as well as deformations. The transverse tip deflection and base moment are compared to the stability function solution given in Clarke et al. (1993). Figure B.3 illustrates the cantilever beam-column and applied loads. The transverse load V is held constant for the analysis, and the axial load is increased linearly, with a constant axial load increment of $\Delta P = 2.5$ kN. The incremental/iterative Newton-Raphson solution scheme is employed in this set of analyses.

The results shown in Table B.3 indicate a reduction in accuracy with increasing axial load, a trend which has been observed by other researchers (Gourley and Hajjar, 1994). This trend is observed for the current analysis, but the inaccuracy remains small, partially due to the small axial load increment. The last row of Table B.3 demonstrates

that a 100X increase in the size of the load step reduces the accuracy of the analysis, but only slightly. The data also indicates an increase in accuracy for a greater number of elements, although this trend is only noticeable for higher values of axial load.

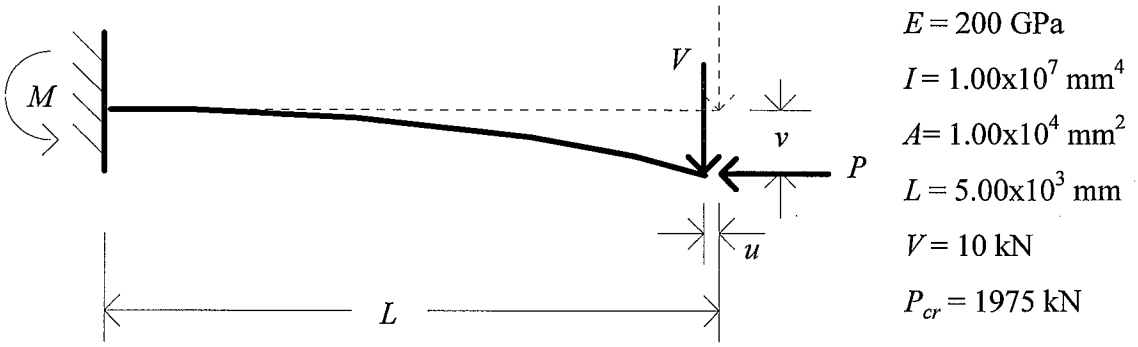

Figure B.3. Cantilever with Transverse and Axial Load

Table B.3. Cantilever Moments and Deflections

		CFTFiber Results Percent Error		
P (kN)	# elements	u (mm)	v (mm)	M (kN-m)
250	stability funct.	0.691	23.80	55.96
	3	0.693 -0.368	23.84 -0.149	56.05 -0.170
	5	0.693 -0.368	23.88 -0.342	56.06 -0.192
500	stability funct.	1.341	27.78	63.89
	3	1.344 -0.189	27.75 0.119	63.98 -0.136
	5	1.346 -0.379	27.86 -0.302	64.03 -0.228
750	stability funct.	2.009	33.38	75.02
	3	2.009 0.000	33.24 0.434	75.04 -0.032
	5	2.014 -0.253	33.47 -0.259	75.21 -0.261

Table B.3. (cont'd)

		CFTFiber Results Percent Error		
P (kN)	# elements	u (mm)	v (mm)	M (kN-m)
1000	stability funct.	2.710	41.83	91.81
	3	2.710 0.000	41.52 0.753	91.65 0.175
	5	2.718 -0.281	41.94 -0.255	92.07 -0.287
1250	stability funct.	3.510	56.09	120.1
	3	3.498 0.362	55.45 1.15	119.5 0.513
	5	3.513 -0.072	56.25 -0.290	120.5 -0.327
1500	stability funct.	4.641	85.27	177.9
	3	4.600 0.876	83.91 1.60	176.1 1.00
	5	4.648 -0.164	85.65 -0.450	178.7 -0.473
1750	stability funct.	8.280	178.1	361.7
	3	8.072 2.52	175.1 1.69	357.0 1.31
	5	8.372 -1.10	180.7 -1.47	366.8 -1.43
	5 ($\Delta P = 250$ kN)	8.402 -1.47	181.4 -1.87	368.0 -1.76

B.1.1.4 Large Deflection Cantilever Beam Example

This verification of the geometrically nonlinear formulation consists of a cantilever beam subjected to a concentrated transverse tip load (Fig B.4.). This problem is intended to demonstrate the accuracy of the formulation for large deformations. The elastica solution is presented by Mattiasson (1981), who used elliptical integrals to obtain results for large deformation problems. The theoretical solution ignores elongation of the

element due to axial loading. Some error is introduced in the finite element formulation by assuming a finite value for the axial rigidity of the elements.

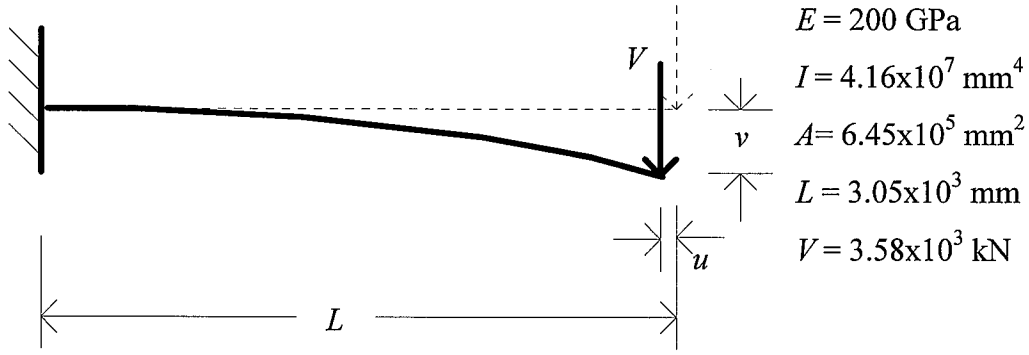

Figure B.4. Cantilever Beam with Transverse Tip Load

Table B.4 shows the analysis results for 3 or 5 elements using either 100 or 1000 load increments with a simple-step incremental solution scheme. Results for an incremental/iterative Newton-Raphson solution scheme using 50 and 100 solution steps are also presented. The final row of Table B.4 presents the solution for the problem when a much higher cross-sectional area ($A = 6.45x10^7$ mm^2). For this example, 5 elements are used along the length. It is important to note that the higher value of area causes numerical errors to occur in the force-recovery procedure unless a very small step size is used. Three hundred steps were required in order to achieve a solution without large, accumulating numerical errors, and four hundred steps were required to achieve results with comparable accuracy to the other examples in the table.

Additional elements or load increments do not add significant accuracy to the analysis. The updated Newton-Raphson solution scheme using 100 steps provides significant improvement over the simple-step strategy using 1000 steps.

The results in Table B.4 indicate that finite element analysis of large deflection problems does not yield solutions which are as accurate as Euler buckling analysis or small deflection problems, due primarily to simplifying assumptions made in the finite element formulation. For the finite element solutions given in Table B.4, an increasing

number of elements does not generally increase the accuracy of the analysis. This may also be attributed to the assumption of small deflections in the finite element formulation.

Table B.4. Cantilever Tip Deflections

(*e* is the distance from the theoretical tip location)

Discretization	*v/L*	*u/L*	% error *(v/L)*	% error *(u/L)*	Total # of matrix factorizations	*e/L*
Theory	0.6700	0.3289	--	--		--
Simple Step Solution Scheme						
3 elems, 100 steps	0.6952	0.3439	3.76	4.56	100	0.0183
3 elems, 1000 steps	0.7090	0.3717	5.82	13.01	1000	0.0261
5 elems, 100 steps	0.6975	0.3598	4.10	9.40	100	0.0221
5 elems, 1000 steps	0.7036	0.3731	5.01	13.4	1000	0.0255
Newton-Raphson Solution Scheme						
3 elems, 50 steps	0.6849	0.3250	2.22	-1.19	179	0.0096
3 elems, 100 steps	0.7040	0.3610	5.07	9.76	300	0.0235
5 elems, 50 steps	0.6962	0.3567	3.91	8.45	179	0.0212
5 elems, 100 steps	0.7016	0.3688	4.72	12.13	300	0.0244
Simple Step Solution Scheme, $A = 6.45 \times 10^{7}$ mm^2						
5 elems, 400 steps,	0.6859	0.3366	2.37	2.34	400	0.0140

Figure B.5 shows the deformed shape of the member drawn to scale for the case of 5 elements and 100 load steps using the incremental/iterative Newton-Raphson procedure. This figure indicates the extreme deformation of the member under the applied loading. Also shown is the theoretical tip location according to the elastica solution from Mattiasson (1981). Since this level of deformation is not expected in the current research, these results are assumed to be sufficient for analysis of members which undergo moderate rigid body motion.

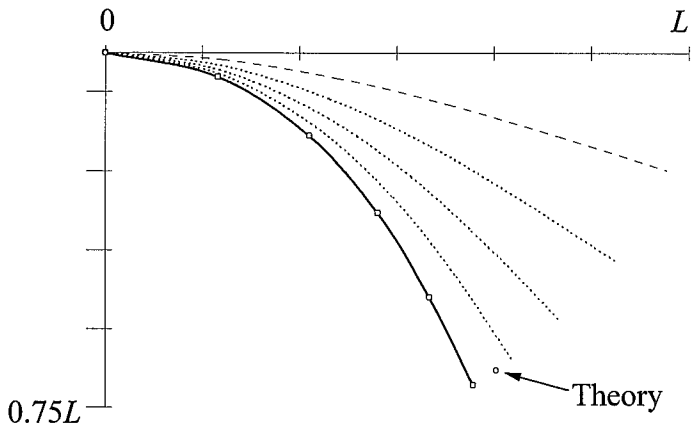

Figure B.5: Deflected Shape of the Cantilever Beam

B.1.1.5 Harrison Portal Frame

The rectangular portal frame with pinned base shown in Figure B.6 has been used as a benchmark problem for testing second-order elastic analysis (Clarke et al., 1993). An analysis of the frame was conducted using three elements per column and three elements for the girder. The results of the analysis using the incremental/iterative Newton-Raphson solution scheme and a constant load increment of $\Delta V = 0.4448$ kN are compared to the stability function analysis solution from Clarke et al. (1993) in Table B.5. Horizontal sway at the point where the horizontal load is applied, as well as the maximum moment in the structure, are compiled.

Table B.5 shows the accuracy of the geometric nonlinear formulation employed by CFTFiber. The results compare well with the stability function analysis, even for the small number of elements used. As the loads increase, the error becomes larger, indicating an accumulating error. The final row of Table B.5 shows the analysis using a much larger load increment. The larger load increment does not appear to affect the solution accuracy. Again this demonstrates the accuracy of the incremental/iterative Newton-Raphson solution technique.

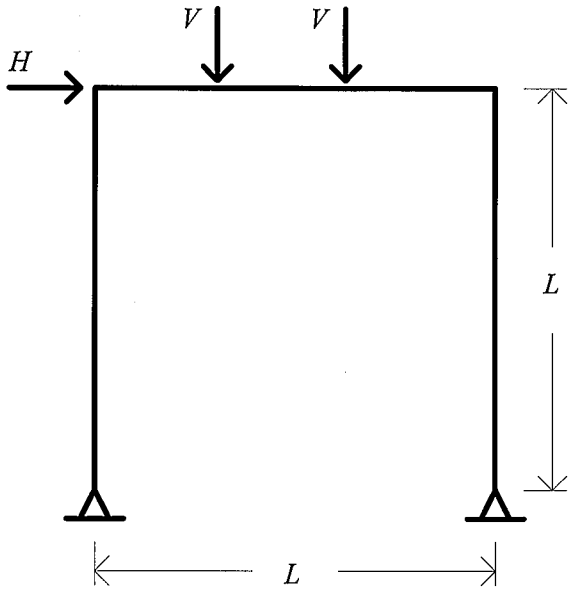

$E = 207$ GPa

$I = 4.16\text{x}10^7$ mm^4

$A = 6.45\text{x}10^3$ mm^2

$L = 7.64\text{x}10^3$ mm

$V = 100H$

$H = 0.4448, 0.8896, 1.3344,$
$1.7792, 2.224$ kN

Figure B.6. Harrison Portal Frame

Table B.5. Frame Sway and Maximum Moment

	Stability Function Analysis CFTFiber Results Percent Error	
V (kN)	Sway (mm)	M_{max} (kN-m)
44.48	7.214 7.163 0.707%	69.04 69.04 0.000%
88.96	18.62 18.44 0.967%	139.4 139.3 0.001%
133.44	38.02 37.54 1.26%	211.7 211.4 0.109%
177.92	77.47 76.15 1.70%	286.6 286.2 0.119%
222.40	205.8 200.3 2.65%	370.5 369.7 0.216%
222.40 (ΔV = 8.896 kN)	205.8 200.3 2.65%	370.5 369.7 0.216%

B.1.2 12 DOF Steel Beam Element Material and Geometric Nonlinear Analysis Verification

Chen and Toma (1994) present a discussion of verification for advanced analysis finite element formulations which model the behavior of steel frames. They suggest which significant geometric and material phenomena are practical to model in advanced analysis software. The program CFTFiber includes the major attributes for steel wide-flange members which are discussed by Chen and Toma, including geometrically nonlinear analysis, material nonlinearity with path-dependent materials, and residual stresses.

Chen and Toma (1994) also discuss the criteria for calibration problems which can be used to verify advanced analysis software. They present an analysis by White (1986) for a single bay portal frame which includes spread of plasticity fiber analysis, geometric nonlinearity, and residual stresses. The finite element mesh is provided, as well as detailed information on loading and material models. CFTFiber has the capability to closely model this frame up to the structural limit point. This problem will be used as a final verification problem for the 12 DOF steel beam element to demonstrate materially and geometrically nonlinear capabilities of CFTFiber.

Figure B.7 shows the relevant finite element meshing and properties for the problem. Figure B.8 shows the fiber mesh and residual stress pattern used.

Figure B.9 shows a comparison of the computational results from CFTFiber with White's results (White, 1986) (using no rigid links in White's analysis). The results of the current analysis compare well with the solution according to White. The discrepancy in maximum load and initial elastic slope may be attributed to the modeling of fillets in the cross-section of the wide-flange beams in CFTFiber. White did not include fillets in the cross-section grid. An additional data series in Figure B.9 shows that the current computational model provides nearly identical results to White's model when the fillets are removed from the cross-sectional grid. Also, the force recovery scheme employed in CFTFiber differs slightly from White (1986) in the way that high order geometrically nonlinear terms are accounted for. The materially nonlinear analysis in CFTFiber for this

example employs Prager's model for steel with an initial slope of 200 GPa and a strain hardening slope of 690 MPa. Chen and Toma (1994) (from which White's data was scaled) suggest that White used the same material model

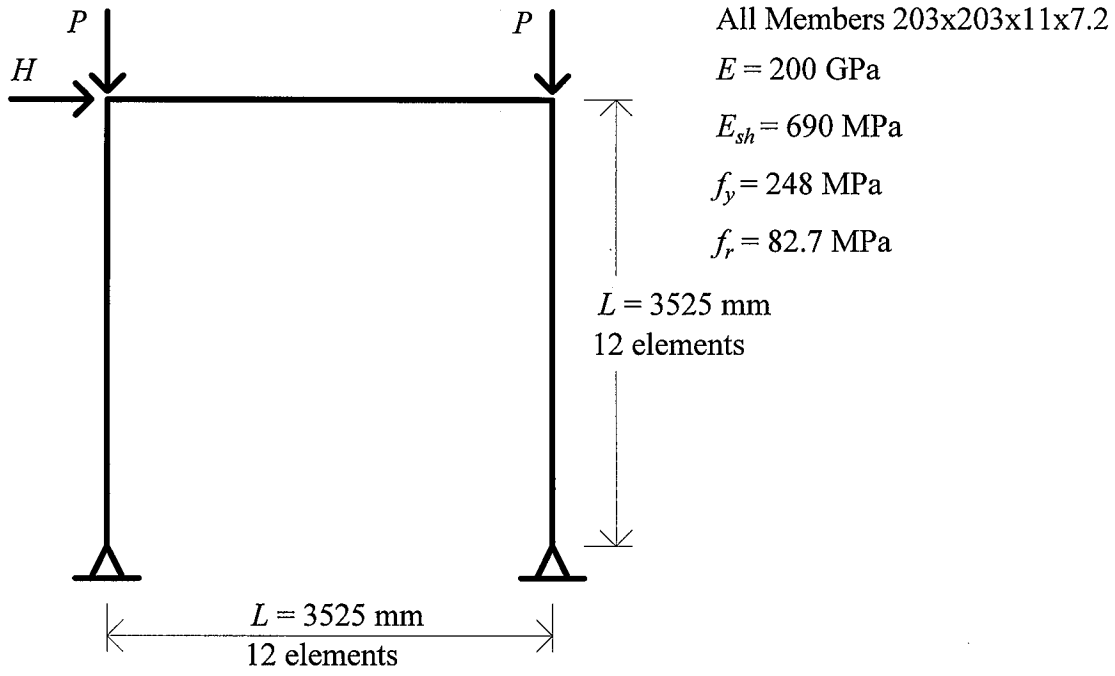

Figure B.7. Calibration Frame (White, 1986)

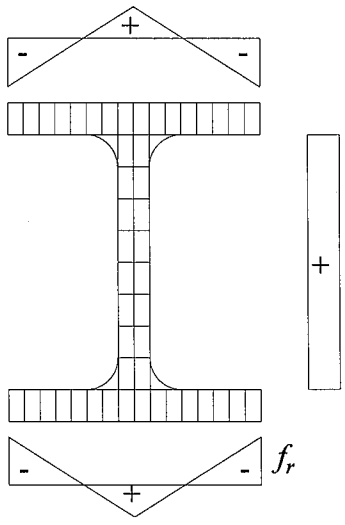

Figure B.8. Fiber Mesh and Residual Stress Pattern (White, 1986)

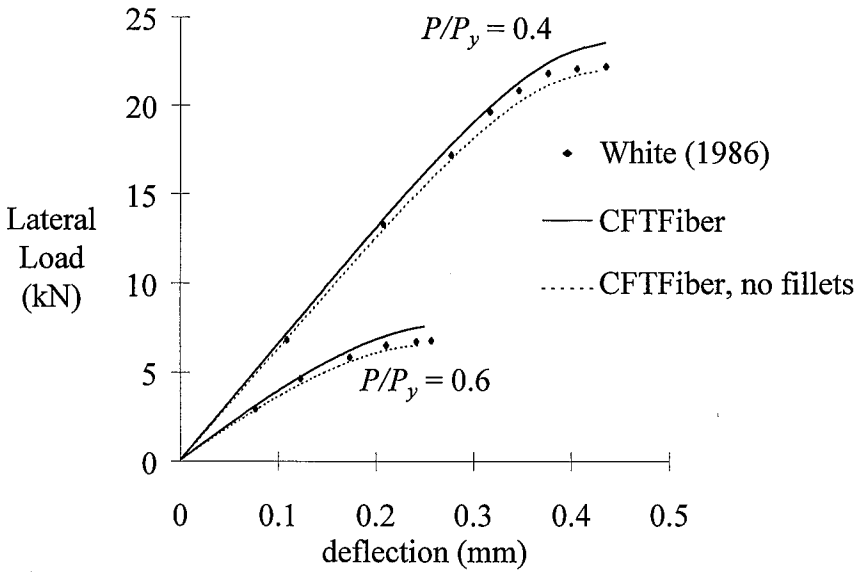

Figure B.9. Comparison with Portal Frame from (White, 1986)

B.2 18 DOF CFT Element Geometrically Nonlinear Analysis Verification

The 18 DOF formulation has been presented in Chapter 2 and Appendix A. In order to verify the geometrically nonlinear stiffness formulation, elastic material behavior is assumed for both steel and concrete. The exact problems for Section B.1.1 can be replicated with the 18 DOF element by adjusting the material properties of the 18 DOF elements so that their axial and bending rigidity are the same as the corresponding 12 DOF wide-flange element. In the following example problems, the effect of separate materials is tested by adjusting the ratio of concrete-to-steel rigidity from approximately 0.5 to approximately 0.0. The ratio 0.0 permits modeling of hollow steel tube beam-columns. This modeling uses the 18 DOF element stiffness matrix with very low axial and bending rigidity assigned for the concrete. Use of the hollow tube section serves to verify the steel portion of the stiffness formulation. In all the analyses, slip is prevented between the steel and concrete at each joint through the use of penalty functions as described in Section 2.2.2.

B.2.1 Detection of Euler Buckling

The two problems presented in this section test the ability of the 18 DOF beam element to detect the elastic Euler buckling load. Figure B.1a in Section B.1.1.1 shows an axially loaded cantilever and Figure B.1b shows a simply-supported column. Both columns are loaded with a concentric axial load with no initial imperfections in the members. For the 18 DOF CFT element, the bending rigidity EI can be estimated as the sum of the steel and concrete bending rigidity. For both of the column configurations, the bending rigidity of the steel and concrete portions of the columns are adjusted as shown in Table B.6 to test the accuracy of the finite element formulation and to determine if the separate materials have any effect on the accuracy of the results.

Table B.6. Material Properties for Euler Buckling Example

	EI^s / EI^{tot}	EI^c / EI^{tot}	EA^s / EA^{tot}	EA^c / EA^{tot}
Case I	1.0	0.0	1.0	0.0
Case 2	0.5	0.5	0.999914	0.000086

Table B.7 compares the computational and analytical buckling loads for the two configurations with 1, 3, and 5 elements per column. The current 18 DOF finite element formulation using 3 or more elements per column predicts the Euler buckling load with excellent accuracy. There is no effect in the accuracy of the solutions when the proportion of rigidity for the steel and concrete is changed.

Table B.7 Euler Buckling Loads (in kN)

	Fixed-Free Column	Simply-Supported Column	%error Fixed-Free	%error Simply-Supported
Theory	2210	8841	--	--
Case I Material Properties				
1 elem	2227	10751	0.769%	21.6%
3 elems	2210	8855	0.012%	0.158%
5 elems	2210	8843	0.004%	0.025%
Case II Material Properties				
1 elem	2227	10751	0.769%	21.6%
3 elems	2210	8855	0.012%	0.158%
5 elems	2210	8843	0.004%	0.025%

B.2.2 Two Span Beam-Column

A two span beam-column with axial load and symmetric transverse point loads at the midpoints of the beams is shown in Figure B.2 of Section B.1.1.2. This problem may assume two possible buckled shapes, with the lower energy mode having a critical buckling load of 7904 kN. Two cases similar to those presented in the previous section are again used to determine the effect of the steel and concrete portions of the element stiffness matrices. The material properties for each case are shown in Table B.8.

Table B.8. Material Properties for Two Span Beam-Column Example

	EI^s / EI^{tot}	EI^c / EI^{tot}	EA^s / EA^{tot}	EA^c / EA^{tot}
Case I	1.0	0.0	1.0	0.0
Case 2	0.5	0.5	0.99866	0.00134

The analysis is performed using a total of eight 18 DOF CFT elements (four in each span) and a constant axial load increment (ΔP = 2.0 kN). The transverse load is applied first, and then the axial load is increased linearly. The incremental/iterative

Newton-Raphson solution strategy is used. The program detects a limit point at P = 7886.3 kN (0.2% error), and the deformed shape conforms to the asymmetric buckling mode. Table B.9 shows the results of the analysis for both cases compared with the results of a stability function analysis of the problem for different levels of axial force (Clarke, et al., 1993). The results of CFTFiber show excellent accuracy when compared with the results of the stability analysis. There is no difference in results between the two cases from Table 8.

Table B.9. Two Span Beam-Column

	Stability Function Analysis Results CFTFiber Results Percent Error				
P (kN)	v_a (mm)	v_c (mm)	M_b (kN-m)	M_a (kN-m)	M_c (kN-m)
Case I Material Properties					
2000	12.88	12.88	207.4	172.1	172.1
	12.73	12.73	207.4	172.2	172.2
	1.18%	1.18%	0.0%	0.07%	0.07%
4000	14.88	14.88	233.4	192.8	192.8
	14.50	14.50	232.4	192.2	192.2
	2.56%	2.56%	0.38%	0.29%	0.29%
6000	17.63	17.63	269.1	221.1	221.1
	16.89	16.89	265.9	219.0	219.0
	4.18%	4.18%	1.18%	0.97%	0.97%
Case II Material Properties					
2000	12.88	12.88	207.4	172.1	172.1
	12.73	12.73	207.4	172.2	172.2
	1.18%	1.18%	0.0%	0.07%	0.07%
4000	14.88	14.88	233.4	192.8	192.8
	14.50	14.50	232.4	192.2	192.2
	2.56%	2.56%	0.38%	0.29%	0.29%
6000	17.63	17.63	269.1	221.1	221.1
	16.89	16.89	265.9	219.0	219.0
	4.18%	4.18%	1.18%	0.97%	0.97%

B.2.3 Cantilever With Lateral and Axial Load

This example tests the behavior of a cantilever beam under axial compression and lateral loading. Figure B.3 of Section B1.1.3 illustrates the cantilever beam-column and applied loads. Again, the relative rigidity of the steel and concrete portions of the elements are varied to test the effect each has on the computational results (Table B.8). In each analysis, the transverse load V is held constant, and the axial load is increased linearly, with a constant axial load increment of $\Delta P = 2.5$ kN. The incremental/iterative Newton-Raphson solution scheme is employed in this set of analyses.

Table B.10. Material Properties for Cantilever Beam Example

	EI^s / EI^{tot}	EI^c / EI^{tot}	EA^s / EA^{tot}	EA^c / EA^{tot}
Case I	1.0	0.0	1.0	0.0
Case 2	0.5	0.5	0.146	0.854

Table B.11 shows the analysis results for case I. The results for case II show only slight differences compared to case I and are therefore omitted from the table. These results are also identical to the results for the 12 DOF element which has the same rigidity as the 18 DOF CFT element (See Table B.3 in Section B.1.1.3).

Table B.11. Cantilever Moments and Deflections

		CFTFiber Results Percent Error		
P (kN)	# elements	u (mm)	v (mm)	M (kN-m)
250	stability funct.	0.691	23.80	55.96
	3	0.693 -0.368	23.84 -0.149	56.05 -0.170
	5	0.693 -0.368	23.88 -0.342	56.06 -0.192

Table B.11. (cont'd)

		CFTFiber Results Percent Error		
P (kN)	# elements	u (mm)	v (mm)	M (kN-m)
500	stability funct.	1.341	27.78	63.89
	3	1.344	27.75	63.98
		-0.189	0.119	-0.136
	5	1.346	27.86	64.03
		-0.379	-0.302	-0.228
750	stability funct.	2.009	33.38	75.02
	3	2.009	33.24	75.04
		0.000	0.434	-0.032
	5	2.014	33.47	75.21
		-0.253	-0.259	-0.261
1000	stability funct.	2.710	41.83	91.81
	3	2.710	41.52	91.65
		0.000	0.753	0.175
	5	2.718	41.94	92.07
		-0.281	-0.255	-0.287
1250	stability funct.	3.510	56.09	120.1
	3	3.498	55.45	119.5
		0.362	1.15	0.513
	5	3.513	56.25	120.5
		-0.072	-0.290	-0.327
1500	stability funct.	4.641	85.27	177.9
	3	4.600	83.91	176.1
		0.876	1.60	1.00
	5	4.648	85.65	178.7
		-0.164	-0.450	-0.473
1750	stability funct.	8.280	178.1	361.7
	3	8.072	175.1	357.0
		2.52	1.69	1.31
	5	8.372	180.7	366.8
		-1.10	-1.47	-1.43
	5	8.402	181.4	368.0
	(ΔP = 250 kN)	-1.47	-1.87	-1.76

B.2.4 Large Deflection Cantilever Beam Example

This verification of the 18 DOF element geometric nonlinear formulation consists of a cantilever beam subjected to a concentrated transverse tip load (Fig B.4 of Section B.1.1.4). This problem is intended to demonstrate the accuracy of the formulation for large deformations and to test the penalty function technique for imposing shear compatibility between the steel and concrete in the 18 DOF elements. As in the previous sections, two cases are included to study the effect of varying steel and concrete properties on the behavior of the element. Table B.12 gives the material properties for the two cases.

Table B.12. Material Properties for Large Deflection Example

	EI^s / EI^{tot}	EI^c / EI^{tot}	EA^s / EA^{tot}	EA^c / EA^{tot}
Case I	1.0	0.0	1.0	0.0
Case 2	0.5	0.5	0.99138	0.00862

Table B.13 shows the analysis results for 3 or 5 elements using either 100 or 1000 load increments with a simple-step incremental solution scheme. The solution using either case I or II is identical to the solution for the 12 DOF analysis of Section B.1.1.4. This result shows that the 18 DOF element geometrically nonlinear stiffness formulation is equivalent (within computer precision) to the 12 DOF element formulation under materially elastic conditions for a large deflection problem. This is significant because it demonstrates that the penalty function technique for ensuring shear deformation compatibility between the steel and concrete results essentially in the same solution for deflections as the 12 DOF element, even though the penalty function technique is approximate. Also, the method developed for updating the global direction of the penalty functions during geometrically nonlinear analysis remains stable during large deflection problems.

Table B.13. Cantilever Tip Deflections

(*e* is the distance from the theoretical tip location)

Discretization	*v/L*	*u/L*	% error (*v/L*)	% error (*u/L*)	Total # of matrix factorizations	*e*/L
Theory	0.6700	0.3289	--	--		--
Simple Step Solution Scheme: Case I						
3 elems, 100 steps	0.6952	0.3439	3.76	4.56	100	0.0183
3 elems, 1000 steps	0.7090	0.3717	5.82	13.0	1000	0.0261
5 elems, 100 steps	0.6974	0.3597	4.10	9.40	100	0.0221
5 elems, 1000 steps	0.7036	0.3731	5.01	13.4	1000	0.0255
Simple Step Solution Scheme: Case II						
3 elems, 50 steps	0.6952	0.3439	3.76	4.56	100	0.0183
3 elems, 100 steps	0.7090	0.3717	5.82	13.0	1000	0.0261
5 elems, 50 steps	0.6974	0.3597	4.10	9.40	100	0.0221
5 elems, 100 steps	0.7036	0.3731	5.01	13.4	1000	0.0255

B.2.5 Harrison Portal Frame

The rectangular portal frame with pinned base shown in Figure B.10 is analyzed using a combination of 12 DOF steel beam elements and 18 DOF CFT elements. The analysis of the frame is conducted using three CFT elements per column and three steel beam elements for the girder. This problem demonstrates the ability of the analytical formulation to combine 12 and 18 DOF elements in the global structural system while retaining the geometrically nonlinear characteristics of both.

The material characteristics of the elements are given in Table B.14. Note that the equivalent stiffness of the CFT elements (as discussed in Section B.2.1) is the same as the steel beam elements.

Table B.14. Material Properties for Portal Frame Example

	EI^s / EI^{tot}	EI^c / EI^{tot}	EA^s / EA^{tot}	EA^c / EA^{tot}
12 DOF elements	1.0	N.A.	1.0	N.A.
18 DOF elements	0.5	0.5	0.138	0.862

The results of the analysis using the incremental/iterative Newton-Raphson solution scheme and a constant load increment of $\Delta V = 0.4448$ kN are compared to the stability function analysis solution from Clarke et al. (1993) in Table B.15. Horizontal sway at the point where the horizontal load is applied, as well as the maximum moment in the structure, are compiled. Note that the moment in an 18 DOF CFT element is computed as the sum of the moments from the steel and concrete portions of the element.

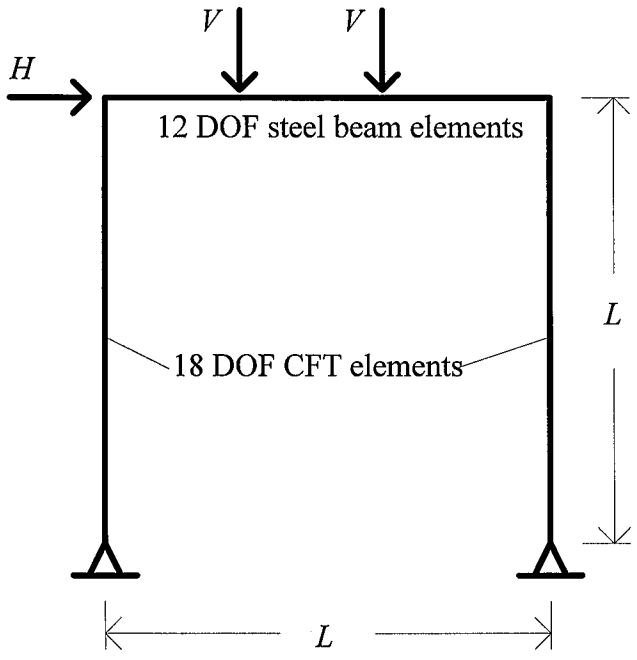

Figure B.10. Harrison Portal Frame

These results shown in Table B.15 are essentially identical to the analysis of the same problem using 12 DOF elements only. This problem demonstrates that the technique for combining 12 and 18 DOF elements remains stable during geometrically

nonlinear analysis, and that the analysis is as accurate as the same analysis using only 12 DOF elements.

Table B.15. Frame Sway and Maximum Moment

	Stability Function Analysis CFTFiber Results Percent Error	
V (kN)	Sway (mm)	M_{max} (kN-m)
44.48	7.214 7.163 0.707%	69.04 69.04 0.000%
88.96	18.62 18.44 0.967%	139.4 139.3 0.001%
133.44	38.02 37.54 1.26%	211.7 211.4 0.109%
177.92	77.47 76.15 1.70%	286.6 286.2 0.119%
222.40	205.8 200.3 2.65%	370.5 369.7 0.216%

B.3 Discussion

This appendix provides verification examples for both the 12 DOF beam finite element and the 18 DOF beam finite element geometrically nonlinear formulations. The example problems demonstrate the accuracy of the two formulations under various geometrically nonlinear conditions including Euler buckling, moderate and large flexural deflections, and deflections of indeterminate frame structures. An example problem is presented which demonstrates the accuracy of the current formulation for combined

materially and geometrically nonlinear analysis of an indeterminate structure composed of 12 DOF wide-flange beam-column elements.

The verification problems indicate that the 18 DOF formulation is essentially equivalent to a comparable 12 DOF formulation under the conditions of materially elastic and geometrically nonlinear analysis, assuming perfect bond between the steel and concrete. In addition, the composite structural frame of Section B.2.5 demonstrates that a structure made up of both 12 and 18 DOF elements behaves identically to the same configuration made up of 12 DOF elements only. The large deflection problem of Section B.2.4 provides verification of the penalty function method for ensuring shear compatibility between the steel and concrete under large deflection geometrically nonlinear conditions.

For all problems, the error measured between the analysis and published solutions is small if a sufficient number of elements and load steps are used. Sources of error include simplifications made during formulation of the stiffness matrices and force recovery procedures (as discussed in Chapter 2), and comparison of analysis which use finite axial rigidity with theoretical solutions that assume infinite axial rigidity.

Appendix C

Key Features of the Computer Implementation (CFTFiber)

This Appendix includes a brief description of the features of the software implementation of the program CFTFiber for the materially and geometrically nonlinear finite element formulation presented in this work. A sample input file is also presented in Table C.1.

The program input file is divided into a number of sections which may be sorted in any order. Each section begins with a section header which is initiated with an asterisk (*).

The program requires the input of the global nodes and nodal restraints. If 18 DOF CFT finite elements are used, the program assumes that the concrete is free to translate at an end that is either free or fixed against translation. In order to restrain the slip between the steel and concrete at a structural node, a separate section is included in the input file under the heading *B_SLIP_RESTRAINTS. In this section, the global nodes which are to have slip restrained are specified, and the global direction of restraint is input for each of these nodes.

The input file also contains a listing of cross sections used in the meshing, and any number of cross sections can be input under the headings *B_CFT_XS for CFT cross sections, and *B_STL_XS for steel cross sections. The cross sections do not all have to be used, but will require some dynamic storage space in the computer. The program accesses the AISC database of manufactured structural shapes, so that the user need only

input a section designation, e.g., W14x53, and the section properties are automatically input. In addition to the section designation, the material properties of the section are required. These include material strength, elastic modulus, and plasticity information. For the CFT cross sections, the bond strength and initial slip stiffness are also specified for each cross-section. The material parameter input line is material model specific. The current computer implementation includes the Shen steel model as discussed in Chapter 4, and also includes the Prager model (Prager, 1956), a single surface plasticity model which includes linear kinematic hardening. This model is more computationally efficient than the Shen steel model, and may be used when a lower degree of accuracy is acceptable. The final line for each cross-section is the element discretization used for the fiber element mesh. For a CFT cross-section, this line contains the discretization for the steel tube and the concrete core as shown in Fig. C.1. The inside corner radius for the tube is assumed to be equal to the wall thickness (AISC, 1994). For a steel wide-flange cross-section, the fillets are included in the discretization, with each fillet composing a single fiber, and the webs and flanges are discretized as shown in Fig. C.1. The listing of cross sections allows the same type of cross-section to be discretized in a number of ways.

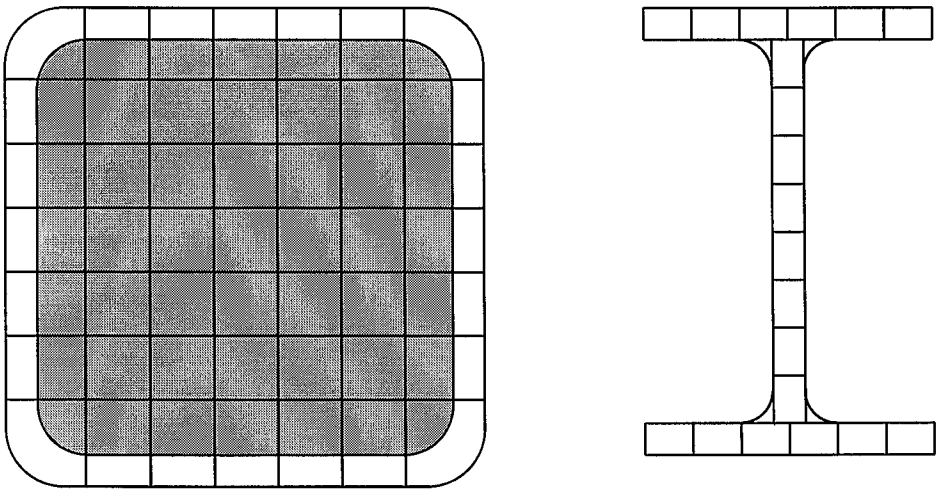

Figure C.1: Fiber Element Discretization

The elements are then input under the heading *B_CFT_ELS and *B_STL_ELS. The element's local x-axis is parallel to its centroidal axis, starting at the i-end. The element definition requires a web vector to be defined in the global coordinate system. For wide-flange beams, this vector is aligned with the element web, perpendicular to the centroidal axis of the member. For a CFT element, the web of the member is assumed to be the longer of the cross-sectional dimensions (for a rectangular cross-section), and the web vector is aligned with the web, perpendicular to the centroidal axis. For both CFT and wide-flange elements, this web vector is considered to be at the i-end of the member, and it establishes the direction of the element's local y-axis. The local element z-axis is considered to be perpendicular to the x and y axes. The element definition also includes the cross-section number from the *B_CFT_XS or B_STL_XS section.

The sections *C_JT_LOAD and *C_LOAD_HIST define the nodal loads and the load history for the structure, respectively. The nodal loads are defined in the global coordinate system, and are always assumed to be applied to the steel portion of the element. The nodal loads are assigned to a specific load history. *C_LOAD_HIST contains the time step, the total time, and the fraction of each load history to be applied at each global time step.

The final section, *C_FLAGS, contains flags which activate or deactivate certain aspects of the program. For example, this section tells the program whether to use the Shen steel model or the Prager steel model for the CFT elements and the steel elements.

Table C.1: Sample Input File for CFTFIBER

```
#2-D portal frame w/ CFT beam-columns (fixed at the base) and steel beam

#*********
*C_START *
#*********


#*******
*C_JTS *
#*******
#Input of the joint coordinates (global structural coordinates)
#Format:
#       Joint number, x coordinate, y coordinate, z coordinate (inches)
#Notes:
#       1) This 2D portal frame is input in global (x, z) coords as recommended
#          in Fig. 1.

1 0.0 0.0 0.0
2 0.0 0.0 100.0
3 100.0 0.0 100.0
4 100.0 0.0 0.0


#*********
*C_JT_RF *
#*********
#List of joint restraints ( 1 = free, 0 = restrained )
#Format:
#       Joint Number, 6 Joint DOFs (XT, YT, ZT, XR, YR, ZR -- See Fig. 2)
#Notes:
#       1) Joints with all DOFs free may be omitted (i.e., joints 2 and 3 below)
#       2) Joints which have 18 DOF CFT elements framing in are assigned 9 DOFs,
#          but the final 3 DOFs are not assigned any restraints.  If you restrain
#          the shear DOFs of an element, you may assume that the concrete shear
#          is automatically restrained also.  If you restrain the axial DOF,
#          YOU ARE NOT restraining the concrete axial deformation.  To restrain
#          the concrete axially, you must assign slip restraints in the section
#          *B_SLIP_RESTRAINTS below.

1 0 0 0 0 0 0
2 1 1 1 1 1 1
3 1 1 1 1 1 1
4 0 0 0 0 0 0

#Alternately, the joint restraints may be entered as:
#1 0 0 0 0 0 0
#4 0 0 0 0 0 0
```

```
#*******************
*B_SLIP_RESTRAINTS *
#*******************
#Joints and global directions for joints with slip prevented
#Format:
#       Joint Number, GLOBAL Restraint Direction (X, Y, Z)
#Notes:
#       1) If the global flag for CFTs is set to no slip, this section must
#          not appear!!! (See C_FLAGS section)
#       2) The joint number should correspond with a joint from the *C_JT
#          section above.  In addition, the joint should be one which has
#          18 DOF CFT elements framing in.
#       3) The restraint should be in global space, and should be a unit vector
#          with three components which is aligned with the CFT element axis.
#       4) These restraints should be used if you are modelling a through-
#          connection, a joint in which the CFT geometry changes, a joint at
#          which mechanical shear connectors are used, a joint at which CFTs
#          frame in from different directions, a column base, or the top of
#          a column where a cover plate is used.
1 0.0 0.0 1.0
2 0.0 0.0 1.0
3 0.0 0.0 1.0
4 0.0 0.0 1.0


#**********
*B_CFT_XS *
#**********
#CFT cross-sections (all data must be in kips and inches)
#Choose either user input format or AISC rectangular tube format
#
#User input format (4 lines per element):
#    line 1: tube depth, tube width, tube thickness, As, Js, Iy of tube,
#            Iz of tube
#    line 2: Steel parameters
#          * DEPENDS ON STEEL MODEL USED!!! See ALSO *C_FLAGS SECTION
#          - if PRAGER model is used: Fy, Fu, Es, Poisson's ratio, Esh,
#            Fy in corners, Fu in corners, Esh in Corners.
#            You may omit the last three parameters if you want the same
#            Fy, Fu, and Esh in the corners as in the rest of the tube.
#          - if SHEN model is used: Fy, Fu, Es, Poisson's ratio, Plastic
#            strain at the end of the yield plateau (use 0.017 if you don't
#            know what this means), Yield in cyclic loading (use 0.191 if
#            you don't know what this means), Initial value of bounding
#            modulus (Similar to Esh, use 260.0 as default),
#            initial radius of the plastic strain space surface (0.0004
#            is the default value for the flats) -- If the corners are
#            different than the flats, input the following 4 values:
#            Fy in corners, Fu in corners, Esh in Corners.
#            initial radius of the plastic strain space surface in the
#            corners (0.0006 is the default value for the corners)
#            You may omit the last three parameters if you want the same
#            Fy, Fu, and Esh in the corners as in the rest of the tube.
#            The Fy, Fu, Esh value is linearly interpolated.
#    line 3: Concrete and Slip parameters (2-6 numbers on one line)
#           fc', Slip stiffness at end i, Slip stiffness at end j,
#           bond strength, initial concrete elastic modulus, strain
#           at peak concrete compressive strength.
#           The last 4 parameters may be omitted if default values are
#           desired.  Use slip stiffness of 1450, bond strength of 0.79
#           if you don't know what this means. If only 2 values are
#           read, the program uses the default values and assumes Kslip
#           at the i-end = Kslip at the j-end.
#    line 4: Discretization grid (10 numbers on one line)
#            # of fibers in steel flange through-thickness direction,
#           # of fibers in steel flange in width-direction,
```

```
#           # of fibers in steel web in depth-direction,
#           # of fibers in steel web through-thickness direction.
#       (The next four discretization parameters refer to the concrete
#        which lies within "t" [the corner radius dimension] of the
#        steel tube walls):
#           # of fibers along flange through-thickness direction,
#           # of fibers along flange in width-direction,
#           # of fibers along web through-thickness direction.
#           # of fibers along web in depth-direction,
#       (The next two discretization parameters refer to the concrete
#        which lies inside core of the section.  This region has
#        dimensions (depth - 4*thickness) x (width - 4*thickness) )
#           # of fibers in core in depth-direction,
#           # of fibers in core in width-direction.
#AISC W-setion format (4 lines per element):
#    line 1: section designation (e.g., TS10x10x1/4)
#    lines 2, 3, and 4: Same as User Input format
#
#Notes:
#       1) Section designation must begin with 'TS' and contain no spaces
#       2) Input for each element may be separated by a blank line
#       3) The CFT cross-sections are automatically numbered beginning
#          with 1 as the first cross-section listed, and continuing in
#          ascending order as listed in this section.
#       4) The cross-sections are automatically number in the order that
#          they appear.
#       5) The sample input line below uses the Prager steel model.
TS6x6x1/4
36 58 29000 0.3 300
5.0 1000.0
2 4 2 4 1 4 1 4 4 4


#***********
*B_CFT_ELS *
#***********
#CFT elements
#
# input format (1 line per element):
#    line 1: CFT element number, i-end, j-end, cross-section number,
#            i-end web vector (x, y, z)
#
#
#Notes:
#       1) I-end unit vector is the orientation of the major axis of the element
#          in GLOBAL coords (based on the orientation in *C_JTS)
#       3) Input for each element may be separated by a blank line
#       4) The CFT elements should be numbered beginning with 1, even if there
#          are steel elements, which must be numbered beginning with 1 also.
1 1 2 1 1.0 0.0 0.0
2 3 4 1 1.0 0.0 0.0
```

```
#**********
*B_STL_XS *
#**********
#Steel cross sections
#Choose either user input format or AISC W-section format
#
#User input format (3 lines per cross-section):
#    line 1: depth, flange width, flange thickness,
#            web thickness, fillet radius, area, Iy, Iz, J
#    line 2: STeel Parameters:
#           DEPENDS ON STEEL MODEL USED!!! SEE ALSO *C_FLAGS SECTION
#           If PRAGER Steel Model is Used:
#           - Fy, Fu, FR (residual stress), Elastic modulus, strain hardening
#              modulus, Poisson's ratio.
#           If SHEN Steel Model is Used:
#           - Fy, Fu, Fr (residual stress), Elastic modulus, Poisson's ratio,
#             plastic strain at the end of the yield plateau (use 0.017 if you
#             don't know what this means), Yield in cyclic loading (use 0.191 if
#             you don't know what this means), Esh (use 260.0 as default),
#             initial radius of the plastic strain surface (use 0.0 if you
#             don't know what this means).  The last parameter may be omitted.
#    line 3: # of fibers in flange in width-direction,
#            # of fibers in flange through-thickness direction,
#            # of fibers in web in depth-direction,
#            # of fibers in web through-thickness direction.
#
#AISC W-setion format (2 lines per element):
#    line 1: section designation (e.g., W14x53)
#    lines 2 and 3: Same as user input format
#
#Notes:
#       1) Section designation must begin with 'W' and contain no spaces
#       2) Input for each element may be separated by a blank line
#       3) The steel cross-sections are automatically numbered beginning
#          with 1 as the first cross-section listed, and continuing in
#          ascending order as listed in this section.
#
W10x45
36 58 0.0 29000 300 0.3
4 2 10 2


#***********
*B_STL_ELS *
#***********
#Steel elements
#Choose either user input format or AISC W-section format
#
#User input format (1 line per element):
#    line 1: Steel elem #, i-end, j-end, steel cross-section number,
#            i-end vector coords (x, y, z)
#
#Notes:
#       1) i-end vector is the vector denoting the orientation of the major
#          axis of the element at the i-end of the member in GLOBAL coords.
#       2) Input for each element may be separated by a blank line
#       3) The steel elements should be numbered beginning with 1, even if there
#          are CFT elements, which must be numbered beginning with 1 also.

1 2 3 1 0.0 0.0 1.0
```

```
#************
*C_JT_LOADS *
#************
#Joint loads
#Format:
#       Jt #, Joint DOF, Load (kips), Load history (LH) number
#
#Notes:
#       1) Joint DOF numbering is based upon the global structural axes.  For
#              the axes shown at the top of this file:  DOF 1 = x transl,
#              2 = y transl, 3 = z transl, 4 = x rot, 5 = y rot, and 6 = z rot
#       2) Joint DOFs may be assigned any LH number.  To apply two or three
#              loads to the same jt. with different LH's, note the following:
#          * By specifying a LH greater than 2, a third load may be assigned
#                       to a given joint direction.  However, LH's greater than
#                       2 are NOT mutually exclusive, i.e., the program stores
#                       at most three LHs, so if the user assigns LH 3 as a
#                       jt dof load and then applies a load to the same dof
#                       with a LH of 4, the LH 4 load will overwrite the LH 3
#                       load.
#       3) This section is not required if there are no joint loads (i.e., all
#          loads are either distributed element loads or accelerogram loads).

2 3 -30.0 1
3 3 -30.0 1
2 1 3.0 2


#************
*C_LOADHIST *
#************
#Load history:  Part I is required for all analyses.
#              Part II is required for all analyses except those with only
#              acclerogram loading (i.e., no joint loads).
#
#PART I
#------
#Format:
#       Number of LHs, Time step, Total time, Output every __ steps
#Notes:
#       1) The input shown below requests 10 time (load) steps
#       2) Output for this analysis is printed after every 2 load steps

2 0.1 1.0 2


#PART II
#-------
#For each load history (1 to number of LHs):
#       Line 1: Load history (LH) number, number of LH points
#       Successive Lines:
#              Individual LH points (50 max) -- (load fraction, time )

1 2
1.0 0.0
1.0 1.0

2 6
0.0 0.0
0.2 1.0
0.4 -1.0
0.6 2.0
0.8 -2.0
1.0 0.0
```

```
#************
*C_NEW-RAPH *
#************
#Newton-Raphson parameters
#Format:
#       Max # of iterations per load step
#
#Notes:
#       1) To turn off Newton-Raphson and run a simple step analysis, enter 1

10


#********
*C_TOLS *
#********
#Tolerances used throughout the program
#
#Notes:
#       1) The values given below are recommended for general analyses.

#Loading and bounding surface tolerance:
0.001

#Newton-Raphson convergence tolerance (work-based):
0.001

#Eigen analysis inverse iteration convergence (use 10^(-s) for s-digit accuracy)
0.000001


#*********
*C_FLAGS *
#*********
#Notes:
#       1) The flags must appear in the order shown below since they are read
#          sequentially by the program.
#       2) Default values are shown.
#       3) There are a total of 14 flags -- make sure all are present.

#**** SPECIAL PLOTFILE REQUEST ****
#---------------------------------
#Enter code number for specified 'cftmacro.plot' output
#Notes: Enter 0 if you do not know what this means
0

#**** ANALYSIS OPTION FLAGS ****
#------------------------------
#Enter the type of analysis--(S)tatic, (D)ynamic, or (E)igen:
#Notes:
#       1) For an Eigen-analysis, both dynamic and eigen analyses are performed.
#       2) Only static analysis is allowed at the present time.
S

#2nd-Order analysis (i.e., include geometric nonlinearities)? (Enter Y, YL, N)
#Notes:
#       1) 'Y' (default) requests use of both the lower order geometric
#          stiffness matrix and the higher order matrix, the latter of which
#          includes terms accounting for geom nonlinear effects due to moments.
#       2) 'YL' requests use of only the lower order matrix (axial force terms).
#       3) 'N' requests a 1st-order elastic or inelastic analysis
Y

#Inelastic analysis (i.e., include material nonlinearities)? (Y or N)
Y
```

```
#**** INPUT/OUTPUT FLAGS ****
#---------------------------
#Echo selected input parameters (member and joint info) to screen? (Y or N)
N

#Print only displacements and forces to 'cftmacro.out'? (Y or N)
N

#Output maximum and minimum forces and displacements? (Y or N)
#Notes:
#       1) These values are printed to 'cftmacro.max'.
#       2) This option is primarily for dynamic or cyclic static analyses.
#       3) This flag is cuirrently not used.
Y

#**** GLOBAL UNITS FLAG ****
#--------------------------
#Use Imperial(Kips and inches) or SI(KN and mm) in input and calculations?
#IMP or SI (IMP is default).
IMP

#**** MAXIMUM FRACTION OF ecc ALLOWED IN EACH LOAD INCREMENT **
# This flag helps the concrete plasticity model function properly.  The concrete
# plasticity function will sub-increment the strain increment given the maximum
# fraction of ec' allowed below (default = 0.1)
0.1

#**** USE CFT ELEMENTS WITH INTERLAYER SLIP? (DEFAULT = YES) ****
# If there is no slip allowed, the section B_SLIP_RESTRAINTS must not be used!
# The no slip case is currently unavailable.
YES

#**** USE CFT PASSIVE CONFINEMENT MODEL? (DEFAULT = NO) ****
# The confinement model is currently unfinish.  Kepp this flag set to NO
NO


#**** WHAT STEEL MATERIAL MODEL TO USE FOR CFTs? (DEFAULT = PRAGER) ****
# SHEN OR PRAGER
# Ensure that the steel section in B_CFT_XS corresponds to this flag
PRAGER


#**** WHAT STEEL MATERIAL MODEL TO USE FOR STEEL BEAMS? (DEFAULT = PRAGER) ****
# SHEN OR PRAGER
# Ensure that the steel section in B_STL_XS corresponds to this flag
PRAGER



#*******
*C_END *
#*******
```

Appendix D

List of Symbols

a	= dimension of the constant moment region for a flexural test
${}^{1}A^{m}$	= area of material *m* at C1
B	= tube width measurement
${}_{1}C_{ijkl}$	= material constitutive tensor at C1
d	= differentiation
$\{\Delta d^{nat}\}$	= incremental natural element deformation vector
D	= tube depth measurement
D_1, D_2	= distance measurements used for subassembly drift rotation measurement
e	= eccentricity of applied axial force
e	= distance of computed node location from theoretical location
e_i	= vector used in the penalty function formulation containing the global constraint equation
${}_{2}e_{ij}$	= engineering strain tensor in C2
${}_{1}e_{ij}$	= linear Green-Lagrange strain terms in C1
Δe_{xx}	= incremental strain at a point measured in the direction of the element centroid
Δe_{xy}, Δe_{xz}	= incremental shear strains at a point

Δe_m^m = incremental elongation between the i-end node and the midpoint node of the material m

Δe^m = incremental elongation between the i-end node and the j-end node of the material m

Δe^{sc} = incremental displacement of the concrete i-end node with respect to the corotational axes (which occurs due to slip)

${}^1E^m$ = uniaxial tangent modulus of material m at C1

E_{sh} = strain hardening modulus of steel

${}^1EA_i^m$ = axial rigidity at the i-end of the element in material m at C1

${}^1EI_{yyi}^m$ = flexural rigidity about the y-axis at the i-end of the element in material m at C1

${}^1EI_{zzi}^m$ = flexural rigidity about the z-axis at the i-end of the element in material m at C1

${}^1EI_{yzi}^m$ = modulus times second moment of the area about the y and z-axes at the i-end of the element in material m at C1

${}^1EQ_{yi}^m$ = modulus times first moment of the area about the y-axis at the i-end of the element in material m at C1

${}^1EQ_{zi}^m$ = modulus times first moment of the area about the z-axis at the i-end of the element in material m at C1

f_{bond} = bond strength of the slip interface

f'_c = concrete compressive strength

f_r = steel residual stress

f_u = steel ultimate strength

f_y = steel yield strength

${}^2f_i$ = body forces in C2

$\{\Delta f^{nat}\}$ = incremental natural element force vector

F_2 = concrete constitutive model parameter which accounts for the multiaxial stress state of the concrete

F_i = generic force resultant or rigidity term at the i-end of a member

$\{F_m\}$ = vector of midpoint forces

H = applied horizontal load

H^P = plastic modulus of concrete

i = simplification variable equal to x/L

^2I = steel-concrete interface at C2

$\hat{k}$ = stiffness per unit area of the slip interface

k = tangent stiffness of the slip interface per unit length

k_{slip} = initial stiffness of the slip interface per unit length

K = damage parameter used for the concrete constitutive model

K_{max} = maximum value of the damage parameter K achieved in the loading history

$[K^{condensed}]$ = condensed natural element stiffness matrix

$[K^e]$ = local element stiffness matrix, including geometric nonlinear terms

$[K_t^G]$ = global tangent stiffness matrix

$[K^{nat}]$ = natural element stiffness matrix

$[K_e^{nat}]$ = natural element elastic stiffness matrix

$[K_{g1}^{nat}]$ = natural element low-order geometric stiffness matrix

$[K_{g1}^{nat}]^*$ = natural element low-order geometric stiffness matrix including the end-of-step axial force (used in force recovery)

$[K_{g2}^{nat}]$ = natural element high-order geometric stiffness matrix

L = element length

L_i = length of the steel-concrete interface

m = shear span for a flexural test

M = applied bending moment

M_o = ultimate moment a member can sustain

${}^1M_{yi}^m$ = internal bending moment about the y-axis at the i-end of the element in material m at C1

${}^1M_{zi}^m$ = internal bending moment about the z-axis at the i-end of the element in material m at C1

$\hat{n}$ = unit vector

${}_1\hat{n}$ = unit vector at C1

$< N_d >$ = shape function for the term d in vector form

p = point inside the element volume

P = applied axial force

P_y = axial force at yield

P_{cr} = Euler buckling load

$P_{\max}$ = maximum observed axial load for a column test

${}_i^j P^m$ = difference in axial force in material m between end j and end i

${}^1P_i^m$ = internal axial force at the i-end of the element in material m at C1

Q = applied shearing force

$\Delta\Re$ = incremental applied load vector for an element

$\{\Delta R\}$ = vector of global incremental applied loads

$\{rb\}$ = vector form of $[RB]$ containing deformation terms

$[RB]$ = matrix containing the rigid body geometric nonlinear stiffness terms (external stiffness)

${}^2S$ = surface of the element in configuration C2

${}_1^2S_{ij}$ = second Poila-Kirchoff stress tensor (PK2) measured at C2 with respect to C1

t = tube thickness

${}^2t_i$ = surface tractions in configuration C2

T = torque

$_2u_i$ = element deformations measured with respect to configuration C2

Δu_c^m = incremental deformation of the element centroid in the corotational x-axis direction for material m

Δu^m = incremental deformation of any point in the element volume in the corotational x-axis direction for the material m

$\{\Delta U\}$ = vector of global incremental displacements

$\{U_i^*\}$ = right-hand side of the global constraint equation used to define penalty functions

Δv_c^m = incremental deformation of the element centroid in the corotational y-axis direction for material m

Δv^m = incremental deformation of any point in the element volume in the corotational y-axis direction for material m

V = applied shear force

V = applied gravity load

^2V = volume of the element in configuration C2

$^1V^m$ = volume of material m at C1

Δw_c^m = incremental deformation of the element centroid in the corotational z-axis direction for the material m

Δw^m = incremental deformation of any point in the element volume in the corotational z-axis direction for the material m

W = applied shearing force

x = distance measured along corotational x-axis

y = distance measured along corotational y-axis

z = distance measured along corotational z-axis

α = constant used to apply penalty functions

α = angle to the major axis at which an eccentrically applied axial load is located

$\Delta\alpha$ = incremental rotation of a node about the global X-axis

β = ratio of the load applied at the connections to the total applied load for a connection test

$\Delta\beta$ = incremental rotation of a node about the global Y-axis

$\Delta\gamma$ = incremental rotation of a node about the global Z-axis

δ = midpoint displacement of a flexural test

δ = variational symbol referring to small perturbations from the equilibrium state

Δ = change over the increment C1 to C2

Δ = deflection of an axially loaded column

$\varepsilon_{p\ initial}$ = initial plastic strain used in the steel constitutive model

${}_1\varepsilon_{ij}$ = Green-Lagrange strain measured with respect to C1

ε^{s} = steel strain

${}_1\eta_{ij}$ = nonlinear Green-Lagrange strain terms

${}^2\pi$ = stress in the slip interface at C2

θ = rotation

θ_{RB} = rigid body rotation

$\Delta\theta_x$ = incremental torsional rotation from the i-end node to the j-end node

$\Delta\theta_{yi}^{m}$ = incremental rotation of the i-end node about the y-axis of the material *m*

$\Delta\theta_{yj}^{m}$ = incremental rotation of the j-end node about the y-axis of the material *m*

$\Delta\theta_{zi}^{m}$ = incremental rotation of the i-end node about the z-axis of the material *m*

$\Delta\theta_{zj}^{m}$ = incremental rotation of the j-end node about the z-axis of the material *m*

ρ = perimeter of steel-concrete interface

${}^1\tau^{m}$ = uniaxial stress in material *m* at C1

${}^2\tau_{ij}$ = Cauchy stress tensor measured in configuration C2

$[\Omega]^{18x12}$ = natural-to-local transformation matrix

${}_2\psi$ = deformation of the slip interface measured with respect to C2 (scalar)

$\Delta\psi$ = incremental deformation in the slip layer

${}^1\zeta^m_{yyi}$ = internal second moment of the stress about the y-axis at the i-end of the element in material *m* at C1

${}^1\zeta^m_{yzi}$ = internal second moment of the stress about the y and z-axes at the i-end of the element in material *m* at C1

${}^1\zeta^m_{zzi}$ = internal second moment of the stress about the z-axis at the i-end of the element in material *m* at C1

<> = row vector

{} = column vector

' = differentiation with respect to x

References

Al-Amery, R. and Roberts, T. (1990). "Nonlinear Finite Difference Analysis of Composite Beams with Partial Interaction," *Computers & Structures*, Vol. 35, No. 1, pp. 81-87.

Alostaz, Y. M. and Schneider, S. P. (1996). "Connections to Concrete-Filled Tubes," Paper No. 748, Proceedings of the Eleventh World Congress on Earthquake Engineering, Alcocer, S. (ed.), Acapulco, Mexico, 23-28 June 1996, Elsevier Science, New York.

Amadio, C. and Fragiacomo, M. (1993). "A Finite Element Model For the Study of Creep and Shrinkage Effects in Composite Beams with Deformable Shear Connections," *Costruzioni Metalliche*, No. 4, pp. 213-228.

American Institute of Steel Construction (1993). *Load and Resistance Factor Design Specification for Structural Steel Buildings*, 2nd ed., AISC, Chicago, Illinois.

American Institute of Steel Construction (1994). *Manual of Steel Construction, Load and Resistance Factor Design*, 2nd ed., AISC, Chicago, Illinois.

American Concrete Institute (ACI) (1995). *Building Code Requirements for Reinforced Concrete Structures (ACI 318-95) and Commentary (ACI 318R-95)*, ACI, Farmington Hills, Michigan.

American Society of Civil Engineers (1982). "State-of-the-Art Report on Finite Element Analysis of Reinforced Concrete," ASCE Task Committee, Nilson, A. (chairman), ASCE, New York.

Ameur-Moussa and Buyukozturk (1990). "A Bounding Surface Model for Concrete," *Nuclear Engineering and Design*, Vol. 121, pp. 113-125.

Architectural Institute of Japan (AIJ) (1980). *AIJ Standard for Structural Calculation of Mixed Tubular Steel-Concrete Composite Structures*, Architectural Institute of Japan.

Aribert, J. M. (1995). "Influence of Slip of the Shear Connection on Composite Joint Behavior," *Connections in Steel Structures II*, Proceedings of the Third International Workshop, Bjorhovde, et al. (eds.), Trento, Italy, May, 1995, Elsevier Science, London, U.K., pp. 11-22.

Azizinamini, A., Prakash, B., Prishtina, B., and Salmon, D. C. (1992a). "Through Connection Detail for Composite Columns in High-Rise Buildings," Proceedings of the SSRC Annual Technical Meeting, Milwaukee, Wisconsin, 6-7 April 1992, pp. 225-236.

Azizinamini, A., Prakash, B., Prishtina, B., and Salmon, D. C. (1992b). "New Steel Beam to Composite Column Connection Detail," *Composite Construction in Steel and Concrete II*, Proceedings of the Engineering Foundation Conference, Easterling, W. S. and Roddis, W. M. (eds.), Potosi, MO, 14-19 June 1992, ASCE, New York, NY, pp. 854-868.

Azizinamini, A. and Prakash, B. (1993a). "Innovative Connection Detail for High-Rise Buildings," *Structural Engineering in Natural Hazards Mitigation*, Proceedings of the ASCE Structures Congress '93, Irvine, CA, 19-21 April 1993, ASCE, New York, NY, pp. 1220-1225.

Azizinamini, A. and Prakash, B.(1993b). "Tentative Design Guideline for a New Steel Beam Connection Detail to Composite Tube Columns," *Engineering Journal*, AISC, Vol. 30, No. 3, 3rd Quarter 1993, pp. 108-115.

Azizinamini, A. and Shekar, Y. (1994). "Rigid Beam-to-Column Connection Detail for Circular Composite Columns," Proceedings of the ASCE Structures Congress '94, ASCE, New York, NY, pp. 1155-1160.

Bathe, K. (1982). *Finite Element Procedures in Engineering Analysis*, Prentice-Hall, Inc., Englewood Cliffs, NJ, 735 pp.

Bode, H. (1976). "Columns of Steel Tubular Sections Filled with Concrete Design and Applications," *Acier Stahl*, No. 11/12, pp. 388-393.

Bradford, M. and Gilbert, R. (1992). "Composite Beams with Partial Interaction Under Sustained Loads," *Journal of Structural Engineering*, ASCE, Vol. 118, No. 7, pp. 1871-1883, July.

Bridge, R. Q. (1976). "Concrete Filled Steel Tubular Columns," *Report No. R283*, School of Civil Engineering, University of Sydney, Sidney, Australia.

BS5400 - Part 5 (1979). *Steel, Concrete, and Composite Bridges. Code of Practice for the Design of Composite Bridges*, British Standards Institution.

Buyukozturk and Ameur-Moussa (1988). "A Bounding Surface Model for Concrete," *Bulletin of the Technical University of Istanbul*, Vol. 41, pp. 169-199.

Carrasquillo, R. L., Nilson, A. H., and Slate, F. O. (1981). "Properties of High-Strength Concrete Subjected to Short-Term Loads," *Journal of the American Concrete Institute*, Vol. 78, No. 3, May, pp. 171-178.

Cederwall, K., Engstrom, B., and Grauers, M. (1990). "High-Strength Concrete Used in Composite Columns," Second International Symposium on Utilization of High-Strength Concrete, Hester, W. T. (ed.), Berkeley, CA, May 1990, pp. 195-214.

Challa, V. and Hall, J. (1994). "Earthquake Collapse Analysis of Steel Frames," *Earthquake Analysis and Structural Dynamics*, Vol. 23, pp. 1199-1218.

Chen, E. S. and Buyukozturk, O. (1985). "Constitutive Model for Concrete in Cyclic Compression," *Journal of Engineering Mechanics*, ASCE, Vol. 111, 797-813.

Chen, W. F. and Chen C. H. (1973). "Analysis of Concrete-Filled Steel Tubular Beam-Columns," *Memoires*, IABSE, Vol. 33, No. II, 1973, pp. 37-52.

Chen, W. F. and Lui, E. M. (1987). *Structural Stability - Theory and Implementation*, Elsevier Applied Science, New York, NY.

Chen, W. F. and Toma, S. (1994). *Advanced Analysis of Steel Frames - Theory, Software, and Applications,* CRC Press, Boca Raton, FL, 384 pp.

Clarke, M. J. (1992), "The Behavior of Stressed-Arch Frames," Ph.D. dissertation, School of Civil and Mining Engineering, University of Sydney, Sydney, Australia, August.

Clarke, M. J., Bridge R. Q., Hancock, G. J., and Trahair, N. S. (1993). "Benchmarking and Verification of Second-Order Elastic and Inelastic Frame Analysis Programs," *Plastic Hinge Based Methods for Advanced Inelastic Analysis and Design of Steel Frames*, White, D. W. and Chen, W. F. (eds.), Structural Stability Research Council, Bethlehem, PA.

Cook, R. D. (1981). *Concepts and Applications of Finite Element Analysis*, John Wiley & Sons, New York, NY, 2nd ed., 537 pp.

Council on Tall Buildings and Urban Habitat (1979). *Structural Design of Tall Steel Buildings*, Monograph on the Planning and Design of Tall Buildings, Vol. SB, ASCE, New York, NY, pp. 671-680.

Crisfield, M. A. (1991). *Nonlinear Finite Element Analysis of Solids and Structures*, John Wiley & Sons, New York, NY.

Dafalias and Popov (1977). "Cyclic Loading for Materials with a Vanishing Elastic Region," *Nuclear Engineering and Design*, Vol. 41, No. 2, pp. 293-302.

Dunberry, E., LeBlanc, D., and Redwood, R. G. (1987). "Cross-Section Strength of Concrete-Filled HSS Columns at Simple Beam Connections," *Canadian Journal of Civil Engineering*, Vol. 14, No. 2, pp. 408-417.

El-Tawil, S., Sanz-Picon, C. F., and Deierlein, G. G. (1993). "Applying the Fiber Element Technique to Composite Beam-Columns," in preparation.

El-Tawil, S. and Deierlein, G. G. (1996). "Inelastic Dynamic Analysis of Mixed Steel-Concrete Space Frames," *Structural Engineering Report No. 96-5*, School of Civil and Environmental Engineering, Cornell University, Ithaca, NY.

Elnashai, A. and Elghazouli, A. (1993). "Performance of Composite Steel/Concrete Members Under Earthquake Loading. Part I: Analytical Model," *Earthquake Engineering and Structural Dynamics*, Vol. 22, pp. 315-345.

Fetterer, K. A. and Hajjar, J. F. (1997). "Prototype Designs of Unbraced Composite Frame Structures Using Concrete-Filled Steel Tube Beam-Columns," *Report No. ST-96-7*, Department of Civil Engineering, University of Minnesota, Minneapolis, MN, in preparation.

Gardner, N. J. and Jacobson, E. R. (1967). "Structural Behavior of Concrete Filled Steel Tubes," *Journal of the American Concrete Institute*, Vol. 64, No. 11, pp. 404-413.

Ge, H. and Usami, T. (1992). "Strength of Concrete-Filled Thin-Walled Steel Box Columns: Experiment," *Journal of Structural Engineering*, ASCE, Vol. 118, No. 11, 1992, pp. 3036-3054.

Goel, S. C. and Yamanouchi, H. (1992). "Proceedings of the US-Japan Workshop on Composite and Hybrid Structures," US-Japan Cooperative Research Program - Phase 5: Composite and Hybrid Structures, Berkeley, CA, 10-12 September 1992, 192 pp.

Gourley, B. and Hajjar, J. (1994). "Cyclic Nonlinear Analysis of Three-Dimensional Concrete-Filled Steel Tube Beam-Columns and Composite Frames," *Structural Engineering Report No. ST-94-3*, Department of Civil Engineering, University of Minnesota, Minneapolis, MN, November.

Gourley, B. C., Hajjar, J. F., and Schiller, P. H. (1995). "A Synopsis of Studies of the Monotonic and Cyclic Behavior of Concrete-Filled Steel Tube Beam-Columns," *Structural Engineering Report No. ST-93-5.2*, Department of Civil Engineering, University of Minnesota, Minneapolis, MN, June.

Grauers, M. (1993). "Composite Columns of Hollow Steel Sections Filled With High Strength Concrete," Ph.D. dissertation, Chalmers University, Göteborg, Sweden, June, 139 pp.

Hajjar, J. F. and Gourley, B. C. (1996a). "Representation of Concrete-Filled Steel Tube Cross-Section Strength," *Journal of Structural Engineering*, ASCE, Vol. 122, No. 11, November, pp. 1327-1336.

Hajjar, J. F., Gourley, B. C., and Olson, M. C. (for Part II) (1996b). "A Cyclic Nonlinear Model for Concrete-Filled Tubes. I. Formulation. II: Verification," *Journal of Structural Engineering*, ASCE, at press.

Hajjar, J. F., Gourley, B. C., Schiller, P. H., Molodan, A., and Stillwell, K. A. (1996c). "Seismic Analysis of Concrete-Filled Steel Tube Beam-Columns and Three-Dimensional Composite Frames," *Composite Construction III*, Proceedings of the Engineering Foundation, Irsee, Germany, 9-14 June 1996, ASCE, New York, NY, at press.

Hajjar, J. F., Gourley, B. C., and Stillwell, K. (1996d). Cyclic Analysis of Concrete-Filled Tubes and Design of Composite Frames, *Analysis and Computation*, Proceedings of the Twelfth Conference held in Conjunction with the ASCE Structures Congress '96, Cheng, F. Y. (ed.), Chicago, Illinois, 15-18 April 1996, ASCE, New York, NY, pp. 43-54.

Hajjar, J. F., Molodan, A., and Schiller, P. H. (1996e). "A Distributed Plasticity Model for Cyclic Analysis of Concrete-Filled Steel Tube Beam-Columns and Composite Frames," *Engineering Structures, Special Volume on Innovations in Stability Concepts and Methods for Seismic Design in Structural Steel*, December, at press.

Hajjar, J. F., Schiller, P. H., and Molodan, A. (1996f). "A Distributed Plasticity Model for Concrete-Filled Steel Tube Beam-Columns with Interlayer Slip," *Engineering Structures*, December, submitted for publication.

Hayashi, N., Fukumoto, T., Inoue, T., Akiyama, H., and Okada, T. (1995). "Shear-Flexural Behavior of Concrete-Filled Square Steel Tubular Columns using High Strength Materials," Proceedings of the Fourth Pacific Structural Steel Conference, Shanmugam, N. E. and Choo, Y. S. (eds.), Singapore, 25-27 October, 1995, Elsevier Science, Inc., Tarrytown, NY, 3 volumes.

Izzuddin, B., Karayannis, C., and Elnashai, A. (1993). "Advanced Nonlinear Formulation for Reinforced Concrete Beam-Columns," *Journal of Structural Engineering*, ASCE, Vol. 120, No. 10, October, pp. 2913-2934.

Ji, H.-L., Kanatani, H., Tabuchi, M., Ishikawa, M. (1990). "Study on Concrete Filled RHS Column to H Beam Connections Fabricated with HT Bolts, Part 1: Elemental Study," *Transactions of Architectural Institute of Japan,* No. 414, pp. 35-45.

Ji, H.-L., Kanatani, H., Tabuchi, M., and Kamba, T. (1991). "Behavior of Encased Concrete in RHS Column Subjected to Transverse Force from Beam Flange," Proceedings of the Third International Conference on Steel-Concrete Composite Structures, Wakabayashi, M. (ed.), Fukuoka, Japan, 26-29 September 1991, pp. 195-200.

Kamba, T., Kanatani, H., and Tabuchi, M. (1991). "Strength and Rigidity of Joint Panel of Concrete Filled CHS Column-to-Beam Connections," Proceedings of the Third

International Conference on Steel-Concrete Composite Structures, Wakabayashi, M. (ed.), Fukuoka, Japan, 26-29 September 1991, pp. 189-194.

Kanatani, H., Tabuchi, M., Kamba, T., Ji, H.-L., and Ishikawa, M. (1988). "A Study on Concrete Filled RHS Column to H-Beam Connections Fabricated with HT Bolts in Rigid Frames," *Composite Construction in Steel and Concrete*, Proceedings of the Engineering Foundation Conference, Buckner, C. D. and Viest, I. M. (eds.), Henniker, NH, 7-12 June 1987, ASCE, New York, NY, pp. 614-635.

Kanchanalai, T. (1977). "The Design and Behavior of Beam-Columns in Unbraced Steel Frames," AISI Project No. 189, Civil Engineering/Structures Research Laboratory Report (CESRL) No. 77-2, Department of Civil Engineering, Structures Research Laboratory, University of Texas at Austin, Austin, Texas, October.

Kato, B., Kimura, M., Ohta, H., and Mizutani, N. (1993). "Connection of Beam Flange to Concrete-Filled Tubular Columns," *Composite Construction in Steel and Concrete II*, Proceedings of the Engineering Foundation Conference, Easterling, W. S. and Roddis, W. M. (eds.), Potosi, MO, 14-19 June 1992, ASCE, New York, NY, pp. 528-538.

Kawaguchi, J., Morino, S., Atsumi, H., and Yamamoto, S. (1991a). "Strength Deterioration Behavior of Concrete-Filled Steel Tubular Beam-Columns Under Repeated Horizontal Loading," Proceedings of the Third International Conference on Steel-Concrete Composite Structures, Wakabayashi, M. (ed.), Fukuoka, Japan, 26-29 September 1991, pp. 119-124.

Kawaguchi, J., Morino, S., and Yasuzaki, C. (1991b). "Elasto-Plastic Behavior of Concrete-Filled Steel Tubular Three-Dimensional Subassemblages," Research Report of the Faculty of Engineering, Mie University, Vol. 16, December , pp. 61-78

Kawaguchi, J., Morino, S. and Sugimoto, T. (1996). "Elasto-Plastic Behavior of Concrete Filled Steel Tubular Frames," *Composite Construction III*, Proceedings of the Engineering Foundation Conference, Irsee, Germany, 9-14 June 1996, ASCE, New York, NY, at press.

Kitada, T. and Nakai, H. (1991). "Experimental Study on Ultimate Strength of Concrete-Filled Square Steel Short Members Subjected to Compression or Torsion," Proceedings of the Third International Conference on Steel-Concrete Composite Structures, Wakabayashi, M. (ed.), Fukuoka, Japan, 26-29 September 1991, pp. 137-142.

Klöppel, K. and Goder, W. (1957). "Traglastversuche mit ausbetonierten Stahlrohen und Aufstellung einer Bemessungsformel," *Der Stahlbau*, Berlin, Vol. 26, No. 1, January.

Lawson, R. S., Vance, V., and Krawinkler, H. (1994). "Nonlinear Static Push-Over Analysis - Why, When, and How?," Proceedings of the Fifth U.S. National Conference on

Earthquake Engineering, Chicago, Illinois, 10-14 July 1994, Earthquake Engineering Research Institute, Oakland, CA, Vol. 1, pp. 283-292

Lu, Y. and Kennedy, D. (1994). "Flexural Behavior of Concrete-Filled Hollow Structural Sections," *Canadian Journal of Civil Engineering*, Vol. 21, No. 1, Feb., pp. 11-130.

Mamaghani, I. H. P., Shen, C., Mizuno, E., and Usami, T. (1995). "Cyclic Behavior of Structural Steels. I: Experiments," *Journal of Engineering Mechanics*, ASCE, Vol. 121, No. 11, November, pp. 1158-1164.

Matsui, C. and Tsuda, K. (1987). "Strength and Behavior of Concrete-Filled Steel Square Tubular Columns with Large Width-Thickness Ratio," Proceedings of Pacific Conference on Earthquake Engineering, Vol. 2, Wellington, New Zealand, 1987, pp. 1-9.

Matsui, C. and Kawano, A. (1988). "Strength and Behavior of Concrete-Filled Tubular Trusses," Proceedings of the International Specialty Conference on Concrete Filled Steel Tubular Structures, Harbin, China, August 1988, pp. 113-119.

Matsui, C., Tsuda, K., and El-Din, H. (1993). "Stability Design of Slender Concrete Filled Steel Square Tubular Columns," Proceedings of the Fourth East Asia-Pacific Conference on Structural Engineering and Construction, Vol. 1, Seoul, South Korea, 20-22 September 1993, pp. 317-322.

Matsumura, H. and Konno, K. (1989). "Effects of Bond Stress Capacity on Structural Properties on Concrete-Filled Square Tube Frames," *Journal of Structural Engineering*, Architectural Institute of Japan, Vol. 35B, March, pp. 287-298.

Mattiasson, K. (1981). "Numerical Results for Large Deflection Beam and Frame Problems Analyzed by Means of Elliptical Integrals," *International Journal for Numerical Methods in Engineering*, Vol. 17, No. 1, pp. 145-153.

Molodan and Hajjar (1997). "A Cyclic Distributed Plasticity Model for Analysis of Three-Dimensional Concrete-Filled Steel Tube Beam-Columns and Composite Frames," Report ST-96-6, Department of Civil Engineering, University of Minnesota, Minneapolis, MN, in preparation.

Morales, Luisa E. (1994). "Object-Oriented Software and Advanced Analysis of Steel Frames," M.S. thesis, School of Civil Engineering, Purdue University, August.

Morino, S., Kawaguchi, J., Yasuzaki, C., and Kanazawa, S. (1993). "Behavior of Concrete-Filled Steel Tubular Three-Dimensional Subassemblages," *Composite Construction in Steel and Concrete II*, Proceedings of the Engineering Foundation Conference, Easterling, W. S. and Roddis, W. M. (eds.), Potosi, MO, 14-19 June 1992, ASCE, New York, NY, pp. 726-741.

Morishita, Y., Tomii, M., and Yoshimura, K. (1979a). "Experimental Studies on Bond Strength in Concrete Filled Circular Steel Tubular Columns Subjected to Axial Loads," *Transactions of the Japan Concrete Institute*, Vol. 1, pp. 351-358.

Morishita, Y., Tomii, M., and Yoshimura, K. (1979b). "Experimental Studies on Bond Strength in Concrete Filled Square and Octagonal Steel Tubular Columns Subjected to Axial Loads," *Transactions of the Japan Concrete Institute*, Vol. 1, pp. 359-366.

Neogi, P. K., Sen, H. K., and Chapman, J. C. (1969). "Concrete-Filled Tubular Steel Columns Under Eccentric Loading," *The Structural Engineer*, Vol. 47, No. 5, pp. 187-195.

Orito, Y., Sato, T., Tanaka, N., and Watanabe, Y. (1987). "Study on the Unbonded Steel Tube Concrete Structure," *Composite Construction in Steel and Concrete*, Proceedings of the Engineering Foundation Conference, Buckner, C. D. and Viest, I. M. (eds.), 7-12 June 1987, Henniker, NH, ASCE, New York, NY, pp. 728-737.

Packer, J. A. (1995). "Concrete-Filled HSS Connections," *Journal of Structural Engineering*, ASCE, Vol. 121, No. 3, March, pp. 458-467.

Pagnoni, T., Slater, J., Ameur-Moussa, R., and Buyukozturk, O. (1992). "A Nonlinear Three-Dimensional Analysis of Reinforced Concrete Based on a Bounding Surface Model," *Computers and Structures*, Vol. 43, No. 1, pp. 1-12.

Prager, W. (1956). "A New Method of Analyzing Stresses and Strains in Work-Hardening Plastic Solids," *Journal of Applied Mechanics*, Vol. 23, pp. 493-496.

Prion, H. G. L. and Boehme, J. (1989). "Beam-Column Behavior of Steel Tubes Filled With High Strength Concrete," Proceedings of the Fourth International Colloquium on Stability of Metal Structures, North American Session: Code Differences Around the World, New York, NY, April 18-19, 1989, Structural Stability Research Council, Bethlehem, PA, pp. 439-450.

Prion, H. G. L. and McLellan, A. B. (1992). "Connecting Beams to Concrete-Filled Steel Columns," Proceedings of the ASCE Structures Congress '92, Morgan, J. (ed.), San Antonio, TX, 13-16 April 1992, ASCE, New York, NY, pp. 918-921.

Ricles, J. M., Lu, L.-W., Sooi, T.-K., Vermaas, G. W., Graham, W. W., Jr. (1995). "Seismic Performance of Concrete Filled Tube Column-to-WF Beam Moment Connections," Proceedings of the Structural Stability Research Council Annual Technical Meeting, Kansas City, MO, 27-28 March 1995, SSRC, Bethlehem, PA, pp. 83-102

Roik, K. and Bergmann, R. (1992). "Composite Columns," *Constructional Steel Design: An International Guide*, Dowling, P. J., Harding, J. E., and Bjorhovde, R. (eds.), Elsevier Science Publishers Ltd., London and New York, 1992.

Sakino, K. and Tomii, M. (1981). "Hysteretic Behavior of Concrete Filled Square Steel Tubular Beam-Columns Failed in Flexure," *Transactions of the Japan Concrete Institute,* Vol. 3, pp. 439-446.

Salani, H. R. and Sims, J. R. (1964). "Behavior of Mortar Filled Steel Tubes in Compression," *Journal of the American Concrete Institute*, Vol. 61, No. 10, pp. 1271-1283.

Sanz-Picon, C. F. (1992). "Behavior of Composite Column Cross Sections under Biaxial Bending," M.S. thesis, School of Civil and Environmental Engineering, Cornell University, Ithaca, New York, January.

Shakir-Khalil, H. and Zeghiche, Z. (1989). "Experimental Behavior of Concrete-Filled Rolled Rectangular Hollow-Section Columns," *The Structural Engineer*, Vol. 67, No. 19, pp. 345-353.

Shakir-Khalil, H. and Mouli, M. (1990). "Further Tests on Concrete-Filled Rectangular Hollow-Section Columns," *The Structural Engineer*, Vol. 68, No. 20, pp. 405-413.

Shakir-Khalil, H. (1991). "Tests on Concrete-Filled Hollow Section Columns," Proceedings of the Third International Conference on Steel-Concrete Composite Structures, Wakabayashi, M. (ed.), Fukuoka, Japan, 26-29 September 1991, pp. 89-94.

Shakir-Khalil, H. (1993a). "Pushout Strength of Concrete-Filled Steel Hollow Sections," *The Structural Engineer*, Vol. 71, No. 13, 6 July, pp. 230-233.

Shakir-Khalil, H. (1993b). "Resistance of Concrete-Filled Steel Tubes to Pushout Forces," *The Structural Engineer*, Vol. 71, No. 13, 6 July, pp. 234-243.

Shakir-Khalil, H. (1993c). "Connection of Steel Beams to Concrete-Filled Tubes," Proceedings of the 5th International Symposium on Tubular Structures, Nottingham, England, UK, 5-ISTS, August, pp. 195-203.

Shakir-Khalil, H. and Hassan, N. (1994a). "Push Out Resistance of Concrete-Filled Tubes," *Tubular Structures VI*, Grundy, P., Holgate, A., and Wong, W. (eds.), Melbourne, Australia, 14-16 December 1994, A. A. Balkema, Rotterdam, the Netherlands, pp. 285-291.

Shakir-Khalil, H. (1994b). "Beam Connection to Concrete-Filled Tubes," *Tubular Structures VI*, Grundy, P., Holgate, A., and Wong, W. (eds.), Melbourne, Australia, 14-16 December 1994, A. A. Balkema, Rotterdam, the Netherlands, pp. 357-364.

Shakir-Khalil, H. and Al-Rawdan, A. (1995). "Behavior of Concrete-Filled Tubular Edge Columns," Proceedings of the Third International Conference on Steel and Aluminum Structures, ICSAS '95, Istanbul, Turkey, May 1995, pp. 515-522.

Shakir-Khalil, H. and Al-Rawdan, A. (1996). "Behavior of Concrete-Filled Tubular Internal Columns," *Composite Construction III*, Proceedings of the Engineering Foundation, Irsee, Germany, 9-14 June 1996, ASCE, New York, NY, at press.

Shen, C. (1993). "Development of a Cyclic Two-Surface Model for Structural Steels With Yield Plateau," Ph.D. dissertation, Nagoya University, Nagoya Japan, February, 1993.

Shen, C., Mamaghani, I. H. P., Mizuno, E., and Usami, T. (1995). "Cyclic Behavior of Structural Steels," *Journal of Engineering Mechanics*, ASCE, 121(11), 1165-1172.

Stolarski, H. K., Belytschko, T., and Lee, S-H. "A Review of Shell Finite Elements and Corotational Theories," *Computational Mechanics Advances*, Vol. 2, No. 2, April, pp. 125-212.

Structural Stability Research Council (SSRC) (1988). *Guide to Stability Design Criteria for Metal Structures*, 4th ed., Galambos, T. V. (ed.), , John Wiley & Sons, New York, NY, 786 pp.

Structural Stability Research Council (SSRC) (1993). *Plastic Hinge Based Methods for Advanced Analysis and Design of Steel Frames*, White, D. W. and Chen, W. F. (eds.), SSRC, Bethlehem, PA, 299 pp.

Sugano, S., Nagashima, T., and Kei, T. (1992). "Seismic Behavior of Concrete-Filled Tubular Steel Columns," Proceedings of the ASCE Structures Congress '92, Morgan, J. (ed.), San Antonio, TX, 13-16 April 1992, pp. 914-917.

Sully, R. M. and Hancock, G. J. (1994). "Behaviour of Cold-Formed SHS Beam-Columns," *Research Report No. R696*, School of Civil and Mining Engineering, University of Sydney, Sydney, Australia, September.

Sully, R. M. and Hancock, G. J. (1996). "Behaviour of Cold-Formed SHS Beam-Columns," *Journal of Structural Engineering*, ASCE, Vol. 122, No. 3, March , pp. 326-336.

Taucer, F., Spacone, E., and Filippou, F. (1991). "A Fiber Beam-Column Element for Seismic Response Analysis of Reinforced Concrete Structures," *Report No. UCB/EERC-91/17*, College of Engineering, University of California at Berkeley, December.

Tomii, M. and Sakino, K. (1979a). "Experimental Studies on the Ultimate Moment of Concrete Filled Square Steel Tubular Beam-Columns," *Transactions of the Architectural Institute of Japan*, No. 275, January, pp. 55-63.

Tomii, M. and Sakino, K. (1979b). "Elasto-Plastic Behavior of Concrete Filled Square Steel Tubular Beam-Columns," *Transactions of the Architectural Institute of Japan*, No. 280, June, pp. 111-120.

Tomii, M., Yoshimura, K., and Morishita, Y. (1980a). "A Method of Improving Bond Strength Between Steel Tube and Concrete Core Cast in Circular Steel Tubular Columns," *Transactions of the Japan Concrete Institute*, Vol. 2, pp. 319-326.

Tomii, M., Yoshimura, K., and Morishita, Y. (1980b). "A Method of Improving Bond Strength Between Steel Tube and Concrete Core Cast in Square and Octagonal Steel Tubular Columns," *Transactions of the Japan Concrete Institute*, Vol. 2, pp. 327-334.

Tomii, M. (1985). "Bond Check for Concrete-Filled Steel Tubular Columns," *Composite and Mixed Construction*, Proceeding of the U.S.-Japan Joint Seminar, Roeder C. (ed.), Seattle, Washington, 18-20 July 1984, ASCE, New York, NY, pp. 195-204.

Tsuji, B., Nakashima, M., and Morita, S. (1991). "Axial Compression Behavior of Concrete Filled Circular Steel Tubes," Proceedings of the Third International Conference on Steel-Concrete Composite Structures, Wakabayashi, M. (ed.), Fukuoka, Japan, 26-29 September 1991, pp. 19-24.

Uy, B. (1996). "Strength and Ductility of Fabricated Steel-Concrete Filled Box Columns," *Composite Construction III*, Proceedings of the Engineering Foundation, Irsee, Germany, 9-14 June 1996, ASCE, New York, NY, at press.

Virdi, P. J. and Dowling, K. S. (1980). "Bond Strength In Concrete Filled Steel Tubes," *IABSE Periodica*, August 1980, pp. 125-139.

Weaver, W. and Gere, J. M. (1990). *Matrix Analysis of Framed Structures*, Van Nostrand Reinhold, New York, NY, 546 pp.

Webb, J. (1993). "High-Strength Concrete: Economics, Design and Ductility," *Concrete International*, Vol. 15, No. 1, January, pp. 27-32.

White, D. (1986). "Material and Geometric Nonlinear Analysis of Local Planar Behavior in Steel Frames Using Interactive Computer Graphics," M.S. thesis, Program of

Computer Graphics and Department of Structural Engineering, Cornell University, June 1986.

White, D. and Hajjar, J. (1991). "Application of Second-Order Elastic Analysis in LRFD: Research to Practice," *Engineering Journal*, AISC, Vol. 28, No. 4, Fourth Quarter, pp. 133-148.

Yang, Y. B. and Kuo, S. R. (1994). *Theory and Analysis of Nonlinear Framed Structures*, Prentice-Hall, Inc., Englewood Cliffs, NJ, 579 pp.

Zienkiewicz, O. C. (1977) *The Finite Element Method*, McGraw-Hill, London, U.K., 787 pp.